ABSTRACT

Title of Dissertation: EVOLUTION OF THE MICROSTRUCTURE AND VISCOPLASTIC BEHAVIOR OF MICROSCALE SAC305 SOLDER JOINTS AS A FUNCTION OF MECHANICAL FATIGUE DAMAGE

Gayatri Cuddalorepatta, Doctor of Philosophy, 2010

Dissertation Directed By: Professor Abhijit Dasgupta, Department of Mechanical Engineering

The effect of mechanical cycling fatigue damage and isothermal aging histories on the evolution of the constitutive and fatigue responses, and microstructure of microscale SAC305 solder joints is investigated. In particular, the study examines if joint dependent behavior should be expected from as-fabricated and cycled microscale SAC305 joints that exhibit an initial non-homogenous coarse-grained Sn microstructure. In addition, the ability of traditionally used macroscale constitutive models based on continuum mechanics to represent the viscoplastic constitutive behavior of the non-homogenous as-fabricated microscale SAC305 specimens is explored. Insights into the effect of key microstructural features and dominant creep mechanisms influencing the measured viscoplastic behavior of SAC305 are provided using a multi-scale mechanistic modeling framework.

Modified lap-shear microscale SAC305 specimens are characterized using the thermomechanical microscale test setup (TMM). Microscale SAC305 solder specimens show significant piece-to-piece variability in the viscoplastic constitutive properties under identical loading histories in the as-fabricated state. The mechanical

response is strongly influenced by the grain microstructure across the entire joint, which is non-repeatable and comprises of very few highly anisotropic Sn grains. The statistical non-homogeneity in the microstructure and the associated variability in the mechanical properties in the microscale SAC305 test specimen are far more significant than in similar Sn37Pb specimens, and are consistent with those reported for functional microelectronics solder interconnects. In spite of the scatter, as-fabricated SAC305 specimens exhibit superior creep-resistance (and lower stress relaxation) than Sn37Pb.

Macroscale creep model constants represent the non-homogeneous behavior of microscale joints in an average sense. Macroscale modeling results show that the range of scatter measured from macroscale creep model constants is within the range of scatter obtained from the stress relaxation predictions. Stress relaxation predictions are strongly sensitive to the inclusion or exclusion of primary creep models.

The proposed multiscale framework effectively captures the dominant creep deformation mechanisms and the influence of key microstructural features on the measured secondary creep response of microscale as-fabricated SAC305 solder specimens. The multiscale model predictions for the effect of alloy composition on SAC solders provide good agreement with test measurements. The multiscale model can be extended to understand the effects of other parameters such as aging and manufacturing profiles, thereby aiding in the effective design and optimization of the viscoplastic behavior of SAC alloys.

Accumulated fatigue damage and isothermal aging are found to degrade the constitutive and mechanical fatigue properties of the solder. The scatter gradually

decreases with an increasing state of solder damage. Compared to the elastic-plastic and creep measurements, the variability in the fatigue life of these non-homogenous solder joints under mechanical fatigue tests is negligible.

Recrystallization is evident under creep and mechanical fatigue loads. Gradual homogenization of the Sn grain microstructure with damage is a possible reason for the observed evolution of scatter in the isothermal mechanical fatigue curves. The yield stress measurements suggest that SAC305 obeys a hardening rule different from that of isotropic or kinematic hardening. The measured degradation in elastic, plastic and yield properties is captured reasonably well with a continuum damage mechanics model from the literature.

EVOLUTION OF THE MICROSTRUCTURE AND VISCOPLASTIC BEHAVIOR OF MICROSCALE SAC305 SOLDER JOINTS AS A FUNCTION OF MECHANICAL FATIGUE DAMAGE

By

Gayatri Cuddalorepattta

Dissertation submitted to the Faculty of the Graduate School of the
University of Maryland, College Park, in partial fulfillment
of the requirements for the degree of
Doctor of Philosophy
2010

Advisory Committee:
Professor Abhijit Dasgupta, Chair/Advisor
Professor Hugh Bruck
Professor Bongtae Han
Professor Patrick McCluskey
Professor Lourdes Salamanca Riba

Dedication

To

the lost warriors in ‘the quest for the thesis’ – my two teeth and esophageal lining,

&

the TMM setup, for all the microscale joys and sorrows.

Acknowledgements

I would like to express my deepest and sincere gratitude to Prof. Dasgupta for instilling in me a passion for quality work and academic excellence. His research advising and philosophy which focuses on providing an approach rather than the solution itself has been one of the most invaluable training I have gained. I am grateful to him for his reassuring counsel during the ‘quagmires’ of my life and for the career counseling. The intense brainstorming sessions where ‘major surgeries’ were conducted on ‘apples and oranges’ up until 3 am will be greatly missed.

I would like to thank my committee members for their invaluable suggestions that helped towards significant improvement of my dissertation from the time of my proposal defense. I would like to acknowledge Profs. Bruck, Han, Balachandran, Solares, Bar-Cohen, and Profs. Sammakia and Andros from Binghamton University, for their inspirational career advices. The support of Zonta International and Surface Mount Technology Association (SMTA) is acknowledged.

I would like to thank Maureen Williams from NIST with a deep sense of gratitude for selflessly helping me out with the EBSD analysis in spite of her packed 60 hour work schedule. I struggled several years to obtain access to an EBSD facility which was critical to explaining the test results. This was made possible mainly due to Maureen. I would like to thank Dr. Ravi Gundakaram from ARCI, India, who was the first one to provide me with insights into the solder grain microstructure. I would like to acknowledge Drs. Kil-Won Moon, Mark Vaudin, and Adam Creuziger, from NIST, and Dr. Riba for their technical inputs on the OIM measurements.

Needless to say the testing conducted here was possible solely due to the immense help and cheerful company of the exchange students from Manheim University and the UMD undergraduate students (Sara, Andreas, Patrick, Roman, Dominik, Ermal, Ken, Andreas and Reza). I would like to extend a special thanks to Lyudmyla for transporting my samples and depriving me of exciting trips on I-495. The assistance of Moustafa on the TMM software is greatly appreciated. I would like to thank Prabhakar Gudla for helping me out with the image analysis, and Kiran Panchamgam whose love for MS Word saved the day.

The comradeship of all the lab members (A-team); present and past, is greatly appreciated. In particular, the companionship of Joe, Dan, Yuxun and Vidyu (my peers in the pursuit of the light at the end of the tunnel), Moustafa and Shiva Subbaraman proved very valuable in keeping my sanity at check. Graduate life would have been less gratifying if not for PhD comics! Apart from providing a constant source for procrastination, the comics provided solace in our weary lives and most importantly, illuminated that drawing cartoons was a viable career option!

I would like to thank my parents and family for their patience, encouragement and support. A special credit goes to my mother, Krupa Omprakash and Usha Virendra who have unconsciously been my role models on work ethics, professionalism and academic excellence since childhood. Last but not the least I would like to thank Pavan, who has been the rock of my life in more than one way! I appreciate his unfailing faith and belief in me while I chased my dreams on creepy solders. The final credit goes to the TMM setup and microscale SAC joints, for constantly opening up a can of worms as I approached the goal post!

Table of Contents

List of Tables

List of Figures

Chapter 1: Introduction

Solder is commonly used in a wide range of applications, such as electrical and mechanical interconnects in electronic packages and photovoltaic cells, and die attach adhesives in power modules (between the heat sink and chip). Solder is known to exhibit viscoplastic constitutive behavior, which can be conceptually partitioned for convenience into elastic, rate-dependent creep deformation and rate-independent plastic deformation[1-2]. Viscoplastic behavior can also be viewed in terms of unified rate-dependent theories such as that used in the well-known Anand's viscoplastic model [3]. However, in the current study the partitioned approach is adopted in order to better understand the competing damage mechanisms introduced by different microscale deformation mechanisms in the solder during complex life cycle environments.

Typical field conditions experienced by these products include cyclic fatigue loads. Solder fatigue is one of the critical failure modes in electronic packages during their service life. In-service mechanical loads on the packages can vary from high temperature, low strain-rate loads such as thermal cycling, power cycling, quasi-static isothermal mechanical cycling at elevated temperatures; to high strain-rate loads at relatively low temperatures, such as vibration, shock, drop and mechanical cycling at ambient temperatures.

From the fatigue damage point of view, the former class of loads causes damage dominated by cyclic creep-mechanisms, and the latter causes damage dominated by cyclic plastic mechanisms. Hence quantifying the viscoplastic constitutive and fatigue

behavior of solder is critical to the understanding of overall performance and reliability of electronic assemblies.

Prior to the ban of Pb products due to environmental reasons, eutectic Sn37Pb alloy had been the traditional choice for solder for decades. The Pb-free solder substitutes recommended by iNEMI [4] include binary eutectic alloys like Sn0.7Cu and Sn3.5Ag, as well as the ternary near-eutectic Sn3.8Ag0.7Cu (SAC387). In recent times, the industry has also opted for hypoeutectic SnAgCu (SAC) alloys with lower Ag percent, such as Sn3.0Ag0.5 (SAC305) and Sn1.0Ag0.5Cu (SAC105), to name a few, owing to their affordability and similarity to SAC387 in their mechanical response.

The reduced Ag % in the SAC alloy is expected to decrease the volume fraction of the intermetallics of Ag_3Sn dissolved in the bulk of the solder, thereby causing degradation in their viscoplastic creep constitutive (decrease in the creep resistance) and cyclic creep fatigue behavior (decrease in cycles to failure under identical cyclic loads). The current work focuses on the behavior of hypoeutectic SAC solders with low Ag%, at microscale length scales.

Comprehensive studies have been conducted on the benchmark Sn37Pb solder over the past few decades. However these studies cannot be directly extrapolated to Pb-free solders owing to the vastly different microstructure exhibited by the two. Sn37Pb solder comprises of Sn matrix with soft Pb islands that can deform significantly via grain boundary sliding. Pb-free solders such as SAC on the other hand comprise of Sn dendrites with hard intermetallic particles of Ag_3Sn and Cu_6Sn_5 embedded around the dendrites [5-9]. The intermetallics, when present in moderate

proportions, are beneficial to the mechanical behavior of solder since they reinforce the solder and also retard the extent of creep deformation via dislocation glide and grain boundary diffusion[10-11].

Thus it is evident that the contrasting microstructures and hence the underlying deformation mechanisms vary significantly in Sn37Pb and Pb-free solders. In general, Pb-free solders exhibit superior creep resistance and superior fatigue behavior under creep dominated loads such as thermal cycling, power cycling and quasi-static mechanical cycling compared to Sn37Pb solders [12-17]. Solder studies on Pb-free solders are not as comprehensive and thorough as the literature on Sn37Pb solders.

Hence, the current dissertation focuses on providing an improved understanding of the constitutive (elastic, plastic and creep) and durability (isothermal mechanical cyclic fatigue) behavior of SAC solder at micrometer length scales, using a combination of material characterization tests and multi-scale modeling approaches. The results of this study are applicable to the response of microscale length scale solder joints such as those seen in microelectronics (e.g. ball grid arrays), rather than to large-area interconnects seen in photovoltaic cells.

As stated above, a wide range of fatigue conditions are experienced by solder. This study however characterizes the fatigue response of solder under low temperature, high strain-rate mechanical cycling loads where plastic deformations dominate over creep deformations. These findings are therefore relevant to similar service conditions. The background and motivation for the current study are detailed in Section 1.1 of this chapter, followed by the problem statement and objectives of

this dissertation in Section 1.2. The scope and overview of the dissertation are provided in Section 1.3.

1.1 BACKGROUND AND MOTIVATION

Since the transition from Sn37Pb to Pb-free solders, a number of studies have focused on characterizing the constitutive and fatigue behavior of Pb-free solders. A detailed literature review on the material characterization and the modeling aspects of the constitutive and fatigue behavior as well as the microstructural aspects of Pb-free solders is provided in Sections 1.1.1-1.1.3. It should be noted here that the microstructural aspects reported here are relevant to and limited to high-Sn Pb-free solders such as SAC alloys and Sn3.5Ag alloys only (which exhibit similar microstructural features to SAC).

In general, the state-of-art on microstructure and deformation behavior reported here is not applicable to high-Sn Pb-free alloys with minor additions of rare earth elements (which exhibit a statistically homogenous microstructure compared to SAC at microscale dimensions [18-20]) or quaternary Pb-free alloys. Prior to addressing the state of art in the mechanical behavior of microscale SAC solders, the microstructure and the length scales associated with this solder need to be understood.

1.1.1. Microstructure of SAC Solders

SAC solders contain a high fraction of Sn with minor proportions of Ag and Cu. The liquidus surface plots for SnAgCu solder as calculated by Moon et al., [21] is presented in Figure 1-1 a-b. Based on their findings the near-eutectic composition of SAC solders is Sn3.5Ag0.9Cu with a melt temperature of 217°C (compared to 182°C

for Sn37Pb solder). Hence the homologous temperature at room temperature is around 0.6, and significant viscoplastic creep deformation is expected in these solders.

Upon solidification, the solder is expected to undergo significant undercooling, that results in a microstructural features of several length scales (from nano-scale to micro-scale to macro-scale features) [22-24]. Liquid SAC solder on solidification comprises of pure Sn phase with hard, brittle intermetallic (IMC) particles of Ag_3Sn and Cu_6Sn_5 dispersed in the bulk and an interfacial intermetallic layer of Cu_3Sn and Cu_6Sn_5 at the interface of the solder and Cu metallization layers. The intermetallic compositions are dependent on the metallization composition. If the metallization layer at the interface of solder and pad varies (e.g., Ni), additional intermetallic compositions (Ni-Sn-Cu) are possible [13].

In comparison, traditionally used Sn37Pb solder comprises of soft islands of Pb embedded in Sn matrix. The Pb islands can accommodate creep deformation via grain boundary sliding. Figure 1-1 c shows the phase diagram of Sn37Pb from literature [25-26]. The melting temperature of Sn37Pb solder is 182°C, which is lower than that of SAC solders. The lower melt temperature combined with the presence of soft Pb islands in Sn37Pb (as opposed to hard intermetallics in SAC solder) causes higher creep damage in Sn37Pb compared to the SAC solders.

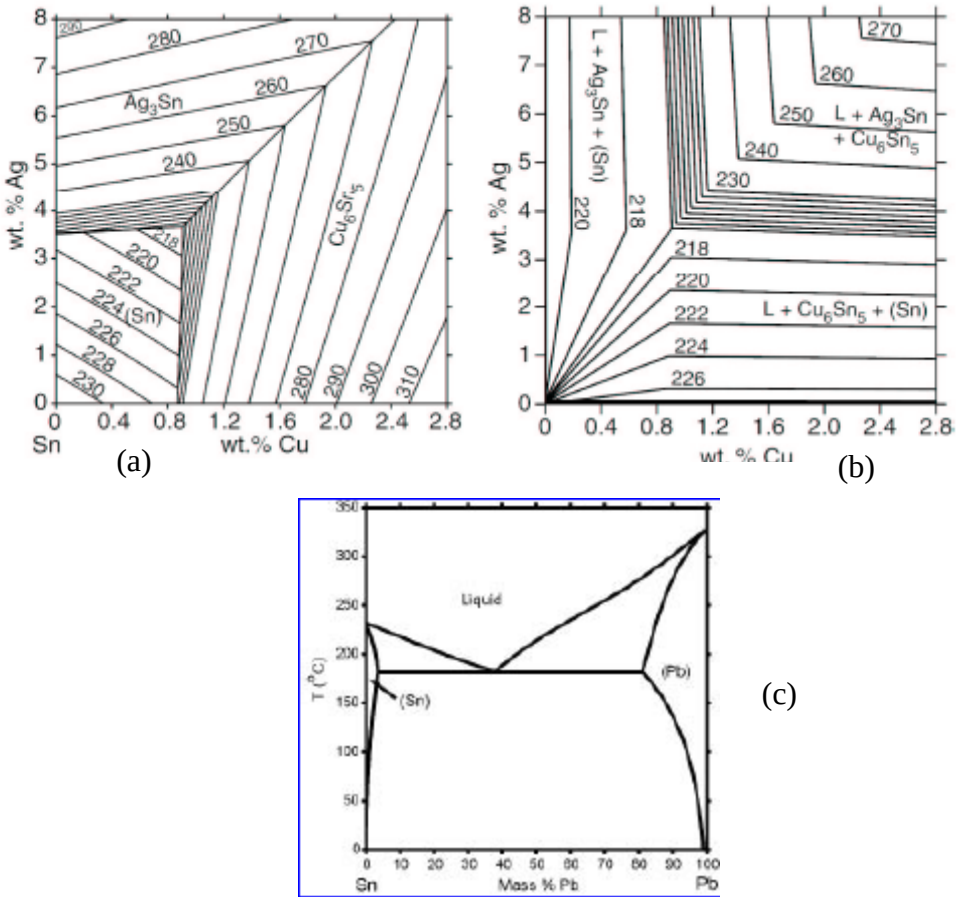

Figure 1-1: a) Liquidus surface, b) Surface of secondary solidification. Image adapted from the results for ternary eutectic composition of 3.66 wt % Ag, 0.91 wt % Cu from [21] (c) Phase diagram of SnPb solder. Image adapted from [25-26]

1.1.1.1. Length Scales and Lack of Statistical Homogeneity in Undamaged Microscale SAC Joints

The microstructural features discussed here are relevant to SAC solder that has not been subjected to any mechanical loads, hence the term ‘undamaged”. Sn solidifies into dendritic structures with a long primary branch and smaller dendritic arms branching from it. A three-dimensional view of the solidification of the Sn

phase into the dendritic arms is provided in Figure 1-2 a. The dendritic arms are nodular in shape and appear as elliptical shapes upon cross-sectioning to a 2-D plane, as shown in Figure 1-2 b-d. Figure 1-2-d is an image adapted from the results of Dutta [27]. Depending on the orientation of the dendritic growth relative to the loading surface, the primary arm could extend across the entire joint dimensions in a microscale scale joint. The smaller dendritic arms are generally around 5-20 μm long in 2-D cross-sections.

The IMC features discussed here are relevant to SAC solders that use copper pad metallization. The region surrounding the Sn dendrite has nano-scale dimension Ag_3Sn intermetallics (IMC) embedded in a pure Sn matrix (Figure 1-2 c-d). This region is termed as the 'eutectic Sn-Ag' phase in the literature. In addition to the nano-scale IMCs, Ag_3Sn also appears as micron-scale IMCs, in the form of platelets with high aspect ratios. In 2-D cross-sections, these wafer-shaped platelets appear as long needle-like shapes. In addition, hollow columnar Cu_6Sn_5 IMCs of micron-scale hexagonal cross-sections are also evident in the bulk of the solder (Figure 1-2 c). In addition, intermetallic layers of Cu_3Sn and Cu_6Sn_5 at the interface of the solder and Cu metallization layers is evident in (Figure 1-2 f).

Recent findings in literature reveal an added complexity (and length scale) associated with the microstructure of microscale SAC solder. Studies reveal that microscale SAC joints comprise of very few grains of highly anisotropic Sn crystals [28-39] across the entire joint area [24, 40-50]. The grain microstructure reported by Sundelin[51] in BGA joints are adapted in Figure 1-2e to demonstrate the coarse-grained nature of these microscale joints. Thus, even though the Sn dendritic

structures and the macro and micro-scale IMCs exhibit a fairly repeatable and periodic distribution and configurations, the presence of very few Sn grains (very few crystallographic orientations), gives the joint a highly non-homogenous microstructure.

Thus the characteristic length scale of the microscale SAC joint is comparable to the structural length scale. This lack of statistical homogeneity and isotropy poses serious challenges in the material characterization of such micro-scale joints since each joint therefore exhibits unique mechanical response under identical loading conditions. In summary, the key microstructural features of microscale SAC joints introduce a wide range of length scales varying from nano-scale dimensions to the structural-scale dimensions of the joint.

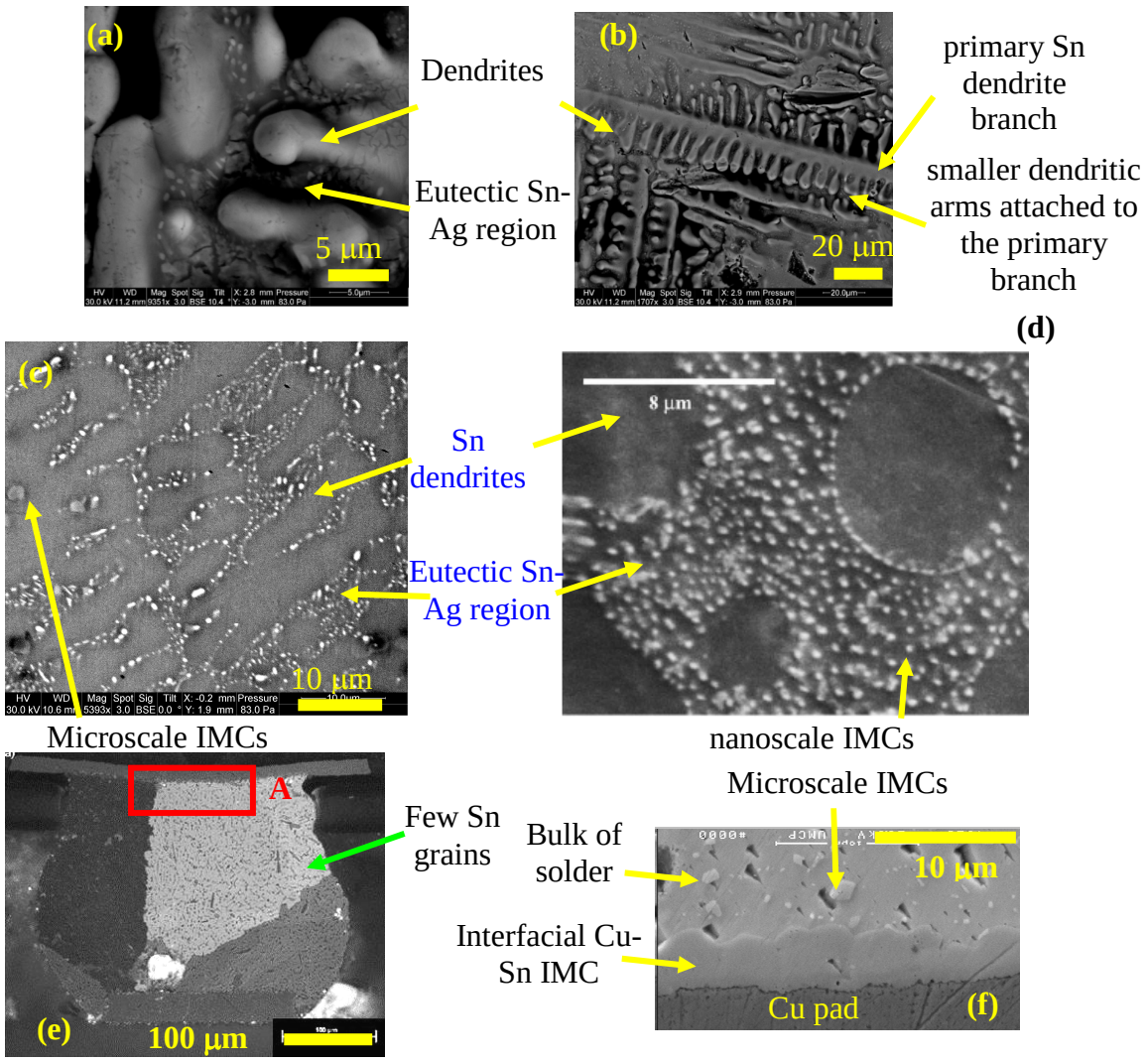

Figure 1-2: Microstructural features in microscale as-fabricated SAC305 solder (a)-(b) 3-D dendritic structures showing the primary branch and the smaller arms (c) 2-D microstructure of the dendritic structures shown in (a) after cross-sectioning. Eutectic Sn-Ag regions and microscale Cu6Sn5 IMCs in bulk, (d) Nanoscale IMCs in dendritic regions from [27] (e) Coarse-grained Sn microstructure in microscale BGA joints from [51], and (f) Intermetallic layer at the interface of copper and solder at region A in (e). Images 1(d) and (e) have been adapted from literature.

1.1.1.2. Microstructural Evolution of As-Fabricated Microscale SAC Joints

In general, most material models are derived from measurements conducted on specimens consisting of undamaged, pristine material. These specimens have not been subjected to any additional loadings past the reflow (except for required pre-conditioning protocols). These specimens are termed as “as-fabricated” joints in this study. However, in reality, the material is subject to an increasing density of homogeneous material damage (in the form of decreasing load-bearing areas due to distributed microcracks and voids), as well as changes to the geometric configurations of key microstructural features such as IMCs, Sn grains and dendrites .

Understanding the microstructural evolution and the length scales involved in the evolved state is of utmost importance to any material characterization study, since it establishes the applicability of the material models developed in the as-fabricated state. Modeling the deformation behavior of the solder material throughout its entire service life, with material properties measured from the initial as-fabricated state, yields non-conservative estimates of the mechanical response (such as fatigue life, damage, strains to name a few). In particular, understanding the microstructural evolution of the Sn grain structure in SAC microscale joints under cyclic loading is extremely important, in order to assess if there is any change in the extent of non-homogeneity and the characteristic length scale exhibited by these initial coarse-grained joints.

Some evidence in the literature exists to suggest that the coarse-grained, non-homogenous Sn-grain microstructure in microscale SAC joints eventually recrystallizes into many finer grains of Sn, transforming the joint microstructure to a

statistically homogenous distribution with respect to the grain texture. In addition, macro damage and micro cracking is also induced by fatigue damage. Table 1-1 provides the state-of-art on the occurrence study of recrystallization under various cyclic fatigue loads.

It should be noted here that the studies reporting the occurrence of recrystallization under isothermal mechanical cycling loads (which is one of the focus of this dissertation) are very limited. Furthermore where available, the studies fail to obtain recrystallization in the joints or do not provide concrete quantitative proof of recrystallization due to the chosen image analysis technique (such as cross polarized microscopy, XPM).

Loads	Analysis Method	Solders	Specimen Type and Scale	Refs	Comments
Thermal cycling	XPM, OIM	SAC and Sn37Pb	Microscale and Bulk	[46, 48, 51-59]	
Power Cycling	XPM	SAC	Microscale	[55]	
Vibration	XPM	SAC and Sn37Pb	Microscale	[54, 60]	
Drop testing	XPM	SAC	Microscale	[61]	
Isothermal mechanical cycling	XPM, OIM	SAC	Microscale and Bulk	[43, 62-64]	[64] specifically investigated if recrystallization occurs and found none
Monotonic Creep	XPM, OIM	SAC	Microscale	[58, 65]	[58] provides quantitative details of the changes in grain orientations and configurations.

Table 1-1: Literature review on the study of recrystallization under cyclic fatigue loads. XPM refers to cross polarized microscopy and OIM refers to orientation imaging microscopy.

1.1.1.3. Dominant Deformation Mechanisms in Microscale SAC Joints

Traditionally used Sn37Pb solder is known to deform through grain boundary sliding [66]. Studies reveal that the presence of nanoscale IMCs of Ag_3Sn in SAC solder provides the benefits of dispersion strengthening. Nanoscale IMCS pin dislocations and retard creep deformation, thereby requiring the dislocations to climb over the IMCs [10]. Thus dislocation climb becomes the dominant rate-limiting creep mechanism. Hence the extent of creep deformation (climb) is dependent on the

volume fraction and dimensions of the IMCs and other obstacles to dislocation motion in the solder. In general, smaller dimensions and denser (higher volume fraction) distribution of nano-scale IMCs in the eutectic region facilitates dislocation climb.

The presence of the IMCs is also expected to restrict the extent of grain boundary sliding [10, 27, 67]. The dimensions of the large grains present in the as-fabricated state of SAC microscale joints suggest that grain boundary diffusion and sliding across such large grain boundary dimensions are not very likely. In comparison, the smaller dimensions of grain boundaries in the recrystallized SAC joints seem to suggest much more favorable diffusion paths compared to those in the coarse-grained, as-fabricated microstructure.

However to the best of the author's knowledge, the absence or presence of grain boundary sliding in the as-fabricated state and recrystallized state of SAC solders, respectively, has not been experimentally established conclusively in microscale SAC joints. Hence the possibility of grain boundary diffusion requires careful experimentation prior to ruling it out as a dominant creep mechanism in SAC.

1.1.1.4. Process Parameters Affecting the Microstructure of SAC Solders

The geometrical configurations and dimensions of each of the phases (Sn dendrites and IMCs) in the SAC solder are functions of several parameters such as manufacturing profile (reflow, soldering time, annealing method), aging histories, solder joint dimensions, composition of alloy and metallization layers, and loading histories [6-9, 55-56, 68-82]. It is worth noting here that the grain microstructure is insensitive to conditions such as aging [24] but is sensitive to the compositions of

solder alloys and metallization layers and the loading histories that cause material damage in the form of cracks and voids. Figure 3-6 in Chapter 3 reveals the insensitivity of the grain microstructures with isothermal room temperature aging.

An increase in the reflow time and temperature increases the volume fraction and size of IMCs formed in the bulk of the solder and at the interface of the metallization and the solder. While an increase in the amount of IMCs in bulk is beneficial, this is also accompanied by coarsening of the IMCs. Past a particular threshold size, additional coarsening can effectively degrade the dispersion strengthening capabilities of nano-scale IMCs. In addition, the coarsening of micro-scale IMCs in the bulk (that serve to provide reinforcement-strengthening), leads to loss of ductility and higher crack propagation rates, thereby degrading the creep and fatigue properties of the solder. Furthermore, the growth of interfacial IMC layers is also accelerated and could lead to a shift in the failure mode from bulk solder fatigue failure to interfacial intermetallic fracture.

Fast cooling rates (annealing) leads to smaller dendritic sizes and denser distribution of Ag_3Sn IMC particles in the eutectic regions (see ref. [75]**)**. However, the extent of IMCs formed in the fast cooling is expected to be lower than that when sufficient heat energy is retained in the system during slow cooling rate for solidification. Isothermal aging causes growth of the average dendritic size and IMC size and is hence detrimental to the constitutive and cyclic fatigue behavior of SAC joints.

1.1.1.5. Length Scale and Configuration of Test Specimen

The length scale of the test specimen used to measure the deformation behavior of SAC alloys has a significant effect on measured response. Since the microscale SAC joint exhibits significant non-homogeneity in the microstructure and mechanical response, it is extremely important that the configuration and length scales of test specimens should be comparable with those of functional solder joints used in surface mount packages. Current SMT packages comprise of solder interconnects of length scales of less than 1000 μm. At such micron-scale dimensions, the structural length scale of the solder joint is comparable to the characteristic length scale of solder microstructure, especially in many currently popular Sn-based Pb-free solders. Hence length-scale effects dominate and the microstructure of these microscale joints (and their material behavior) is significantly different from those of bulk specimens (>1 mm).

The importance of specimen size for measuring Pb-free solder behavior is further supported by studies that report significant differences in the mechanical response and microstructure of bulk specimens compared to micron-scale specimens [72, 80-81, 83-84]. Furthermore, when measuring the mechanical behavior and properties of materials, the test specimen should be designed to minimize the structural effects of the surrounding package architecture on the measured material response. Hence the literature relevant to understanding the material level (not component level) response of current solder joints should be obtained from microscale solder joints with minimal influence from the interfacing materials.

The specimen configuration should be designed such that a uniform stress distribution is obtained in the gage region for an accurate stress measurement during testing. For example, functional solder interconnects such as ball grid arrays have non-uniform stress states with stress concentrations occurring at the neck of the joint close to the pad areas. Hence the stress measured from the force measurements by utilizing the load bearing area represents the average stress state at best.

Similarly material level tests that utilize simplified test specimens such as shear specimens require appropriate design to obtain a uniform measurable stress state. Modified lap shear specimens with notch angles of 90° (Iosipescu specimens) are viable options since a reasonably uniform stress state is generated in the gage area [85-89]. A detailed review on the effect of the notch angles on the uniformity of the shear stress distribution is provided in the above reference. In addition, the uniformity of the stress distributions expected in the solder region of the Iosipescu specimen is studied in Section 5.3.2 in Chapter 5. However planar specimens such as Iosipescu specimens lack the three-dimensional microstructural and geometrical constraints induced in real functional BGA solder balls.

An important observation when using assembly level BGA packages as test specimens, is that the results represent the average behavior of arrays of many joints (e.g. in BGA packages) even though each individual joint is of micron-scale dimensions and might individually exhibit non-homogenous behavior due to its coarse grained nature [90]. On the same lines, compression creep behavior from nano-indentation type of test methodologies represents localized viscoplastic behavior

of the non-homogenous microscale joint and need high repeatability across various sections in the specimen to establish the range of measurements.

Furthermore, the use of bulk specimens also creates a gradient in the cooling rate across the entire specimen. Thus the dendritic and IMC distributions on the edges of the specimen exposed to the ambient are subject to a faster cooling rate compared to those in interior regions. This results in non-uniform geometric configurations across the entire specimen.

In addition the microscale solder joints would be expected to undergo a faster cooling rate than bulk specimens under similar profiles owing to the volume of solder present. It should be noted here that the measurements conducted on bulk specimens are not necessarily incorrect; these measurements are just not applicable to microscale solder applications where length scale effects exist. Bulk-scale SAC solder measurements are in fact best suited for modeling the behavior of large area solder interconnects such as those used in photovoltaic cells [91-92].

1.1.1.6. Alloy Composition and Loading Histories

The compositional changes relevant to SAC solder are addressed here. Literature pertaining to the best possible Pb-free alloys is beyond the scope of this dissertation and not included here. In particular, the effect of weight-fraction of Ag (1%-4%) in SAC alloys is addressed here. Increasing the weight-fraction of Ag in SAC solders is expected to increase the volume fraction of Ag_3Sn IMCs in the bulk of the solder.

In particular, the amount of nano-scale IMCs available for dispersion strengthening increases. The size of the IMCs is expected to be invariant if the manufacturing profile is unchanged. However, detailed microstructural analysis is

required to validate this hypothesis. The changes in the volume fraction of nano-scale IMCS (with increasing weight-fraction of Ag) support the observed improvement in the creep and fatigue properties with increasing Ag content in SAC [13, 15, 93], as shown in Chapter 3 and Chapter 6.

Changes in Ag content in SAC solders are not expected to change the grain configuration of the microscale SAC joints and coarse-grained, non-homogenous joints are expected for all SAC compositions [24]. However an addition of small quantities of rare earth elements to SAC causes statistically homogenous fine-grain configuration in the solder. This microstructure hence leads to characteristic length scales equal to the small Sn grain size or the Sn dendritic size. Thus the characteristic length scale in lanthanum doped Pb-free solder is an order of magnitude smaller than that in coarse-grained microscale SAC joints. Hence it is pertinent to ensure that the composition of the solder prior to testing the alloy is representative of that seen in functional solder joints.

Prior to characterizing the mechanical response of the solder, the microstructural and damage state needs to be verified. As expected, any prior loading histories in the form of mechanical loads or microstructural treatments significantly alters the distribution and configuration of the Sn dendrites, IMCs and the Sn grains, which in turn affect the dispersion strengthening characteristics and the homogeneity of the joints. In addition, any structural damage to the solder in the form of cracks and voids effectively weakens the load bearing capacity of the material.

1.1.2. Challenges

Significant literature exists on the constitutive and fatigue behavior of SAC solders. While each study independently provides useful contributions to the body of literature, the variability in results across different investigators does not permit direct comparisons of solder behavior across different studies. Hence this raises important questions regarding the source of variability as well as the right set of properties to be adopted for modeling solder behavior. For example, Figure 1-3 shows differences in the secondary creep measurements of Pb-free SAC from various investigators. The results comparing several studies has been provided by [94-95].

An examination of the microstructure of Pb-free solder and the test methodologies used reveals that each of the reports may be accurate within their own methodologies. The variations evident in the properties are primarily due to the complexity of the microstructure and constitutive behavior of Pb-free solders combined with the differences in test methodologies used. Specifically, the sources of the discrepancies in the reported properties can be classified as followed.

- Microstructural complexity of SAC solders and sensitivity to parameters such as
    - Fabrication methodology
    - Loading history prior to testing in terms of aging, state of solder damage (macrodamage and microcracking)
    - Alloy composition
    - Interfacing pad material

- Length scale of test specimen and repeatability of solder microstructure at the given length scale (Extent of statistical homogeneity exhibited by solder microstructure)
- Configuration of test specimen, which determines the stress state and uniformity of damage distribution.

As discussed in Section 1.1.1, the mechanical response of the solder is heavily dependent on the underlying microstructure, which is sensitive to processing, loading history and specimen length scales to name a few. Any changes in the microstructural features could generate significantly different material response. Apart from the sensitivity of the Sn dendrites and IMCs to the pre-test conditions, the existence of very few anisotropic Sn grains in the microscale SAC joint is expected to cause each joint to exhibit unique mechanical response [24].

An outcome of the non-homogenous behavior of microscale SAC joints is reflected in their thermal cycling fatigue behavior. In general the first joint to fail is the worst stressed joint, which could be the one at the package corner or that at the die corner. However, thermal cycling results of SAC plastic ball grid array (PBGA) components clearly show that the critical failure joints are not necessarily at the above stated expected locations [96]. Similar conclusions have been suggested from microstructural analysis by [22, 97].

Hence it is important that the mechanical measurements reported are referenced to the microstructure of the specimen/joint that provides the data. The pre-test solder condition needs to be explicitly specified to improve the applicability of the reported measurements. As an example, the measurements conducted in this study are

referenced to “as-fabricated”, “aged” and “state of solder damage”, to name a few. The state-of-art in the constitutive and fatigue behavior of microscale (and bulk) SAC solder is detailed in Section 1.1.3, and the unresolved research questions in the mechanical behavior of microscale SAC solder joints are discussed in Section 1.1.4.

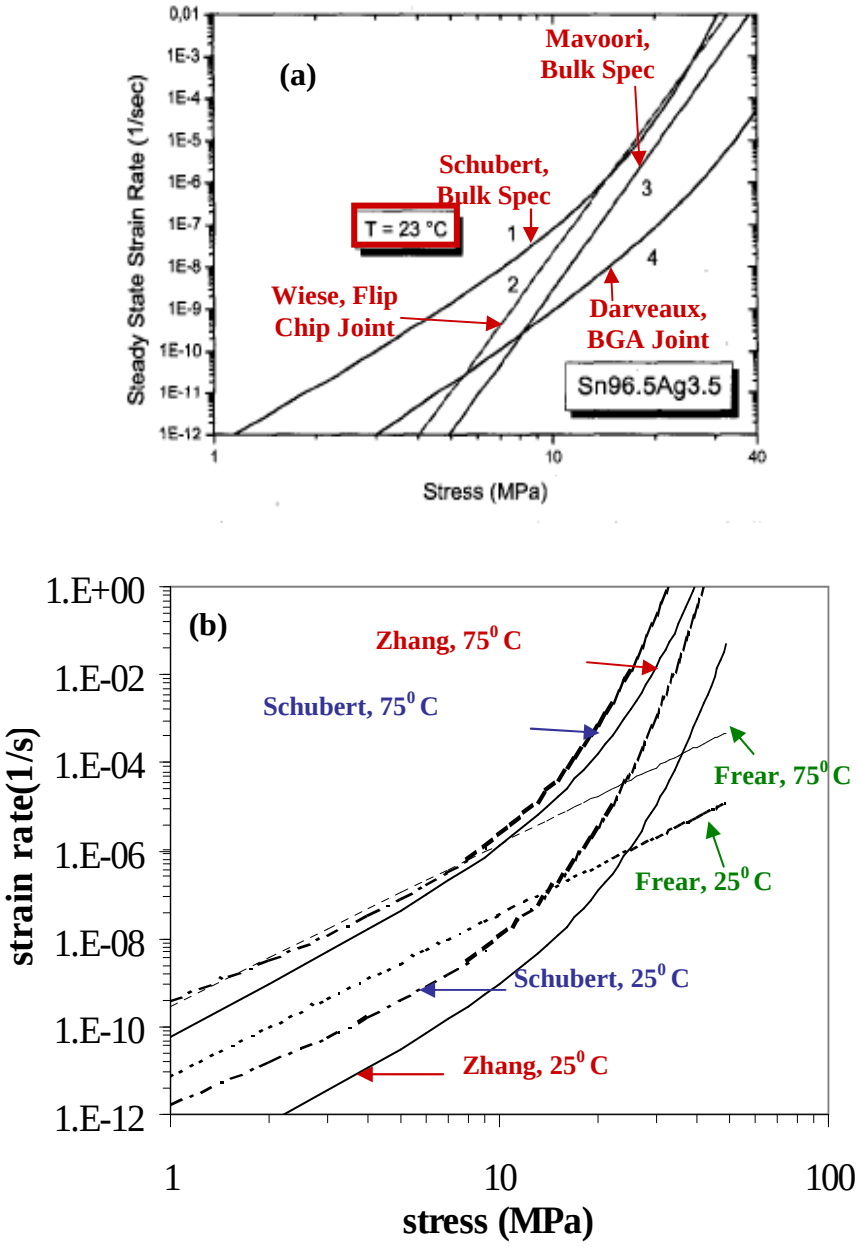

Figure 1-3: Variability in creep properties available in literature (a) Sn3.5Ag and (b) Sn3.8Ag0.7Cu. Images (a) and (b) have been adapted from[94] and [95] respectively

1.1.3. State-of-Art of the Mechanical Behavior of Microscale SAC Solder

The current literature on the constitutive and fatigue behavior of microscale (and bulk) SAC solder joints is detailed in this section.

1.1.3.1. Constitutive Testing of Pb-free Solders

The studies available on the monotonic constitutive behavior of Pb-free solders are included here. Studies listed here are limited to SAC and SnAg solders unless otherwise stated. Studies related to both microscale and bulk SAC solder are included.

1.1.3.2. Elastic-Plastic Testing of Pb-free Solders

Several studies exist on the elastic [71, 95, 98] and plastic [63, 71, 95, 99-103] properties of SAC solders. However most of the elastic measurements are from as-fabricated SAC solder joints and the degradation of the elastic properties under fatigue damage has not been studied to the best of the author's knowledge. The elastic properties are in general measured from nano-indentation tests and are representative of that seen in high strain rate conditions (plasticity dominated) such as vibration and drop testing.

The elastic and plastic properties of microscale SAC387 solder specimens have been characterized by Zhang and Haswell using quasi-static shear tests [95, 104]. The elastic modulus in particular is representative of that seen in low strain-rate loads such as in thermal cycling. A serious limitation of such measurements is that they are probably representative of the deformation due to a few dominant grains in the non-

homogenous, coarse-grained SAC solder joint and are hence require sufficient repeatability to represent the range of joint dependent behavior.

1.1.3.3. Viscoplastic Testing of Pb-free Solders

Significant literature exists on the viscoplastic creep behavior of SAC solders. These studies provide the following useful insights on the creep behavior.

- The creep resistance decreases with isothermal aging [68, 75-78, 105]
- Dislocation climb, assisted by core diffusion, is a dominant creep mechanism [9-11, 27, 61, 65, 76, 105-119]
- SAC solders exhibit superior creep resistance compared to Sn37Pb solder
- Creep resistance improves with increasing Ag weight fraction in SAC [120]
- Creep resistance is a function of various processing conditions [9, 11, 27, 65, 67, 69, 72, 74, 77-80, 87, 113, 119, 121-125]
- Viscoplastic (creep and plasticity) damage model [126], needs to account for deteriorating state of solder (damage) [126-127]

However most of these studies do not provide phenomenological macroscale model constants for the primary and secondary creep behavior. Furthermore, these studies do not provide any comprehensive microstructural insights to explain the observed creep behavior. Furthermore the creep damage models proposed are based on unified viscoplasticity theories (that combine rate-independent plastic and rate-dependent creep deformation).

1.1.3.4. Viscoplastic Stress Relaxation Testing of Pb-free Solders

Viscoplastic deformation is manifested in the form of creep deformation under constant force/stress conditions and as stress relaxation under constant displacement/strain constraints. Stress relaxation refers to a drop in the stress with increasing time under constant displacement loads. Typical field conditions produce constraints on the solder that result in stress relaxation. Stress relaxation is particularly evident during the dwell periods of cyclic displacement or temperature cycling [128-135]. In order to qualify the thermal cycling reliability of electronic products, accelerated testing of electronic packages is conducted. Typical temperature cycling profiles have maximum temperatures of 125°C, 100°C and 75°C while the minimum temperatures are usually 0°C or -40°C. The package is held at the extreme temperatures from 15 minutes to a few hours.

Under the above described temperature loading, if the hysteresis stress-strain response is evaluated using, stresses are seen to relax during ramping to hot temperatures, and more significantly during the isothermal dwell. The hysteresis response seen in the solder of a BGA 256 I/O package subject to thermal cycling using a 125°C to -40°C profiles, with 15 and 3 hours dwells, is shown for illustration purposes in Figure 1-4. Modeling and simulation using finite element analysis is used to obtain these results. Stress relaxation in the solder lowers the peak stresses in the silicon chip adjacent to it, thereby preventing brittle fracture of the chip. While it is beneficial to reduce the peak stresses through stress relaxation, this comes at the price of creep damage that affects the fatigue life of the solder.

Compared to the studies dealing with viscoplastic creep behavior of SAC solder under constant force loading conditions, studies dealing with the viscoplastic stress relaxation behavior of Pb-free solders are very limited [132-134, 136-139]. Furthermore, the reported stress relaxation measurements are not representative of the behavior of undamaged Pb-free solder since limited number of specimens are used.

An additional drawback of the studies is that the Pb-free solder response is not compared with that of Sn37Pb. Owing to higher creep resistance of the SAC solder; stress relaxation at the hot dwell is expected to be lower for SAC than in SP (Figure 1-4). Hence a comparison of the stress relaxation rates of SAC with that of traditionally used eutectic Sn37Pb as a function of initial stress levels and temperature is essential for the design of accelerated test profiles for qualifying Pb-free microelectronics.

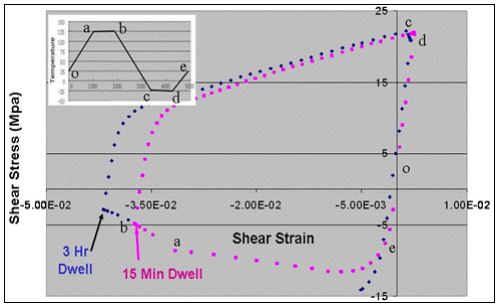

Figure 1-4: Finite element model prediction of hysteresis showing stress relaxation of solder in BGA 256 under thermal cycling (shown in insert)

1.1.3.5. Studies Correlating Viscoplastic Creep and Stress Relaxation Behavior of Pb-free Solders

Viscoplastic creep model constants are routinely utilized to model the mechanical behavior of solder under a wide range of creep-dominated loads. Furthermore the

stress relaxation behavior which is an outcome of viscoplastic deformation is studied using the creep constitutive modeling. With the exception of limited studies on SnPb [136], a correlation between the two viscoplastic deformations has not been provided to date for Pb-free solders. Studies exist on Sn37Pb solder where the stress relaxation measurements are utilized to obtain the creep model constants with reasonable success [136, 140-141]. However, the ability of creep model constants to predict the stress relaxation response of microscale SAC solders has not been investigated.

1.1.3.6. Isothermal Mechanical Cyclic Fatigue Testing of Pb-free Solders

The isothermal mechanical fatigue studies available in literature on Pb-free solder provide an overview of the fatigue constants for SAC and Sn3.5Ag solder alloys [15, 43, 64, 81, 93, 95, 104, 142-163]. However the studies, where available, do not provide a comparison of the fatigue performance of microscale SAC alloys as a function of Ag%. Furthermore studies that provide a comparison of the durability performance relative to the benchmark Sn37Pb alloy using consistent test methodologies are limited (see for example, ref. [3]). Comparisons, where provided, are not conducted using a consistent test methodology and specimen configuration.

Furthermore the evolution of the fatigue properties with increasing damage is required to understand the influence of the non-homogenous microstructure and their subsequent microstructural changes on the fatigue properties. In addition, the effect of isothermal aging on the isothermal mechanical fatigue behavior is not provided. For completeness, literature pertinent to other fatigue loads is included. SAC solders (up to 1% Ag) are seen to exhibit superior fatigue behavior under thermal cycling, power cycling and quasi-static isothermal mechanical fatigue, compared to Sn37Pb [43, 51-

55, 60, 62-63]. However, Sn37Pb exhibits better durability under plasticity-dominated loads such as vibration and repetitive drop loading [61].

1.1.3.7. Microscale Modeling of Mechanical Behavior of Pb-free Solders

Microscale modeling approaches that include inherent length scales and the fundamental physics of the deformation mechanisms are limited in literature, compared to phenomenological material models. Mechanistic models that capture the underlying dominant deformation and microstructural features have been proposed for modeling the cyclic creep fatigue constitutive and fatigue damage behavior of Sn37Pb solder [66, 164]. The dominant creep mechanism for Sn37Pb solder is modeled as grain boundary sliding by Sharma [66]. The constitutive modeling is combined with damage modeling of void growth and collapse and the constitutive properties are updated successively with each load step.

Previously reported microscale creep models on Sn37Pb solders cannot be applied to understand the creep deformation of SAC solder owing to differences in dominant deformation mechanisms resulting from the varying microstructures of the two solders. In the case of SAC solder, the creep measurements and the microstructural evidence point towards dislocation climb [10, 61, 65, 76, 107, 110], thereby suggesting that SAC solders exhibit dispersion strengthening characteristics.

Furthermore studies in literature suggest that the contributions of grain boundary sliding to deformation are negligible compared to the deformation from dislocation climb [11]. In particular this observation holds for as-fabricated coarse-grained SAC solder joints at microscale dimensions but not necessarily for similar SAC joints that

have undergone fatigue damage (and at times significant creep damage) which exhibit a finer grain microstructure due to recrystallization.

Mechanistic models are available in literature to model creep deformation induced by dislocation climb mechanisms [165-181]. Furthermore a review of these dislocation climb based models suggests that the rate limiting mechanism in climb is the athermal detachment of the attractive interaction between dislocation and obstacles after dislocation climb [178-179, 182]. The detachment model was first applied to SAC solders by Sharma et.al [183]. However, this model accounted only for the nanoscale IMCs dispersed in the eutectic Sn-Ag region.

However the microstructure of SAC comprises of several other length scales (see Section 1.1.1**)** whose contributions to the creep deformation need to be included. In order to include the contributions of heterogeneities at other length scales, homogenization techniques (that are widely used in composite materials) have been adopted in this study [184-185]. Homogenization studies have been utilized in literature for predicting rate-independent [186] and rate-dependent properties of SAC solder [20].

In the former study, the deformation behavior of individual phases of the solder were obtained using a mechanistic model, thereby providing microstructural sensitivity in the individual phase properties as well, prior to finding the homogenized properties of the overall alloy. In the homogenization studies conducted on rate-dependent properties by Pei [20], the creep properties of individual phases are obtained via experimentation. Thus the microstructural sensitivity of the resulting homogenized equations is limited. In the current study, the work of Sharma [183] is

extended to include the effects of Sn dendrites and macro-scale IMCs, using homogenization techniques.

Apart from the mechanistic model proposed for SAC solders discussed above, unified viscoplastic damage models with evolving damage metrics have been proposed for SAC solder [44, 126-127, 187-190]. These studies are beneficial towards understanding the damage and stress states resulting from the Sn anisotropy in the non-homogeneous coarse grained, as-fabricated joints, if individual phase properties are provided. However, these models do not predictive capability to estimate the viscoplastic behavior of solder as a function of alloy composition, aging and other processing parameters.

1.1.4. Unresolved Research Issues

The overview in Section 1.1.3 provides an improved understanding of the constitutive and fatigue behavior and microstructure of microscale SAC solder joints. However these studies are not as comprehensive as those on Sn37Pb and there are unresolved areas to be investigated that are critical to understanding the behavior of these alloys. Given the microstructural sensitivity and the length scales involved in functional non-homogenous, coarse-grained, microscale, SAC interconnects, a detailed study of the effect of each of these microstructural parameters on the mechanical behavior is still lacking in literature.

1. An issue of particular interest is that given the lack of statistical homogeneity in the Sn grain structure and the inherent anisotropy of single-crystal Sn grains in these microscale joints in the as-fabricated state, there does not appear to be sufficient data in the literature of specimen-to-specimen variability under identical

test conditions [22, 40, 61, 65]. It is not clear if the studies in literature do in fact observe (microscale) joint-dependent measurements but do not include or comment [65] about the scatter in the report, or if the anisotropy of the Sn grains is not dominant enough across the chosen test specimen joint to influence the mechanical behavior. Hence a study that explicitly investigates if these microscale SAC solder joints should in fact exhibit non-homogenous mechanical response is necessary.

2. Following this line of investigation, it is also important to assess if the non-homogenous microstructure and behavior (if it exists!), persist throughout the life-cycle of the microscale SAC joint, from the as-fabricated state to damaged state (e.g. due to creep or due to fatigue). Hence, studies that assess the evolution of the mechanical properties and microstructure and their variability throughout the life-cycle are important. Many investigators perform stress analysis for durability assessment, using the initial undamaged constitutive properties. This practice needs to be critically examined if the evolution of material properties is found to be significant throughout the life-cycle. In addition, the constitutive properties as a function of solder damage (macro and microcracking) are useful in predicting conservative estimates of the fatigue life of these joints.
3. A third issue to be investigated (which is implicitly tied to the first two issues stated above) is to obtain a correlation between the microstructural configuration and mechanical deformation behavior. While the literature does provide isolated examples of such studies, they are by no means comprehensive enough to cover the entire range of loads and microstructural configurations. Furthermore, as

described in Section 1.1.2, direct comparisons are difficult, owing to the variation in properties across different studies.

4. Given the wide range of service loads and the microstructural states that SAC could evolve to, conducting experimental studies of mechanical behavior across the entire space of feasible microstructures requires prohibitive resources in terms of cost and time. Hence, this warrants a microstructural material model that is mechanistically derived, to capture the effect of key microstructural features on the dominant deformation mechanisms in microscale SAC solder joints.
5. Other issues of secondary interest are that studies which provide a comprehensive understanding of the constitutive and the fatigue behavior of microscale, SAC solder specimens with low Ag weight fraction, which is the focus of this study, are lacking. When available, the studies do not provide comprehensive constitutive and fatigue model constants that could be utilized for material modeling.
    a. In addition, the applicability of the measurements from material level tests (shear specimens) to real functional joint behavior(such as BGAs) in terms of the microstructural state exhibited in field needs to be investigated. Furthermore, the constitutive behavior measurements are routinely quantified with phenomenological continuum mechanics based models, for macroscale modeling of the solder behavior under service loads such as cyclic fatigue. The validity of this practice needs to be explored, given that the microscale "as-fabricated" SAC joints exhibit non-homogenous microstructure.

b. In particular, solder undergoes viscoplastic deformation in the form of stress relaxation during the cyclic fatigue loads. Hence the level of accuracy with which macro-scale creep phenomenological model constants can predict the stress relaxation behavior of non-homogenous microscale SAC joints needs to be investigated.

In summary, a comprehensive understanding of the evolution of the constitutive properties, fatigue properties and correlation of the underlying microstructure of microscale SAC interconnects, using a combination of consistent test methodologies and specimen configurations and multi-scale modeling techniques is lacking and needs further investigation.

1.2 OBJECTIVES OF THE DISSERTATION

Based on the background provided so far, the specific objectives of this study on SAC305 microscale solder are to:

1. Characterize the evolution of the constitutive and isothermal mechanical fatigue behavior of microscale “as-fabricated” SAC305 solder, as a function of loading history, using material level characterization tests.
2. Investigate the microstructural scatter in as-fabricated SAC305 microscale solder specimens, and characterize the microstructural evolution as a function of loading history damage, and provide insights into the influence of the microstructural state on the measured mechanical response and its variabilities.
3. Propose a mechanistic multi-scale modeling framework based on available models in literature, to provide insights into the impact of the microstructural

features on the physics of viscoplastic creep deformation of microscale SAC joints

4. Investigate the level of accuracy with which continuum mechanics based viscoplastic creep model constants measured from non-homogenous microscale specimens predict the stress relaxation measured from similar non-homogeneous solder specimens.

The constitutive properties measured are the elastic, plastic and viscoplastic creep constitutive behavior. In addition, the monotonic viscoplastic behavior of SAC305 solder is investigated under constant displacement loads, namely stress relaxation and compared with that of eutectic of Sn37Pb measured from consistent test protocols. The isothermal mechanical durability tests are conducted at room temperature at sufficiently high strain-rates to provide creep-dominated deformation and damage mechanisms in the microscale solder specimen.

The loading histories investigated in this study for characterizing the evolution of material properties are increasing cyclic fatigue damage (macro and micro cracking and damage) and isothermal aging at room temperature. Table 1-2 provides a detailed overview of the objectives of this study. The term 'Φ' refers to the state of solder fatigue damage and varies between zero and one in this study. Damage state of zero refers to as-fabricated, undamaged solder state while damage state of one refers to a failed or completely damaged solder state which is incapable of supporting any structural loads.

Damage State →	As-Fabricated, Undamaged (Φ= 0)			Evolving Fatigue Damage (Φ =0- 0.5)		Aging Damage
Study Conducted	Tests	Modeling		Tests	Macroscale-modeling	Tests
		Macroscale	Microscale			
Creep	x	x	x	x		
Stress relaxation	x	x		x		
Elastic	x	x		x	x	
Plastic	x	x		x	x	
Yield	x	x		x	x	
Isothermal Mechanical Fatigue	x	x		x	x	x
Microstructure	x				x (post-creep and fatigue)	

Table 1-2: Objectives of the dissertation (experiments and modeling). Parameter 'Φ' refers to the state of fatigue damage in terms of load drop that varies between 0 and 1.

1.3 SCOPE AND OVERVIEW OF STUDY

The current dissertation aims to provide an improved understanding of the effect of the microstructural features on the viscoplastic constitutive and fatigue behavior of microscale dimension SAC solder interconnects as a function of evolving damage state. The microscale modeling framework yields valuable insights into the influence of key microstructural features for improved viscoplastic performance. Constitutive behavior measurements as a function of evolving damage state are useful for obtaining conservative estimates of the fatigue life of the material.

The results pertaining to the objectives of this study are detailed in the following chapters with the limitations and caveats of applicability. The results of this study are

presented in a journal paper format. Hence details of the approach and motivation are included in each chapter for self-sufficiency. The approach used for conducting the material characterization tests is detailed in Chapter 2.

The viscoplastic creep measurements of microscale SAC305 solder specimens in the as-fabricated or undamaged state are given in Chapter 3. The correlation of the microstructure with the observed behavior and the evolution of the damage and microstructure under creep loads are also provided. The chapter highlights critical issues observed in the microscale SAC305 measurements, which form the focus of the following chapters. Macroscale phenomenological models, based on continuum mechanics, are used to describe the primary and secondary creep behavior of microscale, SAC305, solder specimens.

In Chapter 4, a mechanistic framework is presented for understanding the viscoplastic behavior of microscale SAC joints as a function of the microstructural features found under varying processing protocols and alloy compositions. The microscale model is built from available models in literature and utilizes the mechanics of dislocation creep mechanisms and homogenization theories.

Chapter 5 describes a study to assess the ability of macroscale creep model constants, derived from constant force creep measurements, to predict stress relaxation behavior measured from constant-displacement viscoplastic tests. A comparison of the stress relaxation response relative to that of benchmark Sn37Pb is also provided. Once the stress relaxation of material level measurements is investigated, the validated creep model constants are used to design the accelerated thermal cycling profile to be used in accelerated testing of functional microscale

SAC305 ball grid array interconnects (BGA), using a combination of experiments and finite element analysis.

The isothermal cyclic mechanical fatigue curves and the evolution of the constitutive behavior (elastic, plastic, creep and stress relaxation) under increasing fatigue damage states is characterized in Chapter 6. An existing damage evolution model, based on continuum damage mechanics (CDM), is used to examine whether the data obeys CDM principles. In addition, the effect of isothermal aging on isothermal mechanical fatigue is also investigated. The microstructural evolution of the microscale SAC305 joints, which are initially non-homogeneous and coarse-grained, is also investigated under isothermal mechanical cycling loads.

Limitations and applicability of the test measurements and models are included. Chapter 7 summarizes the results and conclusions of the dissertation. The intellectual contributions of the dissertation are provided in Chapter 8. Future work to improve and extend the applicability of the current work is included in Chapter 8.

Chapter 2: Experimental Approaches

The experimental setup used for conducting the material level tests is provided in this chapter. The setup is a well established test system and has been used in previous dissertation on the characterization of Sn37Pb and Pb-free solders [95, 104]. Detailed description of the test system is provided in the dissertation of Haswell [104] and additional details on the design and calibration of the system are provided in [95]. A brief description is provided in the current dissertation for completeness.

2.1 Test System

The experiments in this study are conducted on a custom test setup, Thermo-Mechanical-Microscale (TMM) setup, designed by Haswell [104] to conduct monotonic tests for constitutive properties as well as for cyclic durability tests, at room and high temperatures. The test specimen used in this study is representative of the microscale length scales seen in functional solder joints such as BGAs. Hence the critical length-scale effects of the miniaturized can be captured using the current test specimen. The test specimen comprises of a two copper pieces soldered together with the material of interest. The test system is briefly reviewed in this section and the details can be found in elsewhere [104].

2.1.1. Test Specimen

The objective of the current study is to examine the behavior of solder joints using shear specimens that capture the coarse-grained Sn microstructure and behavior seen in micrometer dimension functional solder interconnects. The current shear specimen configuration captures the critical length scale (shear loading across the 180 μm

width) seen in functional microscale solder interconnects (~100 - 1000 μm), and replicates the associated coarse-grained Sn microstructure and non-homogenous behavior.

The test specimen developed for this work is a simple, notched shear specimen similar to that proposed by Iosipescu [85], which produces a very uniform stress field in the specimen gage zone due to the 90° notch angles [86, 88-89]. The stress fields expected in the solder region of the Iosipecu specimen have been presented in Section 5.3.2 of Chapter 5.

Copper is used in the current study to mimic the pad finish. Hence the results are applicable to solder behavior on OSP finish. As shown in Figure 2-1, the specimen is similar to that of a modified lap shear specimen and the solder joint is typically between 180 -200 μm wide, 3.0 mm long and approximately 1mm thick. The specimen is originally 1.5mm thick and reduced to a thickness of approximately 1mm thickness after fabrication by using standard grinding and polishing procedures. The final specimen is prepared for characterizing the microstructure of the specimen using optical microscopy. This step is crucial to understand the influence of the microstructure on measured mechanical response.

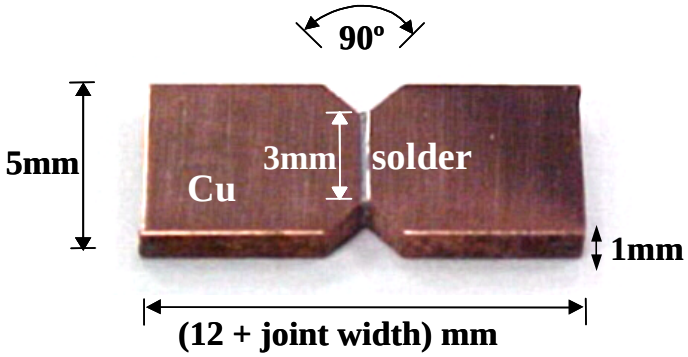

Figure 2-1: TMM specimen schematic

The specimen is prepared by manual soldering by maintaining consistent repeatable procedures for minimizing microstructural variations across specimens. The fabrication methodology used for the fabrication of the TMM specimens mimics typical solder reflow procedures used in functional microelectronics. The procedure includes a slow preheat time, soldering time and post soldering cool down phases. The copper platens are manufactured using electron discharge machining (EDM) to produce repeatable geometric parameters with tight tolerances.

Prior to soldering the copper platens, the soldering edge is prepared using standard grinding procedures to obtain a smooth, oxide free soldering surface. The grinding is conducted on seven pairs of copper platens in a batch grinding fixture. Grinding is conducted using 1200 grit sandpaper, in order to produce a flat, planar and uniform wetting surface. The copper platens are paired based on their position on the grinding fixture and then cleaned using isopropyl alcohol (IPA) and rosin flux.

Each copper platen is first cleaned with IPA using a soft bristle brush. The copper platens are dipped in flux and placed on a hot plate at ~ 132°C for approximately 30 seconds to activate the flux. The residue on the platens is then cleaned with IPA and the cleaning process is repeated thrice or as suited to obtain a clean surface on the soldering face of the platens. The prepared copper platens are then assembled in an alignment fixture and the soldering region gap between the platens is established using a shim to generate solder joints of ~ 180 μm height.

The soldering procedure followed in the current dissertation is strictly controlled to be consistent with that followed by Haswell[104] and Zhang[95], in order to facilitate comparisons of the mechanical behavior of the various solder compositions

tested with the current methodology. The aligned copper platens are secured in the alignment fixture and are then placed on a heating plate at approximately 30°C above the melt temperature of the solder. The assembly is held at this temperature for approximately 45 seconds to ensure the assembly is at an isothermal state. Following this step, a solder wire is manually fed into the gap between the copper platens to yield a uniform rectangular, fillet free solder joint. The soldered specimen is left undisturbed in the alignment fixture on the hot plate for another 30 seconds. The entire soldering and post-soldering time is maintained to be less than 45-50 seconds (one minute at most). The fixture is then slowly moved to a steel heat sink to solidify the solder joint. The resulting cooling rate is approximately 2°C/sec.

The soldered specimens are then inspected to ensure that admissible fillet, void and planarity limits are obtained. Admissible specimens are then prepared for microstructural analysis and further mechanical behavior characterization using standard grinding and polishing procedures. Batch grinding is conducted on 6 specimens using a specially designed fixture. The prepared specimens are then conditioned for 100 hours at approximate 80% of absolute melting temperature (or 0.8 homologous temperature).

Sn37Pb solder has been traditionally aged at 100°C after reflow. Since solder exhibits viscoplastic behavior, the same homologous temperature is maintained in the current studies and in those of Zhang [95] and Haswell [104] across various solder alloys. Pre-conditioning is conducted in order to stabilize the solder microstructure and to relax any residual stresses from the reflow or polishing processes. This step is also referred to as ‘pre-conditioning’ in the current study. The specimens are wrapped

in high-temperature Kapton tape to reduce oxidation during pre-conditioning. The preconditioned specimens are then polished lightly to remove any oxide layers formed during the isothermal aging.

The specimens are then characterized and the geometric parameters and microstructural features are recorded. In particular, the void densities, intermetallic layer at the interface and fillets are examined. This screening is aimed at eliminating defective specimens with a high void content, weak interfacial bonding between the copper and the solder, and other unusual microstructural features (pre-existing cracks) and joint geometries (skewed, asymmetric solder joints).

2.1.2. Test Setup

The TMM test setup designed by Haswell [104] is shown in Figure 2-2. Mechanical tests are conducted in closed loop displacement control using a lead-zirconate-titanate (PZT) piezoelectric stack actuator, which is capable of driving displacements of up to 90μm. The actuator is connected to the shaft holding the grips through flexible link and low friction, Frelon™-lined linear bushing. The flexible link and bushing hence aid in preventing bending loads to the brittle actuator during specimen installation and test loading. Testing is conducted in shear mode.

Close loop displacement control is achieved using a linear variable differential transformer (LVDT) that measures the displacement across the grips. A Keithley data acquisition card with a 16-bit digital-to-analog and analog-to-digital converter is used to collect test data as well as provide a feedback control signal to the PZT actuator. The effective positional resolution is approximately ±10 nm. The force in the system

is measured by a 445N capacity miniature tension/compression load cell with the effective resolution of 0.1N.

The specimen is held securely in the grips using stainless steel wedges and set screws. Insulating ‘ultem’ blocks are placed below and above the copper regions of the specimens. A properly installed specimen results in the solder region being aligned in line with the loading axis of the setup. A schematic of the installed specimens is shown in Figure 2-3.

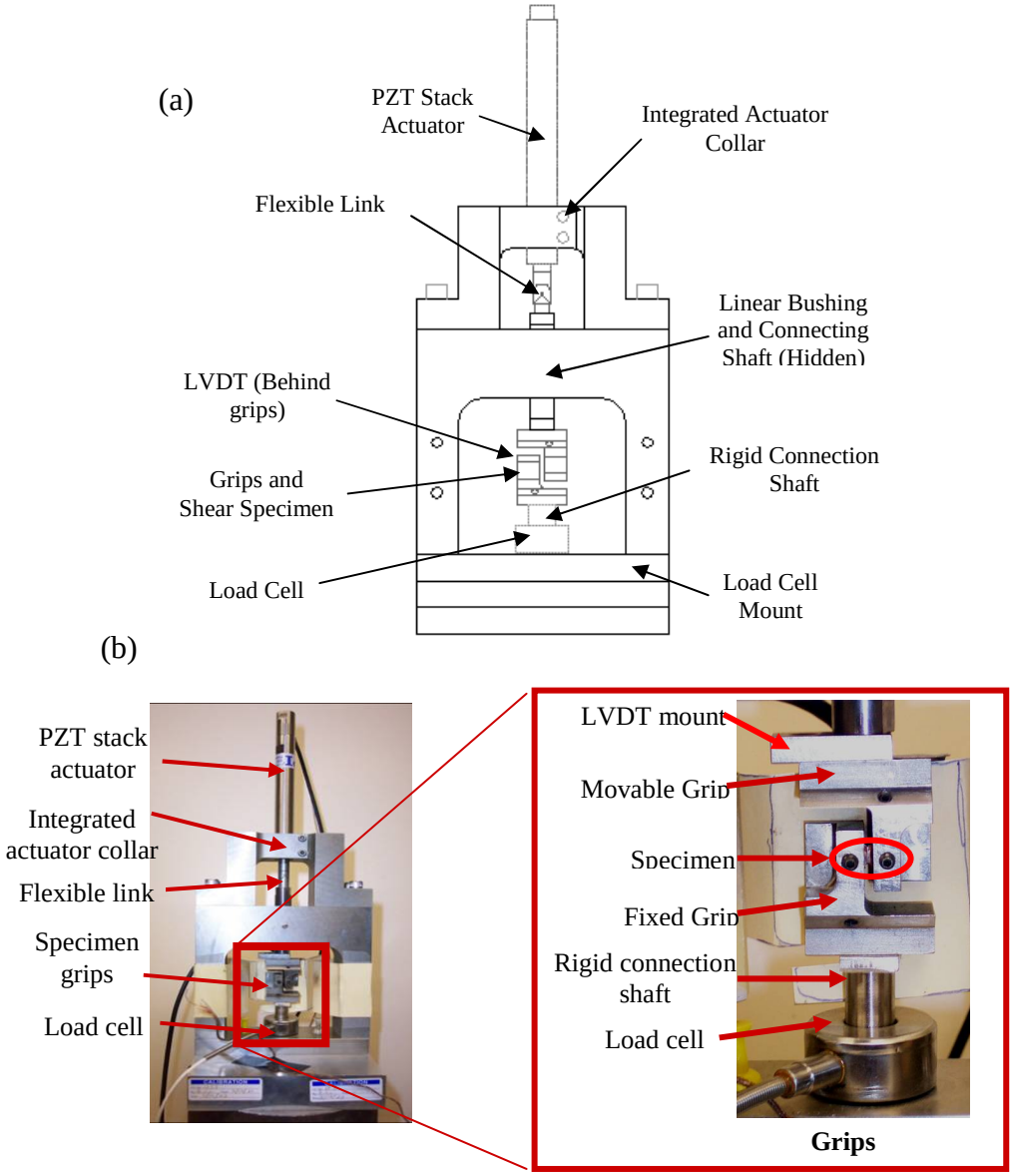

Figure 2-2: (a) Schematic and (b) Images of the TMM test frame [104]

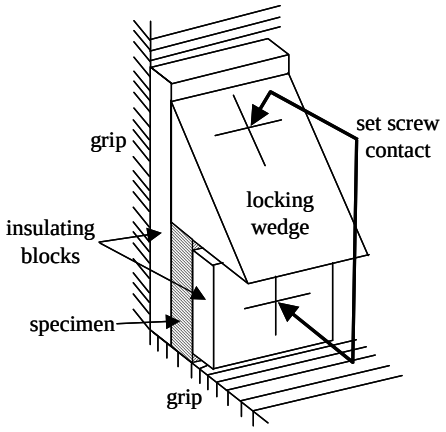

Figure 2-3: TMM grip schematic[104]

The LVDT measures the displacement of the grips, load train and the solder material. Thus the load train compliance is used to isolate the solder deformation from the measured total displacement. The load train compliance has been previously measured by Haswell [104] using digital image correlation methods and was found to be 0.044 μm/N. The control algorithm adjusts the input displacement according to the load train compliance value specified.

The setup is capable of conducting tests at elevated temperatures using pressurized air. The high temperature testing module was developed by Haswell [104] is shown in Figure 2-4. The high temperature testing module consists of a pressure regulator, a high-wattage in-line air heater, a type K thermocouple, a generic proportional-integral-derivative (PID) process controller, nozzles and pipes. Compressed, filtered air at ambient is regulated to approximately 4 psi and then split into two streams. One stream feeds into the heater and leads to a nozzle that is directed over the exposed solder region in the grips.

A thermocouple is secured onto the copper platen adjacent close to the solder region of the specimen for providing closed loop control for the isothermal

temperature loads. The second stream of air at ambient is directed without any further cooling or heating into 4 nozzles that are positioned over the LVDT, load cell and PZT regions. These streams serve to maintain the sensors within operating temperature settings. For a long term test conducted at 125°C, the cooling system ensures that the sensors reach at most 45-50°C.

The test setup with the heating system is shown in Figure 2-5. The setup is capable of conducting a wide range of mechanical tests, such as constitutive properties testing and fatigue testing. In addition the testing is not restricted to only solder material. Any material which can sufficient wet the copper platens or can be fabricated in whole as an Iosipescu configuration can be tested. In addition the setup can be modified to conduct other testing such as bending and tensile testing, with appropriate modification of the specimen grips.

Further details of the tests conducted in this study are detailed separately in the relevant chapters.

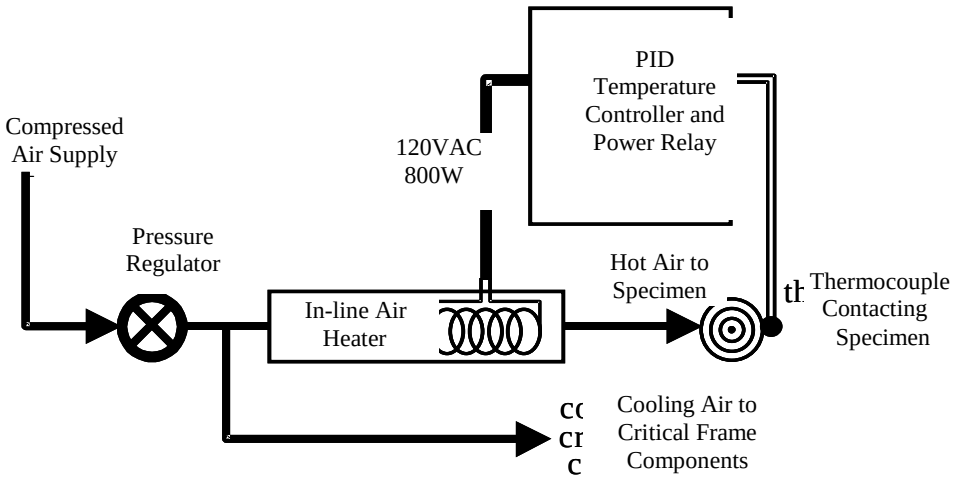

Figure 2-4: Heating module schematic [104]

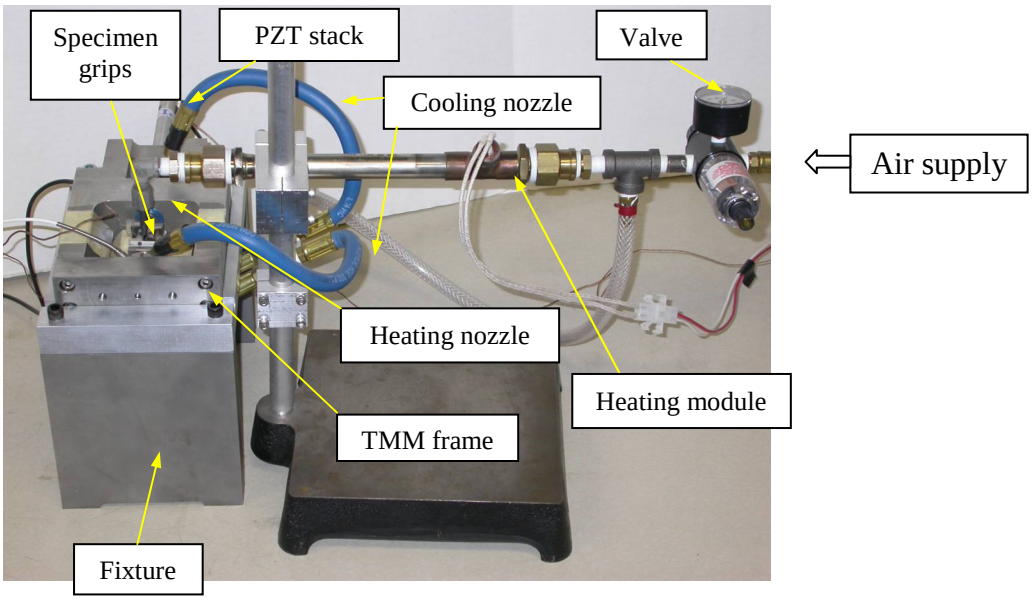

Figure 2-5: TMM apparatus with horizontal fixture [95]

Chapter 3: Viscoplastic Creep Response and Microstructure of As-fabricated Microscale Sn3.0Ag0.5Cu Solder Interconnects

ABSTRACT

The viscoplastic behavior of as-fabricated, undamaged, microscale Sn3.0Ag0.5Cu (SAC305) Pb-free solder is investigated and compared with that of eutectic Sn37Pb solder and near-eutectic Sn3.8Ag0.7Cu (SAC387) solder from prior studies. The tests are conducted on modified lap-shear microscale solder specimens, using a custom-built Thermo-Mechanical Microscale (TMM) test setup.

Creep measurements of microscale SAC305 solder specimens show significant piece-to-piece variability under identical loading. Orientation imaging microscopy reveals that these specimens contain only a few highly anisotropic Sn grains across the entire joint. For the studied loads, the non-homogenous Sn grain microstructure has a more significant impact on the scatter in primary creep compared to secondary creep. The statistically non-homogeneous microstructure and the associated variability in the mechanical properties in the microscale SAC305 joint are consistent with those reported in the literature for functional microelectronics solder interconnects.

Compared to the SAC305 joints, microscale Sn37Pb specimens exhibit a more homogenous microstructure with a large number of small Sn grains. Creep damage in the TMM joint is predominantly concentrated at highly misoriented Sn grain boundaries (if present) and at the Sn grain boundaries adjoining the intermetallic

(IMC) at the interface with the copper platens. The coarse-grained Sn microstructure recrystallizes into new grains with high misorientations angles under creep loading.

In spite of the scatter in the measurements, as-fabricated SAC305 specimens are significantly more creep-resistant than Sn37Pb and slightly less creep-resistant than near-eutectic SAC387 specimens with similar geometry and aging. Average model constants for primary and secondary creep for SAC305 are presented. Since the viscoplastic measurements are averaged over a wide range of grain configurations, the creep model constants represent the effective continuum behavior in an average sense. The model constants for the average secondary creep behavior suggest that the dominant creep mechanism is dislocation climb assisted by dislocation pipe diffusion.

3.1 INTRODUCTION

Several studies have been conducted on the constitutive and fatigue behavior of solders to understand the impact of solder deformation on the reliability of surface mount technology (SMT) assemblies. Solder exhibits non-linear viscoplastic constitutive behavior, which has been partitioned in this study, into rate-dependent creep, rate-independent plastic and elastic components. Fatigue damage due to viscoplastic creep deformation dominates under high temperature and/or low strain-rate cyclic loading *e.g.* during temperature cycling, and isothermal quasi-static mechanical cycling at high temperatures.

Creep deformation is manifested as stress relaxation under constant strain conditions (e.g. during dwell periods of cyclic loads), thereby affecting the durability of SMT assemblies [128-129, 132]. Hence, accurate knowledge of the viscoplastic constitutive properties of solders is critical for improved reliability assessment under

cyclic creep-fatigue loading. This work focuses on the viscoplastic rate-dependent deformation of undamaged, as-fabricated solder under constant stress conditions (creep test).

The solder of interest is a ternary Sn3.0Ag0.5Cu (SAC305) solder, a popular Pb-free substitute for conventional Sn37Pb solder. All concentrations are given as percentages representing mass fraction with the balance being Sn. This solder is preferred over the International Electronics Manufacturing Initiative (iNEMI) [191] recommended near-eutectic SAC387 solder, due to its affordability from the reduced Ag content. However, the lowered Ag content leads to differences in the volume fraction, size and distribution of intermetallics (IMC) and Sn dendrites, compared to SAC387. These microstructural differences alter the constitutive and durability response of the SAC305 relative to that of SAC387 solder.

Previously conducted extensive studies on Sn37Pb cannot be extrapolated to predict the behavior of Pb-free solders owing to significant differences in the microstructure and the underlying deformation mechanisms. Pb-free SAC solders demonstrate superior creep resistance and superior durability under creep-dominated fatigue loads, than Sn37Pb solder [15, 95, 104, 192-193]. Sn37Pb alloy consists of large, soft, equiaxed Pb islands embedded in a Sn matrix [95, 104, 192-193], with grain boundary sliding as the dominant creep mechanism.

In comparison, hard IMCs of Ag_3Sn and Cu_6Sn_5, embedded around a matrix of soft Sn dendrites in Pb-free solders [8, 68, 115], probably limit grain boundary sliding (GBS) to some extent in the early stages and dislocation climb is expected to dominate [10, 61, 76, 110, 194]. However, GBS may progressively increase as the

large Sn grains recrystallize into a finer polycrystalline state due to cyclic fatigue loading [52, 61, 195].

Prior to addressing the current state of art on the viscoplastic behavior of solders, the length scale and microstructure of solder joints used in contemporary SMT assemblies needs to be addressed. Current SMT packages comprise of microscale solder interconnects (< 1000 μm). At such dimensions, the structural length scale of the solder joint is comparable to the characteristic length scale of the microstructure. Hence length-scale effects dominate and the microscale joints microstructure and behavior is significantly different from that of bulk joints (>1 mm).

Recent reports indicate that at the current solder interconnects length scales; Pb-free solders such as SAC and Sn3.5Ag have very few Sn grains after reflow [22, 40, 46, 196] . Furthermore, single crystal Sn is known to exhibit significant anisotropy in the mechanical and thermal properties [39]. Thus microscale high-Sn Pb-free solder joints, such as SAC are expected to demonstrate significant piece to piece variability in their mechanical response in the as-fabricated state [22-24, 40, 45-46, 197], depending on the crystallographic orientation distribution of the few Sn grains in a given joint.

This scatter was not evident or reported in previously used Sn37Pb solder joints and is unique to SAC solders (except rare earth element doped SAC [18]). Hence, given this non-homogeneous microstructure of microscale SAC solder joints and the associated anisotropy of Sn, it is important that the length scales and microstructure of the solder test specimen used are comparable to those in functional solder interconnects.

The importance of specimen geometry is further supported by studies that report significant differences in the mechanical response and microstructure of bulk specimens versus micrometer-scale specimens, and material level tests versus assembly level solder joint tests [80-81, 83-84]. The literature on microscale SAC solder behavior is limited compared to the literature on their bulk behavior. Sn3.5Ag solders are also discussed because their microstructure and properties are similar to those of SAC solders. In addition, studies on the creep characteristics of SAC305 solder are limited [113, 116, 198-199] and, where available, are not comprehensive in terms of the model constants, state of damage in the solder, microstructure and the length scale of the joint, to name a few deficiencies.

Tremendous variability exists in the viscoplastic measurements of solders reported across different research groups. This variability is expected due to the sensitivity of the microstructure of solders to various factors such as the length scale of the test specimen, fabrication process, aging condition, state of damage, and loading conditions [8, 68, 75].

Hence, in order to assess and benchmark the performance of Pb-free solders relative to that of Sn37Pb solder, a consistent set of protocols for specimen configuration, specimen fabrication and test methodology is necessary. Given the microstructural complexity of SAC solders, the observed experimental data need to be interpreted in the context of the underlying microstructure and the extent of piece-to piece variability that can be expected from the mechanical response of these coarse-grained SAC solder interconnects needs to be investigated.

3.1.1. Objectives of the Study

An interesting feature of the measurements in literature is that in spite of the non-homogenous coarse-grained microstructure of microscale SAC joints and the anisotropic properties of single crystal Sn, the studies that explicitly report individual piece-to-piece variability under identical load conditions (especially both the secondary and primary creep response) are very limited [40, 61, 199]. The primary focus of this study is hence to investigate the extent of piece-to-piece variability one could expect from both the secondary and primary creep response of these coarse-grained microscale SAC joints. A comparison of the creep response of solder alloys with fine-grained configuration is also provided to understand the extent of joint dependent response.

Based on the background provided so far, the specific objectives of this study on SAC305 microscale undamaged, (as-fabricated) solder are to:

- Obtain insights into the extent of piece-to-piece that can be expected from the primary and secondary creep response of SAC305 specimens.
- Investigate the microstructure of SAC305 microscale solder specimens in the undamaged condition and correlate with the measured viscoplastic behavior.
- Compare the creep behavior of SAC305 specimens with that of Sn37Pb and near eutectic SAC387 specimens from prior studies that used similar test protocols and specimen configuration [95, 104].
- Investigate the microstructure differences between Sn37Pb and SAC305 solder for understanding the observed differences in the measured specimen to specimen variability between the two solders.

- Obtain insights into the evolution and the effect of as-fabricated Sn grain orientations on the damage exhibited in the post-creep damaged state.
- Obtain phenomenological model constants for average secondary and primary creep response, and provide insights into the underlying creep mechanisms.

3.2. EXPERIMENTAL APPROACH

The test apparatus, test matrices, test specimen configuration, specimen fabrication details, and the microstructural analysis tools used for the material characterization are described in this section.

3.2.1. Test Setup and Test Specimen

The test apparatus used in this work is a custom-built mechanical testing system (Figure 3-1a) for conducting isothermal monotonic constitutive tests as well as cyclic mechanical fatigue tests. The displacements are produced by a piezoelectric stack actuator in closed-loop displacement control. Displacements in the solder are obtained by adjusting for load train stiffness[104]. A hot-air, closed-loop temperature module provides the ability to conduct isothermal mechanical tests at elevated temperatures within +/- 1.5°C. A brief description of the test system is provided here and comprehensive details are available elsewhere [95, 104] .

The specimen configuration used is a modified lap-shear specimen (Iosipescu), that provides a reasonably uniform stress distribution in the solder due to the 90° notch angles (Figure 3-1b) [85-86, 104]. The stress distributions expected in the solder region of the Iosipescu specimen are presented in Chapter 4. The copper platens do not have any metallization layers and the solder behavior corresponds to

those on printed wiring boards with Organic Solder Preservative (OSP) and immersion Sn pad finish. The solder joint is 180 µm wide, 1 mm thick; 3mm long and is nominally deformed in shear.

The objective of the current study is to examine the behavior of solder joints using shear specimens that capture the coarse-grained Sn microstructure and behavior seen in micrometer dimension functional solder interconnects. The current shear specimen configuration captures the critical length scale (shear loading across the 180 µm width) seen in functional microscale solder interconnects (~100 - 1000 µm), and replicates the associated coarse-grained Sn microstructure and non-homogenous behavior.

The solder specimen is fabricated by manual soldering at a reflow temperature of 248°C and 210°C for SAC305 and Sn37Pb solders respectively. The pre-heat time is 45s and the reflow time from the deposition of solder to stationary heating time (time above liquidus) is 60s. The specimen is then air-cooled at ~ 2°C /s. The pre-heat and the reflow profile are strictly monitored to be consistent across all specimens.

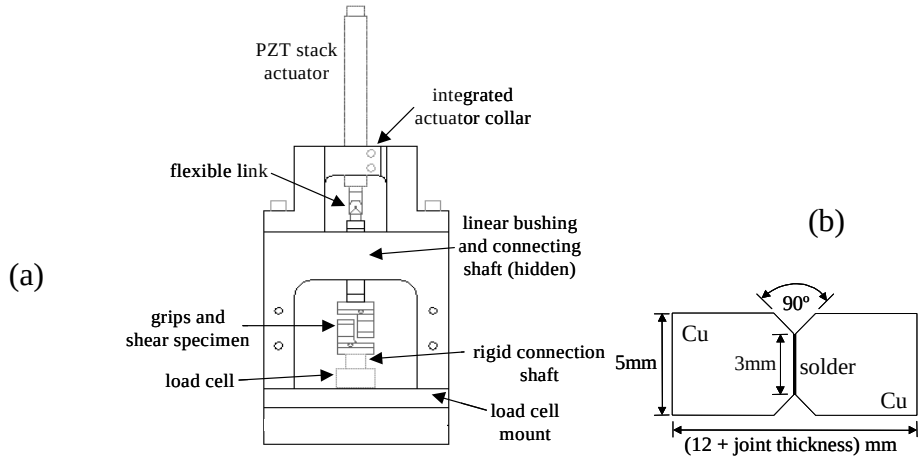

Figure 3-1: (a) TMM test frame (b) Specimen schematic (joint thickness ~0.18 mm)

All specimens are further aged for 100 hours at 0.8 T_{melt} (~132°C in the case of SAC305 solder) prior to testing, to obtain a stable microstructure and also to relax residual fabrication stresses. Sn37Pb is traditionally aged at 100°C, which corresponds to a homologous temperature of 0.8. Since solders exhibit viscoplasticity, the same homologous temperature is chosen for SAC solders (~132°C) to maintain consistency. In the current study, these thermally pre-conditioned joints are termed 'as-fabricated' joints.

Experimental material characterization methodologies are expected to yield non-repeatable stress and strain states in the specimen. Hence the current study attempts to minimize possible contributions from experimental methodologies in order to understand the extent of scatter induced from the non-homogenous Sn grain microstructure of solder. In addition, creep measurements conducted on Sn37Pb

solder using the same test methodologies and protocols are compared with those of SAC305 to verify the differences in microstructure driven variability.

Experimental error has been minimized by following various procedures such as maintaining consistent fabrication times and methodology and pre-conditioning and pre-test storage conditions (to minimize variations in the dendritic and IMC microstructural features), reduce misalignment of specimen relative to loading and jigs, and sequential screening at various stages of the manufacturing and testing to eliminate defective specimens, to name a few. Each test specimen is individually measured to assess the state of stress as opposed to using nominal solder joint dimensions (3mm length x 1mm thickness x 180 µm wide).

Furthermore the storage period from the end of fabrication to start of testing is consistent across all specimens and less than a week to prevent creep degradation resulting from isothermal aging of the SAC microstructure at room temperature. Microstructural image analysis is conducted using X-ray analysis, cross polarized microscopy (XPM), scanning electron microscopy (SEM), and orientation imaging microscopy (OIM).

In order to obtain a joint surface suitable for OIM and subsequent SEM analysis, careful metallographic grinding and polishing is conducted using a fixture. Grinding is first conducted using 800 and 1200 grade silicon carbide paper. Subsequent polishing is conducted using diamond paste (6 µm, 3 µm and 1 µm) and 0.05-µm colloidal silica suspension. The pre-test SAC305 microstructure shows a healthy planar interface IMC layer (Cu_3Sn and Cu_6Sn_5) of around 4 µm thickness for SAC305 solder.

3.2.2. Test Matrices and Constitutive Models

Creep measurements are conducted on SAC305 solder at stress and isothermal temperature loads ranging from 3 MPa – 20 MPa (shear) and 25°C -125°C respectively. The test loading is chosen to be representative of those seen by the solder during the typical service life of SMT packages [95, 128]. A minimum of two tests per load condition are conducted to assess the variability in the responses of specimens. A new undamaged as-fabricated specimen is used for each test load.

The creep behavior of SAC305 solder is compared with that of SAC387 and Sn37Pb results from prior studies [95, 104], using similar fabrication, specimen configuration and aging protocols as those used in the current study. The average homogenized secondary and primary creep behaviors of the microscale SAC305 joints are described using phenomenological models based on continuum mechanics.

The primary region is represented using the generalized exponential model (Equations 3.1 a-b) and the secondary creep models explored are Garofalo sinh model and a two-term version of Weertman's power model (Equations 3.2-3.3) [200] . The purpose of the two-term Weertman model is to understand the transition of the underlying creep mechanisms as a function of stress levels.

$$\varepsilon_{Sat} = C_1\sigma^{C_2}; d = C_3\sigma^{C4}\exp(-\frac{Q_1}{RT})$$

Generalized Exponential Primary Creep Model (3.1 a)

$$\frac{(\varepsilon_{Sat} - \varepsilon_P)}{\varepsilon_{Sat}} = \exp(-dt)$$

Decay and Saturated Primary Creep (3.1 b)

$$(\frac{d\varepsilon}{dt})_{sec} = A_G(\sinh(\alpha\sigma))^{n_G}\exp(-\frac{Q_2}{RT})$$

Garofalo Secondary Creep Model (3.2)

$$(\frac{d\gamma}{dt})_{sec} = A_L(\frac{\tau}{G(T)})^{n_L}\exp(-\frac{Q_L}{RT}) + A_H(\frac{\tau}{G(T)})^{n_H}\exp(-\frac{Q_H}{RT})$$

2 Power-Law Secondary Creep (3.3)

where ε_p= equivalent primary creep strain, ε_{sat} = equivalent primary saturated creep strain, γ = shear secondary creep strain, d = decay, σ = equivalent stress, τ = shear stress, Q = activation energy, R = universal gas constant, T = temperature in K, t = time in s, τ_O = initial shear stress at time zero, G(T) = temperature dependent shear modulus, and C_i (i=1:4), A_i, α , n_i, a and b are model constants.

3.3. RESULTS: VISCOPLASTIC RESPONSE

The experimental creep measurements of as-fabricated microscale SAC305 solders are reported here. Unless otherwise specified, all the data presented here refer to measurements made from individual samples without any data averaging. Images of the grain structure of the SAC305 specimens in the undamaged state (before mechanical testing) are analyzed, to identify the effect of the initial Sn grain configurations on the measured creep behavior and on the post-creep damage

patterns. Furthermore the Sn grain orientations and distributions in as-fabricated Sn37Pb specimens are investigated to understand the difference in deformation behavior of SAC305 versus Sn37Pb.

3.3.1. Material Measurements

The creep strain history of each test specimen is segregated and represented in terms of the secondary and primary regions (see Appendix 3.1 a-b for details on post-processing methods and negative creep). The primary and secondary creep behavior at 25°C, 75°C and 125°C are presented in Figure 3-2 and Figure 3-3a respectively. The primary creep histories to saturation and the rate of decay of the primary creep to saturation are depicted in Figure 3-2 a-b.

An important observation in the viscoplastic measurements of microscale SAC305 solder is that significant piece-to-piece variability exists at similar load conditions (shown by the dotted circles in Figure 3-2 and Figure 3-3). This scatter is particularly exacerbated at higher stresses. The extent of scatter in terms of the primary creep strain history across multiple specimens at the same load conditions is shown in Figure 3-2a.

The scatter observed in the secondary creep behavior is similar to that seen in monotonic test measurements for elastic and plastic behavior of as-fabricated TMM specimens (Appendix 3.2, or Chapter 6). Similar scatter has been reported by other investigators as well [24, 40, 46, 61, 199]. The stress levels at which scatter becomes evident for various creep parameters is represented in Figure 3-3b. The parameter ‘time-prim. sat.’ in Figure 3-3b, refers to the time taken to reach 90% of the primary saturated creep strain.

Data from 75°C exhibits compounded effects of temperature fluctuations and inherent material response and is eliminated from Figure 3-3b for clarity. The results show that the scatter becomes evident at stress levels as low as 4MPa shear stress, but becomes more dominant past 8MPa. The corresponding plots for the primary creep and total creep strain histories showing the extent of scatter are provided in Figure 3-3a and Figure 3-8.

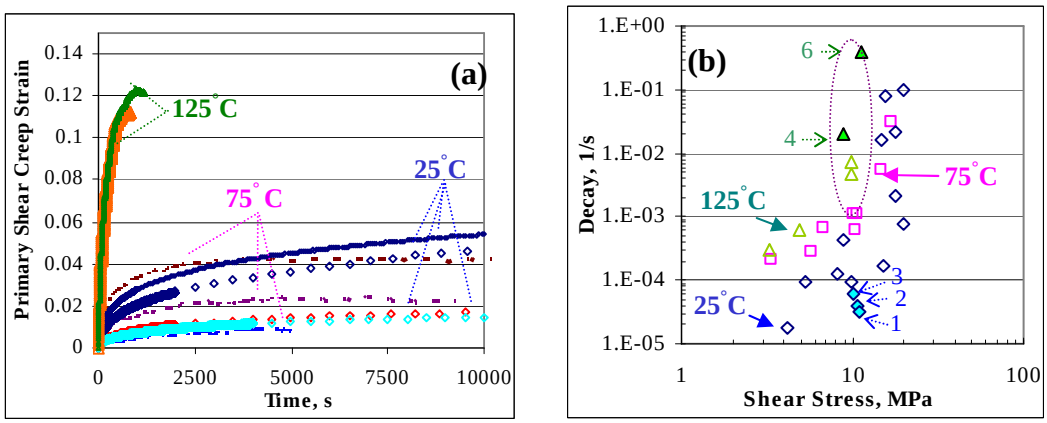

Figure 3-2: (a) Primary creep strain history at 10 MPa across nine samples, (b) Decay term of primary creep strain. Dotted circle shows the stress at which scatter is evident (Data points1-6 refer to specimens used in the OIM study detailed in Section 3.3.2)

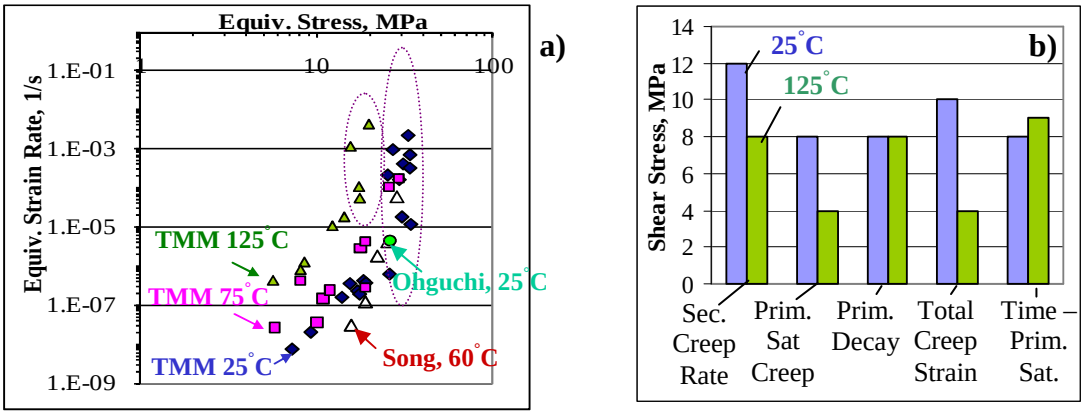

Figure 3-3: (a) Comparison of TMM secondary creep strain rate with literature [116, 198] (b) Plot of shear stress levels where scatter becomes evident for various creep parameters

The creep measurements hence reveal that microscale SAC305 joints exhibit significant piece-to-piece variability which is as high as three orders of magnitude. The scatter observed in the secondary creep behavior is of the same magnitude as that reported by Herkommer on similar microscale shear SAC305 specimens[199]. The following part of the study therefore investigates the source of this scatter from the microstructural standpoint.

First, any experimental bias in the assessment of the stress-strain state in the solder is rectified. For example, the stress state is adjusted to account for the internal voids in the solder region via X-ray analysis. An additional complication is that the creep at high stress levels is extremely sensitive to the stress magnitude due to the high exponents. Therefore any experimental error in stress measurements causes a large scatter in the strain rate versus stress plots. In addition, the creep behavior of Sn37Pb solder measured using the same test methodology and specimen

configuration is presented in Section 3.3.4 in order to understand if the variability is induced due to experimental methodologies.

In spite of this scatter, the results clearly show (the expected) monotonically increasing dependence of creep on stress and temperature (Figure 3-2 and Figure 3-3). Comparison of the measurements with literature show that the secondary creep results from the current study are comparable to those reported by Ohguchi et al. ,[198] but are higher than those measured by Song et al. [116] (Figure 3-3a).

3.3.2. Microstructural Investigations for Understanding the Source of Scatter

In order to understand the influence of the primary microstructural feature of SAC305 solders, three specimens each are tested for repeatability at the same stress level at 25°C and 125°C. The stress level (10 MPa) is chosen to isolate the contributions due the high creep exponent regions (>10 MPa) of the secondary creep rate region. However the measurements made at 125°C were not completely successful in establishing repeatability and isolating the high stress region.

Several length scales exist in microscale SAC joints. The largest length scale is that of Sn grains which are coarse-grained, few and non-repeatable in nature and could be as large as the joint dimensions (hundreds of micrometers) in microscale SAC joints. The lower length scales are those of microscale dimension Sn dendrites, Sn-Ag eutectic regions with nanoscale Ag_3Sn IMCs and microscale IMCS.

Since SAC305 has a high percent of Sn, the variability in joint deformation is particularly exacerbated due to the inherent anisotropy of single-crystal Sn [39] in a multi-grained/coarse-grained joint (Appendix 3.3). Hence the Sn grain texture of the as-fabricated undamaged microscale SAC305 TMM joints is investigated. OIM

analysis is preferred over XPM and focused ion beam (FIB) analysis for quantifying grain orientation, and to unambiguously identify areas of varying crystallographic orientations as sub-grains or grains.

Figure 3-4and Figure 3-5 present the inverse pole figure (IPF) from the OIM study on six TMM joints (numbered 1 to 6) prior to testing at 25°C and 125°C. Successive scans were conducted to cover the entire length of the specimen (3 mm) and compiled together (see Appendix 3.4 for details on the post-processing). The unit triangle with the principal directions in the same figures is a reference for distinguishing the crystallographic orientations in the image. Grains (black lines) are distinguished from sub-grains(silver lines) by grain angle boundaries greater than 5° [201]. Apart from the six specimens shown here, additional specimens were analyzed using XPM, FIB and OIM analyses that further confirmed the coarse grained microstructure reported here.

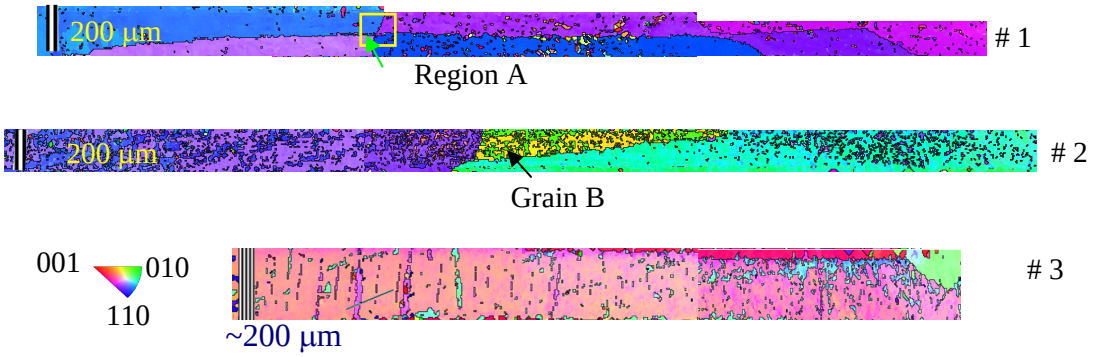

Figure 3-4: OIM Images of SAC305 TMM joints used for 25°C creep tests. Region A in Specimen # 1 is used for referring to the post-creep damage in the sample in Figure 3-10a. Grain B in Specimen #2 is used in the discussion in Section 3.3.6. The unit triangle for bct Sn for referencing the IPF images is shown next to Specimen #3

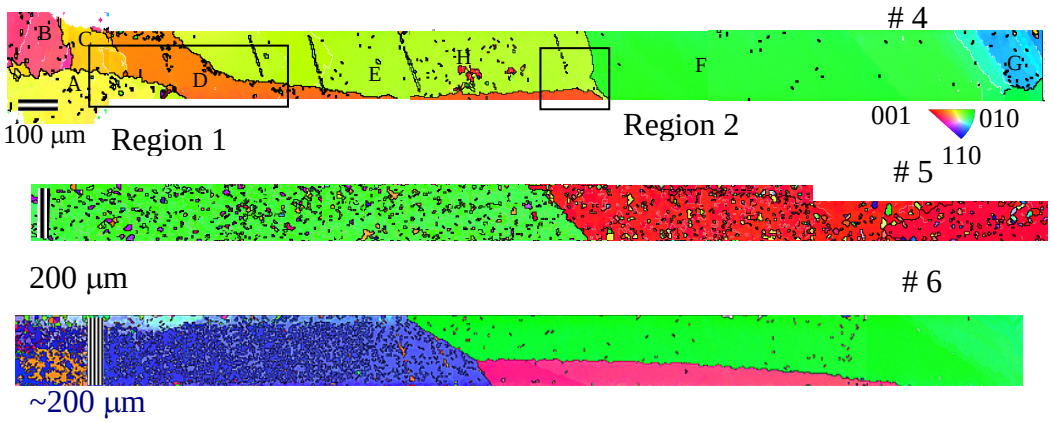

Figure 3-5: OIM Images of SAC305 TMM Joints used for 125°C creep tests. Grains A-H in specimen 4 are used to study the extent of creep damage in Section 3.3.5. Regions 1 and 2 are examined in Figure 3-10

Based on the Sn texture maps from all analyzed specimens, it is seen that typical microscale SAC305 TMM test specimens seem to exhibit around 1 to 7 grains of

approximately 180 μm width, of at most 3 mm length. The joint is hence highly non-homogenous and exhibits misorientation angles as high as 90° with adjacent grains (Table 3-1). An interesting observation is that, as in functional solder joints (Figure 3-7 a-b), the Sn grain texture in the TMM joint varies significantly from one specimen to another, in spite of consistent manufacturing and load histories.

It is worthwhile to note that while most investigators report a non-homogeneous few grained microstructure in functional BGA SAC solder joints [22, 24, 40, 45, 56, 70], one investigator's findings show that the Sn grain texture could be homogenous and polycrystalline at least in some cross-sectional planes, for some cooling conditions and joint sizes[202].

The initial TMM microstructure reported here seems to be representative of the coarse grained Sn microstructure that has been widely reported in real microscale solder interconnects in SMT packages [22, 45] (Figure 3-7 a-b). However, further studies need to be conducted to quantify if Sn exists in polycrystalline state across different cross-sections as reported in literature [202]. Cross polarized microscopy conducted on both sides of the TMM solder region revealed invariance in the Sn grain configuration and number.

Hence the Sn grain orientation distributions in the TMM joints are not expected to vary much along the out-of-plane (thickness) direction of the shear specimen as reported in similar specimens by Telang [196]. The TMM grain microstructure is also not seen to vary with isothermal aging at room temperature as seen from an examination of Figure 3-6 a and Figure 3-6 b/c. Figure 3-6 b and c represent the

microstructure of a SAC305 TMM joint after two weeks of aging at room temperature.

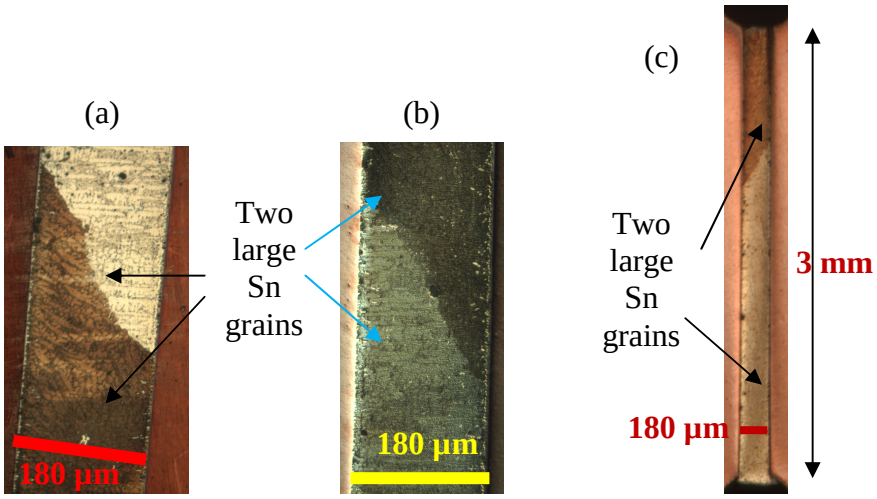

Figure 3-6: XPM images revealing two large Sn grains in the TMM SAC305 specimen (a) in as-fabricated state. Figures (b) and (c) reveal grains on either sides of the specimen after two weeks of aging at room temperature. Images (a), (b) and (c) reveal that the grain microstructure is invariant through the thickness of the joint and also invariant with isothermal aging.

Apart from the Sn grain texture, the microstructure of the distributions of the lower length scales (Sn dendrites, eutectic Sn-Ag phases and bulk IMCs) in SAC305 TMM specimens are also studied (Figure 3-7 c-f). Figure 3-7d reveals that the Sn dendritic arms exist as three dimensional ellipsoidal inclusions with Sn-Ag eutectic regions enclosed in between them. The Sn-Ag eutectic region comprises of pure Sn matrix embedded with nanoscale Ag_3Sn IMCs (~20 nm) of spherical cross-sections (Figure 3-7f). The Sn dendritic phases comprise of a primary long dendritic branch of ~ 200 µm with smaller arms of 10-20 µm attached (Figure 3-7 e). Large Cu_6Sn_5 IMC

rods and Ag_3Sn platelets of micrometer-scale dimensions are found in the bulk of the solder (Figure 3-7 f).

Preliminary studies do not show conclusive trends about the distribution and sizes of dendrites across the six OIM specimens (1-6). Since the manufacturing profiles and aging histories of the TMM specimens are strictly controlled, reasonable repeatability is expected in the dendritic and intermetallic features of the solder joint. Future studies will focus on understanding the effect of variation of these microstructural features on the creep behavior. It is interesting to note that the Sn dendrites exist in distinct colonies with uniform preferred directionality (Figure 3-7 c marked with arrows). Furthermore, Sn crystallographic orientation data do not show any grain boundaries at the intersection of the dendritic colonies. Hence multiple dendritic orientations are possible within a single Sn grain as reported in literature [197].

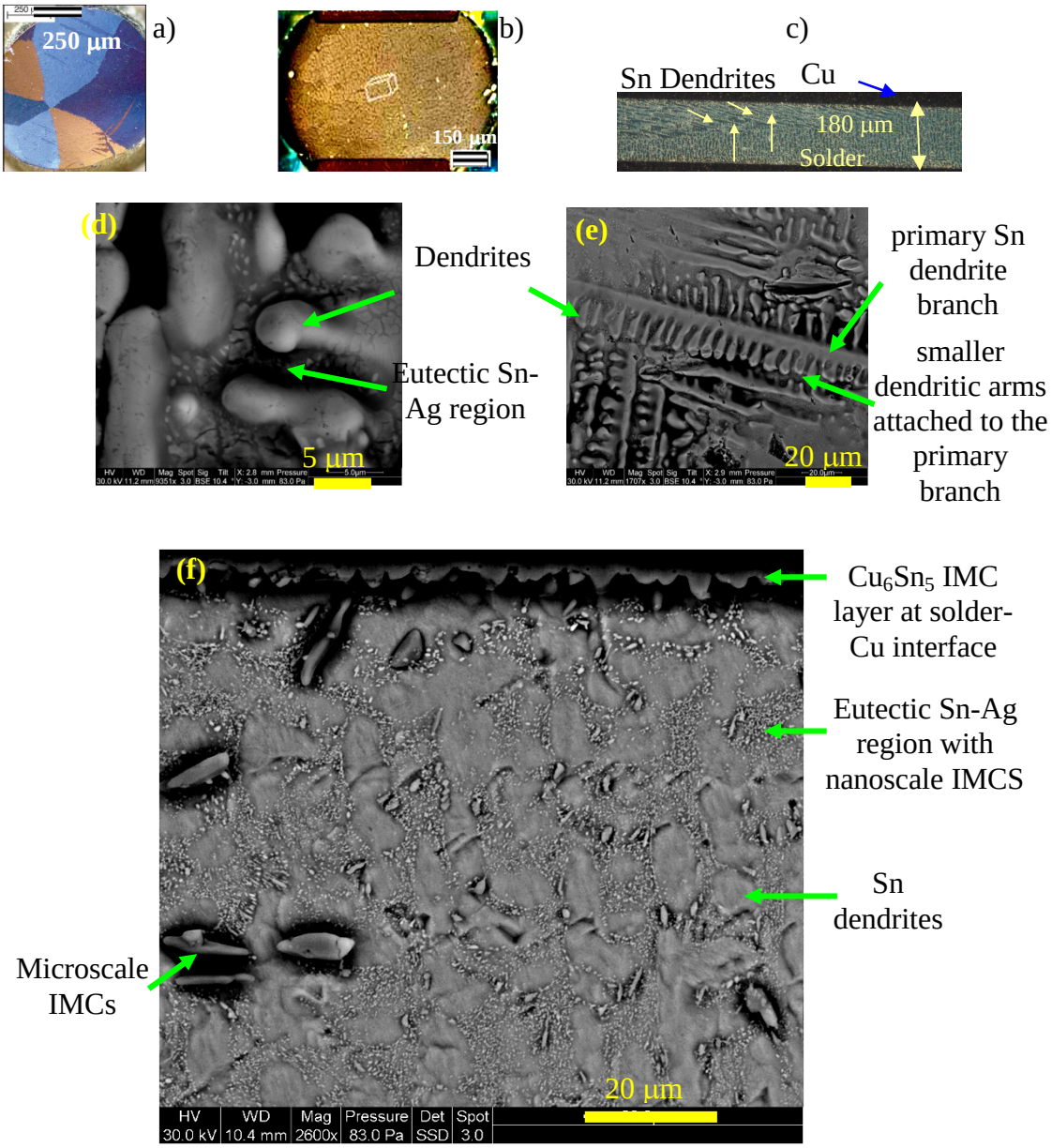

Figure 3-7: XPM images of as-fabricated BGA solder balls showing (a) At least 6 Sn grains in Kara's beach ball structure [22] (b) Probably a single Sn grain [45]. TMM SAC305 solder after fabrication and pre-conditioning (c) Dark field image, arrows showing Sn dendrite orientation and (d) SEM image showing Sn dendrites and IMCs

3.3.3. Correlation between Grain Textures and Scatter in Creep Response

The extent of piece to piece variability expected from the creep response of microscale SAC305 specimens across the entire test matrix is presented in Figure 3-8 a-d. The creep response of the OIM test specimens is identified in these plots using the specimen numbers 1-6.

The creep response of the OIM test specimens in Figure 3-4 and Figure 3-5 are presented in Figure 3-8 e-j. The extent of scatter in the primary creep (Figure 3-8- e-g), secondary creep (Figure 3-8-h), total creep strain history (Figure 3-8-i) and the normalized representation of primary creep strain to saturation, is assessed as a function of the grain orientations reported in specimens 1-6 for both the 25°C and 125°C test data (filled in symbols, green colored triangles and blue colored diamonds respectively). These results show that the strongest influence of the Sn grain distribution is on the saturated creep in the primary region. The decay factor and saturation time for primary creep and the secondary creep rate are not as strongly affected at the tested loads.

The piece-to-piece variability is clearly evident in the test histories of all test specimens at 25°C, 10 MPa (Figure 3-8-i-j). The responses of the multi-grained specimens 1 and 2 are surprisingly repeatable and exhibit significantly higher creep than the single grained specimen 3. Scatter is evident in all the above-mentioned creep parameters at 125°C. However direct correlation to the Sn grains cannot be made since the scatter is due to the combined effect of varying grain microstructure and non-repeatability of stress state. Hence the conclusions here are based on the room temperature data.

The room temperature data reveals that the variability in the secondary creep rate and the primary decay rate is a factor of 2 to 3. This variability is comparable to that exhibited by the elastic and plastic properties of as-fabricated TMM SAC305 specimens (Chapter 6). However, the variability in the saturated primary creep strain is significantly higher, by as much as a factor of 100 (an order of magnitude).

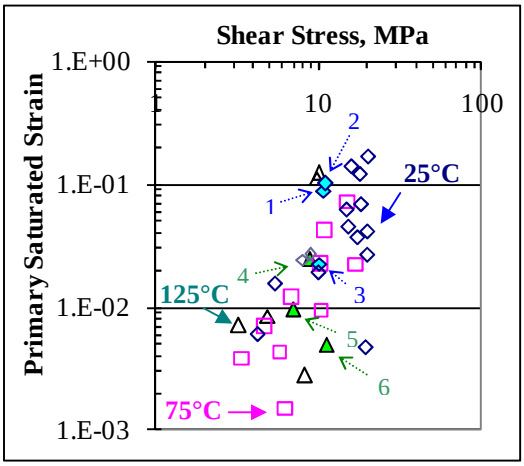
Shear Stress, MPa
Primary Saturated Strain
1.E+00
1.E-01
1.E-02
1.E-03
1
10
100
25°C
125°C
75°C
1
2
3
4
5
6

(a)

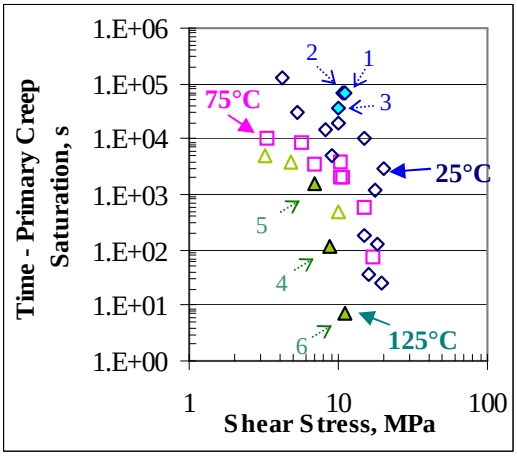
Time - Primary Creep Saturation, s
1.E+06
1.E+05
1.E+04
1.E+03
1.E+02
1.E+01
1.E+00
1
10
100
Shear Stress, MPa
75°C
25°C
125°C
1
2
3
4
5
6

(b)

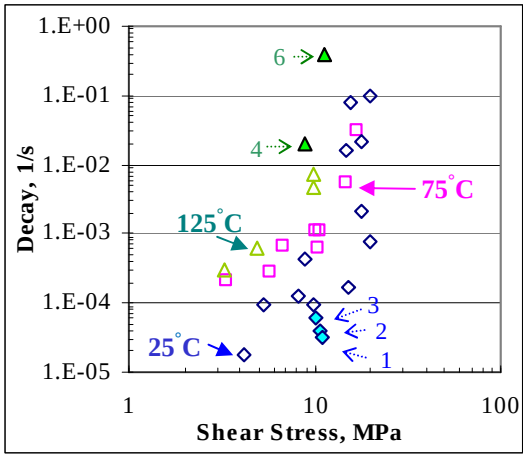
Decay, 1/s
1.E+00
1.E-01
1.E-02
1.E-03
1.E-04
1.E-05
1
10
100
Shear Stress, MPa
75°C
125°C
25°C
1
2
3
4
6

(c)

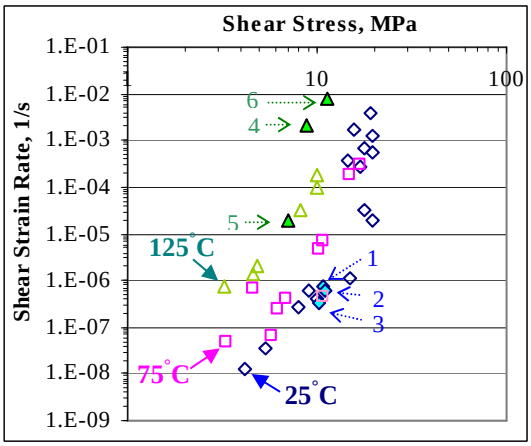
Shear Stress, MPa
Shear Strain Rate, 1/s
1.E-01
1.E-02
1.E-03
1.E-04
1.E-05
1.E-06
1.E-07
1.E-08
1.E-09
10
100
125°C
75°C
25°C
1
2
3
4
5
6

(d)

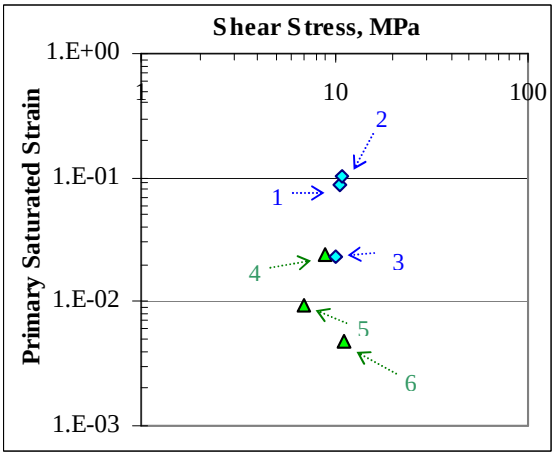
Shear Stress, MPa
Primary Saturated Strain
1.E+00
1.E-01
1.E-02
1.E-03
1
10
100
1
2
3
4
5
6

(e)

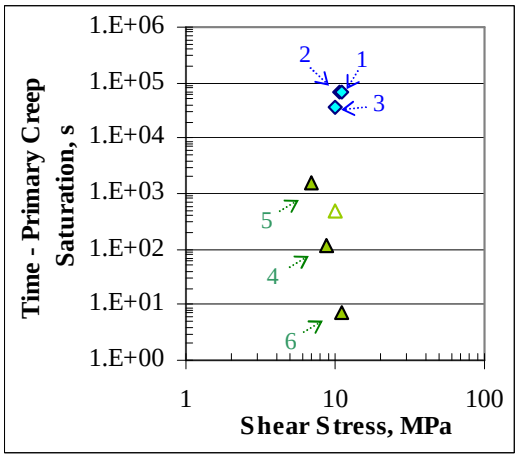
Time - Primary Creep Saturation, s
1.E+06
1.E+05
1.E+04
1.E+03
1.E+02
1.E+01
1.E+00
1
10
100
Shear Stress, MPa
1
2
3
4
5
6

(f)

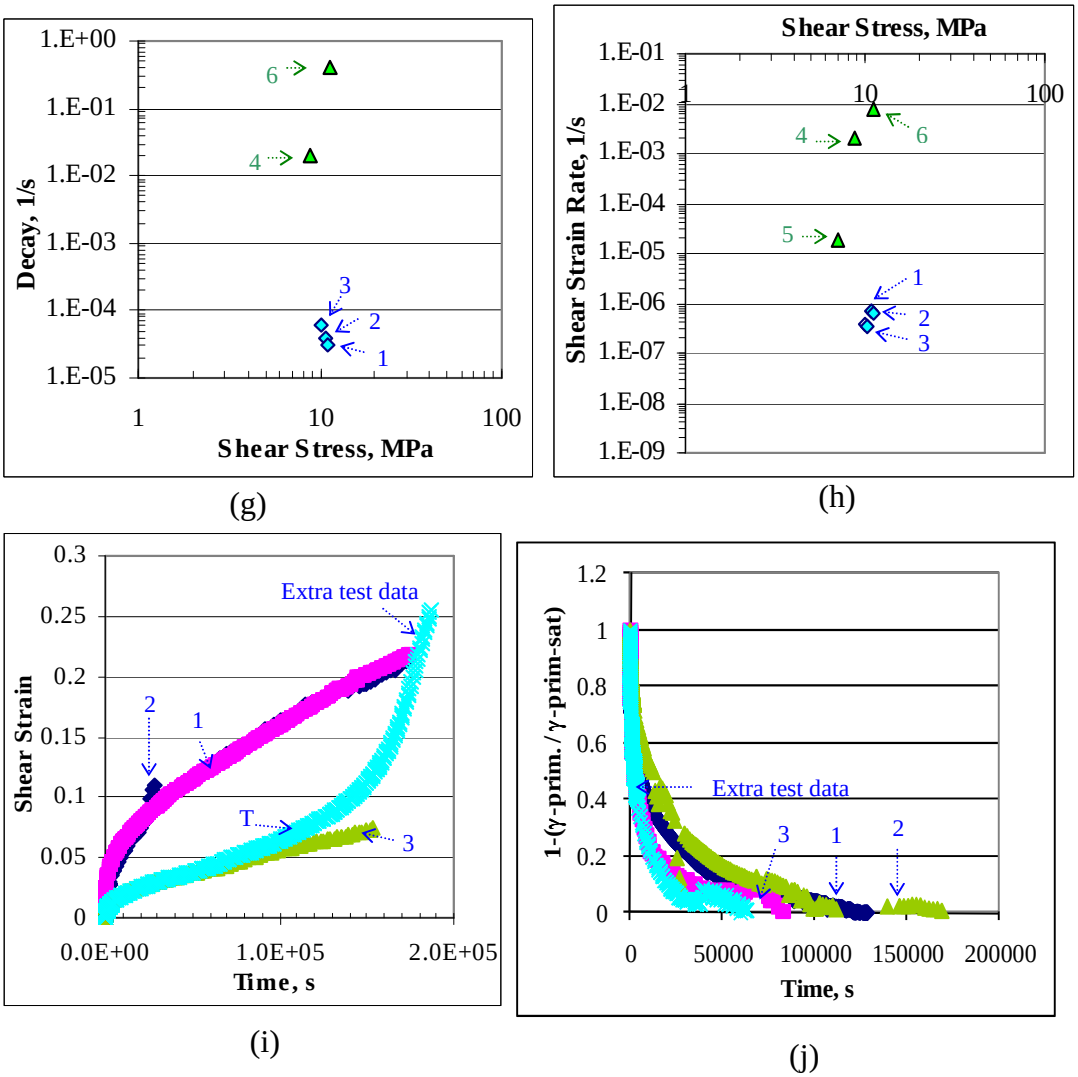

Figure 3-8: Creep measurements (in shear) across entire test matrix (a-d): (a) Primary saturated creep strain, (b) Time for saturation of primary creep, (c) Primary decay, (d) Secondary creep rate (see Section 3.3.7 and Appendix 3.1 for fits). Creep response across OIM specimens 1-6 (in shear) (e)-(i): (e) Primary saturated creep strain, (f) Time for saturation of primary creep, (g) Primary decay, (h) Secondary creep rate, (i) Total strain history (25°C, 10 MPa), (j) Normalized residual primary strain approach to saturated primary creep (25°C, 10 MPa).

The creep response seems to suggest that, in general, the saturated primary creep, and hence the total creep strains, are proportional to the number and orientation of the grain boundaries in the specimen. However, such an observation does not present a

complete picture since the critically resolved shear stress (function of orientation of the Sn grains relative to the applied load) plays a significant role on the extent of deformation. For example, additional test data at 25° C, 10 MPa exhibits very good repeatability with Specimen 3's behavior up to the secondary region, suggesting a possible single grain configuration. However, the specimen accelerates to an early tertiary failure (point 'T' in Figure 3-8-i).

3.3.4. Grain Textures and Creep Response of Sn37Pb Solder

In order to understand the lack of scatter in the mechanical response of microscale Sn37Pb joints compared to microscale SAC305 joints [22, 24, 70], the Sn grain distributions and orientations were studied in Sn37Pb microscale TMM specimens. The Sn37Pb specimens used for these analyses were fabricated using similar fabrication procedures as SAC305 TMM specimens (Section 3.2.1). Sn37Pb solder creep measurements [104] using the same test methodology exhibit much more homogenous deformation than that of SAC305 specimens or previously reported SAC387[95].

The test measurements of Sn37Pb TMM specimens from Haswell's study [104] are included in the Appendix 3.1 for comparing with the secondary creep (Figure 3-8 d) behavior of SAC305. The quality of the creep model fit to Sn37Pb data is better than that to Pb-free solder and is presented in Appendix 3.1. The IPF image of the Sn grain distribution and orientations in Sn37Pb specimen is shown in Figure 3-9a.

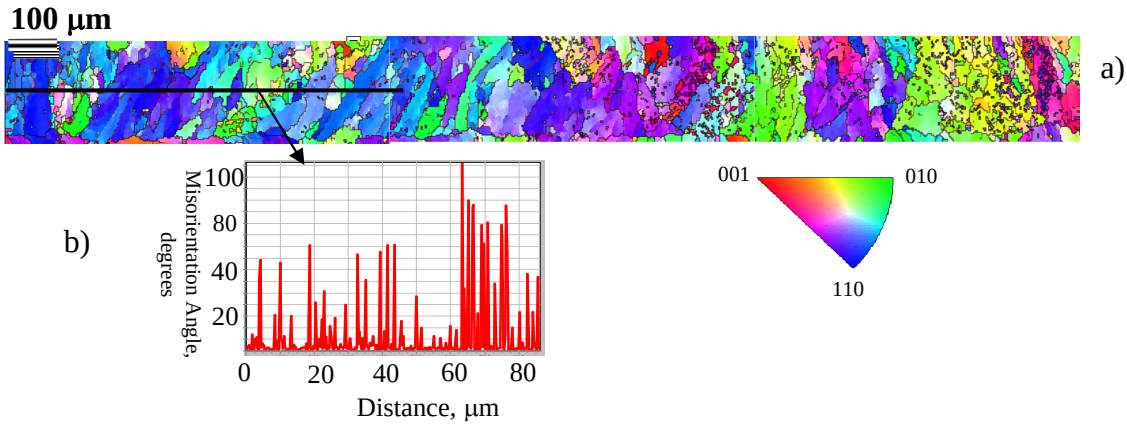

Figure 3-9: OIM images of Sn37Pb TMM joint, showing (a) the IPF figure with multiple Sn grains (b) Misorientation angles as high as 90° between Sn grains along set path (black line)

Compared to the non-homogenous Sn grain microstructure exhibited by microscale SAC305 specimens, the grain size distribution in the Sn37Pb solder specimen is statistically more homogeneous, due to the presence of several hundred small Sn grains (and Pb grains not shown here). The misorientation angles between the Sn grains are as high as 90° implying high angle grain boundaries (Figure 3-9b). Hence the deformation behavior of the resulting joints is much more homogeneous and identical to each other due to the smearing/averaging affect of the anisotropic response of individual Sn grains.

Thus the creep response of coarse grained, non-homogeneous microstructure (as-fabricated SAC) exhibits significantly higher scatter than that of the fine grained homogenous microstructure (as-fabricated Sn37Pb). A reduction in the specimen to specimen variability is also observed in the isothermal mechanical fatigue behavior of as-fabricated SAC305 specimens as the microstructure transitions from the initial

coarse grained, non-homogenous state to a much more homogenized fine grained state through recrystallization (Chapter 6).

3.3.5. Correlation between Damage and Sn Grain Texture in SAC305 Solder

Comparison of the pre-test grain orientation (Figure 3-5) and post-creep damage patterns (Figure 3-10, Table 3-1) shows that the misorientation angles between Sn grains greatly influences the intensity and location of damage distribution. The SEM images of the failure patterns exhibited by Regions 1 and 2 of Specimen 4 in Figure 3-4 are shown in Figure 3-10 b-e. Correlation with the Sn grain orientations shows that damage/decohesion/out-of-plane steps in the bulk of solder are located predominantly at the Sn grain boundaries.

Sn grains with misorientation angles greater than 30° generated sufficient stress concentrations to cause severe cracks and discontinuities at the grain boundary (Figure 3-10, solid white arrows). In the absence of highly misoriented grain boundaries, the damage site moves to the Sn grain boundaries that are closest to Cu_6Sn_5 IMC layer at the copper platen interface (the dashed white arrows in Figure 3-10). Figure 3-10a shows the side view of the out-of-plane grain boundary ledges formed due to high stress concentrations at the grain boundary of highly misoriented grains (60°) in Region A of Specimen 1. The observed failure patterns are similar to those seen in pure Sn and Sn–based alloys under creep, by other investigators [46, 58, 203-204], where GBS and localized grain boundary damage was observed.

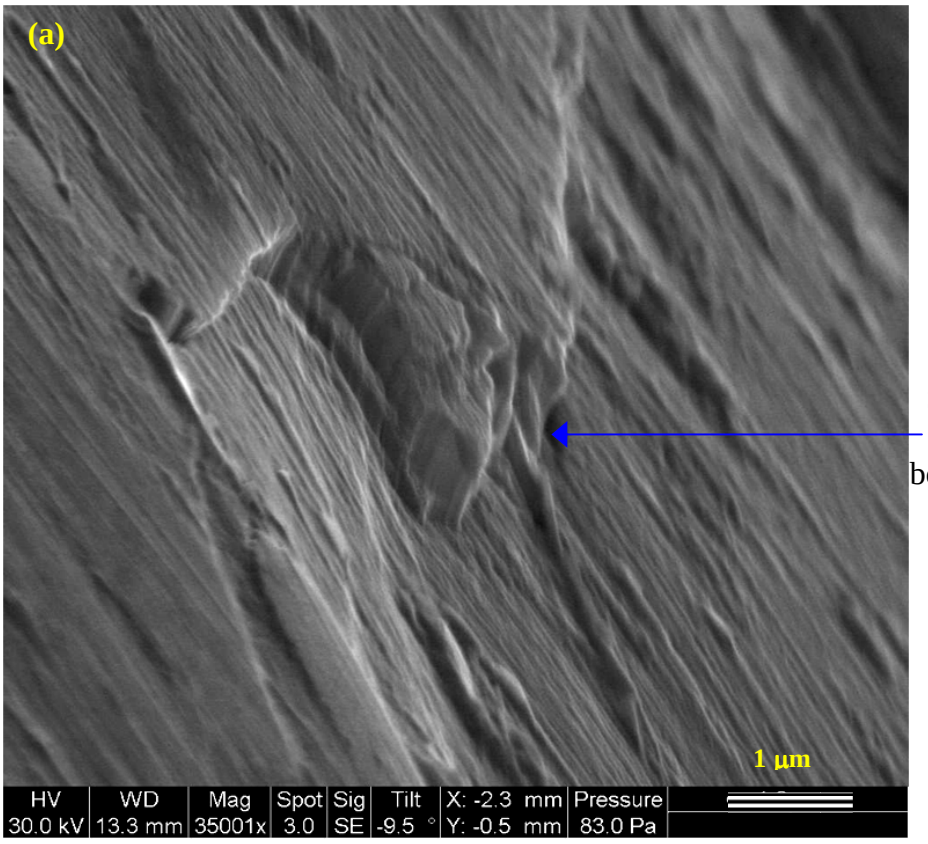
(a)
Step at grain boundary
1 µm
HV 30.0 kV
WD 13.3 mm
Mag 35001x
Spot 3.0
Sig SE
Tilt -9.5 °
X: -2.3 mm
Y: -0.5 mm
Pressure 83.0 Pa

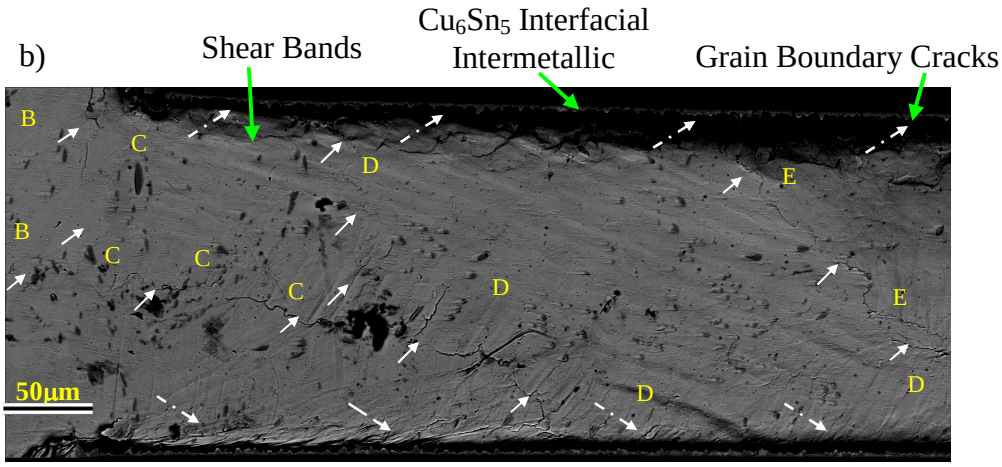
b)
Shear Bands
Cu_6Sn_5 Interfacial Intermetallic
Grain Boundary Cracks
B
C
D
E
50µm

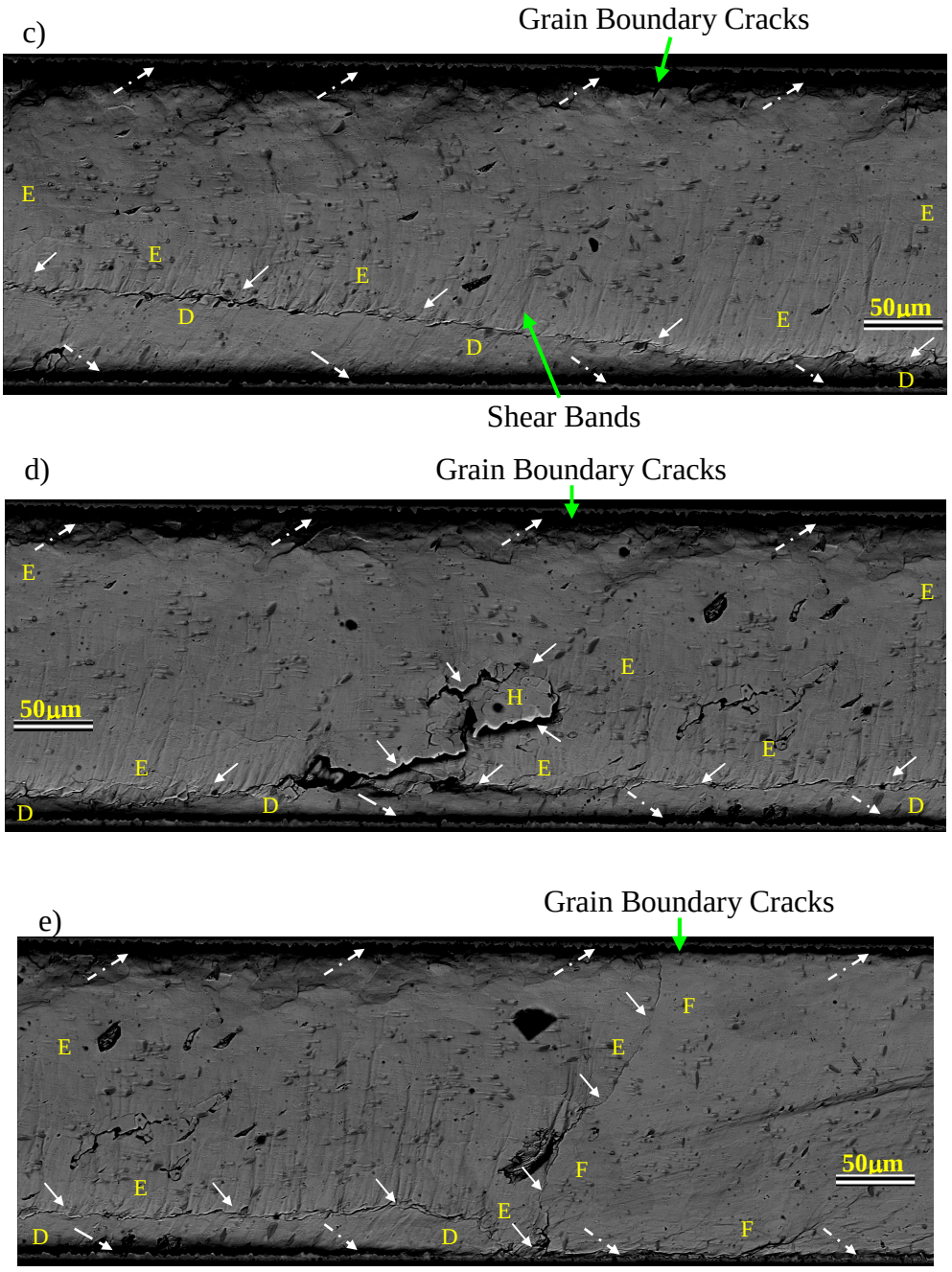

Figure 3-10: Post-failure damage distribution images: a) Grain boundary step in post-creep state in region A of specimen 1(25°C, 10 MPa) (b)-(f) Specimen 4 (125°C, 9 MPa) showing decohesion at grain boundaries (solid arrows) and steps (dashed arrows) at the region close to the interface intermetallic and solder in Regions 1- 2.

Grains	Damage	Misorientation Angles
A-B, A-D, D-E, E-F, around H	Severe	65°, 45°, 60°, 90°, 60°
B-C, F-G, E-F, C-D	Moderate-Mild	30°, 15°

Table 3-1: Sn grain misorientation angles of grains in specimen 4 (Figure 3-5)

3.3.6. Evolution of Sn Grain Texture in SAC305 Solder under Creep Loads

The evolution of the grain microstructure under creep loading is investigated for evidence of recrystallization. The pre-test and post test Sn grain microstructure are investigated and compared for this purpose. The OIM images show that recrystallization occurs in the specimen tested at 125°C. Specimen 5 has two grains misoriented at 80° in the as-fabricated state (see Figure 3-5 and Figure 3-11-a) and eventually recrystallizes to form new grains upon creep loading. Figure 3-11-b shows that the new grains aligned at approximately 45° to the load direction of the solder are formed upon creep loading. The misorientations angles between the newly formed grains are between 60° - 85° (red and green regions). The extent of recrystallization is however not as severe as that observed in TMM joints under mechanical cycling fatigue (Chapter 6).

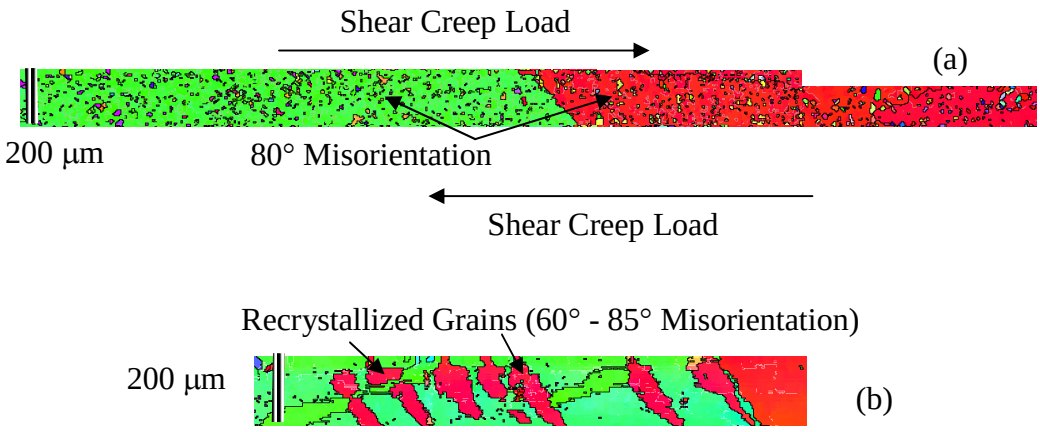

Figure 3-11: Recrystallization in specimen 5 (shown in Figure 3-5) after creep testing at 10MPa, 125°C

When observed using SEM, the position of the newly formed grains corresponds approximately to that of shear bands caused due to creep deformation. In spite of the recrystallization, the grain structure of the joint still remains non-homogenous since the recrystallized grains are few and coarse in nature. Specimen 2 tested at 25° C was also investigated for recrystallization. Though grain B (see Figure 3-5) seems to have grown in size, proof on recrystallization is not conclusive at this load and temperature condition. Hence, recrystallization of the Sn grains in the microscale SAC305 joints occurs at least at loads as high at 10 MPa shear stress at 125° C. Studies that report recrystallization in crept samples include those by Telang [58], Herkommer[199] and Jud [65].

3.3.7. Secondary and Primary Creep Model Constants

Since the microscale SAC305 solder specimens exhibit significant piece-to-piece variability, phenomenological continuum macroscale models can describe the deformation behavior only in an average sense. The primary and secondary creep

models used here are described in Equations 3.1-3.3. Since the models are highly non-linear equations in terms of two independent variables, σ and T, the model constants are numerically estimated by nonlinear least-square fitting techniques. Further details are provided in Appendix 3.1.

Both the Garofalo model (Table 3-2) and the 2-term power-law model (Table 3-3) show comparable fits to the data (see Figures A3.1.2 a-b in Appendix 3.1) The secondary creep behavior, as described by a two-term power-law model, shows a transition at a normalized stress of around 1E-3, which is the expected transition region for a change in the dominant creep mechanism [205]. Based on the chosen transition stress, the power law fits exhibit stress exponents of 3 and 11, respectively, in the low and high stress regions. The activation energies in the high and low stress regions are; 69 kJ/mol and 39 kJ/ mol, respectively.

The activation energies indicate that dislocation core diffusion dominates in the low-stress region and the stress exponent indicates that dislocation climb dominates in the high stress region [10, 61, 76, 107, 111-112, 205]. The constants and mechanisms reported here are indicative of the average behavior across several non-homogenous microscale solder specimens and hence need to be utilized with this underlying caveat.

The constants for the generalized exponential primary creep model are given in Table 3-4. As depicted by the scatter in Figure 3-8, the model constants reflect the measured behavior only in an average sense, and the quality of fit is worse than those in secondary creep (see Appendix 3.1 for the error values). This is consistent with our microstructural observation that the primary creep is more strongly influenced than

the secondary creep, by the Sn grain structure. The secondary creep measurements from these micrometer scale specimens show that as-fabricated SAC305 solder is less creep-resistant than as-fabricated SAC387 but more than as-fabricated Sn37Pb (Figure 3-12). The decrease in creep resistance with decreasing Ag content could be one possible explanation why hypoeutectic SAC305 is less durable than near-eutectic SAC387, under isothermal mechanical cycling conditions[206].

$\alpha(MPa)^{-1}$	n_G	A_G	Q_2 (J-mol-K)
0.18	2.3	6.07	55793

Table 3-2: Garofalo von Mises equivalent secondary creep constants

τ/G			A_L	n_L	Q_L (kJ-mol-K)	A_H	n_H	Q_H (kJ-mol-K)
RT	75^0 C	125^0 C						
1.4E-3		1.0E-3	1.1E10	3.4	39	1.3E36	11	69
1.21E-3		1.0E-3	2.8E6	2.1	43	1.8E32	10	62

Table 3-3: Two-term power-law secondary creep constants (shear components), G =(6.9-(0.00083*T(K))) GPa is used from Ref. [95]

$C_1(MPa)^{-C_2}$	C_2	$C_3(MPa)^{-C_4}$	C_4	Q_1 (J-mol-K)
1.85E-4	1.49	4.1E-2	3.9	39526

Table 3-4: Generalized exponential (equivalent) primary creep constants

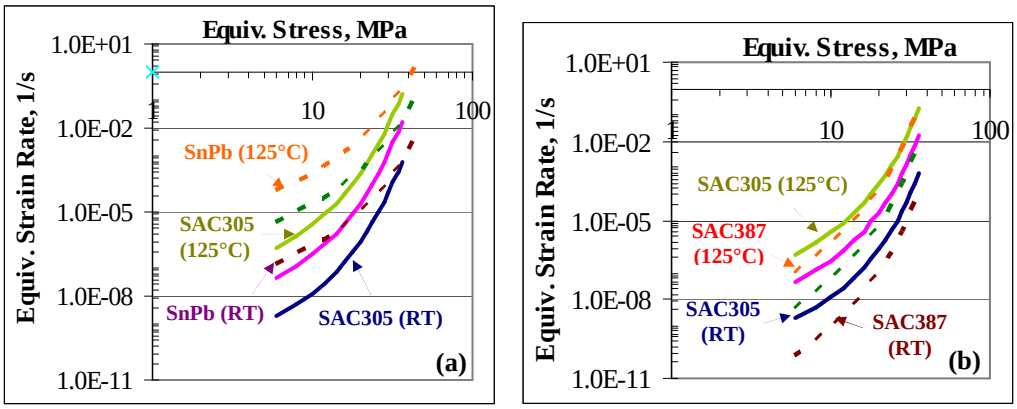

Figure 3-12: Averaged secondary creep strain rate: (a) SAC305 vs. Sn37Pb [104] (b) SAC305 vs. SAC387 [95, 104]

3.3.8. Discussion of Experimental Results

The results of the correlation between the grain microstructure and the measured creep behavior suggest that the grain features strongly influence the primary creep response. However, the variability in the corresponding secondary creep response is much lesser. Most studies on the creep behavior characterization of solder focus on the secondary creep behavior and hence the observed influence of the grain features would not be evident in such studies.

Increasing evidence of the statistically non-homogenous grain microstructure of microscale SAC solder joints (and of the resulting scatter in the viscoplastic behavior) raises serious questions about the validity of reporting averaged test measurements without the associated scatter, and about the value of using homogenized continuum constitutive models to describe their behavior. Constitutive models such as the secondary and primary creep models described here are applicable to statistically homogenous and isotropic materials. At the current length scales of typical SAC solder joints, neither of these conditions hold true. Hence, the use of averaged

continuum models to fit constitutive data of such anisotropic microstructures needs careful examination.

An accurate material representation requires models that include the influence of key microstructural features and dominant creep mechanisms on the measured viscoplastic response. However such a multiscale modeling effort is non-trivial and a preliminary microstructural model based on dislocation mechanics and micromechanics is explored in Chapter 4. This model accounts for the influence of lower length scales on the average secondary creep behavior. Future work should focus on quantifying the influence of key microstructural features on the scatter exhibited by the creep characteristics (ex. primary saturated creep). Suitable metrics that represent the key microstructural features (such as grain orientation distribution and grain boundary morphology, relative to loading direction) need to be developed.

Such an effort to capture the measured range of scatter by modeling key microstructural features is very involved. An approximate and preliminary solution is to conduct macroscale modeling using the averaged properties that are representative of varied grain orientations (Table 3-2,Table 3-3 and Table 3-4), and to investigate the level of accuracy with which these averaged creep properties predict the stress relaxation response. These results are reported in Chapter 5 as continuity to the current report.

Nanoscale IMCs distributed in the Sn-Ag eutectic phase surrounding each Sn dendrite pin the dislocation motion via dislocation climb (Figure 3-7 and Section 3.3.7). The extent of pinning is hence dependent on the size and distribution of IMCs and of the Sn dendrites which vary with manufacturing profile and aging conditions.

In the current study, the manufacturing profile and aging conditions are closely controlled to minimize dendritic variations. However, the role of dendritic orientations cannot be ignored and microstructural studies are in progress to characterize and understand the effect of Sn dendritic and IMC distributions and configurations on the mechanical response of SAC305 solder.

3.4. SUMMARY AND CONCLUSIONS

The creep response of microscale SAC305 solder shear specimens in the as-fabricated state is reported. The monotonic creep measurements show significant piece-to-piece variability, the lower bound of which is similar to the variability measured in the elastic and plastic behavior of similar specimens. Microstructural analysis reveals that the as-fabricated TMM SAC305 specimens exhibit a highly non-repeatable Sn grain microstructure with very few grains similar to that seen in functional solder interconnects. The non-homogenous Sn grain microstructure has a stronger impact on the scatter in primary creep, than in secondary creep, for the studied cases.

The variability in the primary creep response is as high as a factor of 100 compared to a factor of 2 observed in the secondary creep behavior. Microscale Sn37Pb specimens tested using the same test methodology and protocols however exhibit homogenous microstructure and lower specimen to specimen variability than SAC305 specimens due to the presence of a large number of small Sn (and Pb) grains. Thus the fine-grained microstructure demonstrates much more uniform response across the entire test matrix compared to the coarse grained microstructure.

Similar results are observed in the mechanical fatigue response due to increasing homogeneity of the grain microstructure in microscale SAC305 specimens as a function of fatigue damage (Chapter 6). The variability in SAC305 creep results, in conjunction with the associated lack of statistical homogeneity in the Sn grain microstructure; demonstrate that the deformation of microscale SAC solders is heavily dependent on the crystallographic orientation and distribution of the anisotropic Sn grains.

Creep damage in the SAC305 joint is predominantly concentrated at highly misoriented Sn grain boundaries (>30°) if present, or at the Sn grain boundary adjoining the interface IMC layer. The initial coarse-grained Sn microstructure recrystallizes to form new smaller grains with high misorientation angles (> 60°) under creep loading. The extent of recrystallization is however not as severe as that observed in mechanical cycling fatigue.

The creep resistance of microscale SAC305 specimens is higher than that of Sn37Pb but less than that of SAC387, in spite of the scatter. The average creep behavior of SAC305 solder is captured using isotropic, continuum models. Dislocation climb assisted by dislocation pipe diffusion is seen to be the dominant creep mechanism.

Chapter 4: Multi-scale Modeling of the Viscoplastic Response of As-fabricated Microscale Sn3.0Ag0.5Cu Solder Interconnects

ABSTRACT

A mechanistic multiscale framework is proposed, to capture the dominant creep deformation mechanisms and the influence of key microstructural features on the measured secondary creep response of microscale as-fabricated SAC305 solder specimens. Guided by test measurements (Chapter 3) and insights from literature, mechanistic models of dislocation climb and detachment are used to capture the dominant creep deformation and dispersion strengthening mechanisms in the eutectic phase of SAC solders. These microscale models are then combined at the next larger length scale (that of dendritic and eutectic colonies), with traditional micromechanics based homogenization schemes, to capture the load-sharing between eutectic phases, dendritic phases, and Cu_6Sn_5 intermetallic reinforcement particles.

The next higher length scale (that of Sn grain distributions) is not addressed here since the focus is on modeling secondary creep, which is empirically observed in this study to be relatively insensitive to grain microstructure. Starting with the behavior of pure Sn properties and the microstructural morphology of the SAC305 alloy, this modeling approach is used to provide theoretical insights into the influence of key microstructural features on the viscoplastic deformation behavior of microscale SAC305 specimens. Based on these microstructural features, the model effectively captures the effect of alloy composition and aging loads on SAC solders, thereby aiding in the effective design and optimization of the viscoplastic behavior of SAC

alloys. The model can be extended to understand the effect of manufacturing profiles on the secondary creep behavior.

4.1 INTRODUCTION

The mechanical behavior of SAC solders is heavily dependent on microstructural features such as the Sn dendrites and the IMCs (nano and microscale dimensions) dispersed in the bulk, as detailed in Chapter 1. In the case of microscale SAC solder joints; the grain configurations have an additional influence on the viscoplastic creep behavior (Chapter 3). The microstructure of the Sn dendrites and IMCs are dependent on various parameters such as manufacturing profiles, loading history and weight fraction of Ag in SAC alloys to name a few.

As detailed in the introduction (Chapter 1), a comprehensive understanding of the influence of each of these dictating parameters on the mechanical response of SAC from experimental testing is cost and time ineffective. Furthermore, such studies provide only an empirical understanding of the effect of the underlying microstructural features on the mechanical response and cannot be easily extrapolated to other test conditions/material systems. In order to obtain insights into the physics of the deformation induced by each of these microstructural features, a mechanistic modeling framework that captures the dominant deformation mechanism in terms of the key microstructural features is crucial.

4.1.1. Length Scales and Feasible Modeling Themes

Microscale modeling can be conducted to capture the constitutive behavior as well as the damage accumulation under fatigue loading. Damage modeling requires

the constitutive models to be combined with appropriate damage mechanisms for failure such as void formation, growth and coalescence to catastrophic failure in the case of creep failure [66, 207-209]. Similarly constitutive and damage modeling based on plasticity can be found in ref [164]. The constitutive model can be steady or can evolve as a function of accumulated damage. Constitutive damage modeling in which the properties degrade as a function of damage provides conservative estimates of the mechanical response and fatigue reliability of the material.

In the current work, the proposed microscale modeling focuses on the initial undamaged viscoplastic creep constitutive behavior of SAC alloys. Furthermore, creep deformation studied here is based on the partitioned approach, where deformation is partitioned into contributions from elasticity, rate independent plasticity and rate dependent creep. This microstructural model of viscoplastic constitutive behavior can be used to address the evolution due to thermal pre-aging but not the evolution due to cyclic fatigue damage. A continuation to this work could involve the inclusion of the degradation of the constitutive properties due to softening induced by both increasing material damage, as well as due to an evolving grain structure.

Furthermore as described in Chapter 1, there are several length scales involved in the microstructure of SAC solder joints. These scales vary from nanoscale dimensions of Ag_3Sn intermetallics in the eutectic region, which provide the dispersion hardening creep mechanisms, to structural length scale (~mm) dimensions of Sn grains that contribute towards the non-homogenous behavior of microscale SAC joints (Figure 4-1). Based on the level of complexity and parameters required, the underlying

dislocation creep motion can be captured by multi-scale modeling schemes. These schemes could vary from molecular dynamics based schemes to capture the interaction of individual atoms to macro-scale homogenized behavior of the SAC solder (See Appendix 4.1). Prior to addressing all the length scales (non-homogenous grains and relatively homogenous phases of Sn-Ag eutectic regions, Sn dendrites and IMCs); the influence of the homogeneous length scales on the measured creep response is first addressed.

Several microscale models exist for capturing the creep behavior of previously used benchmark Sn37Pb solder whose dominant creep deformation mechanism is grain boundary sliding (see for example [66]). However these studies cannot be applied to SAC solders where grain boundary sliding is expected to be negligible [10-11, 27] and the dominant creep mechanism is dislocation climb over hard nanoscale intermetallics.

In the current study, the smallest length scale modeled is the nano-scale IMCs via analytical dislocation creep models, and the largest length scale is that of the eutectic and dendritic colonies (micrometers). The reason for addressing these length scales is that the test measurements show that dendritic and eutectic regions are expected to dominate in the secondary creep behavior of undamaged microscale SAC specimens. As detailed in Chapter 3 (Figure 3-8), for the observed microstructures, the largest length scale, namely the Sn grains, does not influence the secondary creep region as much as the primary region. Hence it is assumed that the dendritic and eutectic region IMCs influence the secondary creep response (the variability in the secondary creep rates is a factor of two, as opposed to at least two orders of magnitude in the primary

creep). These results are presented in Figure 4-2 as continuity to the multi-scale modeling framework proposed here.

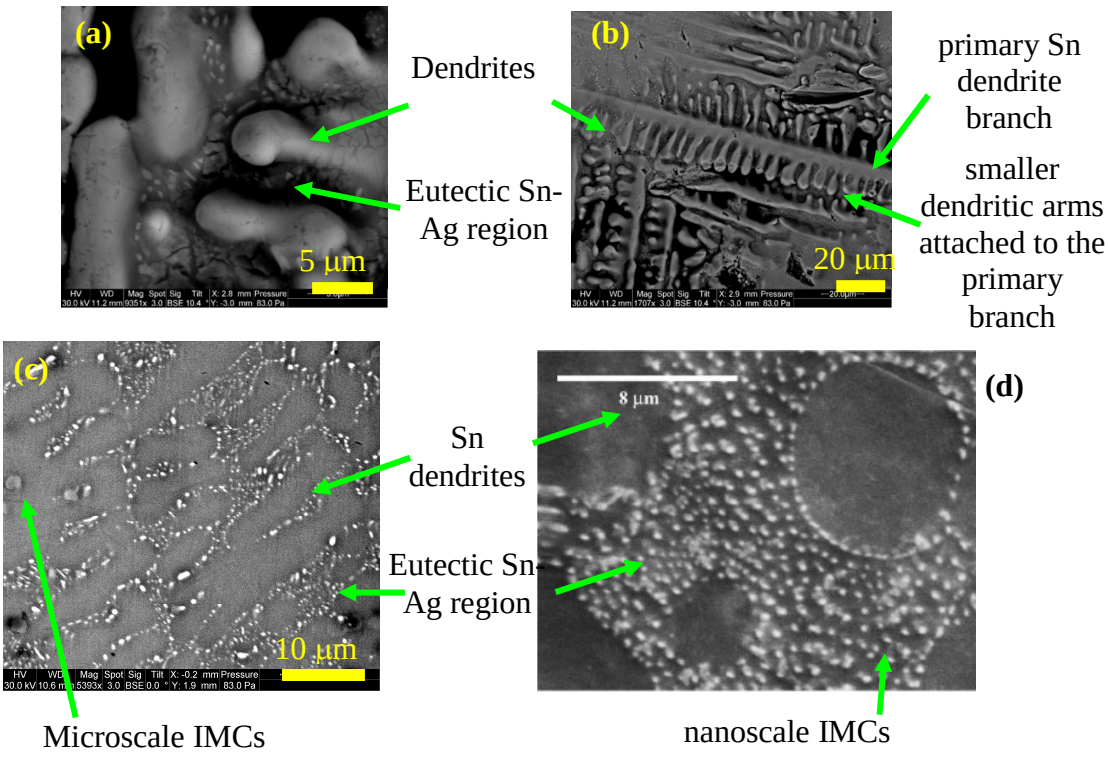

Figure 4-1: Microstructural features in microscale as-fabricated SAC305 solder (a)-(c) 3-D and 2-D view of dendritic structures with (c) Eutectic Sn-Ag regions and microscale Cu_6Sn_5 IMCs in the bulk, (d) Nanoscale IMCs in dendritic regions from [27]. Image (d) has been adapted from literature.

4.1.2. Aspects of Creep Behavior to Model and Motivation of the Study

As described in Chapter 3, the creep constitutive behavior comprises of the primary creep and the secondary creep deformations prior to transitioning to catastrophic failure in the tertiary regions. Typical modeling schemes utilize only the primary and secondary constitutive creep behavior. The extent of specimen to specimen variability exhibited by the primary and secondary creep response of the microscale SAC305 TMM specimens as studied in Chapter 3 are presented here (Figure 4-2 a-d). The grain orientations of six specimens are characterized and tested under similar test loads for repeatability (specimens 1-3 at 10 MPa, 25°C and specimens 4-6 at 10 MPa, 125°C). The grain orientations are presented in sections 3.3 of Chapter 3.

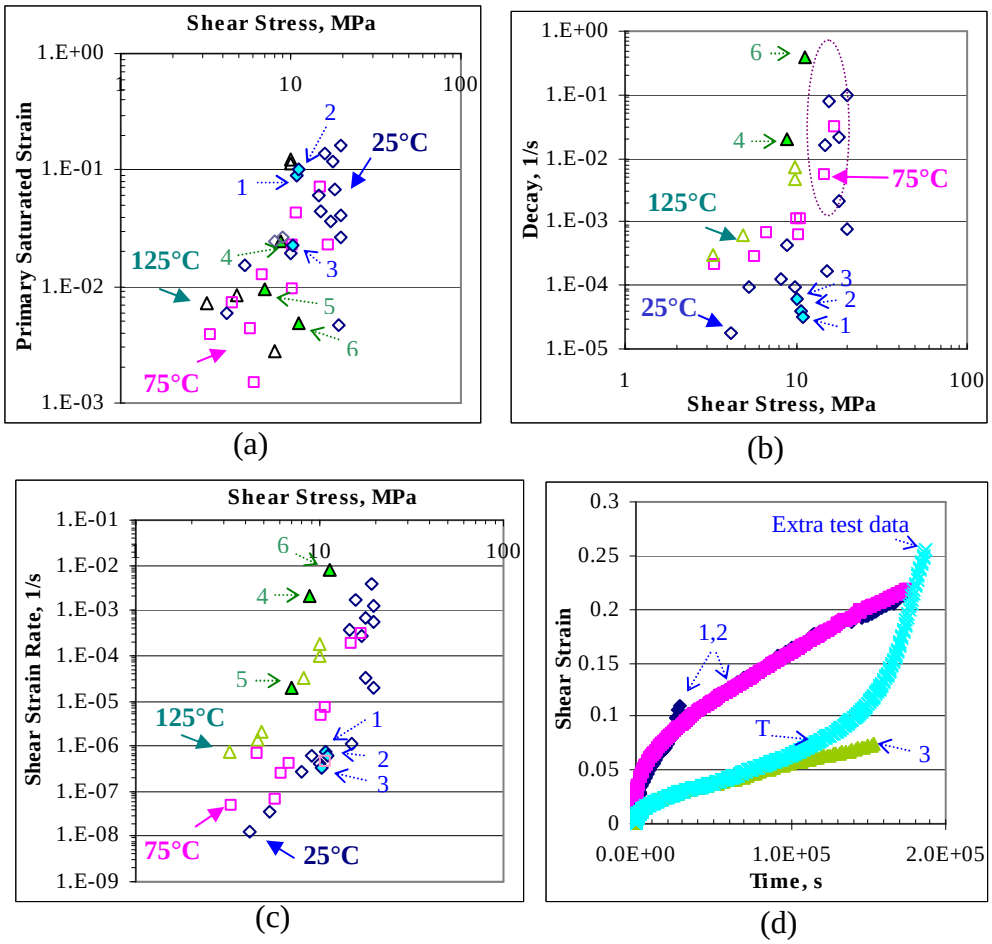

Figure 4-2: Influence of the Sn grain textures on the measured creep behavior (in shear) (a) primary saturated creep strain, (b) decay of primary creep, (c) secondary creep rate, (d) total strain history (25°C, 10 MPa). Dotted circle shows the stress at which scatter is evident (data points1-6 refer to specimens used in the orientation imaging microscopy that are detailed in Section 3.3 of Chapter 3)

The results of the correlation between the grain microstructures and the measured creep response are reported here for continuity. The results (Figure 4-2 a-d) clearly show that the Sn grain configurations and features of the non-homogenous microscale SAC305 specimens strongly influence only the primary creep region (and hence the resulting total creep) of the measured creep response. The results show that the

variability in the secondary creep rates is a factor of two. However the variability in the primary creep (saturated creep strain) is as high as two orders of magnitude (factor of 100).The secondary creep can hence be considered to be relatively insensitive to the non-homogeneous grain microstructure of the microscale SAC305 joint.

As mentioned in Chapter 3, the conclusions are based on the room temperature measurements which are conducted at loads below the high stress sensitivity regions (~12MPa). The secondary creep behavior does not show significant scatter at low-to-intermediate stress levels. However, significant variability (greater than two orders of magnitude) is observed in identical specimens tested at 20 MPa, 25°C and at 10 MPa, 125°C. This change in scatter levels, in conjunction with a change in the sensitivity of secondary creep strain rates to stress level, suggests a transition of dominant creep mechanism.

4.1.2.1. Dominant Creep Mechanisms

TEM studies suggest that the presence of nano-scale dimensions of Ag_3Sn serve as obstacles to pin the dislocation motions [107]. Thus the dispersion hardening behavior causes a retardation of dislocation motion and dictates the creep resistance. The dominant rate-governing creep mechanism is hence dislocation climb over the obstacles and detachment. Apart from the nano-scale Ag_3Sn IMCs, grain boundaries, and other dislocations are also expected to serve as obstacles to dislocation motion. The existence of dislocation climb is further supported by the high stress exponents (~ 9) obtained from the secondary creep measurements in the TMM specimens. (see Chapter 3, Section 3.3.7 and Table 3-3 or Table 4-1). The stress exponents obtained

here for SAC solders and the existence of climb agree well with those from the literature on pure Sn and SAC solders [39, 61, 67, 107, 194].

Dislocation climb has been reported as the dominant creep mechanism for several dispersion strengthened material systems (e.g. aluminum and titanium alloys [166, 178]). TEM studies conducted on dispersion strengthened materials, suggest that dislocation climb occurs in multiple stages; approach, climb and detachment. In particular, TEM results show that some materials exhibit a strong attractive interaction between the dislocation and the particle in the post-climb phase of the dislocation [210] [211].

The TEM result presented by Schroder et al, clearly shows the dislocation segment attached to the particle after climbing over it (see schematic in Figure 4-3) [211]. These studies also suggest that the detachment of the departing dislocation is the rate limiting mechanism rather than the climb of the dislocation. In the current study, a similar attractive interaction between the departing dislocation and nano-scale Ag_3Sn IMCs in the eutectic regions is assumed to exist and athermal detachment models are utilized to capture the dispersion strengthening behavior.

4.1.2.2.Secondary Creep Behavior: Model and Scope

Since experimental results from microscale SAC305 joints at low-to-intermediate stress levels show that Sn grain morphology does not significantly affect secondary creep behavior, the structural anisotropy of Sn grains configurations and grain boundaries can be assumed to be unimportant to the dominant mechanisms for secondary creep. The measured response is now believed to be dictated by the IMCs dispersed in the eutectic phase and by the Sn dendrites. Furthermore, reports in

literature support the chosen microstructural dependence, since parameters such as manufacturing profiles, are known to affect only the Sn dendrites and IMCs, and have relatively little effect on the grain microstructures [24, 82].

Physically, the reduced influence of Sn grain anisotropy (dominant slip direction for dislocation motion) in the secondary region can be hypothesized to be due to the material achieving a higher dislocation density with increasing primary creep strain. Eventually at the secondary creep region, the dominant slip systems may become so 'clogged' due to high dislocation density that many other secondary slip systems may become active in addition to the primary slip system. Thus, the creep response becomes more isotropic and less sensitive to grain orientations. A model that captures the influence of lower length scales may be useful in understanding the effect of various parameters such as manufacturing profiles, aging and % Ag in SAC on the secondary creep behavior.

Scope: The secondary creep mechanistic model captures the influence of the Sn dendrites and IMCs only and hence is applicable to understanding the effect of manufacturing profiles, % Ag variations, and aging histories in SAC behavior. The secondary creep model can be used with anisotropic creep properties of Sn grains to model the primary and total creep strain of the solder (Section 4.1.2.3).

4.1.2.3.Primary and Total Creep Behavior

Primary creep characterization and modeling are complex since measurements from the current study suggest that they include case-specific creep anisotropy from the Sn grains. Since the creep response of single-crystal Sn is not well understood yet, these complex behaviors are postponed to future studies and the focus instead is

on the more isotropic secondary creep behavior described in Section 4.1.2.2 above (see Appendix 3.3 and Appendix 4.2 for more details).

4.1.3. State-of-Art in Multi-Scale Creep Constitutive Models for SAC

In recent times, there has been focus on providing an understanding of the effect of the microstructural features of SAC on the damage evolution under fatigue loads through experiments and modeling. Experimental studies have been discussed in the introduction (see for example, ref. [46, 48, 58, 212]). Modeling efforts contributing towards understanding the effect of microstructural features on the constitutive and fatigue behavior are limited in comparison and discussed next.

Grain configurations: The influence of varying grain orientations and configurations on the overall mechanical deformation of the joint is generally studied in literature using finite element analysis that captures the full coarse grained geometry and orientations. These studies show that the elastic and thermal anisotropy alone is sufficient to produce significant damage under thermomechanical loads [45, 188, 212-214]. As discussed in Chapter 3, damage is evident especially at the grain boundaries of the coarse-grained SAC305 TMM joint (Section 3.3.4 and Figure 3-10).

These studies provide insights on the effect of the grain configurations on the damage concentration and mechanical behavior of the joint, and have successfully implemented complex enriched continuum mechanics modeling techniques (strain gradient, non-local modeling) and cohesive zone damage modeling. While these studies are insightful in understanding the effect of the grain configurations on the mechanical behavior of the joint, the microstructural length scale is limited to that of

the grain dimensions. The effect of the lower length scales, Sn dendrites and IMCs is not captured since macro-scale (length scale independent) viscoplastic models (with an evolving damage variable in some studies) are used to represent the viscoplastic behavior of SAC.

Intermetallics: Gong et.al, [73], however accounted for the nanoscale Ag_3Sn IMCs utilizing microscale models based on mechanics of dislocation climb detachment creep provided by [27, 107]. This model was further coupled with a damage induced coarsening model for nanoscale Ag_3Sn IMCs to account for the degradation of creep properties. This model has the advantage of capturing the IMCs influence and their evolution, as well as the influence of the grain anisotropy in a finite element model. The microscale constitutive model constants used by Gong are based on the work of Kerr and Dutta [27, 107]. The model used is the detachment model proposed by Rosler [215] that captures the effect of IMCs only. Kerr and Dutta's model [27, 107], is among the early works that captures the contributions of the eutectic Sn-Ag and IMC length scales. However the model assumes that the behavior is dictated only by the dispersion strengthening of nanoscale Ag_3Sn IMCs in the Sn-Ag eutectic. Dutta obtained the constants by assuming a critical relaxation parameter, k, (configuration of post-climb dislocation segment) and fitting the constants to the Sn3.5Ag creep measurements.

One of the limitations of this work is that the behavior is assumed to be dictated by the Sn-Ag eutectic region only and the effect of Sn dendrites is not included. The model is also not dependent on the creep behavior of Sn which forms the matrix relative to which dispersion strengthened is achieved in SAC or Sn3.5Ag alloys.

Furthermore, though the model adopted by Dutta which is Rosler's model is intuitive in providing the effect of IMC (radius and spacing), this model has been critiqued by the original authors, Rosler [215] owing to its empirical nature. To overcome the empirical limitation, Rosler and Arzt [182] utilized variational methods to derive a mechanistic detachment model that could predict the effective properties of a composite based on the matrix properties and the geometric parameters of the dispersion particles [178-179, 182].

The first use of this model in the solder literature was by Sharma et al, in predicting the viscoplastic properties of SAC387 solder [183]. Their results indicated that the model constants are stress dependent. An important material constant in Rosler's mechanistic model which is extremely critical to the mechanics of climb is the relaxation parameter, k. The relaxation parameter which represents the ratio of line tensions of dislocation on the particle versus the matrix regions is not easily measureable. In Sharma's work, an analytical derivation for dislocation relaxation parameter is provided but the basis and source of this formulation is not indicated. Their work also accounts for the eutectic Sn-Ag region only and does not account for other scales.

Dendrites: Most of the microscale models reviewed this far on constitutive modeling account for the nanoscale Ag_3Sn IMCs and the eutectic Sn-Ag region that are embedded in. Such a model strategy inherently assumes that the contribution of the Sn dendrites is negligible. The load-sharing effect of the dendrites is included in this dissertation using homogenization methods, by modeling the dendrites as soft inclusions in a hard Sn-Ag eutectic 'matrix'.

Homogenization techniques have been utilized for effective medium approximation of numerous material systems for average elastic, plastic and viscoplastic properties. Examples of homogenization techniques in solders include finding the effective creep properties under growing void densities [66] and effective plastic properties [186]. An interesting study by Pei [20], evaluates the effective creep properties of Pb-free SAC solders by homogenizing the measured properties of individual phases (eutectic phase and dendritic phase). However, this technique does not utilize mechanistic equations for predicting individual IMC phase properties. Thus it lacks the predictive capability for extrapolating the response to other SAC alloys or fabrication protocols.

4.1.4. Objectives and Scope of the Study

Studies that provide/utilize mechanistic models to capture the physics of the underlying creep mechanisms of the viscoplastic creep behavior of SAC solder are very limited in literature. Furthermore, multi-scale studies that provide the influence of both the Sn dendrites and the eutectic Sn-Ag region on the creep behavior are required. Thus, the primary objective of the current study is to combine available dislocation detachment models at the lattice scale and homogenization techniques at the length scale of dendritic and eutectic colonies, to understand the strengthening effects they produce in Sn matrix.

Prior to utilizing this multi-scale model for understanding the effect of aging and composition on the creep behavior of SAC solder, the model constants have to be calibrated using the creep behavior of pure Sn matrix, of Sn-Ag eutectic phases and of the final SAC solder alloy. The calibration procedure is demonstrated with sample

properties typical of SAC solder systems. The main objective of the study is to utilize the mechanistic model with typical sample model constants, to provide parametric insights on the effect of % Ag in SAC and aging profiles on the secondary creep response.

4.2. MODELING APPROACH

The models used to account for the influence of the Sn dendrites, and the IMCs on the creep response of SAC solders are described in this section.

4.2.1. Models

The multiscale model captures the following two length scales (Figure 4-1):

- Length scale 1 (Sn matrix with nanoscale Ag_3Sn IMCs): dilute approximation for dislocation climb & detachment within eutectic region
- Length scale 2 (Micron dimension dendrites embedded in eutectic Sn-Ag regions): effective medium approximation (homogenization) to address load-sharing between dendritic phase, eutectic phase and Cu_6Sn_5 IMC.

The secondary creep measurements do not show any sensitivity to the coarse-grained Sn microstructure in the microscale SAC305 specimens (Section 3.3.6, Figure 3-8). This finding significantly reduces the complexity of the microscale modeling effort required since geometric modeling of the grains and grain boundaries is not necessary. In fact, an analytical formulation of the effective properties of the Sn matrix and the microstructural properties suffices. The creep behavior of pure Sn is utilized as the matrix of the composite. For the purpose of the secondary creep model, polycrystalline, isotropic properties (elastic and creep) are chosen for Sn.

In the first level, the properties of the eutectic Sn-Ag region is evaluated, by assuming Sn as the matrix and nano-scale Ag_3Sn and microscale Cu_6Sn_5 as the inclusions. The nano-scale Ag_3Sn IMCs are assumed to be spherical inclusions and microscale Cu_6Sn_5 are assumed to be cylindrical rods. In the second level, the effective creep properties of this eutectic Sn-Ag region are then utilized as the matrix of the composite which has soft spherical inclusions of pure Sn dendrites. The microstructural images that represent these scales are shown Figure 4-1 a-d.

4.2.1.1.Effect of Nano-scale Ag_3Sn on Properties of Sn-Ag Eutectic Phase

Intermetallics of nano-scale dimensions (with ~180 nanometer spacing) primarily serve to provide the dispersion strengthening mechanisms due to dislocation climb and detachment. The superior creep properties of SAC solders are mainly due to these fine IMC particles. The creep deformation exhibited by these particles is modeled using Rosler's athermal detachment model for dislocation climb [178-179, 182], which is formulated from energy considerations of the mechanics of climb.

The model inherently assumes that an interaction exists between the dislocation and the Ag_3Sn IMCS after climb (see Figure 4-3 for the schematic of the dislocation climb and detachment process). The model accounts for the role of the IMC dispersions to the Sn matrix material and hence provides the effective properties of the eutectic Sn-Ag regions. However, in its present form, this model only provides a 'dilute approximation' since it does not explicitly account for the interactions between neighboring obstacles at high volume fractions or between neighboring dislocation fronts at high dislocation densities.

Thus the eutectic Sn-Ag region creep rate $\dot{\gamma}_{eut-SnAg}$ is a combination of the Sn matrix creep rate $\dot{\gamma}_{mat}$ and the Ag_3Sn IMC dispersion hardening creep rate $\dot{\gamma}_{disp-IMC}$, as given in Equations 4.1 a-f. The net creep rate $\dot{\gamma}_{eut-SnAg}$ can be derived from the assumption that the time taken by a dislocation to traverse through a unit cell of the Sn-Ag eutectic composite is the sum of the time it takes to travel through the Sn matrix phase and the time to travel through the IMC phase.

$$\frac{1}{\dot{\gamma}_{eut-SnAg}} = \frac{1}{\dot{\gamma}_{mat}} + \frac{1}{\dot{\gamma}_{disp-IMC}} \qquad (4.1a)$$

Where $\dot{\gamma}_{disp-IMC}$ is given by: $\frac{\dot{\gamma}_{disp-IMC}}{\dot{\gamma}_0} = \exp\left(-\frac{\boldsymbol{G}_{\det}\boldsymbol{b}^2\boldsymbol{r}\left[(1-\boldsymbol{k})(1-\boldsymbol{\tau}/\boldsymbol{\tau}_d)\right]^{3/2}}{\boldsymbol{k}_B\boldsymbol{T}}\right)$ (4.1b)

in which the athermal detachment stress is: $\boldsymbol{\tau}_d = \boldsymbol{c}\frac{\boldsymbol{G}_{\det}\boldsymbol{b}}{2\boldsymbol{\lambda}}\sqrt{1-\boldsymbol{k}^2}$ (4.1c)

and the reference strain rate $\dot{\gamma}_0 = \frac{6\lambda\rho}{\boldsymbol{b}}[\boldsymbol{D}_{0L}\exp(-\frac{\boldsymbol{Q}_L}{\boldsymbol{RT}}) + \boldsymbol{D}_{0H}\exp(-\frac{\boldsymbol{Q}_H}{\boldsymbol{RT}})]$, (4.1d)

and the particle spacing $\boldsymbol{\lambda} = \boldsymbol{r}(\frac{\pi}{6\boldsymbol{f}_{IMC-Ag_3Sn}})^{0.5}$, (4.1e)

and the Sn matrix creep $\dot{\gamma}_{mat} = \boldsymbol{A}_L(\frac{\tau}{\boldsymbol{G}_{Sn}(\boldsymbol{T})})^{n_L}\exp(-\frac{\boldsymbol{Q}_L}{\boldsymbol{RT}}) + \boldsymbol{A}_H(\frac{\tau}{\boldsymbol{G}_{Sn}(\boldsymbol{T})})^{n_H}\exp(-\frac{\boldsymbol{Q}_H}{\boldsymbol{RT}})$

…… (4.1f)

where: $\dot{\gamma}_0$ is a normalization constant, G_{det} is the shear modulus of tin, G_{Sn} is the stress normalization constant in Sn matrix creep, b is the burger's vector for tin (Appendix 4.3), r is the average nanoscale Ag_3Sn dispersoid radius, λ is the interparticle spacing (estimated from square packing and the stoichiometric volume

fraction), c is the kock's factor, ρ is the dislocation density in SAC (Appendix 4.3), k_B is Boltzmann's constant, and T is the absolute temperature (Table 4-1, Table 4-2 and Table 4-3).

The relaxation parameter k is defined as the ratio of line tensions of the climbing dislocation at the particle-matrix interface versus that in the matrix. This parameter is a key parameter to the mechanics of climb since it determines the configuration attained by the dislocation in the post-climb regime. The dispersoid is a void when k is zero and has the properties as matrix when k is unity. τ_d the athermal detachment stress, refers to the stress required in the absence of thermal energy for the dislocation to overcome the obstacle in the post-climb regime and detach itself. The diffusion properties and the matrix creep constants of Sn (Equation 4.1d and f) are detailed next.

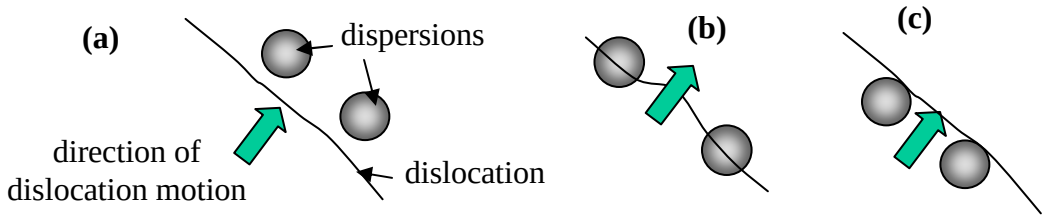

Figure 4-3: Schematic of dislocation climb and detachment of dislocation (a) before reaching the obstacle, (b) during climb over particle (c) experiencing attractive interaction with particle after climb and eventually departing from the particle (detachment)

4.2.2. Effect of Pure Sn Matrix

Isotropic creep and elastic properties of polycrystalline Sn from the work of Adeva [216] are used in this study**.** However, the creep measurements are applicable

only for tensile stress levels of 4 MPa, and most studies in literature are restricted to low stress levels. The activation energy and stress exponent for pure Sn match those obtained from SAC305 measurements in the low stress range in this dissertation. SAC solder is expected to exhibit superior creep properties (namely stress exponent and coefficient) than Sn in the high stress region. However for a conservative estimate of the Sn creep response in the high stress region, the n and Q from SAC305 are used to determine the high stress properties. The stress coefficient in the high stress region (A_H) is calculated from the low stress properties of Adeva (Table 3-3 for the 2-P model constants for SAC305).

The Sn creep constants (two-power law Weertman's equation 4.1f) and shear modulus are provided in Table 4-1 and Table 4-2**.** G_{Sn}, the shear modulus used by Adeva for normalizing the stress is much lower than that expected for Sn, and hence G_{det} the shear modulus of Sn matrix in detachment model is based on the measurements of Fraizier [217]. ($D_{oL,}$ D_{oH}) and (Q_L,Q_H) used in the reference strain rate (Equation. 4.1d), refer to the diffusion coefficients and activation energies in the low and high stress regions. The activation energies in $\dot{\gamma}_{mat}$ and $\dot{\gamma}_0$ are the same for a given stress regime (low or high).

4.2.3. Effect of Microscale Cu_6Sn_5 & Ag_3Sn IMCs on Alloy Properties

Unlike the nanoscale Ag_3Sn IMC particles, the microscale Cu_6Sn_5 and Ag_3Sn IMC particles(~5μm) cannot contribute to dispersion strengthening through dislocation climb type of mechanisms[179]. As the dispersion size (r) gets larger, the strengthening from dislocation inhibiting mechanisms decreases (see Eqns. 4.1 b, c

and e). However particles of larger dimensions are still useful, since they strengthen the creep of the matrix via reinforcement strengthening. Reinforcement strengthening from microscale IMCs occurs in the creep contributions from both the Sn matrix and nanoscale Ag_3Sn dispersoid creep by reducing the magnitude of applied stress in the material for dislocation motion, via a strengthening coefficient, Λ in Rosler's formulation [179]. The formulation for Λ used by Rosler [179] is based on the finite element results of [218-219].

Creep strengthening obtained through nano-scale and micro-scale dispersions in the matrix via dispersion hardening and reinforcement strengthening has been termed as dual-scale particle strengthening [179]. With reinforcement strengthening included, the dislocation detachment formulations in Equations 4.1 a-e, take the form shown in Equations 4.2 a-d. All microscale Ag_3Sn IMCs are replaced by microscale Cu_6Sn_5 in this work, which are assumed to be cylindrical rods. The nano-scale Ag_3Sn IMCs are assumed to be spherical inclusions.

In addition, the base Sn matrix properties are also improved by the reinforcement strengthening via Cu_6Sn_5 and Ag_3Sn IMCs (Equation 4.2c). However, the extent of reinforcement strengthening is not as significant as dispersion strengthening and serves only to produce a parallel shift (constant n) in the creep resistance as a function of stress. Furthermore, larger sizes of reinforcement particles could lead to embrittlement and loss of ductility of the composite. The geometrical parameters for Cu_6Sn_5 have been obtained from image analysis on SAC305 as-fabricated TMM specimens and from the work of Chawla [220] as detailed in Table 4-3.

The creep rate of the eutectic Sn-Ag region reinforced with the microscale Cu_6Sn_5 IMCs and dispersion strengthened by nanoscale Ag_3Sn IMCs, $\dot{\gamma}_{eut-SnAg-rein}$ is

$$\frac{1}{\dot{\gamma}_{eut-SnAg-rein}} = \frac{1}{\dot{\gamma}_{mat-rein}} + \frac{1}{\dot{\gamma}_{disp-IMC-rein}} \tag{4.2a}$$

where the dispersion strengthening of the nanoscale Ag_3Sn IMCs $\dot{\gamma}_{disp-IMC-rein}$ is given by:

$$\frac{\dot{\gamma}_{disp-IMC-rein}}{\dot{\gamma}_0} = \exp\left(-\frac{G_{\det} b^2 r\left[(1-k)(1-\tau/\Lambda\tau_d)\right]^{3/2}}{k_B T}\right) \tag{4.2b}$$

and the microscale Cu_6Sn_5 IMCs reinforced Sn matrix creep is:

$$\dot{\gamma}_{mat} = A_L\left(\frac{\tau/\Lambda}{G_{Sn}(T)}\right)^{n_L} \exp\left(-\frac{Q_L}{RT}\right) + A_H\left(\frac{\tau/\Lambda}{G_{Sn}(T)}\right)^{n_H} \exp\left(-\frac{Q_H}{RT}\right) \tag{4.2c}$$

$$\text{where } \Lambda = 1 + 2*\left(2 + \frac{l_{rein}}{R_{rein-Cu_6Sn_5}}\right)* f_{rein}^{1.5}, \tag{4.2d}$$

where Λ is the strengthening coefficient, l_{rein} , R_{rein}, and f_{rein} are the length, radius and volume fraction of the micrometer dimension Cu_6Sn_5 IMCs (Table 4-3). Equations 4.1c-e are invariant.

4.2.4. Effect of Sn Dendritic Colonies on Alloy Properties

At the larger length-scale of dendritic colonies (~10 μm), the alloy is treated as a composite consisting of soft pure Sn dendrite inclusions and hard Cu_6Sn_5 IMC inclusions embedded in a dispersion-strengthened Sn-Ag eutectic 'matrix'. The properties of the Sn-Ag eutectic phase are obtained from the formulations in Equations 4.1 and 4.2. The effective properties of this composite are obtained using

self-consistent homogenization schemes (SCM) from micromechanics theories. Homogenization schemes for evaluating the effective elastic, plastic and creep properties are available in the literature. The creep properties of this effective medium approximation (EMA) are defined in terms of viscosity given by Equation 4.3. 'f' refers to the volume fractions and μ refers to the viscosity of the material (τ/γ-rate)

In the current dissertation, the dendrites are assumed to be spherical shaped inclusions (with effective isotropic properties). The effect of the dendrites is accounted only through their volume fractions via the Eshelby's tensor. The creep properties of this effective medium approximation (EMA) are defined in terms of viscosity using a closed form equation derived by Rangarajan et al., [221] for spherical shaped inclusions (Equation 4.3). 'f' refers to the volume fractions and μ refers to the viscosity of the material ($\tau/\dot{\gamma}$). The subscripts 'eff', 'incl' and 'matrix' refer to the SAC composite, Sn-Ag eutectic matrix (reinforced with microscale Cu_6Sn_5 IMCs from Equation 4.2) and Sn dendritic inclusions (Table 4-3). The volume fractions of the Sn-Ag eutectic region and Sn dendrites equal unity.

$$\mu_{eff} = \frac{1/5}{\{\frac{f_{incl}}{3\mu_{eff} + 2\mu_{incl}}\} + \{\frac{f_{matrix}}{3\mu_{eff} + 2\mu_{matrix}}\}} \tag{4.3}$$

$A_L(s^{-1})$ [216]	n_L [216]	Q_L (kJ-mol-K)[216]	τ_{knee} (MPa) [222]	n_H [222]	Q_H (kJ-mol-K)[222]
2.3E25	3.4	39	10	11	69

Table 4-1: Two-term power-law secondary creep constants for Sn (shear components), $G_{Sn}(T) = E(T)/2/(1+\nu)$; $\nu = 0.35$, $E(T) = (8046 - (8.66* T))$MPa, [216, 223], $A_H = A_L(\tau_{knee})^{nL-nH}\exp((-Q_L+Q_H)/R/T)$

D_{0L} (m^2/s)[216]	Q_L (kJ-mol-K)[216]	D_{0H} (m^2/s)[216]	Q_H (kJ-mol-K)[222]
1E-4	31	1E-4	69

Table 4-2: Diffusion constants of Sn in the reference strain rate in Equation 4.1d (shear components)

ρ (m^{-2})	b (nm)	c	G_{det}(GPa), Sn	r (nm)	l_{rein}(μm), R_{rein}(μm)	f_{Ag3Sn}, f_{Cu6Sn5}	$f_{dendrite}$
1E21	0.32	0.84	26.5-(12.6*T/505.1)	25	20, 4.5	5%, 3%	55.6%
Appendix 4.3 [39, 224]		[179]	[217]	Current study, [84]	[220], current study	current study	Current study

Table 4-3: : Mechanistic model constants. f_{Ag3Sn} refers to the volume fraction of nano-scale Ag_3Sn IMCs in the eutectic Sn-Ag region of TMM SAC305 specimens as used in the detachment model (Equation 4.1 e). f_{Cu6Sn5} refers to the volume fraction of micrometer scale Cu_6Sn_5 IMC reinforcements in SAC305 solder apart from the volume fractions of eutectic Sn-Ag region and Sn dendrites (see Equation 4.2 d)

4.2.5. Approach for Calibrating Model Constants

The secondary creep modeling approach described above is based on several simplifying assumptions which are summarized here:

- An attractive interaction between the dislocation and the nano-scale IMC is assumed in SAC solders at the departing stage of the dislocation climb mechanism. TEM studies on SAC solders such as those provided by Schroder et al, and Arzt et al, on Cu and Al alloys [210-211] are required to validate this assumption.

- Sn is modeled using polycrystalline and isotropic properties, thereby rendering insensitivity to the grain configuration.
- Dislocation climb of a single dislocation is modeled. The model does not account for interaction effects of the dislocation with the forward and rear dislocation fronts. These dislocations are assumed to be far enough to avoid back stress or cooperative effects on the dislocation. Hence this corresponds to a dilute solution. This assumption also justifies the approach of extending the calibrated material constants of the detachment model from SAC305 to other microstructural configurations with non-interacting dislocations and intermetallics, resulting from changes in composition, aging and fabrication protocols.
- The nanoscale IMCS are assumed to be distributed uniformly as spherical dispersoids and are sufficiently far away to avoid non-local interaction effects.
- Sn dendrites are modeled as spherical inclusions in the eutectic regions. Hence this microstructural feature is accounted only through the volume fractions and geometric dimensions are not included. The spherical shape also does not contribute towards possible anisotropic behavior introduced by the orientation of ellipsoidal inclusions.
- Self consistent method (SCM) homogenization which is utilized here is acceptable up to moderate volume fraction of dendrites as modeled here. As these volume fractions increases, the SCM approach loses accuracy and alternate schemes are needed.

Calibration results: The relaxation parameter and other model constants need to be calibrated, to accurately capture the secondary creep behavior of the SAC alloys. The

data required for this calibration include measured creep properties of pure Sn and Sn-Ag eutectic phase, as well as the morphological details of the IMCs, eutectic colonies and dendritic colonies. The creep properties of the Sn-Ag eutectic regions are required to calibrate the constants of the dislocation climb detachment model discussed in Equation 4.2 of Sections 4.2.1.1 and 4.2.3. The resulting calibrated dislocation detachment model (Sn-Ag eutectic region) is then invoked in conjunction with the homogenization scheme (Sn dendritic region in Section 4.2.4), to yield the properties of the SAC solder. At this stage, the constants from the homogenization are calibrated in the combined model, to obtain the measured creep properties of SAC.

The creep properties of the Sn-Ag eutectic regions have been measured by Pei using nanoindentation of their test samples [20]. However, owing to the sensitivity of the size and distributions of the IMCs in the eutectic regions with fabrication method and test protocols, these results cannot be utilized to represent the eutectic regions response in the SAC305 specimens fabricated in this study. Hence the modeling approach is demonstrated below, using typical sample results from creep measurements, for illustrative purposes.

Typical test measurements from this study show that the relaxation parameter ‘k’ is a function of stress and temperature in order to capture the stress-strain rate curvature of the measured creep properties of SAC solders. Furthermore, k decreases with increasing stress levels and temperature and can be described with a polynomial fit (Figure 4-4). The k values show saturation at low stress levels and have been truncated to describe the stress dependence with a polynomial fit (see Appendix 4.4 for the untruncated k curves). The corresponding polynomial fit constants are listed in

Table 4-4. The values of k are typically between 0.7 and 1 for typical material systems [179, 182]. k equals one when the matrix and inclusion material are the same and k equals zero for a void.

The plot in Figure 4-4 shows the calibrated k values as a function of stress and temperature for the measured creep behavior. The performance of the calibrated mechanistic microscale model relative to the test measurements is plotted in Figure 4-5. Figure 4-5 clearly shows that the reinforcements serve to offset the matrix properties only and do not alter the stress exponent. The load-sharing by the dendrite inclusions appears to have a much weaker effect on the creep properties of the alloy, compared to the effect of the dispersion strengthening in the eutectic phase. This observation is expected in view of the high creep resistance offered by the eutectic region and is in agreement with the results of Pei [20].

Temp. (°C)	C_1	C_2	C_3	C_4	τ (MPa)
25	-1.5E-23	-2.2E-16	-1.0E-08	0.96	19
75	-1.8E-23	-2.7E-16	-1.1E-08	0.95	17
125	-2.3E-23	-3.2E-16	-1.3E-08	0.94	15

Table 4-4: Polynomial coefficients (3rd order) of the calibrated relaxation parameter, k, as a function of shear stress and temperature (Figure 4-4). $k = \Sigma C_i(\tau)^{4-i}$, i= 1 to 4, units of C_i $(MPa)^{i-4}$

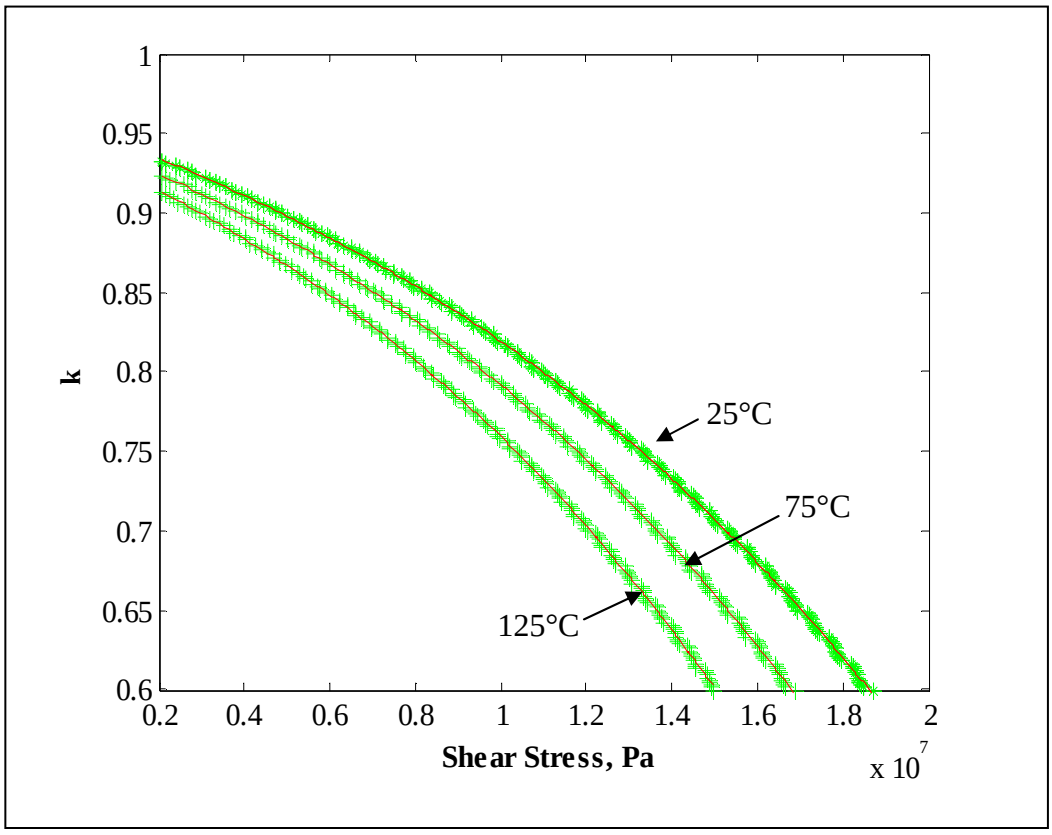

Figure 4-4: Dependence of the 'k' on stress as a function of temperature, showing the calibrated values (green) and the polynomial fit (red, see Table 4-4).

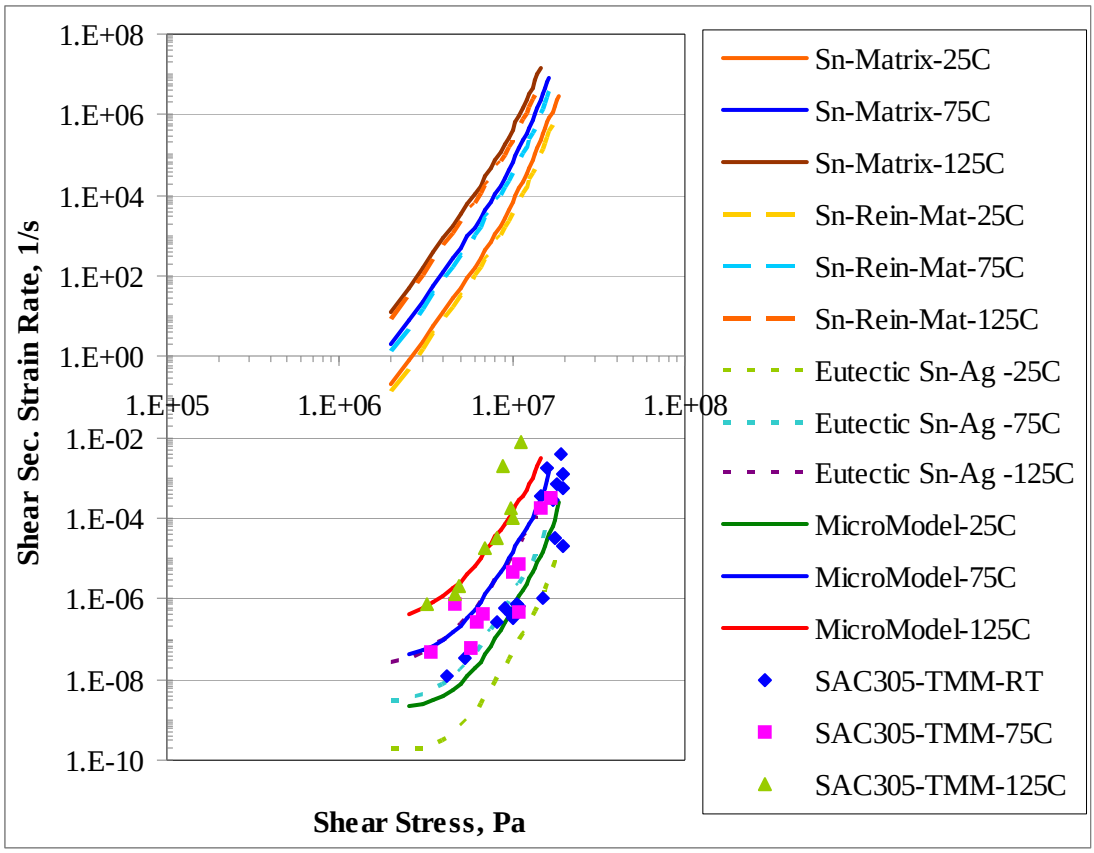

Figure 4-5: **Calibrated microscale model relative to test measurements for SAC305**

The effective creep properties obtained from homogenization of the eutectic Sn-Ag region and Sn dendrites yields the creep behavior of the SAC solder. All parameters of the mechanistic framework can be empirically determined except for the relaxation factor. The relaxation factor (ratio of line tension of particle and matrix) is used to calibrate the model with test measurements. This parameter is chosen for calibration since it is the least understood of all the parameters used in the formulation to obtain from experimental testing.

In the work of Sharma [183], the reference strain rate, $d\gamma_0/dt$ is chosen to calibrate the model. However, the reference strain rate in reality is derived from nucleation

theories and is based on measurable quantities such as diffusivity, burger's vector and dislocation densities in Sn. Since the resulting framework does not yield a closed form analytical solution, an iterative scheme is employed to obtain the relaxation parameter that minimizes the error between the modeling prediction and the test measurements.

Once the mechanistic model is calibrated with the SAC305 test measurements, the effect of Ag% in SAC and manufacturing procedures, and aging is obtained by utilizing the calibrated k values from SAC305 data, and varying the geometric parameters and volume fractions of the Sn dendrites and IMCs in accordance to the specific fabrication, load or microstructural condition. It should be noted that the use of a constant 'k' for different microstructural morphologies resulting from consistent manufacturing protocols is justified based on the primary assumption that interaction effects between adjacent IMCs and dislocations are negligible and do not affect the line tensions of the dislocation at the IMC particle or in the Sn matrix (see the assumptions stated at the beginning of this section).

In order to estimate if the qualitative trends provided by the current model are accurate, test measurements are conducted on SAC105 and compared with the model predictions. In addition, prior measurements from SAC387 [95, 104] are used for the SAC387 predictions. Secondary creep behavior obtained by interpolating the micromodel with limited test data of SAC105 are then fit to Garofalo creep model that is traditionally used in continuum mechanics based model such as that in finite element analysis (Equation 3.2 or Equation 4.4). Similar model constants are obtained for sample aging conditions represented by the micromodel.

$$\frac{d\gamma}{dt} = A(\sinh(\alpha\tau))^{n} \exp(\frac{-Q}{RT}) \quad \dots\dots\dots\dots\dots\dots\dots\dots\dots\dots\dots\dots\dots\dots\dots \text{(4.4)}$$

where dγ/dt is the shear secondary creep rate, τ is the shear stress, R is the universal gas constant, T is the absolute temperature. Q is the activation energy, n the stress exponent and A, α are the stress coefficients.

4.3. RESULTS

The performance of the proposed framework in predicting the SAC composite properties as a function of % Ag, and aging is presented next. The contributions of each microstructural feature are presented first followed by the predictive capability at other configurations of the microstructural features. The material constants utilized in the parametric study are listed in Table 4-5. All other constants remain the same as those listed in Table 4-3

Model	k	ρ (m^{-2})	b (nm)	G_{det}(GPa), Sn	f_{Ag3Sn}, f_{Cu6Sn5}	$f_{dendrite}$
Case 1	0.7-0.9	1E14 [179]	6.6293e-10 [39]	Tensile Modulus: (76.1-(0.109*T))*1E9 [Rotherham, 1990]	0.1	0.40
Case 2			4.12e-10 [216]			0.50

Table 4-5: Mechanistic model constants used for parametric studies(Case 1 and 2). f_{Ag3Sn} refers to the volume fraction of Ag_3Sn IMCs in the eutectic Sn-Ag region as used in the detachment model (Equation 4.1 e). f_{Cu6Sn5} refers to the volume fraction of Cu_6Sn_5 IMCs in SAC solder apart from the eutectic Sn-Ag region and Sn dendrites (Equation 4.2 d)

4.3.1. Parametric sensitivity Studies

The effect of the geometric parameters of the IMCs and dendrites, Sn matrix properties and the parameters relevant to dislocation climb over the dispersoid are discussed next. These results serve to provide insights into the influence of each of these parameters into the magnitude and curvature of the strain rate versus stress behavior in the secondary creep regime. The results are listed in Table 4.6.

(a): Effect of increasing magnitudes of k, ρ, r			
Parameter	k	ρ	r
Effective creep strain rate	inc	inc	dec
$\tau_{detachment}$	dec	NA	inc
γ_0	NA	inc	inc
E_d	inc	NA	dec
Sensitivity	strong	moderate	strong
Qualitative trends	Effects both magnitude and slope of creep rate vs. stress	Pre-multiplier to creep rate vs. stress	Effects both magnitude and slope of creep rate vs. stress

(b): Effect of increasing magnitudes of b, G, f_{imc}, $f_{dendrite}$				
Parameter	f_{imc}	$f_{dendrite}$	b	G
Effective creep strain rate	dec	inc	dec	dec
$\tau_{detachment}$	inc	NA	inc	inc
γ_0	inc	NA	dec	
E_d	inc	NA	inc	dec
Sensitivity	strong	weak	strong	strong
Qualitative trends	Effects both magnitude and slope of creep	Negligible effect on slope and provides an offset in	Effects both magnitude and slope of creep	Effects both magnitude and slope of creep

	rate vs. stress	magnitudes of curve	rate vs. stress	rate vs. stress

Table 4-6: **Qualitative trends of the parameters in the mechanistic framework**

4.3.2. Model Predictions: Effect of Ag% in SAC

For illustrative purposes, the calibrated model is used to find the creep properties of SAC105 and SAC387 based on the configurations expected from the IMCs and dendrites. In order to estimate if the qualitative trends provided by the current model are accurate, test measurements are conducted on SAC105 and compared with the model predictions. In addition, prior TMM measurements of SAC387 [95, 104] are used for the SAC387 predictions. The measurements are conducted on as-fabricated TMM solders using consistent test methodology and protocols.

Test measurements show that increasing Ag weight fractions in SAC improves the creep resistance (decrease secondary creep strain rate). Increase in Ag % is expected to increase the volume fraction of nano-scale IMCs available for pinning dislocations. Since the fabrication procedure is controlled, namely the cooling and solder reflow time, the sizes of the IMCs are assumed to be invariant (same values as those presented in Table 4-3). The dendrites are expected to decrease in size and volume fraction, though not too significantly. Comparison of the changes expected in the dendritic and Sn-Ag regions microstructural features of the TMM solder specimens with reduced Ag% in SAC are provided in Appendix 4.5. Based on these observations, the volume fractions of the IMCs and dendrites are changed parametrically to assess if qualitative trends towards the creep behavior of SAC105 and SAC387 are obtained.

In the case of SAC105, an extensive test matrix as that of previously reported SAC305 is not explored in this work. Nevertheless, the results show that the model predictions provide the right qualitative trends, and, quantitatively match the test measurements very well for volume fractions of IMCs and dendrites of 4.8% and 57% (Figure 4-6). Similarly SAC387 measurements from prior studies using the TMM setup and consistent test protocols by Zhang and Haswell [95, 104] are predicted with reasonable agreement (Figure 4-7) with the model using volume fractions of IMCs and dendrites of 5.2% and 49%. These values compare with 5% (IMC) and 55.6% (dendrites) respectively in SAC305.

The volume fractions are in the correct qualitative trend with respect to changing Ag% in SAC. However, the sensitivity of the model to the IMC features is very high to the extent that it could be within the measurable error (experiment). Hence the microstructural analysis needs to be conducted with considerably large number of samples to improve the accuracy of the measured configurations of the microstructural features.

The proposed micromodel can be utilized to interpolate the creep response of solder from test measurements. Thus when combined with the microscale model, the extent of experimental testing can be significantly reduced. Continuum mechanics based Garofalo secondary creep constants that are representative of the average behavior of SAC105 solder specimens are obtained based on the micromodel predictions and limited SAC105 secondary creep measurements (Table 4-7).

Solder/Condition	α $(MPa)^{-1}$	n	A	Q(kJ/mol)
SAC105-as-fab	0.21	4.6	173	54
SAC305-aged. Case 1 - $f_{Sn\ Dendrite}$ = 0.6, r_{IMC} = 30 nm	0.15	9.5	492E3	48
SAC305-aged. Case 2 - $f_{Sn\ Dendrite}$ = 0.6, r_{IMC} = 28 nm	0.18	5.9	20E3	48

Table 4-7: Garofalo secondary creep model constants (shear based), aged configurations represented by Case 1 and 2 refer to microstructural aging reported in Figure 4-8 and Figure 4-9 respectively

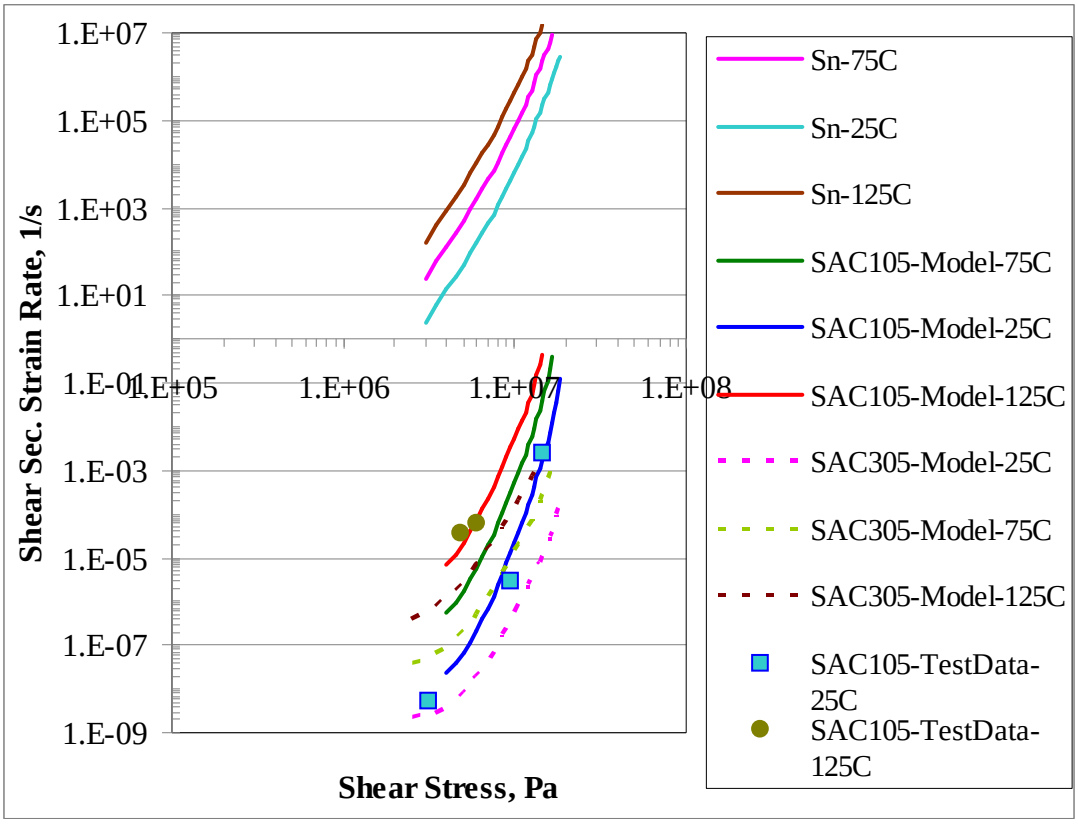

Figure 4-6: SAC105: comparison of prediction from calibrated microscale model relative to TMM test measurements for SAC105

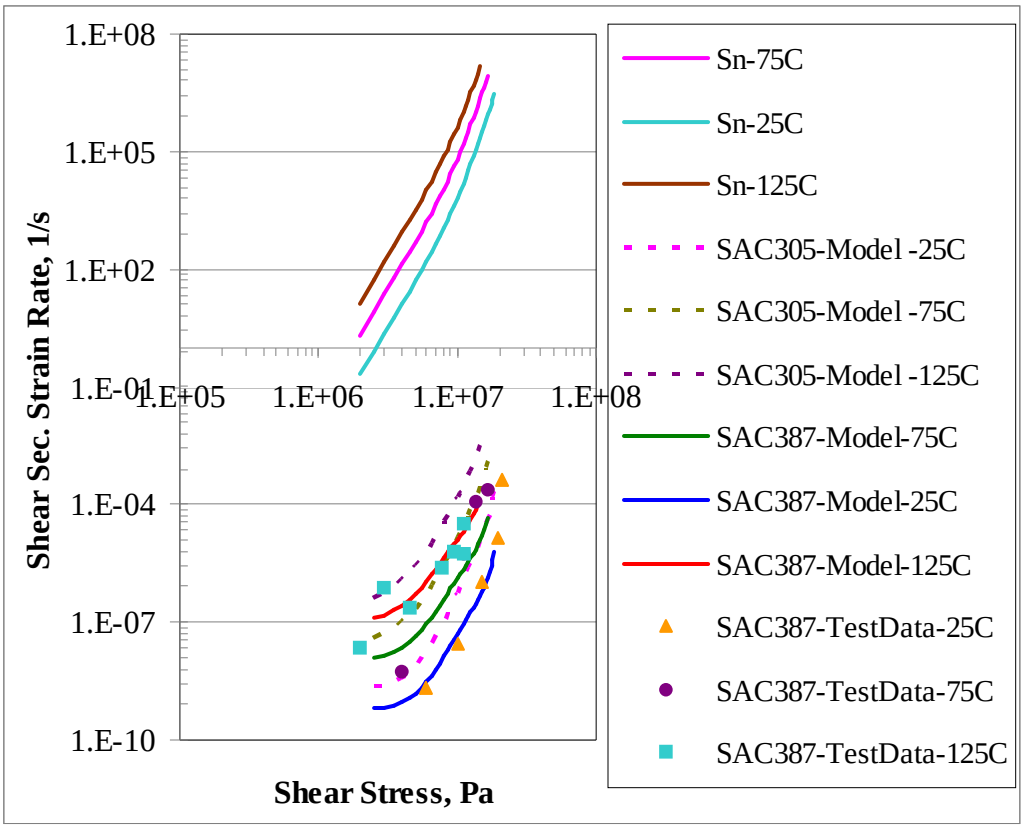

Figure 4-7: SAC387: Comparison of prediction from calibrated microscale model relative to test measurements for SAC387 from [95, 104]

4.3.3. Model Predictions: Effect of aging loads in SAC305

The calibrated model is used to investigate the creep properties of SAC305 as a function of aging. As aging time increases, the size of the Sn dendrites and IMCs (nano and microscale) increases [68, 75, 225]. Images of SAC solder microstructure as a function of aging are provided in Appendix 4.5. This results in an increase in the volume fraction of dendrites per unit volume. In this framework, the change in the volume fraction of microscale Cu_6Sn_5 IMCS is assumed to be negligible with aging. Furthermore, the sum of volume fractions of the dendritic phases, eutectic phase and microscale Cu_6Sn_5 IMCS remains constant (unity). Since the dendrites are modeled as

spherical inclusions, only the changes in their volume fractions can be captured through the proposed framework.

Creep measurements as a function of aging are not available in the current study for comparisons. Furthermore, measurements made on aged samples from literature cannot be used unless as-fabricated solder creep measurements are available from the same study (for model calibration of k using the as-fabricated solder measurements). However, in order to understand the model capability in predicting the right qualitative trends, a parametric study of the microstructure is conducted. For sample results, the dendritic volume fraction ($\nu_{\text{Sn Dendrite}}$) is assumed to increase by 5% (from ~56% in the unaged condition) due to thermal aging. The eutectic phase volume fraction ($\nu_{\text{Eutectic SnAg Phase}}$) is calculated from equation 4.5. The volume fraction of nano-scale Ag_3Sn IMCs ($\nu_{\text{Ag3Sn IMCs in Eutectic SnAg}}$) in the unaged (preconditioned) SAC305 solder is 5% based on the image analysis conducted on the TMM solder specimens.

The volume fraction of Ag in solder ($\nu_{\text{Ag in Solder}}$) is constant for a given solder composition irrespective of aging. Based on Equations 4.5-4.6, the volume fraction of nano-scale Ag_3Sn IMCs in eutectic phase is found in the aged state. Furthermore, the size of the nano-scale Ag_3Sn IMCs in eutectic phase increases with aging. Parametric studies are conducted on the radius of the nano-scale Ag_3Sn IMCs in eutectic phase as shown in Figure 4-8 and Figure 4-9. The results show that the creep resistance significantly decreases (by at least two orders of magnitude for the chosen microstructural configurations) with increasing aging time. These results match the expected behavior qualitatively and future work involving microstructural parameters

and creep behavior of the aged solder are needed to obtain quantitative predictability. Continuum mechanics based Garofalo secondary creep constants based on the micromodel predictions on the effect of aging in SAC305 solder are presented in Table 4-7.

$$\nu_{Sn\ Dendrite} + \nu_{Eutectic\ SnAg\ Phase} + \nu_{microscale\ Cu6Sn5\ IMC} = 1 \quad \ldots\ldots\ldots\ldots\ldots\ldots\ldots\ldots\ldots\ldots \quad (4.5)$$

$$\nu_{Ag\ in\ Solder} = \nu_{eutectic\ SnAg} * \nu_{Ag3Sn\ IMCs\ in\ Eutectic\ SnAg} \quad \ldots\ldots\ldots\ldots\ldots\ldots\ldots\ldots\ldots\ldots\ldots\ldots\ldots \quad (4.6)$$

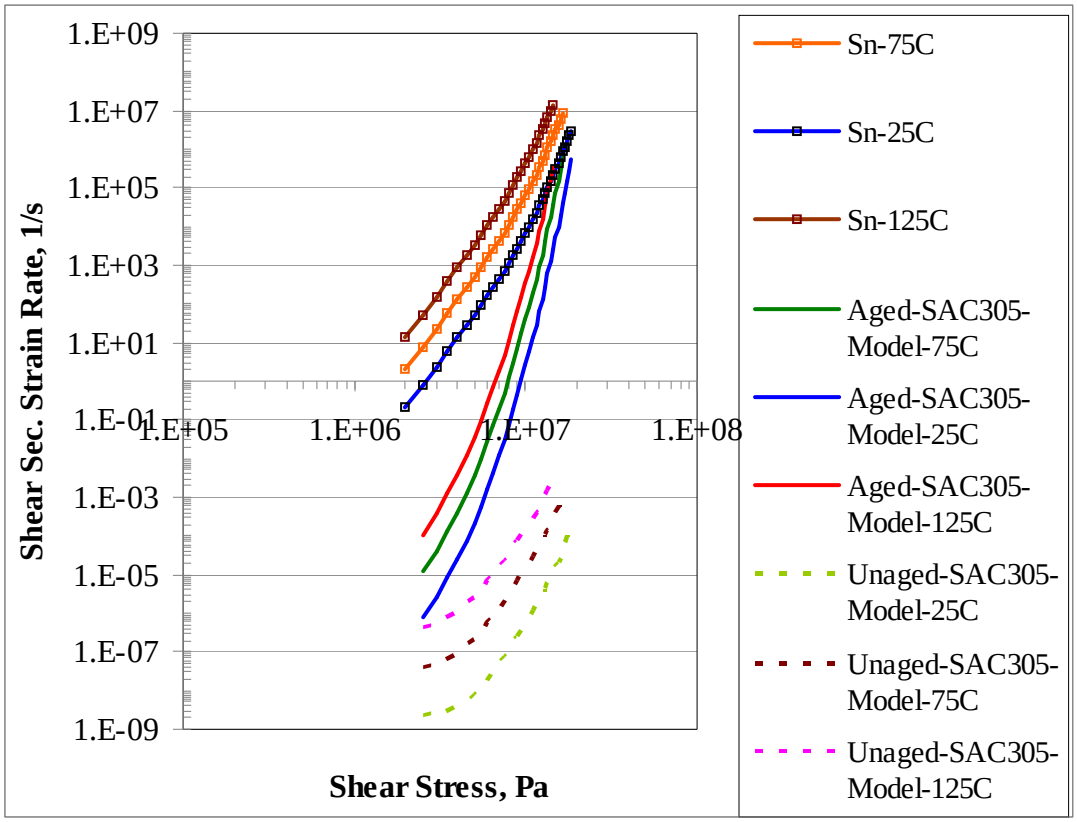

Figure 4-8: Effect of aging on SAC305 - prediction from calibrated microscale model – $f_{Sn\ Dendrite}$ = 0.6, r_{IMC} = 30 nm

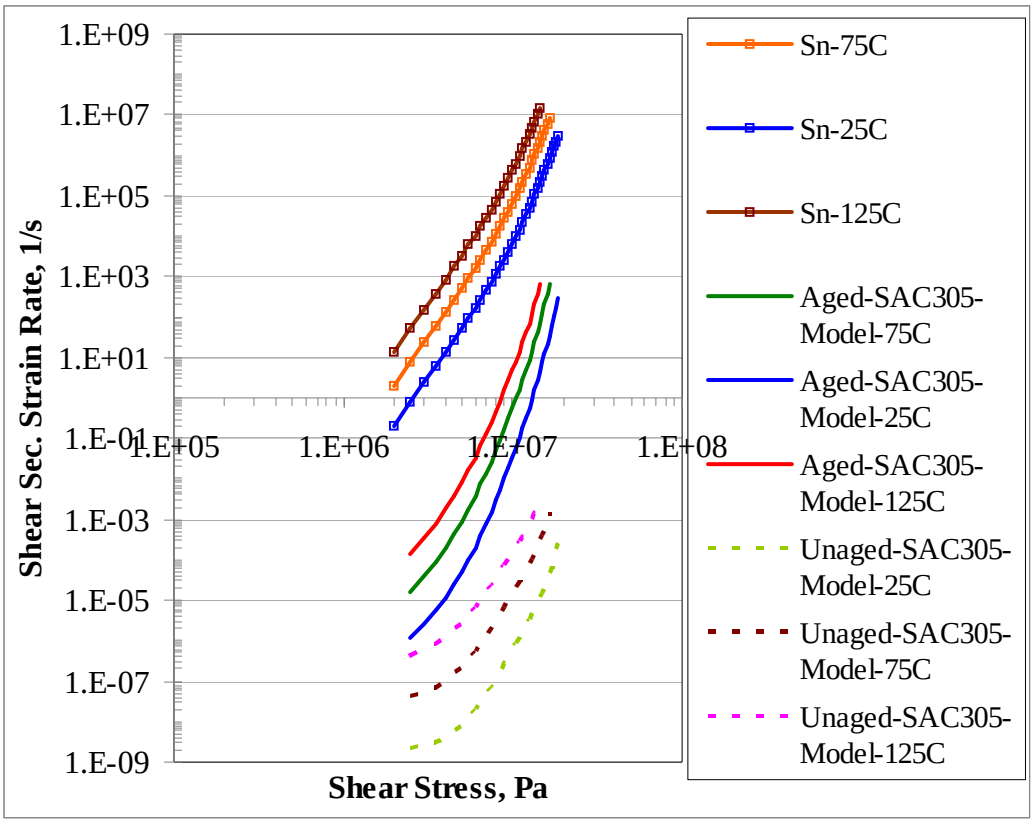

Figure 4-9: Effect of aging on sac305 - prediction from calibrated microscale model - $f_{Sn\ Dendrite} = 0.6$, $r_{IMC} = 28$ nm

4.4. LIMITATIONS AND FUTURE WORK

The proposed mechanistic framework provides theoretical insights into the effect of key microstructural features and detachment creep mechanism on the secondary creep behavior of SAC alloys reasonably well. The model's capability of capturing the effect of varying microstructures resulting from aging, and compositional effects is demonstrated. However, the model is based on certain simplifying assumptions and requires further improvement for extending the accuracy and capability for modeling the total and primary creep regimes as stated below.

- The dendrites are modeled as spherical inclusions. Hence the Eshelby's tensor which represents the geometric parameters of the inclusions is independent of the inclusion dimensions. The effect of dendrites is included only through the volume fraction in the SAC alloy. Future studies should include dendrites as ellipsoidal inclusions and include the effect of randomization of the inclusion orientation relative to the loading.
- The sensitivity of the model to the nano-scale IMCs is extremely high. Thus the changes in the microstructural features for capturing various states relative to those in the calibrated microstructural state could be within the experimental error of measurements. Microstructural analysis is required to experimentally verify the changes in the topological features and volume fractions of the IMCs, dendrites, and eutectic regions.
- The model is also restricted to the secondary creep region and requires to be extended to primary creep. An option for implementing this is by introducing an evolution parameter to the threshold detachment stress and the dislocation density. Furthermore the dislocation density used in the current study is based on a hypothetical assumption that all the slip planes in bct Sn are completely clogged with dislocations. This assumption needs to be reexamined and the range of dislocation densities obtained need to be obtained experimentally in the crept SAC specimens.
- The relevance of the observed stress and temperature dependence of 'k' needs to be understood and these results need to be verified through molecular dynamics simulations.

- The current model is based on the climb of a single dislocation over a particle. In reality, piled up dislocations and grain boundaries also could act as obstacles. The current model uses a dilute approximation and assumes that the interaction affects of other dislocation fronts and obstacles are negligible. The mechanics of climb of several dislocations (as opposed to a single dislocation) over particles with the associated interaction effects expected in SAC materials needs to be investigated.
- The current framework is applicable to the as-fabricated stage of microscale SAC solders with large Sn grains, where dislocation climb is expected to dominate over GBS [11]. However, GBS may progressively increase as the large Sn grains (in microscale joints) recrystallize into a finer polycrystalline state due to cyclic loading [61, 195]. In such a case, creep deformation due to GBS needs to be included in conjunction with dislocation climb and detachment models described here.
- Furthermore, the proposed creep model can be coupled in future with grain boundary sliding models for predicting the secondary creep behavior of fine grained homogeneous microstructure solders with dispersion strengthening such as that seen in Lanthanum doped Sn-Ag solder. (La doped Pb-free solders are also expected to deform by dislocation climb and exhibit a homogenous Sn grain microstructure and are probably a better option than SAC for creep dominated loads).

4.5. SUMMARY AND CONCLUSIONS

A mechanistic multiscale framework is proposed, to capture the dominant creep deformation mechanisms and the influence of key microstructural features on the

measured secondary creep response of microscale as-fabricated SAC305 solder specimens. Mechanistic models of dislocation climb and detachment are used to capture the dominant creep deformation and dispersion strengthening mechanisms in the eutectic phase of SAC solders. These microscale models are then combined at the next larger length scale (that of dendritic and eutectic colonies), with traditional micromechanics based homogenization schemes, to capture the load-sharing between eutectic phases, dendritic phases, and Cu_6Sn_5 intermetallic reinforcement particles. Starting with the behavior of pure Sn properties and by conducting a parametric variation of microstructural morphology of the SAC305 alloy, this modeling approach is used to provide theoretical insights into the influence of key microstructural features on the viscoplastic deformation behavior of microscale SAC305 specimens.

The contributions of the soft Sn dendrites and microscale Cu_6Sn_5 IMC reinforcements to the overall secondary creep resistance of SAC solders is less significant compared to that of the eutectic Sn-Ag regions with the nanoscale Ag_3Sn dispersions. Higher volume fractions and smaller sizes of nanoscale Ag_3Sn are seen to be beneficial to the creep strength of SAC. The model effectively captures the effect of alloy composition and aging loads on SAC solders on the secondary creep behavior, thereby aiding in the effective design and optimization of the viscoplastic behavior of SAC alloys. Garofalo secondary creep model constants are provided based on the micromodel predictions as a function of % Ag in SAC and aging. Limitations and suggestions for improving the modeling accuracy and applicability are included.

Chapter 5: Macroscale Modeling of the Viscoplastic Response of As-fabricated Microscale Sn3.0Ag0.5Cu Solder Interconnects: Stress relaxation and Creep

ABSTRACT

Viscoplastic creep measurements conducted on microscale SAC305 TMM specimens exhibit significant piece-to-piece variability. Microstructural investigations reveal that SAC305 solder comprises of very few anisotropic grains of Sn at microscale dimensions, which cause the mechanical response to be heavily joint dependent. Thus microscale SAC305 joints lack statistical homogeneity and isotropy and the constitutive material models are required to incorporate key microstructural features to capture individual joint behavior. Macroscale phenomenological models which are length scale independent hence capture the non-homogenous creep behavior only in an average sense.

The current study investigates the predictive capability of the macroscale creep constitutive model constants measured from microscale non-homogenous SAC305 joints. In particular, the study aims at understanding the level of accuracy with which the creep constants measured from constant force loads predict the viscoplastic stress relaxation response measured from constant displacement loads on microscale TMM SAC305 joints. Since the viability of using SAC305 as a substitute for Sn37Pb is to be assessed, viscoplastic stress relaxation behavior of Sn37Pb is characterized and compared with that SAC305.

Test measurements show that SAC305 relaxes at a much slower rate than Sn37Pb, owing to its superior creep resistance. Finite element results show that the range of scatter measured from macroscale creep model constants is within the range of scatter obtained from the stress relaxation predictions. The stress relaxation predictions are strongly sensitive to the inclusion or exclusion of primary creep models. Furthermore, the stress relaxation behavior is captured reasonably well without the inclusion of primary creep to the secondary creep material model.

5.1 INTRODUCTION

The viscoplastic creep measurements conducted on microscale SAC305 TMM specimens in Chapter 3, reveal that significant piece-to-piece variability exists. The OIM studies clearly show that the microscale TMM joints mimic the non-repeatable, coarse-grained microstructure of anisotropic Sn grains seen in functional microscale interconnects. Macroscale continuum mechanics based phenomenological model constants are hence seen to capture the measured creep behavior of these non-homogeneous joints only in an average sense (Chapter 3, Section 3.3.7). Owing to the lack of statistical homogeneity and anisotropy exhibited by the microscale SAC305 interconnects, it is pertinent that material models incorporate an inherent length scale representative of the dominant microstructural features and corresponding deformation mechanisms.

However the formulation of such a mechanistic framework is a non-trivial exercise and has been explored in Chapter 4. As an initial approximation, macroscale continuum mechanics based models can be used to obtain the average behavior of these non-homogenous joints with the corresponding range of scatter that could be

expected from these material model predictions. Furthermore from an application standpoint, the predictive capability of these macroscale constants needs to be assessed under loads applicable to the solder interconnects under service life.

5.1.1. Background and Motivation

The constitutive viscoplastic creep properties of solder are typically used in modeling efforts to assess the fatigue damage induced in solder joints under cyclic loads. The viscoplastic behavior of solders manifests itself as creep and stress relaxation behavior. Creep is the deformation induced under constant stress conditions and stress relaxation is the drop in stresses due to viscoplastic damage under constant displacement conditions. Stress relaxation in particular is of extreme importance under cyclic creep fatigue loads such as thermal cycling, power cycling and high temperature isothermal mechanical cycling loads [129, 135, 226].

Stress relaxation is particularly dominant during the dwell portions of the thermal or mechanical cycling loads. Stress relaxation of the solder serves to reduce the peak stresses attained by the materials adjacent to the solder. In particular, this is beneficial to brittle materials such as the silicon chip which undergoes catastrophic cracking under high stresses. However the reduction of peak stresses occurs at the cost of creep damage in the solder. Hence a tradeoff exists on the beneficial effects of stress relaxation versus the creep material damage induced in solder.

Stress relaxation occurring in solder under fatigue loads is generally studied utilizing numerical modeling studies by modeling the material behavior of solder using measured viscoplastic creep constitutive properties [95, 128, 190]. Thus the predictive capability of the creep model constants from the non-homogenous

microscale SAC305 joints can be best assessed by comparing the modeling predictions with stress relaxation measurements from similar joints tested and fabricated using consistent test methodologies.

Stress relaxation studies on Pb-free solder are limited in literature and cannot be adopted for the current purpose owing to differences in test protocols, microstructure, length scales and solder composition to name a few [136-137, 139-141, 227-228]. In order to accurately validate the predictive capability of the creep macroscale model constants of SAC305 measured from the current dissertation, stress relaxation measurements using consistent test methodologies and protocols are crucial.

Such an objective is interesting since it reveals the applicability of using viscoplastic constants measured under constant stress conditions for predicting the viscoplastic behavior under constant displacement. This objective was undertaken by Bang et al., for Sn37Pb [136, 227]. Their study concluded that the stress relaxation measurements can be utilized to derive the creep model constants. Studies exist that independently explore stress relaxation [129, 132-134, 137, 229] and creep behavior [11, 76, 111, 116] (see Section 1.1.3.3 in Chapter 1 and Chapter 3 for a detailed literature review) of Pb-free solders. However a unified study to correlate the two viscoplastic responses is lacking in literature.

Furthermore, the eventual goal of Pb-free solder studies is to assess the viability of using SAC305 as a Pb-free substitute for Sn37Pb solder. Hence the stress relaxation behavior of Sn37Pb measured from similar test protocols and specimens is necessary for comparing the behavior of Pb-free solders. Once the accuracy of the measured creep constitutive model constants is assessed using material level tests,

these constants can be applied to understand the behavior of solder in functional assembly level interconnects under typical fatigue loads encountered during the life cycle.

5.1.2. Problem Statement and Objectives

Based on the background provided and the non-homogenous viscoplastic creep behavior exhibited by microscale SAC305 TMM specimens, this chapter aims to validate the macroscale modeling efforts for modeling the average viscoplastic behavior of microscale SAC305. The previous chapter investigates microscale mechanistic models that can capture the influence of lower microstructural length scales on the behavior of SAC305 interconnects at microscale dimensions. The objectives of this study are hence as follows:

- Asses the stress relaxation predictive capability of macroscale continuum mechanics based phenomenological constants used to represent the viscoplastic behavior of non-homogenous microscale SAC305 joints.
- Characterize and compare the stress relaxation behavior of microscale as-fabricated SAC305 and Sn37Pb solder specimens using TMM test methodology.

5.2. APPROACH

The consequence of utilizing the averaged creep model constants derived from the mechanically non-homogenous joints, to predict the measured stress relaxation in similar non-homogenous TMM specimens is investigated. In particular, the study verifies the level of accuracy with which the averaged viscoplastic constants derived from constant force creep tests predict the stress relaxation behavior under constant

displacement loading, using finite element analysis (FEA) and material level characterization. The experimental testing approach for characterizing the stress relaxation behavior of eutectic Sn37Pb and hypoeutectic SAC305 solders is described first followed by the modeling strategy used.

5.2.1. TMM Testing: Stress Relaxation

The creep measurements conducted on microscale SAC305 solder TMM specimens have been previously reported in Sections 3.3.1 and 3.3.7 in Chapter 3. The creep model constants presented in Table 3-2, Table 3-3 and Table 3-4 represent the average behavior of SAC solder. In this study, the upper and lower bounds of the creep model constants are obtained based on the outliers of the variability exhibited by the test specimens across the entire test data reported earlier in Section 3.3.1 in Chapter 3 .

The test apparatus used in this work is the TMM setup that has been described previously in Chapter 2 and in Section 3.2 of Chapter 3. A brief description of the test system is provided here for continuity and comprehensive details are available elsewhere [95, 104]. The setup is a custom-built mechanical testing system[104] (Figure 5-1a), for conducting isothermal monotonic constitutive tests as well as cyclic mechanical fatigue tests. The displacements are produced by a piezoelectric stack actuator in closed-loop displacement control. Displacements in the solder are obtained by adjusting for load train stiffness [104]. A hot-air, closed-loop temperature module provides the ability to conduct isothermal mechanical tests at elevated temperatures within +/- 1.5°C.

The modified Iosipescu shear specimen used here ((Figure 5-1 b) provides a reasonably uniform stress distribution in the solder due to the 90° notch angles [85-86]. The stress distribution expected in the solder region of the Iosipescu specimen is provided in Figure 5-10, Figure 5-11 and Figure 5-12. The copper platens do not have any metallization layers and the solder behavior corresponds to those on printed wiring boards with Organic Solder Preservative (OSP) and immersion Sn pad finish. The solder joint is 180 μm wide, 1 mm thick, 3mm long and is nominally deformed in shear.

The objective of the current study is to examine the behavior of solder joints using shear specimens that capture the coarse-grained Sn microstructure and behavior seen in micrometer dimension functional solder interconnects. The current shear specimen configuration captures the critical length scale (shear loading across the 180 μm width) seen in functional microscale solder interconnects (~100 - 1000 μm), and replicates the associated coarse-grained Sn microstructure and non-homogenous behavior.

The solder specimen is fabricated by manual soldering at a reflow temperature of 248°C and 210°C for SAC305 and Sn37Pb solders respectively. The pre-heat time is 45s and the reflow time from the deposition of solder to stationary heating time is 60s. The specimen is then air-cooled at ~ 2°C/s. The pre-heat and the reflow profile are strictly monitored to be consistent across all specimens.

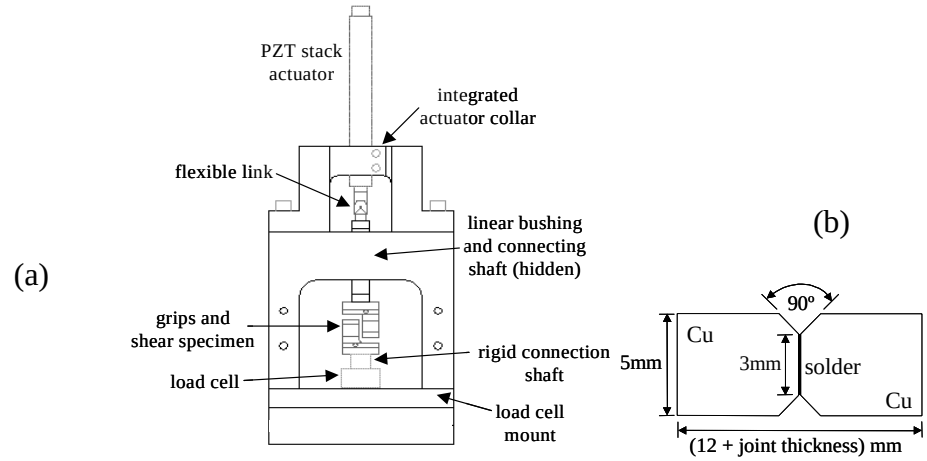

Figure 5-1: (a) TMM test frame (b) TMM specimen schematic (joint thickness ~0.18 mm)

All specimens are further aged for 100 hours at 0.8 T_{melt} (~132°C and 100°C for SAC305 and eutectic Sn37Pb solder) prior to testing, to obtain a stable microstructure and also to relax residual fabrication stresses. Sn37Pb is traditionally aged at 100°C, which corresponds to a homologous temperature of 0.82. Since solders exhibit viscoplasticity, the same homologous temperature is chosen for SAC solders (~132°C) to maintain consistency. In the current study, these thermally pre-conditioned joints are termed 'as-fabricated' joints.

All the specimens are screened prior to testing using microstructural imaging to eliminate defective specimens due to manufacturing voids, poor wetting, weak intermetallic interface (insufficient thickness) and other anomalies. The pre-test SAC305 microstructure shows a healthy planar interface IMC layer (Cu_3Sn and Cu_6Sn_5) of around 4 µm thickness for SAC305 solder. The test matrix for the stress relaxation test is listed in Table 5-1. The ramp rate to achieve the required starting stress (τ_o) is relatively high (10 µm/s) to reduce the effect of creep damage during the loading stage. The stress history measurements are described using exponential decay

power law fits as a function of initial stress (Equation 5.1). Power law fits were examined and were found to produce non-physical (compressive) behavior at infinite time as opposed to relaxing to zero value of stress.

Temp(°C)	25	75
Stress (MPa)	8 - 25	4 - 9

Table 5-1: Test matrix for stress relaxation

$$\tau = \tau_o e^{-at^b}$$ Exponential Power Law Stress History (5.1)

5.2.2. Macroscale Modeling: Limit Analysis

The aim of the study is to determine if the accuracy of the stress relaxation predictions based on the macroscale creep models are within the range of scatter evident in the creep measurements. In order to assess the range of scatter in the stress relaxation predictions, the creep constants are evaluated at the upper and lower ranges of scatter in addition to the average behavior. The details of the material model constants and the finite element modeling are described next.

5.2.2.1. Creep Model Constants: Upper Bounds, Lower Bounds, and Average Fits

The viscoplastic behavior of the solder is modeled using partitioned, temperature-dependent elastic, plastic, and creep properties. For comparison purposes, solder creep is modeled using only secondary creep behavior, as well as with combined primary and secondary creep behavior. In the current study, primary creep deformation is modeled using a generalized exponential model (Equation 5.2) and secondary creep deformation is modeled using the Garofalo creep model (Equation 5.3). The Garofalo secondary creep model used to represent the solder behavior in the

finite element analyses is available as an in-built option in ANSYS. The primary creep model is not available as an in-built option and is implemented using a user written subroutine in ANSYS.

$$\varepsilon_{Sat} = C_1 \sigma^{C_2}; d = C_3 \sigma^{C4} e^{-\frac{Q_1}{RT}}$$ Generalized Exponential Primary Creep Model (5.2 a)

$$\frac{(\varepsilon_{Sat} - \varepsilon_P)}{\varepsilon_{Sat}} = \exp(-dt)$$ Decay and Saturated Primary Creep (5.2 b)

$$(\frac{d\varepsilon}{dt})_{\sec} = A_G (Sinh(\alpha\sigma))^{n_G} \exp(-\frac{Q_2}{RT})$$ Garofalo Secondary Creep Model (5.3)

where ε_p= equivalent primary creep strain, ε_{sat} = equivalent primary saturated creep strain, d=decay, σ = equivalent stress, Q = activation energy, R = universal gas constant, T = Temperature in K, t = time in s, τ_o = initial shear stress at time zero, , and C_i (i=1:4), A_i, α , n_i, a and b are model constants.

The model fits to measurements are obtained by following the procedures described in Appendix 3.1. The upper and lower bounds of the model fit to the creep measurements are obtained at each temperature by force fitting parallel curves to the average curves through the outlier creep measurements at each temperature. The coefficient and exponent of the stress contributions and the activation energy are hence invariant resulting only in a change in the normalization constant (A_G for the secondary creep model and C_1 and C_3 for the primary creep model). The corresponding creep model constants for the average behavior, and the upper and lower bounds are presented in Table 5-2 and Table 5-3. The corresponding model fits to the creep data are presented in Figure 5-2, Figure 5-3 and Figure 5-4.

Behavior	$\alpha(MPa)^{-1}$	n_G	A_G	Q_2 (J-mol-K)
Average	0.18	2.3	6.07	55793
RT-Lower	0.18	2.3	0.22	55793
RT-Upper	0.18	2.3	361.8	55793
75°C-Lower	0.18	2.3	0.138	55793
75°C-Upper	0.18	2.3	20.13	55793
125°C-Lower	0.18	2.3	3.43	55793
125°C-Upper	0.18	2.3	144.1	55793

Table 5-2: Garofalo equivalent secondary creep constants

Behavior	$C_1(Pa^{-C_2})$	C_2	$C_3(Pa^{-C_4})$	C_4	Q_1 (kJ-mol-K)
Average	2.1E-13	1.49	2.7E-25	3.9	39526
RT-Lower	1.4E-14	1.49	2.0E-26	3.9	39526
RT-Upper	8.1E-13	1.49	1.3E-23	3.9	39526
75°C-Lower	2.9E-14	1.49	4.9E-26	3.9	39526
75°C-Upper	3.7E-13	1.49	1.3E-24	3.9	39526
125°C-Lower	3.6E-14	1.49	8.1E-26	3.9	39526
125°C-Upper	1.1E-12	1.49	4.2E-24	3.9	39526

Table 5-3: Generalized exponential (equivalent) primary creep constants

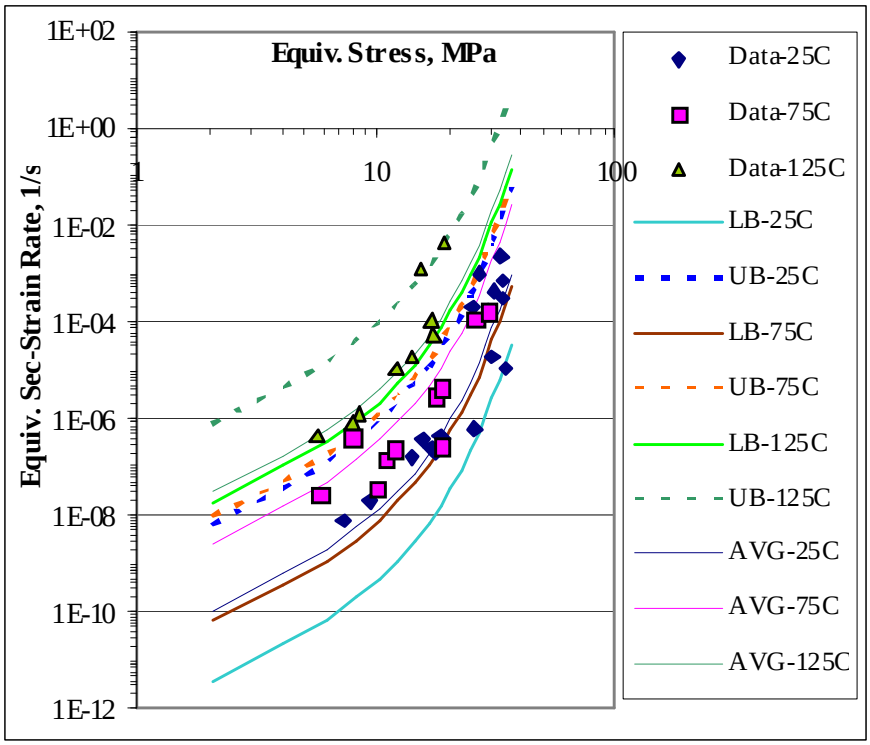

Figure 5-2: Garofalo secondary model fits to TMM creep measurements (Equation 5.3). LB, UB and AVG represent the model fits to the lower bound, upper bound and average behavior of the equivalent creep measurements.

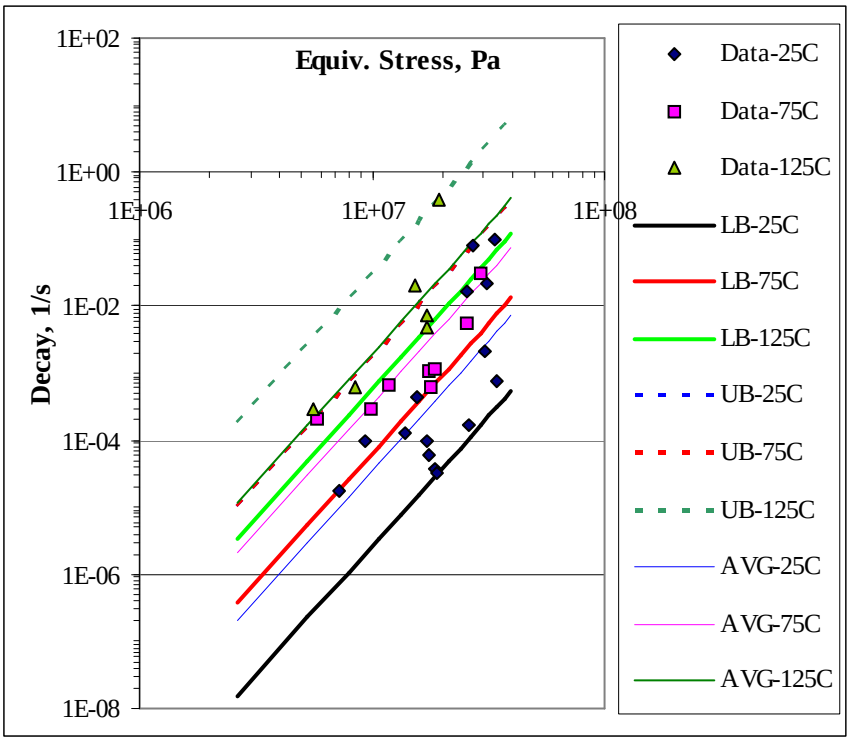

Figure 5-3: Primary creep decay model fits to TMM creep measurements (Equation 5.2a-b). LB, UB and AVG represent the model fits to the lower bound, upper bound and average behavior of the equivalent creep measurements.

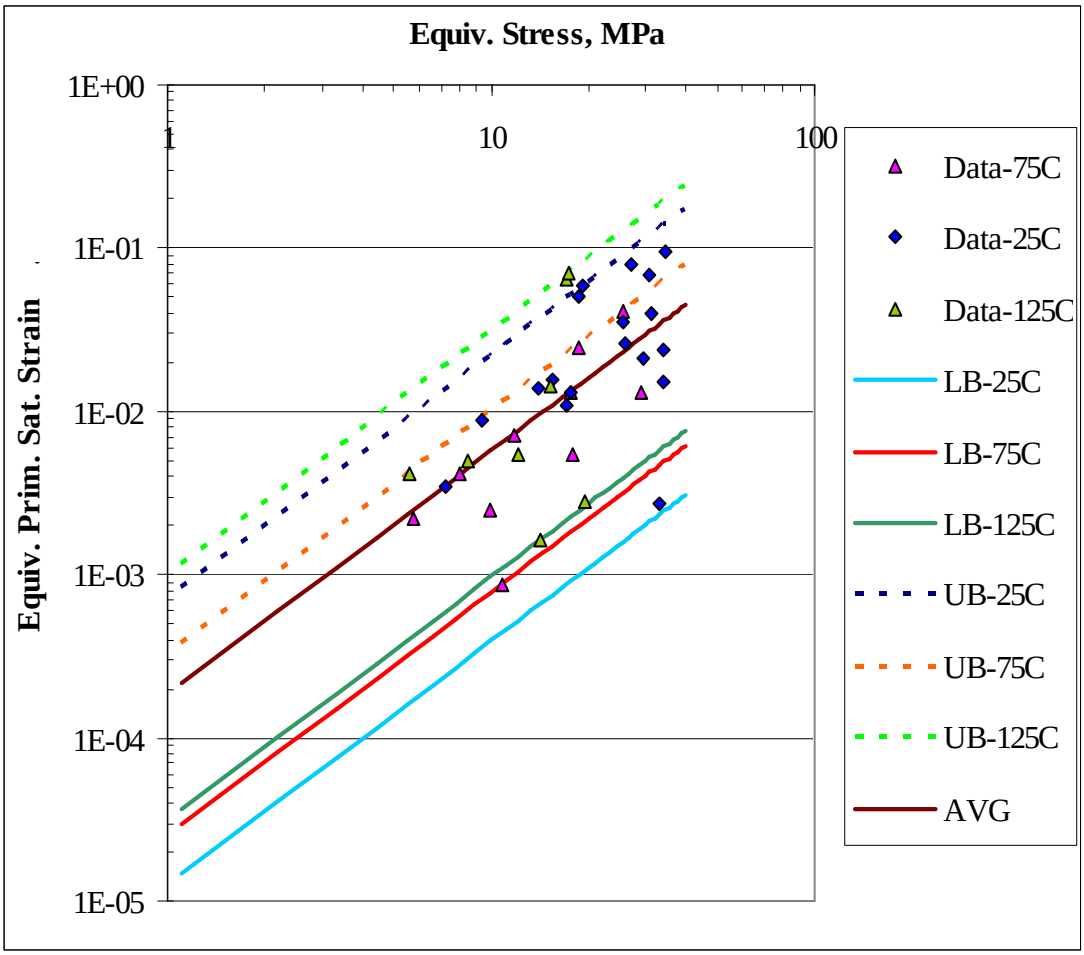

Figure 5-4: Primary saturated creep strain model fits to TMM measurements (Equation 5.2a-b). LB, UB and AVG represent the model fits to the lower bound, upper bound and average behavior of the equivalent creep measurements.

5.2.2.2. Finite Element Model

In order to simulate the stress relaxation tests, a simple 2-D finite element model of the TMM test specimen between the two grips is used. The model therefore includes the solder layer and the tapered portion of the copper platens, as shown in

Figure 5-5. The model uses eight-noded, quadratic, plane stress elements with finite thickness. Solder is modeled using partitioned elastic, plastic and creep behavior. The viscoplastic behavior of solder is modeled using the creep properties described in Section 5.2.2.1. The elastic and plastic properties of SAC305 solder were not measured at this point of the study. Hence as an initial approximation, TMM measurements of near-eutectic SAC387 solder from Zhang's study are used to model SAC305 solder [95]. Copper is modeled as an elastic material. The material constants used to describe the elastic and plastic deformation of both materials is listed in Appendix 5.1.

Prior to addressing the accuracy of the creep constants measured from microscale non-homogeneous SAC joints in predicting the measured stress relaxation response of similar joints, the accuracy of the chosen modeling strategy is validated. In particular, the accuracy of the user programmed subroutine needs to be validated using a constant force creep simulation to predict the measured creep response of the TMM specimen across various temperature and stress ranges.

The loading comprises of a constant shear loading in X-direction on the free edge corresponding that in the TMM tests for the given stress and temperature conditions. The nodes on the fixed edge are constrained in all directions while the nodes on the free edge are constrained only in the Y- direction. The constant load comprises of a constant force load in the creep study and a constant displacement load in stress relaxation study.

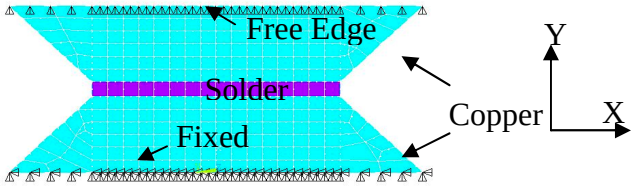

Figure 5-5: 2-D FE model of test specimen for stress relaxation

5.2.2.3. Matrix of Modeling Runs

The matrix of modeling runs is detailed here. As described earlier, these runs should include sanity checks for validating the adopted modeling approach prior to obtaining results on the stress relaxation. This step is crucial since the primary creep is implemented using a user written subroutine. This exercise also verifies that the modeling methodology and measured creep constants are capable of replicating the measured creep response with reasonable accuracy. Hence FE runs are conducted under constant stress loads and compared with the measured creep strain histories.

Furthermore the creep strain predictions for the upper and lower bounds of creep constants can be verified to bound the measured scatter in the creep tests. Once the creep constants are verified to generate physically relevant results, the performance of these constants in predicting the stress relaxation measurements of the non-homogenous SAC305 solder is investigated. In particular, the runs are conducted using creep constants representative of the upper and lower bounds and the average behavior to generate the bounds of stress relaxation behavior as well. These predictions are then compared with the range of scatter obtained from the test measurements.

5.3. RESULTS

The performance of the macroscale (length scale independent) creep constants in predicting the stress relaxation behavior of the non-homogeneous SAC305 solder specimens is presented here. In particular, the range of scatter in the stress relaxation predictions obtained from the bounds of the creep constants is compared with that obtained from the stress relaxation measurements. In addition, a comparison of the stress relaxation measurements of SAC305 solder relative to Sn37Pb solder from the microscale TMM specimens are presented. The stress distributions expected in the solder region of the Iosipescu specimen configuration is included to understand the uniformity in the shear stress generated due to the 90° notch angles of the copper platens.

5.3.1. Stress Relaxation Measurements of Microscale As-Fabricated Specimens: SAC305 versus Sn37Pb

Stress relaxation measurements of SAC305 and eutectic Sn37Pb solders at various stress levels and temperatures levels are presented here. The test matrix for stress relaxation is not as comprehensive as that of creep tests. However, the test results do show some scatter in the measurements under identical load conditions though not as severe as that in creep tests. The model constants used to describe the decay of stress relaxation history exponentially at various stress and temperature ranges (Equation 5.1) are listed in Table 5-4 and Table 5-5 for SAC305 and Sn37Pb solders respectively. A plot of these constants for SAC305 solder shows instances of non-repeatability in the measured constants (a,b) at 10 MPa shear stress(circles in Figure 5-6). However, the constants exhibit repeatability at ~15 MPa (circles).

Sn37Pb solder on the other hand exhibits very good repeatability (circles in Figure 5-7).

The conclusions presented here on the scatter are based on the measurements conducted at room temperature. At high temperature (75°C), the stress relaxation measurements are highly sensitive to minor fluctuations in the temperature of hot air jet. Hence additional noise in induced in the measurements owing to the stresses induced from the thermal expansions of grips. Furthermore the conclusions are based on limited repeatability tests and further testing and study is required to conclusively quantify the extent of scatter as a function of various regimes in the stress relaxation histories.

The measurements show that the relaxation of SAC305 solder is much lower and slower than SnPb solder. This result is expected due the superior creep resistance of SAC305 relative to Sn37Pb. The stress relaxation behavior of SAC305 relative to Sn37Pb at room and high temperature are plotted in Figure 5-8 a-b. The 75°C temperature data show the extent to which the stress relaxation rate increases at high temperature. Table 5-6 provides quantitative comparisons of the stress relaxation response as a function of temperature and solder composition.

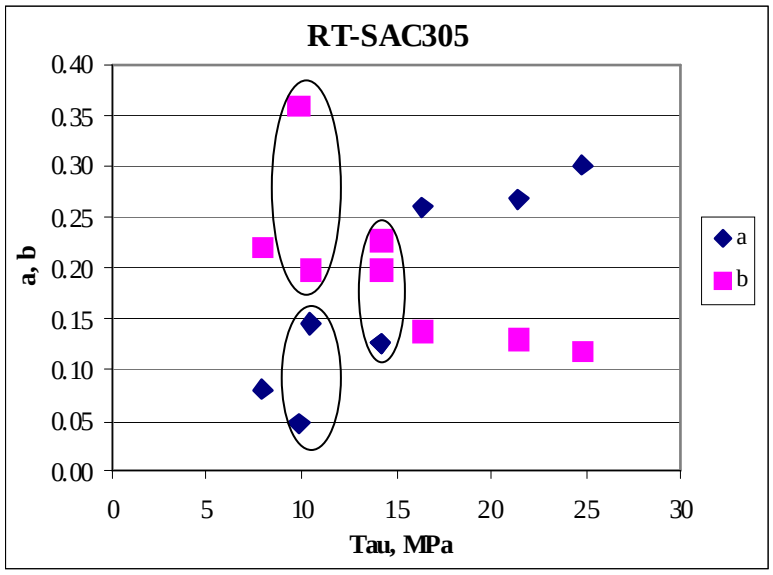

Figure 5-6: Stress relaxation model constants at room temperature for SAC305.

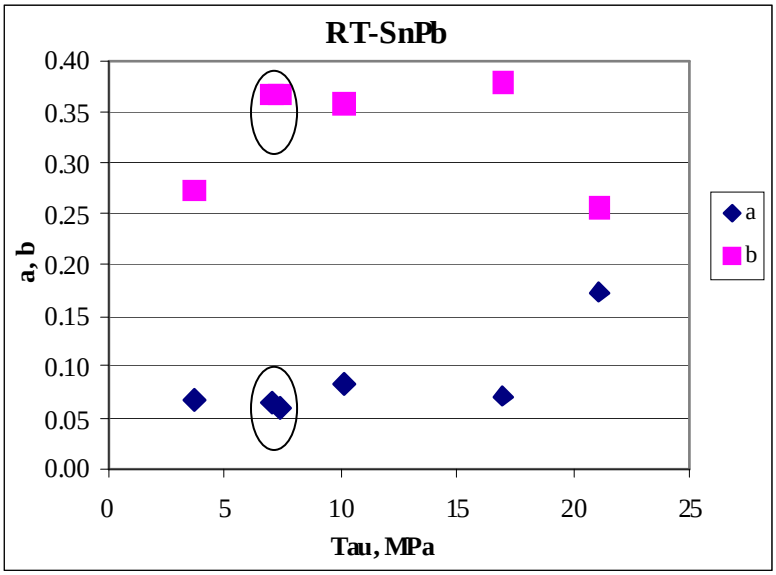

Figure 5-7: Stress relaxation model constants at room temperature for Sn37Pb solder

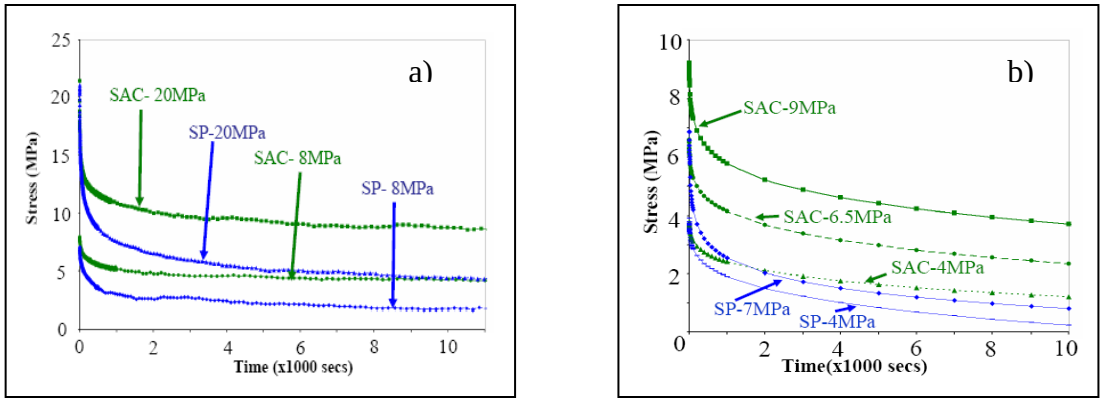

Figure 5-8: Stress relaxation measurements of SAC305 versus Sn37Pb solder at a) RT and b) 75°C

25°C			75°C		
τ_0	a	b	τ_0	A	b
8.0	8.00E-02	2.20E-01	3.7	2.42E-02	4.14E-01
9.9	4.65E-02	3.59E-01	5.1	4.31E-02	3.09E-01
10.5	1.44E-01	1.98E-01	6.6	4.30E-02	3.44E-01
14.1	1.26E-01	1.98E-01	9.2	3.81E-02	3.55E-01
14.2	1.26E-01	2.25E-01	10.6	2.14E-02	3.61E-01
16.3	2.59E-01	1.38E-01	11.7	2.04E-01	1.93E-01
21.4	2.66E-01	1.30E-01	12.6	2.07E-01	1.70E-01
24.8	3.01E-01	1.17E-01	16.4	1.96E-01	1.94E-01
			18.1	2.92E-01	1.33E-01

Table 5-4: Stress relaxation history fit constants for SAC305 solder

25°C			75°C		
τ_0	a	b	τ_0	a	b
3.7	6.69E-02	2.72E-01	3.5	2.24E-02	4.73E-01
7.0	6.40E-02	3.67E-01	3.9	6.03E-02	3.62E-01
7.4	5.82E-02	3.68E-01	6.9	9.17E-02	3.47E-01
10.2	8.32E-02	3.57E-01	8.1	1.04E-01	4.02E-01
17.0	7.08E-02	3.78E-01	17.6	1.49E-01	3.41E-01
21.1	1.72E-01	2.55E-01			

Table 5-5: Stress relaxation history fit constants for Sn37Pb solder

t, τ (MPa), T (°C)	SAC305	SP	Ratio (SAC/SP)
15 min (7, 75)	36	62	0.58
3 hours (7, 75)	65	90	0.72
15 min (7, 25)	30	52	0.57
3 hours (7, 25)	46	83	0.54

Table 5-6: Comparison of % relaxation as a function of solder, time and load

As seen from room temperature comparison (Figure 5-8a), for a given initial stress of 20 MPa, SAC305 relaxes only by 56% in the time Sn37Pb relaxes by 80% (i.e. 1.7 hrs). At 75°C, a similar comparison at 20 MPa shows that SAC305 relaxes only 52% in the time that Sn37Pb relaxes by 80% (i.e. 20 min). The load drop in SAC305 versus Sn37Pb at different stress levels at RT, shown in Figure 5-9, gives a clear indication that the stress drop rate in Sn37Pb is much higher compared to SAC305, at different stress levels.

The relaxation response for both solders has two distinct portions; an initial steeply descending portion followed by a "steady state" decrease at a much lower slope. The steady state slope of eutectic Sn37Pb is seen to be higher than that of SAC305 solder, with the difference being more pronounced with increasing temperatures. Increase in the initial stress increases the relaxation in both cases, but more severely in SAC305 than in Sn37Pb (Figure 5-8). Unlike SAC305, a majority of the relaxation (~70%) in Sn37Pb is seen to occur in the initial 15 minutes and saturation is achieved. Comparison with results from literature is not possible due to varied reasons such as range of load conditions, scale and state of damage in the specimen [135, 137, 157].

The stress relaxation results obtained here suggest that for the purposes of accelerated thermal cycling (ALT) profiles with T_{max} < = 75^0 C, dwelling the packages beyond 20-30 minutes does not relax the stress in SAC305 significantly. The stress relaxation measurements from this study are used in conjunction with modeling and simulation results for saturation of thermal cycling fatigue acceleration factors to determine the optimal dwell time for SAC305 solders relative to Sn37Pb (Appendix 5.2).

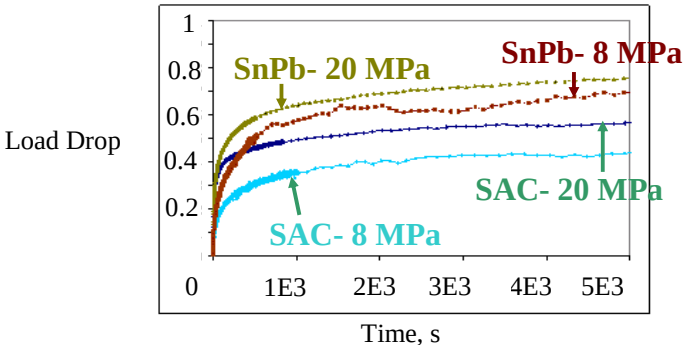

Figure 5-9: Stress relaxation at 25°C in terms of load drop

5.3.2. Finite Element Modeling

The performance of the creep constants in predicting the stress relaxation behavior of non-homogeneous SAC305 solder specimens is presented here. The modeling results for the upper bound, lower bound and the average creep fits are presented. In addition the effect of inclusion/ exclusion of primary creep to the secondary creep are included. The results of the sanity check conducted by using creep test loads is presented first followed by the stress relaxation predictions.

As described in Section 2.1.1, Section 3.2.1 and Section 5.2.1, the Iosipescu specimen configuration chosen in this study has the advantage of producing a uniform shear stress distribution, and negligible tensile stresses in the solder region owing to

the 90° notch angles in the copper platens. The stress distributions expected in the solder region of the Iosipescu specimen configuration subject to a constant force creep loading that generates 11 MPa shear stress at 75°C are presented in Figure 5-10, Figure 5-11 and Figure 5-12. The results show that the shear stress is uniform across the solder region (except the edges which constitute <10% of joint length) and that the tensile stresses are negligible (around 1-2MPa) across majority of the joint (90% of joint length).

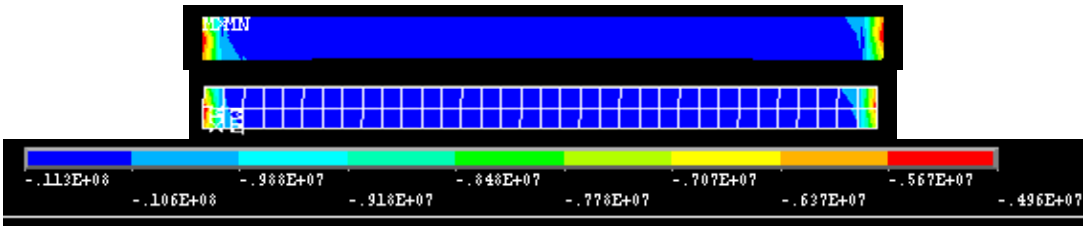

Figure 5-10: Contour plot of the elemental shear stress τ_{xy} distribution (in Pa) in the solder region under creep loading at 75°C and 11MPa load.

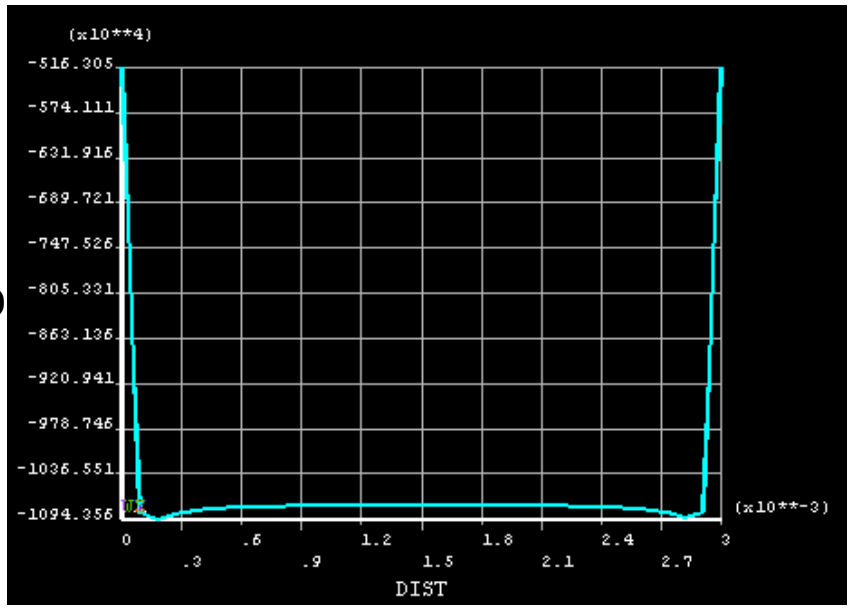

Sxy (Pa)

Figure 5-11: Plot of the shear stress, τ_{xy} (Y axis in Pa) across the 3mm length (X axis in 'm') of the solder region under creep loading at 75°C and 11MPa load. Shear stress is seen to be ~11 MPa across majority of the joint except at the edges where the peak stresses are seen.

Stress (Pa)

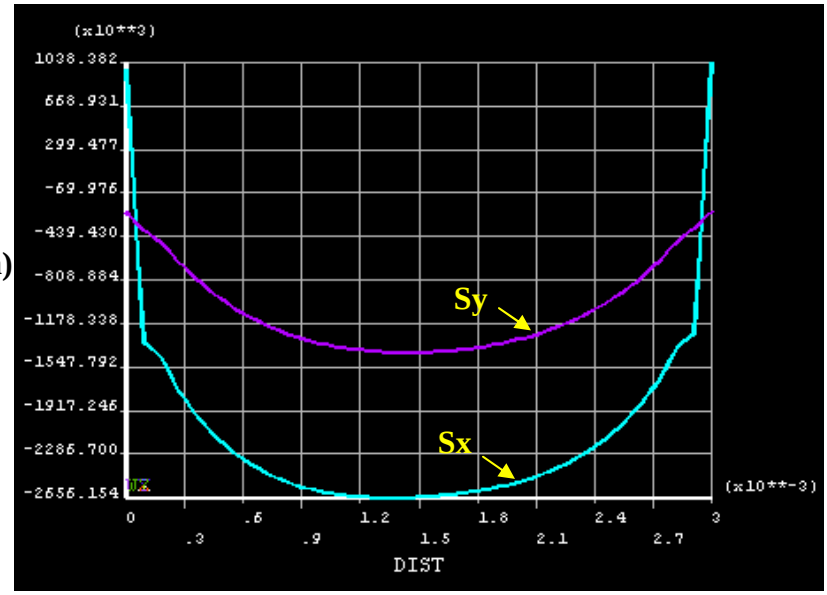

Figure 5-12: Plot of the tensile stresses (in Pa) across the length (3mm) of the solder region under creep loading at 75°C and 11MPa load. Stress values are seen to be around 1-2 MPa in the bulk of the joint except at the edges(<6% of joint length).

5.3.2.1. Sanity Check: Creep Loading

Comparison of the results from the modeling and experiments under creep loading conditions reveal that the predictions from creep constants that are representative of the upper and lower bounds of scatter do bound the test measurements (Figure 5-13 and Appendix 5.3). For the high stress regions which show the maximum scatter in the creep measurements, the bounds cover a wide range of strains under similar load conditions.

A direct correlation between the trends of the error in stress relaxation predictions and the difference in the creep fits and measurements at a given load level is not feasible. This is because the scatter bounds are evaluated across the entire stress range rather than an individual stress loading for a given isothermal temperature condition.

The sanity check results verify the accurate functionality of the user programmed subroutine for primary creep.

Table 5-7 summarizes the results from the creep FEA runs. Figure 5-13 compares the modeling results and test measurements at 11 MPa, 75°C. The creep strain predictions based on the lower bound and the average creep fits approximately match the measured lower bounds and average creep behavior across the specimens measured at identical loads of 10MPa. The FE result based on the upper bounds of the creep constants over predicts the measured creep strain history significantly. Hence similar over prediction of stress relaxation can be expected in the stress relaxation runs. The modeling results at other creep test loads are provided in Appendix 5.3.

Load (MPa, °C)	Bind Creep Tests	Performance of bounds
11, 75	yes	A and L bound measurements. U over predicts
15, 25	yes	U corresponds to largest creep measurements, A to approximately at the mean and L under predicts.
20, 25	yes	A and L bound measurements. U over predicts

Table 5-7: Results of creep loading sanity checks as a function of shear stress and temperature. U, A, and L refer to the predictions from upper bound, average fit and lower bound based creep models. Both primary and secondary creep is modeled here.

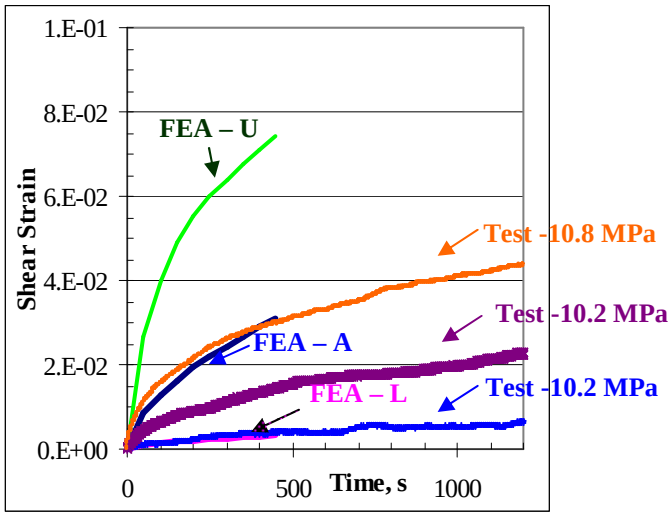

Figure 5-13: Results of creep loading sanity checks at 11 MPa, 75°C. U, A, and L refer to the predictions from upper bound, average fit and lower bound based creep models. The material model uses both primary and secondary creep.

5.3.2.2. Modeling: Stress Relaxation

The contributions of secondary and primary creep to stress relaxation of SAC305 solder are investigated here. Owing to the piece to piece variability exhibited by the non-homogenous and anisotropic TMM solder specimens, the emphasis is more on average trends rather than on exact quantitative predictions. Isothermal stress relaxation is predicted at 25°C and at 75°C, and compared with test results.

The results of the stress relaxation runs at 11 MPa, 75°C and 20 MPa, 25°C are presented in Figure 5-14 and Figure 5-15. These stress levels are representative of the shear stresses expected at 25°C and 75°C seen in the solder interconnects during service loads under thermal cycling loads. The plots of FE predictions at other load levels are presented in Appendix 5.4.

In addition, the effect of the displacement loading rate (to reach a constant displacement history) is studied in Figure 5-16 and Figure 5-17. The results show that the displacement loading rate does not affect the stress relaxation histories predicted in the finite element analysis (both with and without the inclusion of primary creep to the secondary creep). The slight offset seen between the FEA predictions from the different ramp rates in Figure 5-17 is due to a small difference in the initial stress achieved at the start of the relaxation loading (0.3 MPa difference).

Results show that the addition of primary creep behavior to the secondary creep model increases the magnitude and rate (curvature) of stress relaxation. The stress relaxation predictions reveal that the use of limiting constants for creep do bound the stress relaxation behavior. The use of the average creep behavior fits alone is not accurate in capturing the range of the measured stress relaxation behavior (Figure 5-14, Figure 5-15 and Appendix 5.4**)**.

In general, the creep constants based on the lower bounds of 75°C data are best suited for capturing the stress relaxation measurements conducted in this study. The predictions based on the average and upper bounds of the creep data fits at 75°C are comparable (Figure 5-14). The average behavior and the lower bounds creep fits at room temperature are best suited for capturing the stress relaxation at room temperature (Figure 5-15).

In addition, the use of secondary creep constitutive models without the inclusion of primary creep is more successful in capturing the stress relaxation behavior. The use of primary creep material constants measured in this study highly over predicts the relaxation behavior especially in the initial stages of the time history. This region

is subject to much higher stresses leading to a higher sensitivity to the viscoplastic deformation.

A comparison of the errors in the stress relaxation predictions with the measurements at 25°C and 75°C are provided in Table 5.8 and Table 5.9. A comparison is provided on the magnitudes of error in the predictions relative to the measurements at 15 minutes and 3 hours. These times are chosen owing to their relevance to the possible hot dwell times that are applicable to Sn37Pb and SAC solders (see the Appendix 5.2 for a detailed study).

These results suggest that when the creep curves fit well with the creep test data, the stress relaxation predictions can provide a reasonable fit to the test data. Discrepancies in stress relaxation predictions can be of the same magnitude as the scatter in the creep test data.

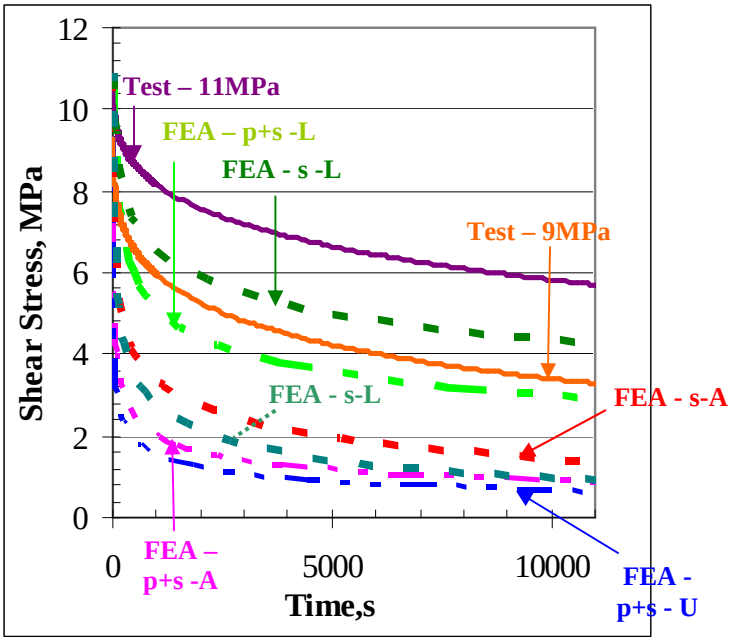

Figure 5-14: Results of stress relaxation predictions at 11 MPa, 75°C. U, A, and L refer to the predictions from upper bound, average fit and lower bound based creep models. The material model uses both primary and secondary creep.

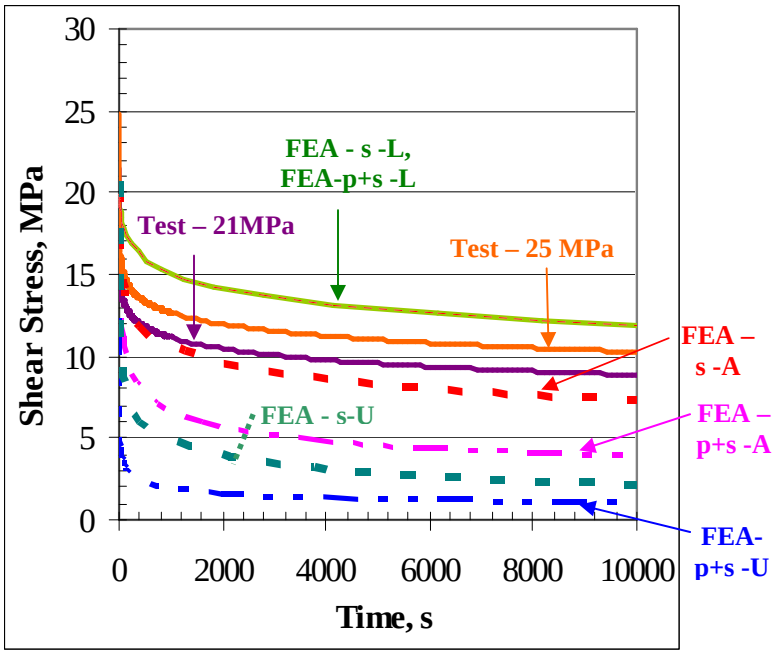

Figure 5-15: Results of stress relaxation predictions at 20 MPa, 25°C. U, A, and L refer to the predictions from upper bound, average fit and lower bound based creep models. The material model uses both primary and secondary creep.

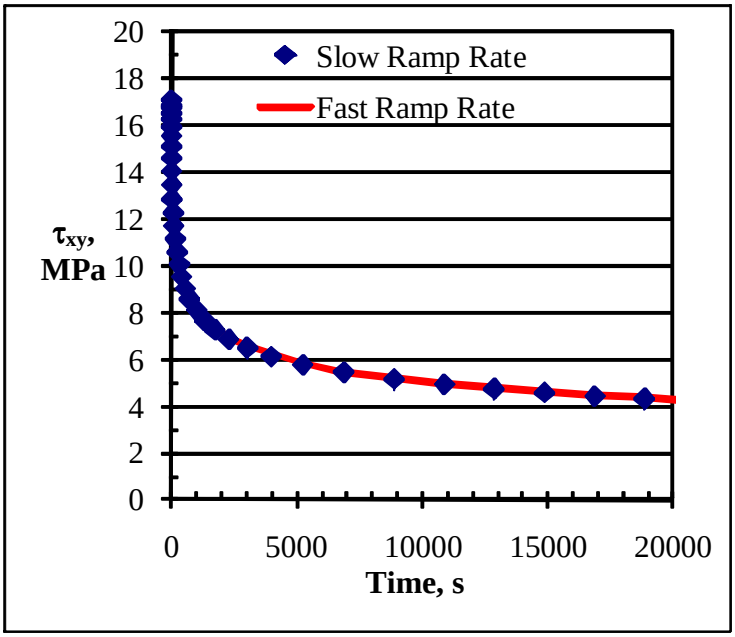

Figure 5-16: Effect of pre-loading ramp rate on the stress relaxation predictions (shear stress) at 17 MPa, 75°C using primary and secondary creep constants of the lower bounds. The slow and fast ramp rates are 0.6 µm/s and 10 µm/s.

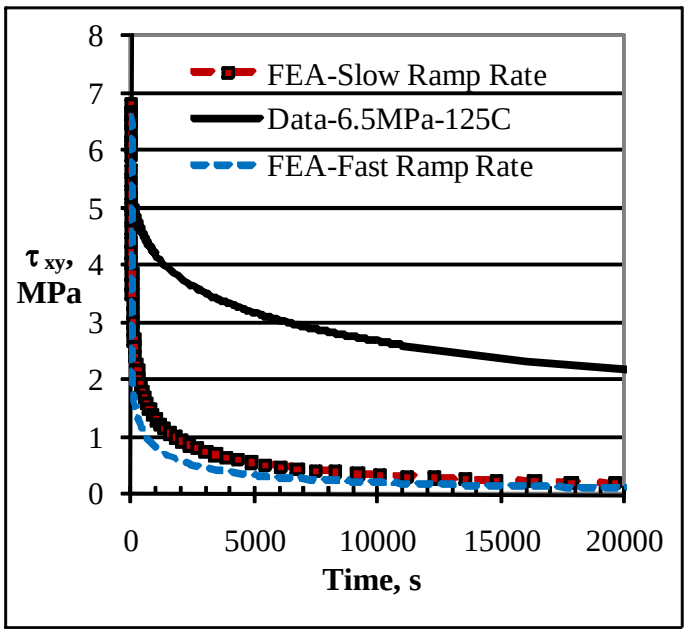

Figure 5-17: Effect of pre-loading ramp rate on the stress relaxation predictions (shear stress) at ~6 MPa, 125°C using secondary creep constants of the lower bounds. The slow and fast ramp rates are 0.3 µm/s and 10 µm/s respectively.

Load / Material Model	Offset in FE s vs. Test Data			
	Upper	Average	Lower	Performance of bounds
4 MPa, Primary + Secondary	τ_{test} @ 3 hours =1.3 MPa			• Predictions using L bounds of creep data match test data • U and A results are comparable and over predict significantly
	-1.1	-1	0.4	
	τ_{test} @ 15 min =2.4 MPa			
	-1.9	-1.7	-0.7	
4 MPa, Secondary	τ_{test} @ 3 hours =1.3 MPa			• Qualitative trends similar to that as primary + secondary results • Magnitude and rate of relaxation is lower.
	-1.0	-0.8	+0.2	
	τ_{test} @ 15 min =2.4 MPa			
	-1.5	-1.2	-0.3	
7 MPa, Primary + Secondary	τ_{test} @ 3 hours =2.4 MPa			• Predictions using L bounds of creep data match test data • U and A results are comparable and over predict significantly
	-1.8	-1.6	+0.1	
	τ_{test} @ 15 min = 4.2 MPa			
	-2.3	-2.2	-0.2	
	τ_{test} @ 1 min = 5.5 MPa			
	-1.7	-1.8	+0.3	
7 MPa, Secondary	τ_{test} @ 3 hours =2.4 MPa			• Qualitative trends similar to that as primary + secondary results • Magnitude and rate of relaxation is lower.
	-2.1	-1.9	-0.63	
	τ_{test} @ 15 min = 4.2 MPa			
	-3.3	-2.9	-1	
	τ_{test} @ 1 min = 5.5 MPa			
	-3.5	-2.9	-0.2	
10.5 MPa Primary + Secondary	τ_{test} @ 3 hours =5.8 MPa			• Predictions using L bounds of creep data match test data (slight over prediction) • U and A results are comparable and over predict significantly
	-5.2	-5	-2.9	
	τ_{test} @ 15 min =8 MPa			
	-6.7	-6.2	-3	
10.5 MPa Secondary	τ_{test} @ 3 hours =5.8 MPa			• Qualitative trends similar to that as primary + secondary results. L under predicts • Magnitude and rate of relaxation is lower.
	-5	-4.4	-1.5	
	τ @ 15 min =8 MPa			
	-5.3	-4.8	-1.6	
12 MPa Primary + Secondary	τ_{test} @ 3 hours = 3.5 MPa (11.7MPa test data)			• Predictions using L bounds of creep data match test data (slight over prediction) • U and A results are comparable and over predict significantly
	-2.7	-2.4	-0.5	
	τ_{test} @ 15 min = 5.5 MPa			
	-3.6	-3.2	-0.2	
	τ_{test} τ @ 15 min = 7.7 MPa			
	-5.8	-5.4	-2.4	

Table 5-8: Comparison of stress relaxation FE results and TMM data at 75°C. U, A, and L refer to the predictions from upper bound, average fit and lower bound based creep models

Load, Material Model	Offset in FE s vs. Test Data			
	Upper	Average	Lower	Performance of bounds
20 MPa, Primary + Secondary	τ_{test} @ 3 hours = 9 MPa			• Predictions using L bounds of creep data is best match to test data • A is the lower bound and is at the mean of U and L results. (U over predicts significantly)
	-7.9	-5.1	+2.1	
	τ_{test} @ 15 min = 11.2 MPa			
	-9.2	-4.5	+3.5	
20 MPa, Secondary	τ_{test} @ 3 hours = 9 MPa			• Qualitative trends similar to that as primary + secondary results • Magnitude and rate of relaxation is lower.
	-3.9	-1.8	+2.9	
	τ_{test} @ 15 min = 11.2 MPa			
	-2.6	-0.5	+4.1	
14 MPa Primary + Secondary	τ_{test} @ 3 hours = 6.5 MPa			• Predictions using A bounds of creep data match test data (slight over prediction) • A is at the mean of U and L results. (U over predicts)
	-5.5	-2.7	+4.2	
	τ_{test} @ 15 min = 8 MPa			
	-5.9	-1.2	+5.8	
8 MPa Primary + Secondary	τ_{test} @ 3 hours = 4.3 MPa			• Predictions using A bounds of creep data match test data (slight over prediction) • A is at the mean of U and L results. (U over predicts)
	-3.3	-0.6	+3.6	
	τ_{test} @ 15 min = 5.6 MPa			
	-3.6	-1.9	+2.6	

Table 5-9: Comparison of stress relaxation FE results and TMM data at 25°C. U, A, and L refer to the predictions from upper bound, average fit and lower bound based creep models.

5.4. LIMITATIONS AND FUTURE WORK

Stress relaxation testing is challenging since repeatability in obtaining the initial stress state accurately across different specimens is difficult to achieve. Furthermore, conducting measurements at high temperatures poses severe challenges since minor fluctuations (of order +/-1°C) in the isothermal temperature setting results in stress

fluctuations as large as +/- 3 MPa due to thermal expansions of the grips and specimen. The variations in the measurements at 75°C are hence a combined effect of temperature induced noise and material behavior. Hence minimizing noise in the stress relaxation at high temperatures (>75°C) is difficult and temperature compensated expansions need to be included in the measured stress history.

The test matrix for the stress relaxation does not provide sufficient repeatability for quantifying the extent of scatter as reported in the creep measurements of these non-homogeneous joints. Future testing should investigate this issue. Furthermore, the modeling predictions in the current study are based on 2-D FEA and the three dimensional effects of the solder joint deformation should be explored using a 3-D model.

Owing the capability of the temperature module, measurements at 125° C have not been conducted. Future study should improve the temperature capability of the TMM setup for providing these measurements. As an approximate estimate, modeling predictions based on the validated FE model in this study can be provided to understand the extent of relaxation at 125°C.

5.5. SUMMARY AND CONCLUSIONS

The accuracy of the macroscale continuum mechanics based creep model constants measured from non-homogenous SAC305 specimens in predicting the stress relaxation measurements of similar specimens is investigated using modeling and simulation. The piece-to-piece variability observed under identical loading conditions in the stress relaxation measurements is not as significant as that in creep measurements. The scatter is evident predominantly in the initial time histories

(higher stress levels), and gradually decreases with increasing time (damage). The stress relaxation of SAC305 proceeds at a much slower rate than Sn37Pb (SAC 305 relaxes approximately 50% of Sn37Pb at 7 MPa, 25°C load). A quantitative comparison of % relaxation of SAC305 achieves relative to Sn37Pb is provided.

Modeling results show that the error in the stress relaxation predictions is within the same range of scatter observed in the creep measurements. The effect of the inclusion of primary creep to the secondary creep for representing the solder behavior is investigated. The results show that utilizing the average macroscale creep constants do not necessarily capture the stress relaxation behavior. The range of stress relaxation modeling predictions based on the creep constants representative of the bounds of measured scatter do capture the range of scatter exhibited by the relaxation measurements.

Inclusion of primary creep significantly increases the rate and magnitude of relaxation, leading to an over prediction of the stress relaxation relative to the measurements. Results of the 2-D FE analysis suggest that material models using secondary creep alone capture the stress relaxation behavior effectively (inclusion of primary creep is not necessary). The predictions that use the secondary creep constants (exclusive of primary creep) based on the lower and average bounds capture the measured stress relaxation behavior more effectively than those with the upper bounds.

Chapter 6: Microstructure and Property Evolution of Sn3.0Ag0.5Cu Solder with Aging and Cyclic Loading

ABSTRACT

This study examines the effect of cyclic fatigue damage and aging histories on the evolution of the constitutive and fatigue responses and microstructure of microscale SAC305 solder joints. In particular, the study examines if the variability exhibited by the viscoplastic properties of as-fabricated microscale SAC305 joints is also evident in the elastic, plastic and fatigue properties of the same joints. Microscale specimens are fabricated to produce microstructures that are representative of functional microelectronic solder interconnects. All specimens are aged at 0.85 homologous temperature for 100 hours, to reduce microstructural instability. These specimens are termed as as-fabricated specimens.

Cyclic damage is induced through isothermal, mechanical cycling tests at 5E-2 s^{-1} strain rate and room temperature, in microscale joints. Insights into the evolution of the measured properties are provided by correlating microstructural grain evolution of microscale SAC305 solder as a function of cyclic damage. The effect of aging history is studied by subjecting the as-fabricated specimens an additional isothermal aging for 3000 hours at room temperature before mechanical cycling. These are termed as “aged” joints.

Accumulated fatigue damage and isothermal aging are found to degrade the constitutive and mechanical fatigue properties of the solder. The hysteresis response, and the elastic, plastic and yield measurements from the initial cycles show piece-to-

piece variability (similar to that seen in the initial viscoplastic secondary creep measurements), owing to the non-homogenous coarse-grained Sn microstructure. The scatter gradually decreases with an increasing state of solder damage (increasing load cycles). In particular, the variability in the final fatigue life of these non-homogenous solder joints under mechanical fatigue tests is negligible compared to that seen in the constitutive behavior of undamaged solder.

The non-homogenous coarse Sn grain microstructure exhibited in the as-fabricated state undergoes grain homogenization due to recrystallization. This is a possible explanation for the reduction in scatter in the fatigue curves with increasing fatigue damage. The grain evolution observed in microscale joints is similar to that reported in functional solder joints under life-cycle loading. The mechanical fatigue durability of SAC305 solder reduces with isothermal aging. However the fatigue durability is higher than that of unaged eutectic Sn37Pb. The yield stress measurements suggest that SAC305 obeys a hardening rule different from that of isotropic or kinematic hardening. The measured degradation in elastic, plastic and yield properties is described with a model from the literature, based on continuum damage mechanics.

6.1 INTRODUCTION

Studies conducted in the previous chapters investigated the extent of scatter exhibited by microscale SAC305 shear specimens under identical viscoplastic loads. An important aspect of these material characterization tests is that the reported constitutive properties are those of undamaged and as-fabricated solder specimens. After reflow, all specimens are aged at 0.85 homologous temperature for 100 hours,

to reduce microstructural instability. These joints are termed as “as-fabricated” joints. The material characterization tests are conducted using a custom built test setup, thermomechanical microscale machine (TMM). The test specimens are modified lap-shear Iosipescu microscale solder specimens.

Apart from constant stress (viscoplastic creep test) or constant strain (stress relaxation test) loads, functional solder interconnects are also subjected to monotonic plasticity-dominated loads as well as cyclic fatigue loads during their service life. As described in earlier chapters, solder exhibits non-linear viscoplastic deformation which is partitioned, for convenience, into elastic, plastic and creep behavior. Hence as continuity to the viscoplastic measurements reported in Chapter 3, the extent of scatter exhibited by the elastic, plastic and cyclic fatigue properties of microscale TMM specimens in the undamaged, as-fabricated state is investigated in the current study. The cyclic fatigue loads investigated here are isothermal mechanical cyclic loads.

In reality, however, the microstructure of solder constantly evolves throughout the service life and does not retain the as-fabricated microstructural features. Under service conditions, electronic solder interconnects are subjected to continuous degradation (macro cracks, and distributed micro damage) and continuous microstructural evolution [22, 51, 60, 70]. Hence the constitutive response, which is a function of the underlying microstructural state, also evolves as a function of the loading history. Hence an understanding of the mechanical response as a function of load history is crucial for the design and modeling of solder reliability.

Most predictive studies (analytical or numerical) on the mechanical response of solder (durability and stress response) utilize constitutive properties measured from as-fabricated and undamaged pristine joints. These predictions are often non-conservative since they do not account for the degradation of constitutive response due to fatigue damage. The accuracy of these predictive studies can be improved by suitably updating the constitutive properties as a function of the damage induced by the loads [230]. Alternatively, post-damage constitutive properties can be used to provide a conservative estimate.

Furthermore, it is important to understand how the initial coarse-grained, non-homogenous microstructure of as-fabricated, pristine, microscale SAC305 joints evolve under the loading experienced during the entire service life. Literature reports that Pb-free solder joints in microscale dimensions, such as BGA joints, undergo recrystallization when subjected to accelerated thermal cycling, power cycling, drop and vibration fatigue[43, 51-55, 60, 62-63]. In particular, this study investigates if similar recrystallization and grain refinement occur in TMM samples, under isothermal cyclic mechanical fatigue. This similarity governs the relevance of post-damage constitutive properties measured here.

In the current study, the evolution of the monotonic constitutive properties, fatigue properties and microstructural grain features of the microscale TMM joints is studied as a function of the loading history. The influence of two kinds of loading histories is investigated here. The first loading type is cyclic fatigue loading that leads to damage accumulation such as those seen by functional solder joints under operating field conditions. In order to mimic the damage induced under cyclic loads

in field, cyclic damage is induced in SAC305 TMM specimens through isothermal mechanical cycling tests at room temperature. The other load history investigated is long-term isothermal aging, such as that seen by solder joints during transportation and idle time. The microstructure, and hence the mechanical response of Pb-free solder, is known to be sensitive to long-term thermal aging [5, 7-8, 54, 69, 71]. This study characterizes the change in solder properties due to long-term aging at room temperature.

In addition to understanding the evolution of the material properties as a function of fatigue damage, a phenomenological model that can capture the changes in the material properties is investigated. A previously proposed continuum damage mechanics model is applied, to explore whether it captures the degradation in the constitutive response as a function of mechanical fatigue damage with sufficient accuracy [231] [104, 232-233].

6.1.1. Objectives of the Study

Based on the background provided so far, the specific objectives of this study on SAC305 microscale solder are to:

- Investigate the extent of scatter exhibited by the constitutive (elastic and plastic) and isothermal mechanical fatigue properties in the initial as-fabricated state.
- Characterize the evolution of the constitutive (elastic, plastic and viscoplastic) and scatter as a function of increasing fatigue damage to the solder.

- Investigate whether the observed degradation of constitutive properties as a function of cyclic fatigue loading can be characterized by a previously proposed [104, 231-232] model based on continuum damage mechanics.
- Investigate the microstructural evolution of as-fabricated SAC305 microscale solder specimens as a function of isothermal mechanical fatigue damage and compare with that of functional microscale solder joints.
- Investigate the evolution of isothermal mechanical fatigue properties as a function of isothermal aging (and % Ag content in SAC).

6.2. APPROACH

Details of the test methodology, test matrices, specimen fabrication and loading history, and the damage model used are described in this section.

6.2.1. Test Setup and Test Specimen

A microscale test setup, termed the thermomechanical microscale (TMM) setup, is used for conducting isothermal cyclic mechanical fatigue tests, as well as periodic monotonic tests to characterize constitutive behavior as a function of cyclic fatigue damage. The specimen configuration and fabrication are described in detail in Chapter 2 (Experimental Approach). Hence only the details relevant to the current study are provided here. All specimens undergo similar fabrication steps until the as-fabricated stage. Any additional changes to the microstructural state of the solder joint in the TMM specimen in terms of damage accumulation or aging histories are described in Sections 6.2.1.1 and 6.2.1.2. Details of the fabrication process are described next for continuity.

The solder specimen is fabricated by manual soldering at a reflow temperature of 248°C and 210°C for SAC305 and Sn37Pb solders respectively. The pre-heat time is 45s and the reflow time from the deposition of solder to stationary heating time is 60s. The specimen is then air-cooled at ~ 2°C /s. The pre-heat and the reflow profile are strictly monitored to be consistent across all specimens. All specimens are further aged for 100 hours at 0.8 T_{melt} (~132°C in the case of SAC305 solder) prior to testing, to obtain a stable microstructure and also to relax residual fabrication stresses. Sn37Pb is traditionally aged at 100°C, which corresponds to a homologous temperature of 0.8. Since solders exhibit viscoplasticity, the same homologous temperature is chosen for SAC solders (~132°C) to maintain consistency. In the current study, these thermally pre-conditioned joints are termed 'as-fabricated' joints.

6.2.1.1. Manufacturing History of Specimens Subjected to Damage Evolution Studies

The tests for characterizing the fatigue properties and the evolution of elastic, plastic and yield properties as a function of fatigue damage are conducted on 'as-fabricated' joints. The changes in state of microstructural damage are induced by subjecting these joints continuously to isothermal mechanical fatigue loads. The resulting changes in the elastic and plastic properties are monitored from the cyclic hysteresis loops. The creep and stress relaxation properties are monitored as a function of fatigue damage, by conducting monotonic viscoplastic tests after predetermined amounts of cyclic fatigue damage (defined by predefined amounts of load drop) on different specimens.

6.2.1.2. Manufacturing History of Specimens Subjected to Aging Studies

The effect of aging on the isothermal mechanical fatigue properties is observed by subjecting 'as-fabricated' specimens to additional aging for 3000 hours at room temperature, prior to the cyclic fatigue tests.

6.2.2. Test Matrix and Phenomenological Damage Models

The effect of aging on the isothermal mechanical fatigue properties is investigated on as-fabricated specimens that are subject to additional aging in the unstressed state for 3000 hours at room temperature. Since the constitutive properties are measured as a function of increasing isothermal mechanical fatigue damage, the details of the fatigue testing are provided first followed by the details of the constitutive tests. Table 6-1 lists the fabrication, aging and loading history of the specimens for each of the conducted tests.

Damage State →	As-Fabricated, Undamaged	Fatigue Damage		Aging Damage
Study Conducted (below)	Φ= 0	continuously evolving damage from Φ= 0 to 0.5	end state of damage Φ = 0.5	3000 hours @ RT
Elastic	x	x	x	
Plastic	x	x	x	
Yield	x	x	x	
Creep	x		x	
Stress Relaxation	x		x	
Isothermal Mechanical Fatigue	x	x	x	x
Microstructure	x		x (post-creep and fatigue)	

Table 6-1: Test matrix describing the constitutive and fatigue properties characterization as a function of loading histories (damage and aging). Parameter 'Φ' refers to the state of fatigue damage in terms of load drop that varies between 0 and 1.

6.2.2.1. Test Matrix: Isothermal Mechanical Fatigue Properties

Since plastic and creep deformation mechanisms result in different characteristics of material damage, as assumed in various partitioned damage models (strain-range partitioning [1] and energy partitioning [95]), it is desirable to choose test conditions that isolate the separate effects of these mechanisms (Appendix 6.1). Fatigue damage due to creep deformation is rate-dependent and progressively becomes the dominant damage mechanism in solders, as the homologous temperature increases and strain rate decreases. On the contrary, fatigue damage due to rate-independent plastic

deformation becomes the dominant contributor to solder damage at low homologous temperature and high strain rate.

In the current work, cyclic tests are conducted at room temperature at a relatively high deformation rate of 10 μm/s, which corresponds to a strain rate of $5E\text{-}2s^{-1}$. Hence, the room temperature, high strain rate test condition provides a relatively low ratio of creep to plastic damage. Furthermore, both Sn37Pb and SAC solders have creep deformation even at room temperature due to the high homologous temperature (0.63 and 0.6 respectively). In this study, testing at this condition is labeled as a 'low-creep' test, for convenience.

The displacement loading profile used in the mechanical fatigue tests is triangular (no dwell) and is shown in Figure 6-1, where δ_u and δ_l are the upper and lower displacement amplitudes, t_{cycle} is the total cycle time, and δ_r is the constant displacement rate. The test matrix for low-creep isothermal mechanical cyclic tests is detailed in Table 6-2. Fatigue tests in this study are conducted at a constant cyclic inelastic strain range (ISR). As damage in solder progresses (with increasing cycles), the stiffness of the solder decreases, and the ISR is held constant by continuously varying the load profiles in accordance with the damage accumulation. Fatigue damage is quantified in terms of either the ISR or the initial plastic work W (area inside the initial stabilized hysteresis loop).

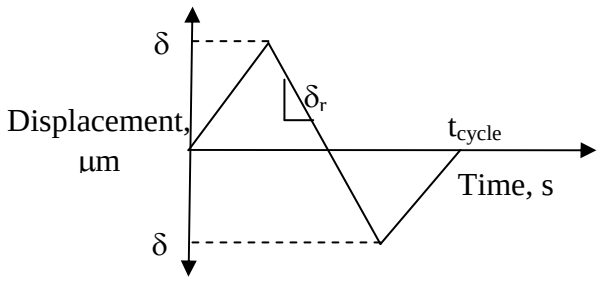

Figure 6-1: Cyclic displacement loading profile for mechanical fatigue tests

Due to ISR-controlled cycling, cyclic W gradually decreases with progressive load drop due to the softening of solder with accumulated damage. However, the initial W is still a reasonable metric for characterizing durability because cyclic W experiences a similar decay in real joints under cyclic field loading, as the solder accumulates damage (Appendix 6.2). Furthermore, compared to ISR, W is a more comprehensive descriptor of the loading history, since it includes both stress and strain responses. A detailed review of the various control modes used in isothermal fatigue tests in the TMM setup is given by Haswell [104].

Test Conditions (Temperature, Strain Rate)	Load Levels (Deformation Range,μm)		
25°C, 5.5 E-2 s^{-1}	-5.5 ~ 5.5	-8 ~ 8	-10 ~ 10

Table 6-2: Test matrix for characterizing the isothermal mechanical fatigue properties of SAC305 as a function of aging. The same test matrix is used for measuring the elastic, plastic and yield properties of microscale SAC305 solder as a function of cyclic damage

Solder undergoes cyclic softening under isothermal mechanical fatigue due to distributed damage and evolving microstructure. A plot of the typical softening behavior expected in SAC305 solder under ISR control condition is shown in

Appendix 6.2. The maximum load-bearing capacity of solder decreases with progressive damage, and hence strain-controlled mechanical cyclic failure models typically use load drop as a failure criterion. The load drop is monitored as a function of number of cycles for various load levels (Section 6.2.3).

Similar to the Coffin-Manson fatigue model [1], a power law relationship is used to relate the various damage metrics (D) to the cycles to failure (N_f) as follows:

$$D = CN_f^n \qquad \text{Equation (6.1)}$$

where, *C* and *n* are material constants obtained by least square fits of test data. The load drop with progressive cyclic damage and cyclic softening is monitored and failure is defined at 50% load drop (Figure 6-2).

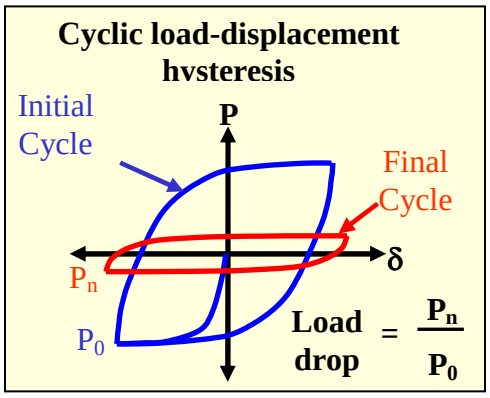

Figure 6-2: Schematic of the load drop failure criterion used in the fatigue tests

6.2.2.2. Test Matrix: Elastic, Plastic and Yield Properties and Microstructural Evolution as a Function of Fatigue Damage

The elastic, plastic and yield properties are evaluated using the hysteresis loops continuously generated during the mechanical fatigue tests in Table 6-2. The properties are evaluated for the stress-strain curves generated up to a threshold damage state (load drop) of 0.50. Testing is continued until 0.80 load drop at which

point the solder load bearing area is effectively reduced due to macro and microcracking. Hence the measured properties suggest lower stress state than those experienced by the joint at this damage state. Furthermore, 0.50 is chosen for comparison with results in literature since this is a commonly used criterion for mechanical cycling tests.

In addition to the stress-strain data, the load drop history is also measured as a function of increasing damage/ load drop. Figure 6-3 shows a typical load drop history generated from a mechanical fatigue test at strain amplitude of +/-5.5E-2 (displacement amplitude of 10 μm). The microstructure of the TMM joints is analyzed for evidence of Sn grain recrystallization, for the most damaging mechanical fatigue loads (strain amplitude of +/-5.5E-2)

The elastic, plastic and yield behavior are evaluated by subtracting the creep strain, from the total measured strain, as shown in Equations 6.2-6.6 below. Average creep strains are estimated with the constitutive models presented earlier in Chapter 3. A simple 1-D analytical viscoplastic model is used to isolate and identify the elastic, plastic and creep contributions in the hysteresis loops. The methodology adopted is similar to that presented earlier [95, 104] and the partitioned constitutive equations are listed in Equations 6.2-6.6 for completeness.

Once the creep strains are eliminated, the slopes of the unloading and loading portions of these loops are evaluated to obtain the effective elastic modulus at this strain rate. The resulting elastic strain is subtracted to obtain the hysteresis loops between stress and plastic strain (see Appendix 6.3 for the resulting elastic, plastic, creep and total strain). The Ramberg-Osgood power law model [234] is used to

describe this resulting plastic hysteresis loop, in terms of the plastic model constants (C_p, n). The yield stress is measured based on 0.2% plastic strain offset at zero stress state. The evolution of all these constants is monitored as a function of cyclic damage.

$$\varepsilon_{tot} = \varepsilon_{elas} + \varepsilon_{crp} + \varepsilon_{plast} \quad \text{Equation 6.2}$$

$$\varepsilon_{crp} = \varepsilon_{sec} + \varepsilon_{prim} \quad \text{Equation 6.3}$$

$$\varepsilon_{elas} = \sigma/E(D) \quad \text{Equation 6.4}$$

$$\varepsilon_{elas} = \varepsilon_{tot} - \sigma/E(D) - \varepsilon_{sec} - \varepsilon_{prim} \quad \text{Equation 6.5}$$

$$\sigma = C_p(D)\,(\varepsilon_{plast})^{n_p(D)} \quad \text{Equation 6.6}$$

where, σ is the stress,; ε_{tot}, ε_{plas}, ε_{crp}, ε_{sec}, ε_{prim} are the total, plastic, total creep, secondary creep and primary creep strain; C_p, C_{p0} are current and initial Ramberg-Osgood plastic coefficient; n_p is Ramberg-Osgood plastic exponent; E is the elastic modulus; and D is the instantaneous damage state (varies from 0 in undamaged state to 1 in completely damaged state)

6.2.2.3. Test Matrix: Viscoplastic Creep and Stress Relaxation Properties as a Function of Fatigue Damage

As-fabricated TMM SAC305 joints are subjected to isothermal mechanical cycling loads of the highest intensity until the solder reaches a damage state of 0.5 load drop. These joints are subsequently tested under creep and stress relaxation loads (Table 6-3).

Test Type	Test Conditions	Load Levels		
Isothermal Mechanical Cycling	25°C, 5.5E-2 s^{-1}, 0.5 (Temperature, Strain Rate, Load Drop)	-10 to +10 μm (Cyclic Deformation Range)		
Creep	25°C	5 MPa	8 MPa	10 MPa
Stress Relaxation	25°C	10-12 MPa	13-16 MPa	22MPa

Table 6-3: Test matrix for characterizing the creep and stress relaxation behavior of microscale SAC305 solder as a function of cyclic damage

6.2.3. Phenomenological Damage Model for Degradation in Constitutive Properties

A study is conducted to explore whether the constitutive degradation measured in the test matrices described in Section 6.2.2.2 above can be described in terms of the measured cyclic load drop (Figure 6-3), using a continuum damage mechanics (CDM) model based on Kachanov's linear damage degradation theory [232]. The use of load drop for the damage metric was first proposed by Haswell [104] for accounting for the instantaneous load bearing area of the TMM joint.

This model was later improvised to account for the softening in mechanical properties [232] and utilized in the study of [231]. Equation 6.7 shows the proposed CDM equation for the degradation in shear elastic modulus, where G_0 refers to the initial shear modulus in as-fabricated undamaged state, and the damage state variable D is the cyclic load drop. The equations for C_p, n, σ_y follow similar relations.

$$G=G_0 * (1-D); \quad \text{Equation 6.7}$$

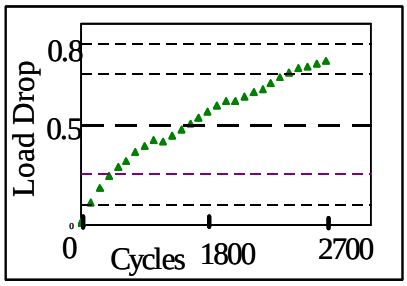

Figure 6-3: Load drop history in an ISR controlled mechanical fatigue tests (25°C, 5.5E-2 s^{-1} strain rate, and 5.5 E-2 strain amplitude)

6.3. RESULTS: VISCOPLASTIC RESPONSE

The fatigue results are presented first followed by the evolution of the constitutive properties and the microstructure with increasing fatigue damage accumulation in the solder. The effect of isothermal aging loads on the fatigue behavior of microscale SAC305 is investigated next. The fatigue behavior of as-fabricated microscale SAC305 solder specimens is compared with that of near eutectic SAC396 and Sn37Pb specimens with similar aging and fabrication history from prior studies [95, 104].

6.3.1. Effect of Cyclic Fatigue Damage on the Mechanical Properties and Microstructure

Isothermal mechanical fatigue durability of SAC305 solder and the effect of such fatigue damage accumulation on the constitutive properties and microstructure (damage and Sn grain features) of SAC305 solder joints are investigated here.

6.3.1.1.Isothermal Mechanical Fatigue Properties at Various Load Drop Criteria

The results of the isothermal room temperature mechanical durability tests of microscale SAC305 solder specimens are presented here. The fatigue S-N curves for SAC305 solder based on failure criterion of 50% load drop are presented in Figure 6-4 using both ISR and W as damage metrics. The power-law constants from Equation 6.1, derived for SAC305 solder alloy for both W-based and ISR-based fatigue data, are listed in Table 6-4. The fatigue exponent (n) obtained from this study for the ISR based fatigue curve of SAC305 is -0.495. In comparison, Kariya et al. [151] report an exponent of -0.55. The test specimen used by Kariya is approximately thrice as large as this study, with a width of 500 μm. Comparison with other reports on isothermal mechanical fatigue is not feasible since most other researchers report results from bulk specimens with non-representative microstructures and some do not report fatigue constants.

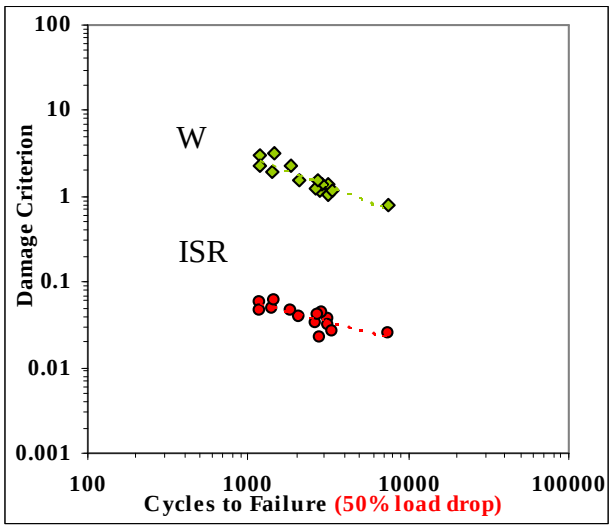

Figure 6-4: Low-creep (25°C, 5.5E-2 s^{-1} strain rate) cyclic fatigue S-N curves for SAC305 alloy (failure criterion is 50% load drop)

An interesting observation is that the fatigue data based on 50% load drop does not show as much variability and scatter as that observed in monotonic creep and stress relaxation measurements from similar microscale TMM SAC305 specimens. In both the fatigue and constitutive property testing, the specimens were in as-fabricated state at the start of testing. This is an important observation because the scatter observed in the initial monotonic properties was attributed to the highly non-homogeneous and coarse grain structure (Figure 6-11) shown earlier in Section 3.3.2 of Chapter 3. The lack of similar scatter in cyclic results could be indicative of microstructural refinement and recrystallization during mechanical cycling, leading to greater statistical homogeneity in the joints, and will be explored further in Section 6.3.1.1 and Section 6.3.1.3 below. The scatter in the durability data is somewhat less (higher R^2 value) in the W-based curves than in the ISR-based curves.

In order to understand the minimal scatter in the final fatigue properties (at load drop of 50%), the evolution of scatter in the fatigue properties from the initial as-fabricated state up to 50% load drop is investigated. Fatigue curves are plotted at increasing load drop levels between 10% and 50%, and the power-law Coffin-Manson model of equation 6.1 is used to describe the data (Figure 6-5). The durability coefficient (C), durability exponent (n) and the goodness of fit (R^2) are tabulated in Table 6-4 and plotted in Figure 6-6.

Figure 6-6 shows that there is significant scatter in the durability curves at 10% load drop (as expected) which gradually diminishes with increasing damage (increasing load drop), until about 40% load drop. This reduction in scatter is consistent with the hypothesis that the highly non-homogeneous as-reflowed

microstructure may be evolving and recrystallizing to a more homogeneous and refined form, during the mechanical cycling and fatigue damage accumulation. The damage criterion W is found to provide a better fit than ISR, to the durability data.

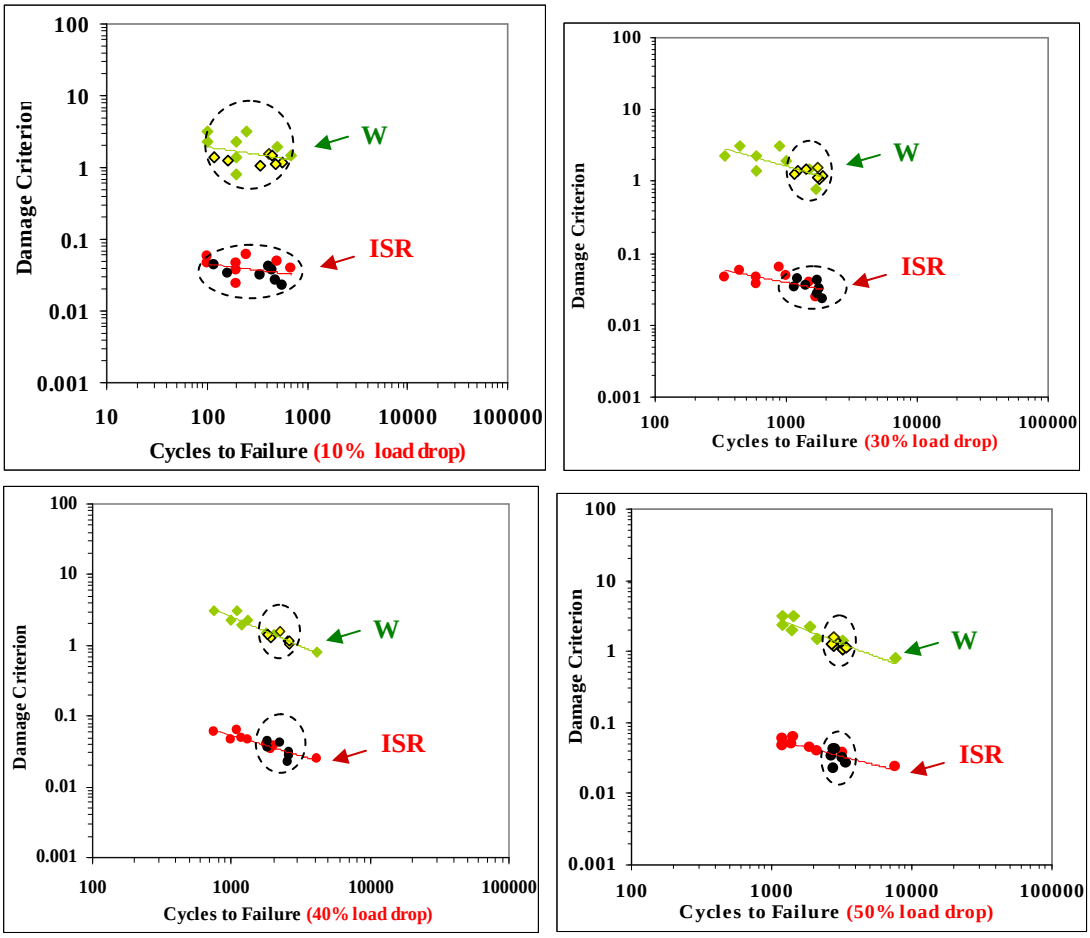

Figure 6-5: Evolution of scatter in fatigue S-N Curves as a function of load drop (dotted circles around yellow and black filled data points represent tests at identical displacement cycling loads)

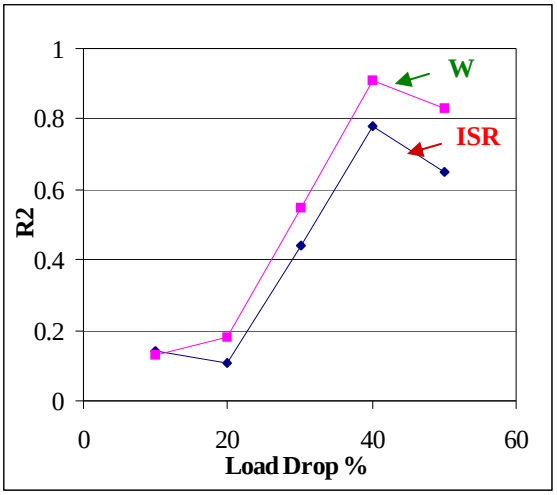

Figure 6-6: Goodness of fit (R^2 value) of the power-law fatigue models, as a function of load drop

	ISR			W		
Φ (%)	**C**	**n**	**R^2**	**C**	**n**	**R^2**
50	1.84	-0.50	0.65	472	-0.73	0.83
40	3.120	-0.59	0.78	781	-0.83	0.91
30	0.46	-0.36	0.44	61	-0.52	0.55
20	0.1	-0.15	0.11	8	-0.25	0.18
10	0.1	-0.18	0.14	5	-0.21	0.13

Table 6-4: Fatigue constants of SAC305 as a function of load drop

6.3.1.2. Evolution of Constitutive Properties

The effect of accumulated fatigue damage on the monotonic elastic, plastic, yield, and viscoplastic constitutive behavior are reported here. Furthermore, the measured evolution of the constitutive data is compared to the CDM damage model of Equation 6.7.

6.3.1.2.1. Elastic, Plastic and Yield Properties

The evolution of the inelastic stress-strain response and yield strength, as a function of cyclic fatigue damage is reported here. The evolution of the elastic-plastic behavior is compared to the CDM damage model of Equation 6.7. All results presented here are in terms of shear behavior. Results show that the creep contribution to the inelastic stress-strain curve is relatively insignificant at the test conditions reported in this study (Appendix 6.3). Hence the error introduced by using the total strain in place of the elastic-plastic strain is negligible, when plotting the inelastic stress-strain curves.

Based on these results, the shear elastic modulus (G), plastic coefficient (C_p) and yield strength (τ_o) (Figure 6-7, Figure 6-8 and Figure 6-9) are found to monotonically decrease with increasing fatigue damage, for any given load condition. In contrast, the plastic exponent (n_p) does not show any monotonic trend with damage. Furthermore the variation in 'n_p' is found to be negligible as a function of damage and across samples tested at identical load conditions. Hence the plastic exponent can be assumed to be invariant with damage for modeling purposes. As expected, the rate of degradation of the mechanical properties is proportional to the intensity of the displacement amplitude of the fatigue loading. The intensity of the fatigue load is represented by the work density (W) in Figure 6-7, Figure 6-8 and Figure 6-9**.**

An important observation is that the yield stress (τ_o) in the loading cycle is the same as in the unloading cycle, thereby suggesting that the SAC305 solder follows a hardening rule similar to an independent hardening law but only in the initial cycle

[234]. The measured hardening behavior is different from the isotropic or kinematic hardening laws traditionally used to model SAC solders [95, 104, 231].

The shear modulus measured from the current test measurements (~3 GPa, see Appendix 6.4) are significantly lower than those reported in literature (~45 GPa) [98, 100-101, 235]. This arises because the strain rates used (and achievable) in the current test methodology are lower than the acoustic level strain rates typically used for measuring elastic modulus. Similar magnitudes of modulii were reported by Zhang and Haswell [95, 104] using the same test methodology for near eutectic SAC387.

An important aspect of the elastic-plastic stress-strain measurements is that significant piece-to-piece variability exists in the properties in the initial undamaged state (indicated by circles in Figure 6-7, Figure 6-8 and Figure 6-9). For example, the normalized modulus measurements plot in Figure 6-8 shows that the deviation in properties can be as high as 60%. The upper and lower bounds of the data are shown in these figures. The scatter is comparable to that observed in the viscoplastic secondary creep properties of pristine, undamaged solder specimens.

The scatter is believed to be due to the very low number of highly anisotropic Sn grains in the TMM specimen reported in Chapter 3. Another interesting observation is that, with increasing fatigue damage, the piece to piece variability in the modulus diminishes, possibly due to homogenization of the microstructure caused by recrystallization. However the scatter is not negligible, as in the case of the final fatigue durability constants. The extent of variability in the properties measured in samples at identical test loads is discussed in detail in Appendix 6.4.

The prediction of the CDM damage model described in Section 6.2.3 is included in Figure 6-7, Figure 6-8 and Figure 6-9**.** The results show that the damage model does a reasonable job of predicting the damage degradation up to 25% of the failure life of most specimens but fails past this point. Possible reasons include a combination of data post-processing limitations and non-homogeneous damage distributions past this point (Appendix 6.5).

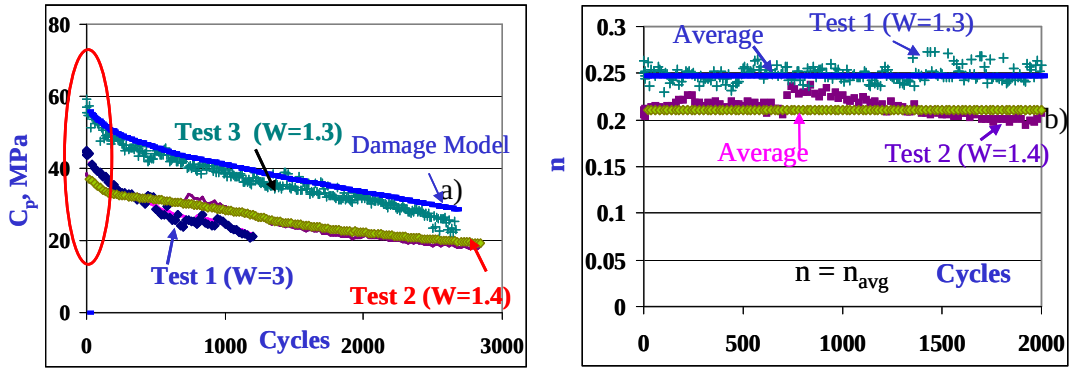

Figure 6-7: Evolution of plastic properties, (a) C_p and (b) n as a function of damage. Work density W (mJ/mm^3) represents the severity of the fatigue load

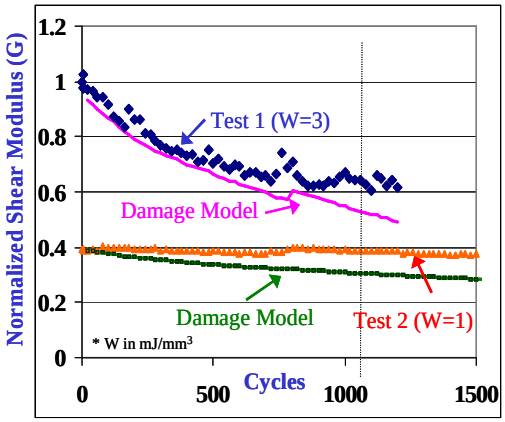

Figure 6-8: Elastic properties as a function of fatigue damage. Work density W (mJ/mm^3) represents the severity of the fatigue load

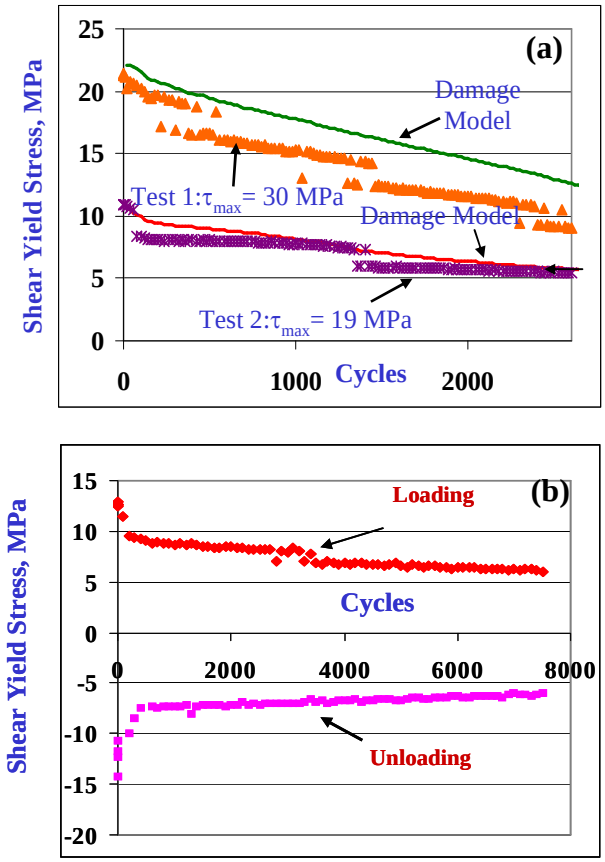

Figure 6-9: (a) Yield Stress in loading cycle as a function of fatigue damage (range of scatter), (b) Yield stress in loading and unloading cycles as a function of fatigue damage

6.3.1.2.2. Viscoplastic Properties as a Function of Fatigue: Creep and Stress Relaxation

Softening and degradation of the effective creep resistance of SAC305 solder with increasing cyclic fatigue damage is presented here. Creep measurements conducted on as-fabricated solder specimens show that although the effective creep resistance of SAC305 specimens is initially much higher than that of Sn37Pb specimens, after cyclic fatigue the creep resistance is much lower (even less than that of undamaged Sn37Pb specimens). Similarly stress relaxation measurements reported in Section

5.3.1 of Chapter 5 shows that the magnitude and rate of stress relaxation in as-fabricated SAC305 is much lower than that of Sn37Pb. Stress relaxation of undamaged SAC305 does not catch up with Sn37Pb even past 3 hours at 125°C (Table 5-6 and Figure 5-8). However, measurements on cycled SAC305 solder show that with prior mechanical fatigue damage, the effective relaxation rate of fatigued SAC305 increases so much that it is comparable to that of undamaged Sn37Pb solder.

a)

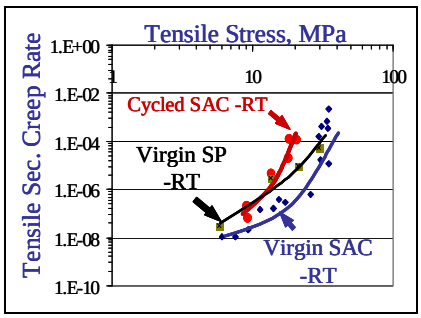

b)

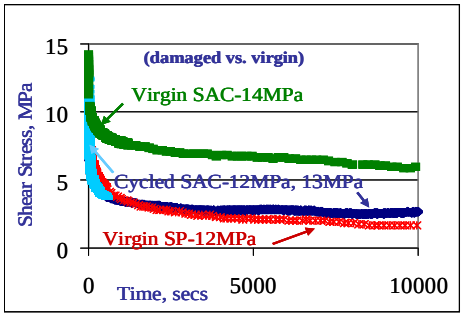

Figure 6-10: (a) Creep and (b) Stress relaxation measurements as a function of cyclic fatigue damage. Measurements conducted on specimens stressed to 50% load drop (Table 6-3)

6.3.1.3. Evolution of Sn Grain Microstructure

The microstructural analysis of as-fabricated pristine (unstressed and undamaged) microscale SAC305 solder joints from Section 3.3.2 of Chapter 3 is included for understanding the microstructural evolution after mechanical fatigue. Typical TMM specimens seem to exhibit around 2-5 grains of around 180 µm width (at most 3mm length). The non-homogeneous structure in the as-fabricated specimen is shown in Figure 6-11. The as-fabricated microstructure of TMM specimens is representative of that in as-fabricated functional solder joints in electronic packages.

Figure 6-11: OIM Images of as-fabricated TMM joint showing 5 Sn grains across the length of the joint

The final microstructure that these non-homogeneous joints achieve under mechanical fatigue at room temperature is presented next. Since the focus of the investigation is primarily on grain refinement through recrystallization, some prior knowledge of potential recrystallization sites is required. These regions are identified by preliminary SEM analysis to identify potential failure paths and high stress concentration regions such as cracks and voids.

Regions of interest for analyzing recrystallization typically have an area of 20-150 µm x 180 µm. The SEM image of a specimen cycled to an initial maximum stress of ~20 MPa at RT is shown in Figure 6-12a. Apart from the macro-fatigue crack, Figure 6-12 b also shows the crack path in the solder which seems to be intergranular, i.e., decohesion at grain boundaries. Evident in the same figure are Sn dendrites and intermetallic particles at different locations; interlacing Sn dendrites (white particles) and bigger IMCs (grey particles).

The macro-crack is a potential site for recrystallization and the grain microstructures are analyzed in this region. Results from the focused ion beam microscopy (FIB) clearly show regions of varying crystallographic orientations in the solder after mechanical cycling (Figure 6-13a). Appendix 6.6 provides details on the FIB analysis. The contrast variation in the cycled solder seen in the FIB images could

be attributed either to the formation of new grains due to recrystallization or due to new subgrains that precede recrystallization[201].

Based on the FIB image, the sizes of these recrystallized structures vary from approximately 4µm to 40µm. The grain size decreases close to the crack boundaries, due to higher stress fields. Analysis of the size and distribution of these grain and sub-grain structures as characterized by the FIB analysis in the newly recrystallized solder is shown in Figure 6-14. The results indicate a bi-linear trend with increasing distance from the crack surface. The size reported here is the largest dimension in each grain (or sub-grain) region and the distance is from the crack to the centroid of the grain/sub-grain regions. Recrystallization leads to a maximum reduction in average grain size of around 98%. The SEM image (Figure 6-13 b) of the same region analyzed with the FIB shows discernable grain features as well (marked by grain numbers 1-2).

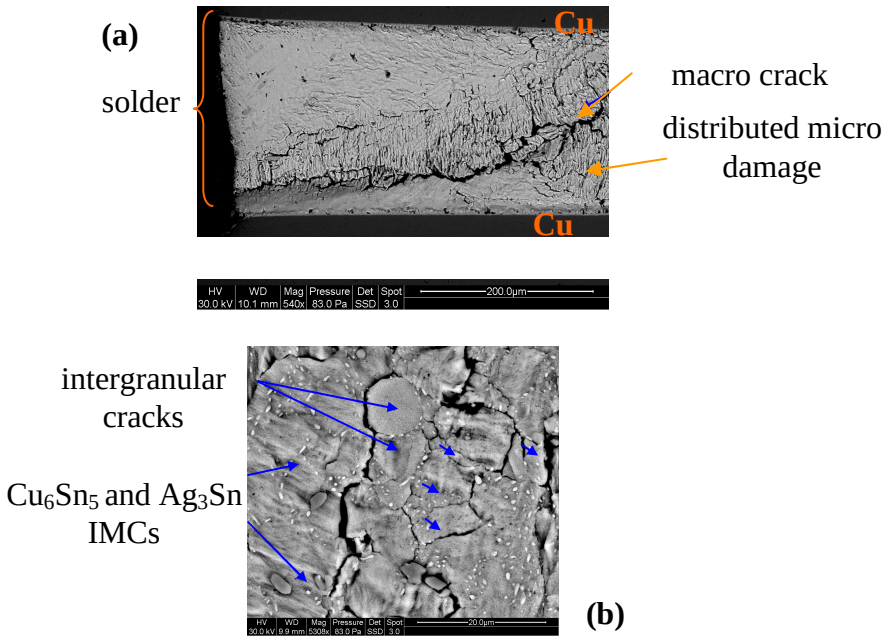

Figure 6-12: SEM images showing a) macro and micro damage b) intergranular cracks (indicated by arrows) in mechanically cycled SAC305 solder

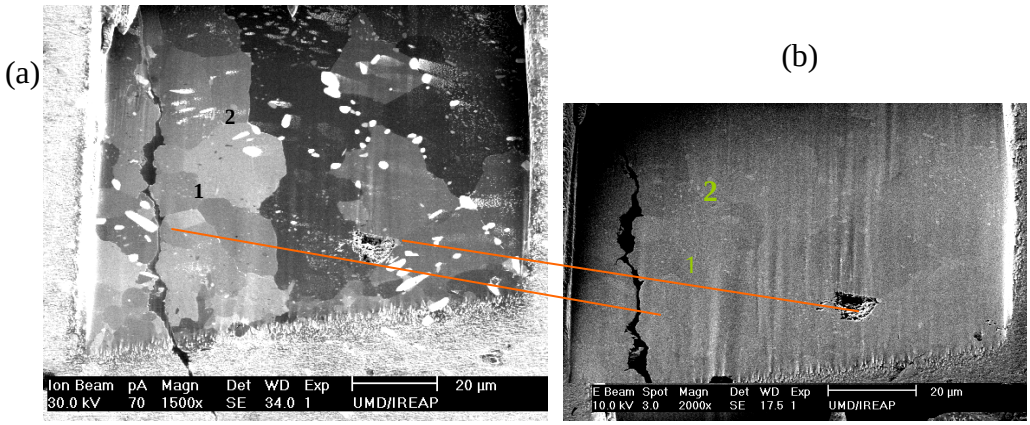

Figure 6-13: FIB cut at crack showing recrystallized grains (or sub-grains) in (a) FIB image (b) SEM image

However the biggest challenge in recognizing new grain/subgrain formation using FIB analysis is that the regions are discerned based on qualitative parameters such as the contrast variation in the image. This in turn depends on the amount of sputtering, stage alignment and surface finish, among other factors. Hence the accuracy of discerning grains and the quantitative grain size analysis conducted by this method is limited.

In spite of this drawback, an important outcome of the FIB study is that this analysis does confirm the formation of regions of new crystallographic orientations in microscale SAC305 solder joints after isothermal mechanical cycling, even at room temperature. To obtain quantitatively definitive proof of recrystallization and to distinguish between subgrains and grains, orientation imaging microscopy (OIM) is conducted on cycled TMM SAC305 specimens.

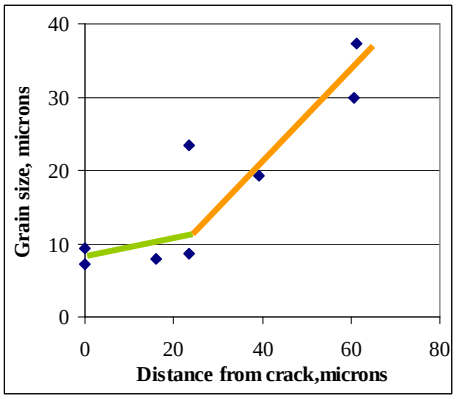

Figure 6-14: Size distribution of recrystallized regions, based on FIB analysis

Results of the OIM analysis are presented in Figure 6-15, Figure 6-16 and Figure 6-17. A step size of 1 μm is used for the mapping the grain microstructures. Dark regions in the EBSD image could potentially be regions where the crystallographic orientation data did not reach the detector owing to bad surface finish or due to the

presence of cracks and damage from cyclic mechanical testing. The crystal structures are identified as hexagonal structure for Cu_6Sn_5, orthorhombic structure for Ag_3Sn and body center tetragonal (BCT) unit cell for Sn.

Figure 6-15 and Figure 6-16 depict the subgrains and recrystallized grains around the macrocrack of a cycled specimen based on the OIM analysis. The grains and subgrains in Figure 6-16a are distinguished based on grain boundary angles. All three phases, namely the IMCs and Sn phase are included in this image. The distinction between grains and subgrains is made based on mismatch angles at boundary being greater than or less than 5° respectively [201].

The grain boundary angle and crystallographic orientation of Sn phase only are shown in Figure 6-16 a-b. As is evident from Figure 6-16 a, majority of the recrystallized grains comprise primarily of high grain angle boundaries (between 15° -180°). In addition to the individual crystallographic orientations and grain characteristics, such as grain mismatch angles at boundaries, a statistical analysis of the distribution of the dominant grain size in the region is provided by the OIM data (Figure 6-17). The dominant grain size in the analyzed region is in the 2-4 μm range and the largest grain size in the region is ~25 μm.

Hence the OIM study clearly confirms that recrystallization occurs in the microscale TMM specimen under isothermal mechanical cycling even at room temperature. This study hence validates that the TMM specimens used this study mimic not only the initial microstructure of functional solder joints used in electronic packages, but also mimic the microstructural evolution seen in functional joints under life cycle loads (e.g. thermal and power cycling, mechanical cycling due to vibration,

shock and drop). This observation improves the confidence that the measured viscoplastic and mechanical fatigue properties from the TMM microscale specimens are representative of the material behavior expected in functional solder interconnects.

Another interesting observation from the recrystallization observed under the mechanical cycling (and thermal cycling[51]) is that new grain features could significantly alter the underlying dominant creep mechanisms that dictate the SAC305 viscoplastic deformation. In the as-fabricated, pristine state, based on Ochoa's findings[11]**,** dislocation climb was expected to dominate. Furthermore, apart from the IMCs inhibiting grain boundary sliding (GBS), GBS is also possibly not feasible across the large length scale of grain boundaries shared by the few grains in the non-homogeneous microscale joint.

In the case of the cycled joint however, due to the formation of larger number of new and small grains sharing smaller grain boundaries, GBS might now be more feasible in the cycled joint. The inherent state of damage (in the form of distributed microcracking) may also possibly assist the GBS. Hence, as damage progresses, the contribution of GBS to the creep deformation could possibly increase.

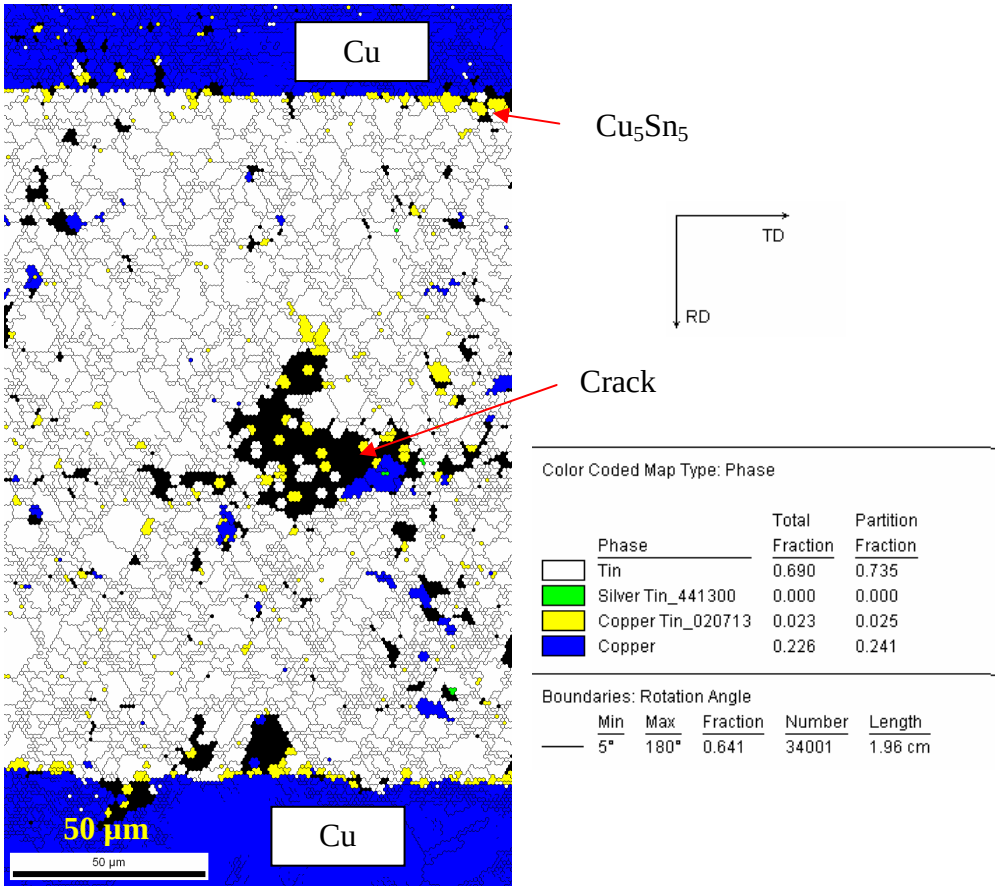

Figure 6-15: Grain boundaries of various phases of solder (Sn, Ag_3Sn, and Cu6Sn5) cross-referenced with the GB angles. Grain angle boundaries between 5° and 180° are depicted here.

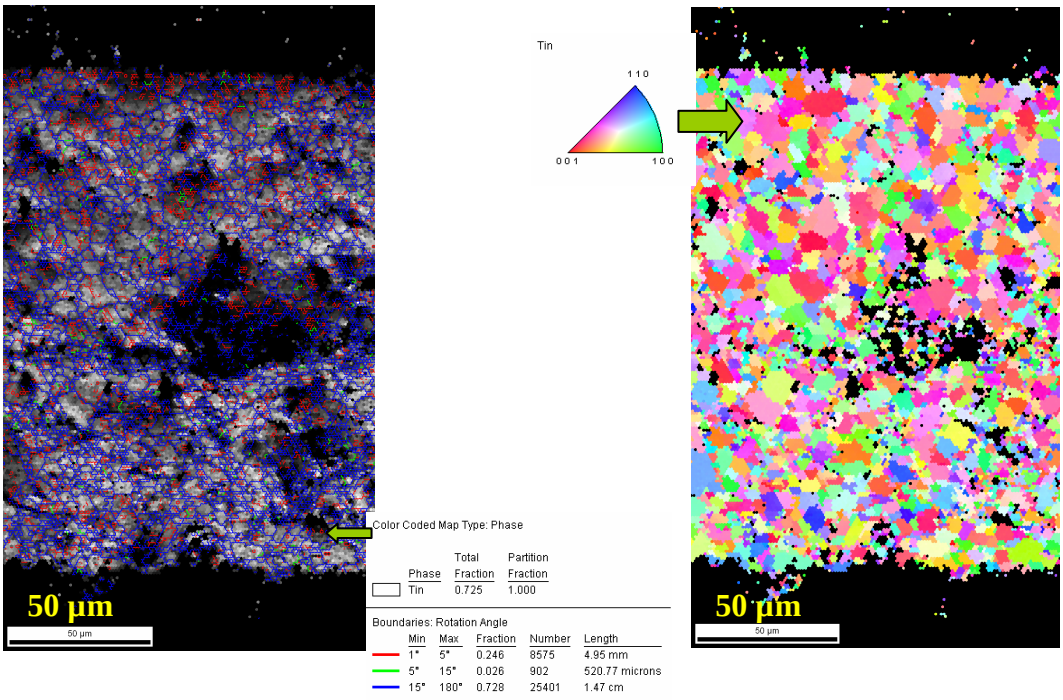

Figure 6-16: (a) Grains with low-angle grain boundaries (LGB) and high-angle grain boundaries (HGB) and subgrains of Sn distinguished based on the grain boundary angles;(b) crystallographic orientations of bct Sn grains in SAC305 cross-referenced with the unit triangle

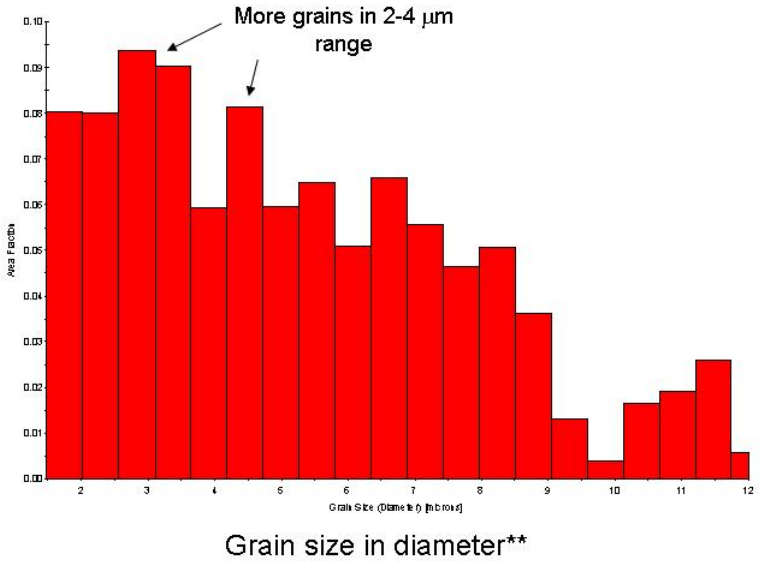

Figure 6-17: Statistical distribution of the grain sizes evident in the area of scan

6.3.2.Effect of Alloy Composition and Isothermal Aging on Mechanical Properties

The effect of isothermal room temperature aging history on the mechanical fatigue behavior of as-fabricated, unstressed microscale SAC305 solder is investigated and compared with that of similar as-fabricated SAC387 and eutectic Sn37Pb from prior studies [95, 104].

6.3.2.1. Isothermal Mechanical Fatigue Properties in As-Fabricated State: Effect of Alloy Composition

The fatigue durability of as-fabricated SAC305 solder from Section 6.3.1.1 is compared with that of near-eutectic SAC387 and eutectic Sn37Pb, under similar test conditions. Summaries of the test data and power-law fits for Sn37Pb and SAC387 are presented in Table 6-5 and in Figure 6-18 for completeness [95, 104]. SAC305 is found to be more durable than eutectic Sn37Pb, but not as durable as the near-eutectic SAC387. The difference in durability of the solders is more visible in the W-based plots. All the solder alloy results are based on test results from identical specimen configurations, pre-aging protocols and test procedures.

Damage Criterion, D	Sn3.0Ag0.5Cu		Sn3.8Ag0.7Cu		Sn63Pb37	
	C, n	R^2	C, n	R^2	C, n	R^2
ISR	1.84, -0.497	0.65	2.37, -0.492	0.92	0.67, -0.428	0.99
Work	472, -0.729	0.83	201.2, -0.575	0.96	88.8, -0.56	0.99

Table 6-5: Power-law durability parameters using W and ISR damage criterion, of SAC305, near-eutectic SAC387 and eutectic Sn37Pb

Microstructural investigations and the underlying damage progression mechanisms in SAC alloys with varying Ag content are useful in understanding the reasons behind the observed drop in durability with Ag content. Since Pb-free solders are dispersion-strengthened materials, dislocation pinning and climb at nanoscale IMCs and other obstacles is expected to dominate. Kerr et al. investigated creep mechanisms in Sn3.5Ag solders and found evidence of pinning of dislocations by Ag_3Sn particles as a dominant cause of creep resistance. Increasing Ag content in SAC is found to decrease the interparticle separation between nano-scale Ag_3Sn intermetallics in eutectic regions[15]. Thus with increasing Ag% the mean free path for dislocation motion between pinning at obstacles is decreased thereby leading to increased creep resistance.

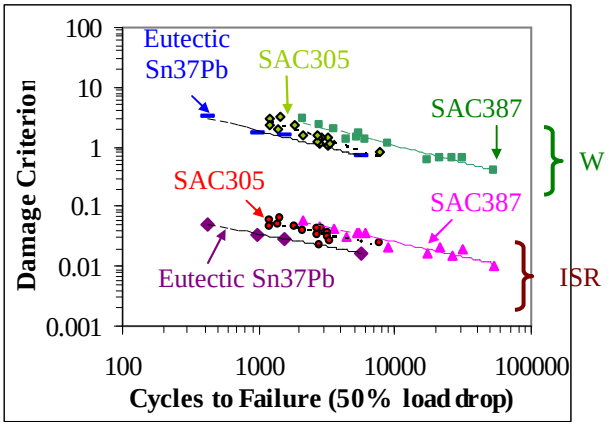

Figure 6-18: Comparison of creep-minimized (25°C, 5.5E-2 s^{-1} strain rate) cyclic data; hypoeutectic SAC305, near- eutectic SAC387 [95, 104] and eutectic Sn37Pb alloy[104]

This leads to higher creep resistance and thereby a better fatigue resistance for the near-eutectic SAC387 compared to the hypoeutectic SAC305. This trend was also seen in thermal cycling fatigue (which corresponds to high creep loading condition)

of SnAgCu solders with varying Ag content by Terashima [15] and Nurmi[13]. The dominant creep mechanism in Sn37Pb is known to be grain boundary sliding. Due to the lack of intermetallic particles to pin the mobile dislocations and restrict grain boundary sliding, Sn37Pb solder undergoes higher creep deformation than SnAgCu solders. This could be one possible explanation for the observed improved durability of the SAC305 and SAC387 solders compared to Sn37Pb solder.

6.3.2.2. Isothermal Mechanical Fatigue Properties under Isothermal Aging

The effect of storage-induced aging on mechanical durability of SAC305 is explored in this section using additional aging protocols described earlier in Section 6.2.1.2. Fatigue test measurements show that room temperature aging significantly reduces the mechanical durability of the solder. The work-based (W) damage criterion shows a much more significant drop than ISR-based damage criterion (Figure 6-19). Table 6-6 lists the ISR-based and W-based fatigue constants for these additionally aged solder specimens. Although the overall trends are quite unambiguous, further testing and microstructural studies would help quantify the precise statistical significance of these results.

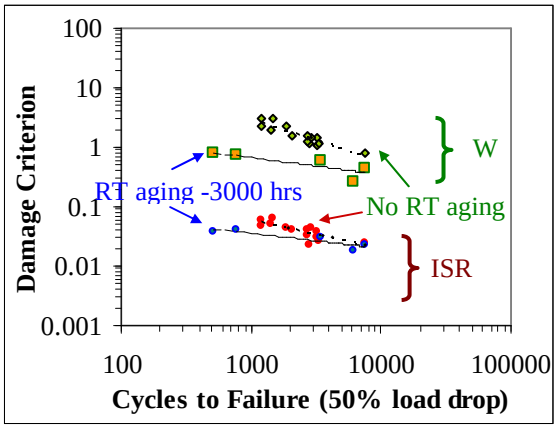

Figure 6-19: Effect of aging at room temperature on durability under low creep loading (25°C, 5.5E-2 s^{-1} strain rate) for SAC305

Damage Criterion, D	No RT aging		3000 hours RT aging	
	C, n	R2	C, n	R2
ISR	1.84, -0.497	0.65	0.21, -0.257	0.83
Work	472, -0.729	0.83	4.96, -0.289	0.65

Table 6-6: Power law constants of ISR and W-based damage curves at 50% load drop for low creep loading (25°C, 5.5E-2 s^{-1} strain rate) for SAC305 as a function of RT aging

Studies in literature show that additional isothermal aging causes increased dendrite size, increased volume fraction and size of the intermetallics in the bulk of the solder, and increased thickness of intermetallics at the solder interface with the bond pad at RT [52]. Hence, while intermetallic addition to the softer Sn matrix does increase the stiffness of the solder, a significant increase in the intermetallic volume fraction (as seen in the aged specimens) can also lead to embrittlement [51]. Furthermore as the nanoscale IMC sizes and mean-free separation increase, the extent

of dispersion strengthening decreases via dislocation pinning and climb. The loss of dispersion strengthening capability (leading to increased creep damage) and the loss of the ductility (leading to increased crack propagation rates), thus effectively degrade fatigue resistance.

Post-failure analyses of the SAC305 mechanical durability test specimens as a function of room temperature aging are shown in Figure 6-20. Failure images of the aged specimens at all load levels tested show that the failure mode is predominantly closer to interface intermetallic (Figure 6-20 b). Macrocracks were found in the bulk of the solder along with large amount of solder-copper interface cracking. Shear bands and micro-cracks were also found to surround the macro-crack.

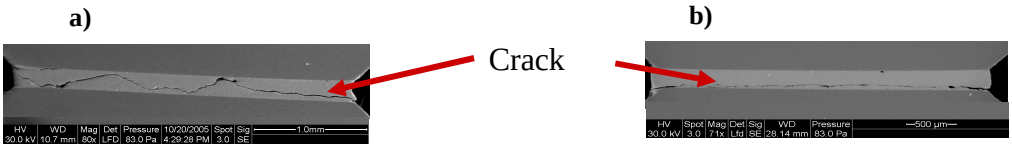

Figure 6-20: Post-failure images of hypoeutectic Sn3.0Ag0.5Cu specimens: (a) fatigue crack far away from IMC interface in joints without RT aging and (b) fatigue crack close to interface IMC in joints with 3000 hrs of RT aging

6.3.3. Discussion of Experimental Results

Microscale SAC305 solder exhibits significant anisotropy in the mechanical behavior in the as-fabricated state, due to the coarse-grained Sn microstructure and the anisotropy of single crystal Sn. The grain microstructure attains a much more homogenous fine-grain state owing to the formation of several recrystallized grains under creep and mechanical fatigue loads. The extent of homogenization of Sn grains microstructure is particularly stronger under fatigue loads. Hence the admissibility of utilizing the as-fabricated mechanical properties for modeling the behavior of solder

throughout the entire service life is questionable. Furthermore the use of undamaged properties provides non-conservative estimates of mechanical response of solder. Hence modeling the material behavior with evolving constitutive properties as a function of damage (where available) is recommended.

An important observation in the fatigued solder microstructure is that the degradation of the mechanical response is initially due to distributed micro-damage, but is eventually due to a combination of macro-cracks and microdamage (structural damage as seen in Figure 6-21) and evolving coherent grain microstructure (Figure 6-16). Hence, evaluating the effective load-bearing area (and corresponding true stress) as a function of increasing structural damage pose significant challenges. The current study presents average effective behavior of the specimen, assuming that the initial undamaged load bearing area remains unchanged. Studies focusing on evaluating the effective area are hence necessary, in order to accurately assess and isolate the contributions of structural macro-damage deformation from that of evolving grain microstructure, and distributed micro-damage, which should be the focus of future studies.

Following on the same note, the elastic-plastic properties as a function of damage are obtained by isolating the contributions of the creep deformation from the total strain-stress loops. However the creep constants used here are those measured from as-fabricated joints and do not include the effect of evolving grain features and damage with continued cyclic loading. Thus the elastic-plastic strains evaluated based on the as-fabricated solder properties are expected to be higher than that in reality and need to be updated using creep properties as a function of damage.

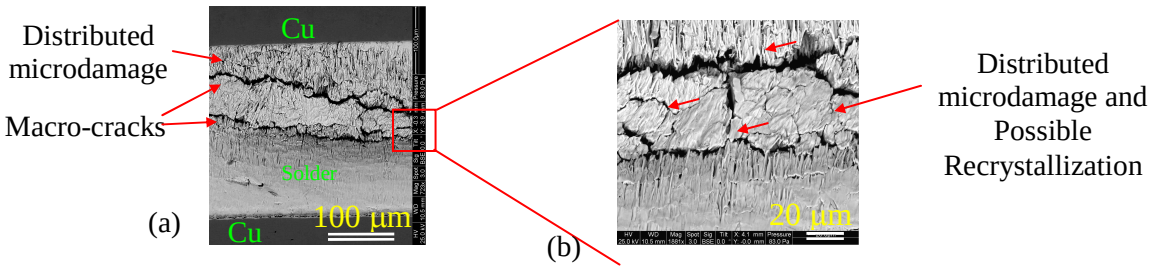

Figure 6-21: TMM SAC305 solder joint showing (a) macrocracks, (b) microdamage, due to mechanical fatigue

6.4. SUMMARY AND CONCLUSIONS

The evolution of the constitutive and the microstructure of microscale SAC305 solder specimens as a function of loading histories is investigated. The loads considered include cyclic fatigue damage in the presence of different amounts of isothermal aging. The test measurements show that the scatter previously reported in the measured initial creep response of undamaged SAC305 specimens is also observed in the initial elastic-plastic response, yield strength. The properties degrade with increasing cyclic fatigue damage and the rate of degradation is proportional to the load severity.

The scatter is also seen to decrease with increasing fatigue damage. In particular, the final fatigue properties exhibit negligible scatter. Microstructural investigations reveal that the coarse-grained Sn microstructure exhibited by the microscale SAC305 joints evolve into a much more homogenized fine-grained microstructure due to the formation of several hundreds of small (2 - 4 μm) , recrystallized Sn grains around regions of high deformation gradients and stress concentrations, e.g. around macrocracks. The chosen TMM microscale solder specimens are hence seen to

mimic the microstructural evolution (and hence mechanical behavior evolution) of functional solder joints in the as-fabricated state and under service conditions.

The isothermal fatigue properties of as-fabricated SAC305 solder are seen to degrade with additional isothermal room temperature aging. However, even after 3000 hrs of aging at room temperature, SAC305 solder is still found to be more durable than as-fabricated eutectic Sn37Pb solder. Results of yield strength measurements under reversed loading suggest that SAC305 solder follows hardening rules different from the isotropic or kinematic hardening rules that are traditionally used for modeling SAC solder behavior. CDM modeling does a reasonable job of describing the degradation of elastic, plastic and yield behavior, as a function of mechanical cycling. After substantial cyclic damage (50% load drop) the effective average creep and stress relaxation behavior of SAC305 becomes comparable to those of as-fabricated, undamaged Sn37Pb. Further studies are required to refine this conclusion, by considering the effect of growing macro-cracks on the evolution of the effective load bearing area of the TMM specimen.

Chapter 7: Summary and Conclusions

Based on the current state-of-the-art of the constitutive and fatigue behavior of microscale Pb-free SAC solders, this dissertation focused on four critical unresolved research issues, that would enhance our understanding of these solder alloys. The four critical issues are:

1. Do microscale SAC305 joints indeed exhibit non-homogeneous microstructure (lack of statistical homogeneity) in the as-fabricated state? If so, what effect does this non-homogeneous microstructure have on the mechanical viscoplastic constitutive behavior and what is the magnitude of the variability exhibited by these joints under identical loading conditions? Can the constitutive response be characterized with conventional continuum-scale, phenomenological models?
2. If the microstructure is non-homogeneous (in the as-fabricated state), does this piece-to-piece variability exist just in the as-fabricated state or in the fatigue damaged state as well under isothermal mechanical cycling? Is there a microstructural explanation for the observed evolution of mechanical properties? How do the viscoplastic constitutive properties evolve with isothermal cyclic mechanical loading and can this evolution be characterized with damage models based on continuum damage mechanics?
3. Is there a mechanistic microscale model that could capture the influence of key microstructural features on the physics and mechanics of the dominant viscoplastic creep mechanisms?

4. What is the accuracy of macroscale phenomenological models measured from constant force tests (creep) on the non-homogenous microscale SAC305 joints in predicting the measured stress relaxation behavior of the same joints?

The conclusions of these investigations are presented next in the sequence of the chapter presentation.

1. Constitutive creep behavior of as-fabricated microscale SAC solders
    i. Microscale as-fabricated SAC solder test specimens used in this study do exhibit significant piece-to-piece variability under identical loading conditions in the measured monotonic elastic, plastic and creep behavior. The variability is more significant in the creep behavior compared to the elastic and plastic behavior.
    ii. The primary creep behavior exhibits significantly higher (orders of magnitude) variability than the secondary creep rate (factor of two). In particular, the saturated primary creep strain exhibits more scatter compared to the rate of decay to the saturated regime of the primary creep.
    iii. The observed scatter in creep behavior is expected since these joints lack statistical homogeneity and comprise of a non-repeatable, coarse-grained microstructure of anisotropic Sn in the as-fabricated state. The grain configurations vary between one to at most seven grains across the entire length of the TMM specimen. The microstructural features exhibited by the TMM test specimens are representative of those seen in functional microscale SAC joints.

iv. For the grain configurations and loads studied, the Sn grain microstructure in the microscale SAC305 specimens heavily influences the primary creep behavior compared to the secondary creep behavior. The variability in the primary creep behavior is high as a factor of 100. In comparison the secondary creep behavior varies by a factor of 2-3 (similar to the elastic-plastic curves) in specimens tested under identical conditions.

v. The secondary creep rate is very sensitive to stress levels above 15 MPa. This increase in the stress sensitivity and the associated increase in the scatter predominantly evident in this region are probably indicative of a change in the creep mechanism. Measurement accuracy in this high stress-sensitivity region is limited by the current experimental technique which could be a possible contributor for the magnification of the scatter.

vi. For the grain configurations obtained in this study, the specimen with the single Sn grain across the entire length exhibits superior creep resistance compared to the multi-grained configurations. However further statistical evidence is required to conclude that single grained configurations are the optimal grain configurations for improved mechanical properties. This aspect is further discussed in the limitations and future work (Chapter 8)

vii. Sn grains with misorientation angles in excess of 30° show significant damage (in the form of out-of-plane steps) at the grain boundaries in the post – creep and fatigue state.

viii. The coarse-grained microstructure of the as-fabricated microscale SAC305 specimen undergoes recrystallization during creep deformation. The creep

tested samples show new grains with their principal axes oriented at 45° to the loading direction. However since the dimensions of the recrystallized grains are large, the specimens still exhibit a coarse-grained, non-homogenous microstructure.

ix. In spite of the variability exhibited by the microscale SAC305 specimens; the creep resistance is higher than that of microscale eutectic Sn37Pb specimens. A decrease in Ag content decreases the creep resistance of SAC305 relative to near-eutectic SAC387. The creep measurements exhibited by microscale SAC305 specimen are higher than (or comparable to) those reported by other investigators.

x. The macroscale phenomenological models based on continuum mechanics (e.g. Garofalo model or multi-term Weertman model) capture only the average behavior of the measured creep response of the microscale non-homogenous joints. Both the primary and secondary creep constants are provided.

xi. The measured macroscale creep model constants suggest that dislocation climb assisted by core diffusion is the dominant mechanism in SAC alloys. These conclusions are consistent with those reported in literature.

xii. Microscale Sn37Pb specimens tested using the same test methodology and protocols however exhibit homogenous microstructure and lower specimen to specimen variability than SAC305 specimens due to the presence of a large number of small Sn (and Pb) grains. Thus the fine-grained

microstructure demonstrates much more uniform response across the entire test matrix compared to the coarse grained microstructure.

2. Macroscale modeling: creep versus stress relaxation behavior

   i. Stress relaxation behavior of microscale SAC305 specimens exhibits joint dependent behavior. However the variability if not as significant as that seen in the secondary creep behavior. The variability is prominent in the initial stages of the relaxation history similar to the primary creep behavior region of the creep history.

   ii. FE results, utilizing the macroscale continuum creep models that are calibrated to the non-homogenous creep response of microscale SAC specimens, suggest that the viscoplastic stress relaxation response to constant-displacement tests can be captured using the creep constants obtained from constant-force tests.

   iii. If the measured upper and lower bounds of the creep constants are used in the stress relaxation FEA, then the measured relaxation curves do fall within the predicted bounds for RT and 75°C. However, further testing is required to improve this conclusion and is discussed in Chapter 8.

   iv. The prediction based on the upper bound (and in some cases the average fit) overestimate the extent of the measured stress relaxation. This occurs since the bounds are estimated from the scatter exhibited by the data across the entire stress range and not from individual load levels.

   v. The limit analysis shows that the creep constants based on lower bounds/average behavior are best suited for predicting the stress relaxation

measurements at room temperature. In contrast, the lower bound creep constants appear to be more suitable for the 75°C stress relaxation data.

vi. Inclusion of primary creep models for representing the solder behavior increases the extent and rate of stress relaxation.

vii. Modeling the solder behavior using only secondary creep models (in addition to elastic and plastic models) provides a better correlation between the modeling predictions and measured stress relaxation behavior. Hence the inclusion of primary creep to secondary creep behavior can be avoided.

viii. SAC305 relaxes at a slower rate and reaches a higher stress level than that of microscale Sn37Pb specimens. In particular, Sn37Pb relaxes to close to 10% stress within 10 minutes and SAC305 does not reach the same relaxation even past 3 hours. This study hence suggests that if stress relaxation is taken as the metric for designing the dwell in SAC solders, traditionally used 15 minute dwell time for Sn37P is not a feasible option

ix. The guidelines developed for estimating the optimal dwell time to be used in accelerated thermal cycling of functional SAC BGA joints suggest that the time could be as low as 15 minutes if acceleration factors are used as the criterion, and as high as 3 hours if stress relaxation is used as the criterion. These results are based on modeling the solder using secondary creep behavior only. Hence these results serve as conservative estimates.

3. Microscale modeling of secondary creep behavior

i. Microscale viscoplastic constitutive model, based on the athermal detachment of dislocation climb and effective medium homogenization, captures the sensitivity of the secondary creep deformation to the intermetallic and Sn dendrite configurations reasonably well. When calibrated to properties in the eutectic Sn-Ag regions, the calibrated model has the potential to predict the effect of varying alloy compositions of SAC and thermal aging on the secondary creep response.

ii. The contributions of the soft Sn dendrites and microscale Cu_6Sn_5 IMC reinforcements to the overall secondary creep resistance of SAC solders is less significant compared to that of the eutectic Sn-Ag regions with the nanoscale Ag_3Sn dispersions. Higher volume fractions and smaller sizes of nanoscale Ag_3Sn are seen to be beneficial to the creep strength of SAC.

iii. The creep resistance increases with decreasing nano-scale IMC size, increasing volume fractions of nano-scale IMCs, increasing k, decreasing dislocation densities, and decreasing volume fractions of dendrites.

iv. The model can provide estimates of the amount of drop in creep resistance with decreasing Ag content.

v. Garofalo secondary creep model constants are provided based on the micromodel predictions as a function of % Ag in SAC and aging.

4. Evolution of properties and microstructure as a function of isothermal mechanical fatigue damage

i. Significant scatter is exhibited by the elastic and plastic properties and the hysteresis curves of the as-fabricated microscale SAC305 specimens.

ii. The fatigue S-N curves however exhibit negligible scatter in the measured damage versus cycles to failure. The conclusion is based on a commonly used failure criterion of 50% load drop.

iii. However, fatigue curves using failure criteria of 10%-40% load drop reveal that significant scatter exists in the load drop rates measured during the initial stages of the fatigue damage accumulation (0%-30%). The scatter gradually decreases to insignificant amounts beyond load drops of 40%. The evolution of the measured elastic and plastic properties and the hysteresis stress-strain curves also suggest that scatter decreases with increasing fatigue damage (as quantified by load drop).

iv. Microstructural insights point towards the homogenization of the coarse-grained Sn (~ 180 μm length scale) microstructure to a homogeneous fine grained (~ 10 μm length scale) recrystallized state at high stress concentration regions (such as macrocracks and distributed microcracks, shear bands, IMCs, interface of solder and Cu_6Sn_5 interfacial IMC and GBs in the as-fabricated coarse-grained solder). The observed recrystallization and decrease in variability in fatigue properties suggests that the transition from coarse grained to a homogenized microstructure is a possible explanation to the reduction in scatter with increasing damage. This recrystallization agrees with observations reported under other cyclic loads like temperature cycling, power cycling, vibration, and repetitive drop.

v. The constitutive properties are seen to degrade (softening) as a function of increasing fatigue damage.

vi. The CDM model available in literature does a reasonable job in capturing the degradation in the elastic and plastic properties as a function of fatigue damage up to 25% of the fatigue life of most specimens. Possible reasons for the deviation past this point is due to (i) evolving material damage in the form of macro and micro damage (discussed in the future work) and (ii) reduction in the available data (acquired) per cycle (smaller hysteresis loops) with increasing damage.

vii. Creep strains do not contribute significantly to the total strain measured in the isothermal mechanical cycling tests conducted at 5.5E-2 strain rate at room temperature.

viii. Microscale SAC305 specimens exhibit hardening yield behavior different from that of isotropic and kinematic hardening, that are routinely used to model solder behavior. The measured hardening behavior exhibits the same yield stress in the loading and unloading regimes and does not exhibit Bauschinger's effect.

ix. The effective creep resistance of SAC305 specimens is initially much higher than the initial creep resistance of Sn37Pb specimens, but drops below this level after mechanical cycling fatigue damage.

x. Similarly, prior testing shows that the magnitude and rate of stress relaxation in as-fabricated SAC305 is initially much lower than that of Sn37Pb but becomes comparable to that of as-fabricated Sn37Pb after mechanical cycling fatigue damage.

xi. Apart from the Sn grain recrystallization, significant macro and distributed micro-damage is evident in the fatigued joint. The degradation/softening effect of the material properties is hence hypothesized to be due to effects of smaller recrystallized grains and growing material damage.

xii. Isothermal mechanical fatigue resistance of microscale as-fabricated SAC305 specimens is lower than that of microscale as-fabricated SAC387 but superior to that of microscale as-fabricated Sn37Pb solder.

xiii. Thermal aging reduces the fatigue durability of SAC305 solder and SAC305 is marginally higher than that of unaged as-fabricated Sn37Pb.

Primary Conclusion

This study demonstrates that although SAC305 alloy exhibits superior viscoplastic constitutive and cyclic creep-fatigue behavior over Sn37Pb solder, their mechanical behavior is heavily dependent on the individual joint microstructure. The lack of statistical homogeneity and isotropy of its microstructure limits their superior behavior relative to Sn37Pb. The benefits of its superior properties therefore have to be considered in the context of the probability of formation of grains that are orientated favorable, relative to the loading direction under application conditions. Theoretically their utility can be enhanced if a systematic study is conducted on obtaining controlled and repeatable grain configurations (not necessarily making the joint statistically homogenous) that are oriented favorably relative to the loading in the manufactured joints under application conditions. Alternatively, for microscale applications, it may be advisable to utilize doped Pb-free solders such as Lanthanum-

doped SnAg alloys, which exhibit both superior mechanical properties and a statistically homogenous microstructure.

Chapter 8: Contributions and Future Work

The contributions and limitations of the dissertation are listed in the sequence of presentation of the chapters.

1. Constitutive creep behavior of as-fabricated microscale SAC305 specimens
   i. This study has demonstrated the ability to produce microscale SAC test specimens that have coarse-grained, non-homogeneous microstructure (lack of statistical homogeneity) similar to that observed in functional microelectronic solder interconnects.
   ii. Based on the measured mechanical behavior of the microscale test specimens, this study provides valuable insights into the extent of piece-to-piece variability that can be expected in SAC interconnects due to the non-homogenous, non-repeatable microstructure. In the same context, the fine grained homogeneous specimens (as-fabricated Sn37Pb and mechanically cycled SAC305) produce a much more homogenous behavior and lower specimen to specimen variability. Finer grain sizes (and increasing grain numbers) reduce the joint dependent behavior.
   iii. Average macroscale continuum model constants are provided based on measured viscoplastic constitutive behavior of SAC305 solder. The experimental measurements from the study provide insights into the dominant deformation creep mechanism in these joints. The scatter in the model constants due to the non-homogenous behavior of microscale SAC305 joints are provided.

iv. This is one of very few studies that has pointed out that the Sn grain distributions have a more severe effect on primary creep response than on secondary creep response.

v. Experimental evidence on the effect of the initial Sn grain orientation and successive grain evolution on the creep damage mechanisms in the test specimens is provided. Damage observed here refers to shear bands and out-of-plane steps at the grain boundaries. The insights provided by the current study are important since they point towards the following unresolved issues:

   i. To what extent do grain boundaries contribute towards the total creep measurements?

   ii. If grain boundaries do contribute, as a corollary, it is important to understand the history and the extent of recrystallization that occurs during the creep history.

   iii. An understanding of the above questions could also provide insights into the lack of scatter in the secondary creep response at the loads levels where the microstructural study was conducted.

vi. The creep behavior of microscale SAC305 solder specimens is compared to that of microscale Sn37Pb solder specimens, using identical test protocols. Furthermore, the effect of reducing the Ag weight fraction in SAC is provided (near-eutectic SAC387 vs. SAC305). The measurements of SAC387 and Sn37Pb used for this comparison are taken from test protocols that are very similar to those used in this study [95, 104].

2. Macroscale modeling: creep versus stress relaxation behavior of SAC solder

   i. The existence of joint-dependent behavior in the stress relaxation response of microscale SAC305 specimens is provided.

   ii. The macroscale creep models used here (and their associated constants), in principle, are applicable to statistically homogenous and isotropic joints. However most solder modeling efforts utilize macroscale modeling strategies at microscale length-scales where the joint is neither statistically homogeneous nor isotropic. The accuracy of using macroscale creep models based on continuum mechanics, with model constants obtained from non-homogenous microscale SAC305 specimens, is addressed in this study.

   iii. The accuracy of using constants measured from constant force creep tests for predicting viscoplastic stress relaxation from constant displacement tests has not been experimentally demonstrated in prior studies for SAC solder. The accuracy of these stress relaxation predictions is investigated using stress relaxation measurements from consistent test methodologies with due attention to predicted versus measured scatter ranges.

   iv. The measured stress relaxation of microscale SAC305 joints is compared to that measured from Sn37Pb joints using comparable test methods. Similar comparisons in the literature are primarily based on modeling approaches and have not been validated with experiments. The current study contributes to improving this understanding.

v. The role of primary creep constitutive behavior in the stress relaxation history is provided. Guidelines are provided regarding the inclusion of primary creep for capturing the measured stress relaxation.

vi. Guidelines are provided, based on the measured viscoplastic constitutive response and FE modeling, for optimizing the hot dwell time in accelerated thermal cycling of functional SAC305 BGA joints. In particular, the optimal dwells for SAC305 are compared to current optimal standards adopted by the microelectronics industry for Sn37Pb solder.

3. Microscale modeling of secondary creep behavior of SAC solders

i. A mechanistic framework for capturing the key microstructural features and dominant creep mechanisms in the secondary creep response of microscale SAC joints is provided.

ii. When calibrated to properties in the eutectic Sn-Ag regions, the calibrated model has the potential to predict the effect of varying alloy compositions of SAC and thermal aging on the secondary creep response. The mechanistic model can be combined with minimal testing to obtain the averaged secondary creep continuum model constants such as those in the Garofalo model.

4. Evolution of the mechanical properties and microstructure of SAC solder as a function of isothermal mechanical fatigue damage

i. The evolution of the elastic-plastic, hysteresis response and of the viscoplastic constitutive behavior of microscale SAC305 specimens is quantified as a

function of mechanical cycling damage. The study verified that for the same reasons quoted in 1- (ii), microscale SAC305 specimens are expected to exhibit scatter in the above mentioned properties. However the variability exhibited by these properties is not as significant as that seen in the primary creep behavior. The amount of scatter generally decreases with increasing fatigue damage, possibly due to dynamic recrystallization.

ii. Isothermal mechanical fatigue properties (S-N curves based on load drop) are provided. The scatter in the fatigue curves are provided as a function of increasingly severe failure criteria (increasing load-drop), and shown to be negligible beyond load drop of approximately 30-40%. Recrystallization is confirmed to occur under isothermal mechanical cycling studies. Hence the study qualifies that TMM joints are representative of the microstructure and properties of functional joints not only in the as-fabricated stage but also in the damaged state. The study provides a qualitative correlation between the microstructural evolution (that homogenizes the initial coarse grained Sn microstructure through recrystallization), and the measured drop in the variability of the measured constitutive and fatigue properties.

iii. The study quantifies the rate of degradation of properties with increasing fatigue damage. These properties is important for: (i) conservative estimates of solder constitutive behavior in as-damaged state; (ii) modeling of progression of cyclic fatigue damage progression in solder interconnects. CDM model constants to represent the evolution in elastic and plastic properties with increasing fatigue

damage are provided. In some cases, model trends are shown to be discrepant with test data.

iv. Room-temperature cycling at 5E-2 1/s strain rate is shown to produce a negligible extent of cyclic creep damage.

v. The current study is among the first few studies to discuss that under mechanical cycling, the yield strength of SAC305 solder follows a hardening law different from that of an isotropic hardening law or a kinematic hardening law, that are routinely used to model the behavior of SAC solders. Since the yield stress from the measured hardening behavior is lower than that of isotropic hardening and higher than that kinematic hardening, the state of stress and damage is significantly different from that observed with previously used hardening laws for the solder. Future work on the identifying the consequence of this assumption is discussed in Chapter 8.

vi. The study also provides an understanding of the relative ranking of the isothermal mechanical fatigue of SAC305 relative to two bench-mark solders: near-eutectic SAC387 and eutectic Sn37Pb solders. Furthermore the effect of isothermal aging of SAC305 on the mechanical durability is quantified.

Future Work

While this dissertation provides insights into the evolution of the mechanical behavior and microstructure of SAC solder systems for microscale and bulk application, the results reveal several new unresolved research issues. The understanding obtained from the current study can be enhanced by improving on the following limitations:

1. Constitutive creep behavior of as-fabricated, microscale, SAC solder

i. The current study provides a qualitative correlation between the measured creep behavior and the microstructure from the Sn grain microstructure only. The effects of dendritic and IMC configurations play an important role, as suggested by the microscale model. However these aspects have not been sufficiently explored in the current study and need be carefully examined.

ii. The influence of the grain microstructure on the creep behavior of microscale SAC305 solder is studied using OIM measurements and TMM measurements using three specimens each at two load levels. Further repeatability should be explored to obtain a statistically significant evidence of the role of the grain numbers and orientations on the measured creep response. Possible reasons as to why the single grain specimen exhibits superior creep resistance compared to the multi-grained specimens needs to be explored.

iii. The reasons for the extent of scatter observed in the primary and secondary creep regions need to be quantified and understood in terms of the grain orientations and configurations observed relative to the loading and the dislocation motion through the material. The lack of scatter in the secondary region has been hypothesized to be due to lack of dominant slip planes with increasing dislocation densities (see Chapter 4). This hypothesis needs to be explored further. In addition, the influence of grain boundaries and the recrystallized grains on the observed scatter needs to be examined.

iv. Preliminary studies show that the recrystallized grains observed in the OIM images correspond to shear bands in the post-creep samples. Future studies should investigate this aspect, since it helps explain the correlation between damage and the sources of recrystallization. Furthermore identifying key locations of recrystallization from the SEM images helps perform localized OIM analysis.

v. The secondary creep rates are very sensitive to shear stresses beyond approximately 12 MPa. Scatter is dominant only at these high stress levels in the secondary creep. Possible reasons for this observation should be explored, including the possibility of a creep mechanism transition.

vi. Primary creep is described using a continuum-scale generalized exponential model. This model does not include the influence of the secondary creep strain rates. Future studies should investigate the effectiveness of alternate models such as the Pao-Marin model [236] that include the effects and history of secondary creep behavior in the primary creep behavior.

vii. The current study can be combined with the viscoplastic creep measurements conducted by other investigators across different stress and temperature conditions, to yield the Ashby deformation maps for SnAgCu solders.

2. Macroscale modeling: creep versus stress relaxation

i. The test matrix utilized for stress relaxation is limited compared to that of creep characterization. In particular, the existence of scatter in the stress relaxation response of microscale SAC305 specimens is deduced from non-

monotonic trends to stress and temperature. More replicates are needed at identical load levels, to reinforce the current conclusion.

ii. Guidelines for the optimal hot dwell time to be used in the accelerated thermal cycling of functional SAC BGA joints are provided by modeling only the secondary creep portion of the creep behavior of solder. The effect of including primary creep for modeling the stress relaxation in BGA joints should be explored. Furthermore the stress relaxation studied through modeling of BGA joints should be validated with experimental techniques such as DIC.

iii. The effect of the yield hardening rules, (isotropic vs. independent vs. kinematic hardening) should be explored to understand the differences in the stress-strain and durability behavior.

3. Microscale modeling of secondary creep behavior

i. The athermal detachment of dislocation climb is captured through dilute concentrations approximations and needs to account for the interactions of the dislocations.

ii. The model needs to be extended to include the effect of the microstructural features on the measured variability in the primary creep.

iii. The dendritic geometry needs to be extended to non-spherical geometries to account for dimension changes from aging studies.

iv. The micro-model calibration needs to be improved in future by separately tuning the dislocation model with respect to the eutectic phase properties, and that of the homogenization scheme with respect to the final solder properties.

v. The micro-model currently used polycrystalline isotropic properties of Sn. This work needs to be extended to include anisotropic phase behavior.

vi. On the same lines, the micro-model needs to be extended to include the effect of the grain length scales so that grain boundary sliding can also be included as a creep deformation mechanism.

4. Evolution of properties and microstructure as a function of isothermal mechanical fatigue damage

i. Fatigue damage is induced through isothermal mechanical fatigue at room temperature. The effect of high temperature fatigue loads on the evolution of the constitutive properties, hysteresis curves and the microstructure of as-fabricated microscale SAC305 specimens needs to be studied. In addition the fatigue life at high temperature also needs to be studied. This investigation will provide insights into the material behavior under creep-dominated damage loads.

ii. The statistical significance of the test measurements need to be improved by including more replicates per load conditions and by exploring a much more extensive test matrix (more load levels, temperatures, strain rates relevant to plasticity dominated loads)

iii. The current study provides qualitative evidence towards understanding the evolution of constitutive properties and associated scatter at fatigue damaged state, as well as the fatigue life. A quantitative correlation between the effect of the grain orientation and the observed mechanical behavior needs to be

provided. Furthermore recrystallization has been hypothesized to be playing a major role. The existence of recrystallization to such fine grain sizes points towards possible grain boundary sliding as a creep mechanism and needs to be explored.

Furthermore softening of the material occurs due to grain recrystallization as well as material fatigue damage. The contributions of the latter (macrodamage, microcracking) and other microstructural features (dendrites, grains, IMCs) have not been explored. A comprehensive understanding as to why the fatigue properties do not exhibit scatter and for understanding dominant deformation mechanisms in the damaged state are necessary. In addition, proof of recrystallization has been provided only in the final damaged state (after the tertiary region is reached in creep, and at fatigue failure state of 50% load drop). Figure 6-5 and Figure 6-6 clearly indicate a transition to reduced levels of scatter at fatigue damage at around 30% load drop. Characterization of the corresponding grain size and numbers will facilitate a stronger understanding of the start and evolution of grain recrystallization.

iv. Literature suggests that thermal aging affects only the dendritic and IMC morphology, and not the grain microstructure (as seen in the TMM joint in Figure 3-6). In the current work, degradation of fatigue properties with aging is observed. However this degradation is not connected to the associated microstructural evolution of the dendritic and IMC configurations. Such an

insight is valuable in the design of solder systems under various pre-testing loads and should be presented in future studies.

v. Microscale SAC305 solder exhibits significant anisotropy in the mechanical properties in the as-fabricated state, due to the coarse-grained Sn microstructure and the anisotropy of single crystal Sn. The grain microstructure attains a much more homogenous fine-grained state owing to the formation of several recrystallized grains under creep and mechanical fatigue loads. The extent of homogenization of Sn grains microstructure is particularly stronger under fatigue loads. Hence the practice of utilizing the as-fabricated mechanical properties for modeling the behavior of solder throughout the entire service life is questionable and needs to be investigated.

vi. An important observation in the fatigued solder microstructure is that the degradation of the mechanical response is initially due to distributed micro-damage, but is eventually due to a combination of macro-cracks and microdamage (structural damage) and evolving coherent grain microstructure. Hence, evaluating the effective load-bearing area (and corresponding true stress) as a function of increasing structural damage pose significant challenges. The current study presents average effective behavior of the specimen, assuming that the initial undamaged load bearing area remains unchanged. This assumption is a serious limitation of this study and future efforts should focus on evaluating the effective load-bearing area.

vii. Furthermore, the softening /degradation of the material properties is a combined effect of the evolving grain and damage microstructure. In order to

accurately assess the degradation of properties, the contributions of the two factors needs to be separated.

viii. The elastic-plastic properties as a function of damage are obtained by subtracting the contributions of the creep deformation from the total strain. However the creep constants used here are from the initial as-fabricated properties and do not include the evolution due to evolving grain microstructure and cyclic damage. Thus the elastic-plastic strains are over-estimated as a function of damage. This has to be rectified in future studies.

Appendices

Appendix 3.1: Negative Creep and Post-processing of Creep Data

An interesting occurrence in the long-term tests at room and elevated temperatures is the occurrence of negative creep (Figure A3.1.1a). Negative creep is incremental creep strain in a direction opposite to that of the applied stress and has been reported in SAC[77]. The negative creep occurrence shown here are from room temperature measurements. However this phenomenon was observed at elevated temperatures as well. Negative creep observed in the current study is similar to that reported by Vianco et al., on SAC396 solder[78].

Reports of negative creep have also been reported in epoxy and hypothesized to be due to the chemical shrinkage in epoxy after curing[237]. Li, et al., and Vianco,et al.,[78, 238] suggested that the source of negative shrinking in solders to be due to a metastable microstructure. Studies conducted by Van Petegem and co workers[239] on nanocrystalline Nickel, explain negative creep in terms of the influence of local and long-range stress fields on the ability of dislocations to bypass an obstacle [77, 237-239]. This explanation seems more plausible and applicable to solders due to their dispersion strengthened microstructure. Recent studies by Vianco, 2009 [240] suggest that fluctuations in creep strain history, such as that in negative creep, could be possible indications of grain recrystallization.

Creep Regimes Identification: The creep strain rate and creep strain histories are used to identify the primary, secondary and tertiary creep phases. A robust local regression method utilizing weighted linear least squares method is used to smooth the creep strain history. Moving averages (with an appropriate span) of this strain

history are estimated using quadratic or linear functions. This scheme is found to work well for the secondary creep but not necessarily for the primary creep as is visible in Figure A 3.1.1-b where the strain (pink curve) is overestimated during the early parts of the history. The corresponding slope of the smoothed data provides the creep strain rate history.

The initial rapid decrease in the strain rate signifies the primary creep stage, followed by a constant strain rate, which is the secondary creep stage. The tertiary stage is marked by an increasing strain rate. At high stress/temperature conditions, the time spent at the secondary phase is not very conspicuous, and is generally identified by the minima of the strain rate history [241]. The secondary creep rate is first obtained using moving averages of the strain rate data in the secondary regime. The dependence of the corresponding strain rate on stress and temperature is used to extract the Garofalo secondary creep model constants. Since the model is a non-linear function of α and n, non-linear least square fitting procedures are used to first obtain the values of α and n that minimizes the root mean square error (RMSE) of the stress normalized fit across all test data. The optimal values of α and n are then utilized to obtain the constants A and activation energy using the temperature dependence.

The primary creep strains are obtained by subtracting the measured secondary creep strain history from the total strain history. The primary creep strain history is characterized by a monotonically increasing creep strain (with high initial strain rates) that plateaus out to reach saturation. The primary creep model constants are obtained from this data. The primary saturated creep strain is the moving average of the strain

in the saturation regime and the decay term describes the rate of approach of the primary creep strain to saturation creep.

The decay is captured here by using an exponential fit to describe the normalized difference of the primary strain from the saturated strain as a function of time. The measured primary saturated creep strain and decay parameters are consequently fit to the proposed primary creep models using the same regression procedures as those used for the secondary creep model constants. The fit of the creep models to the test data are provided in Figures A3.1.2 a-b. RMSE values for the secondary Garofalo creep model fit and the primary decay model fit compare as 1.24 versus 1.37 (both models have the same dimensions for o*rdinate* and *abscissa)*. The RMSE error in Sn37Pb indicates lower scatter than that in SAC305 solder (0.4 in Sn37Pb as opposed to 1.3 in SAC305). The error metric is the natural log of the error between the data and fit. Figure A3.1.3 presents the creep measurements conducted by Haswel[104] on TMM Sn37Pb solder specimens.

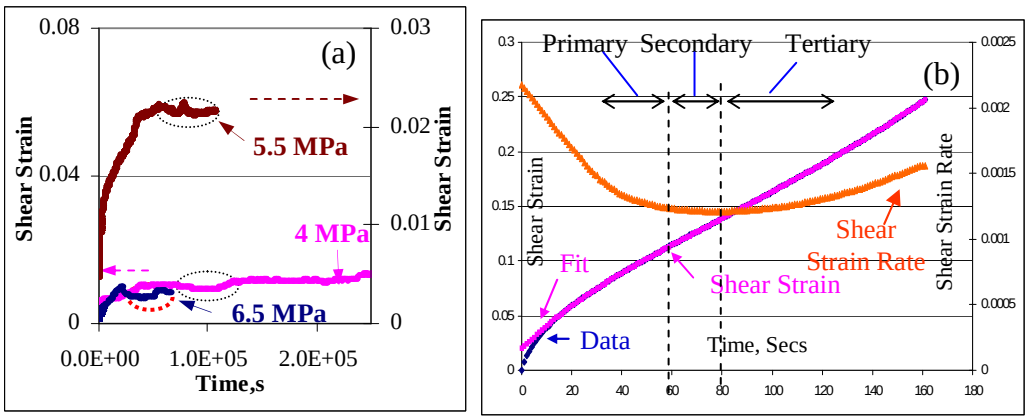

Figure A3.1.1: (a) Negative Creep at RT (depicted by circles), (b) Creep Strain and Strain Rate History (20 MPa and 25°C). Secondary creep regime is between 60-80 s.

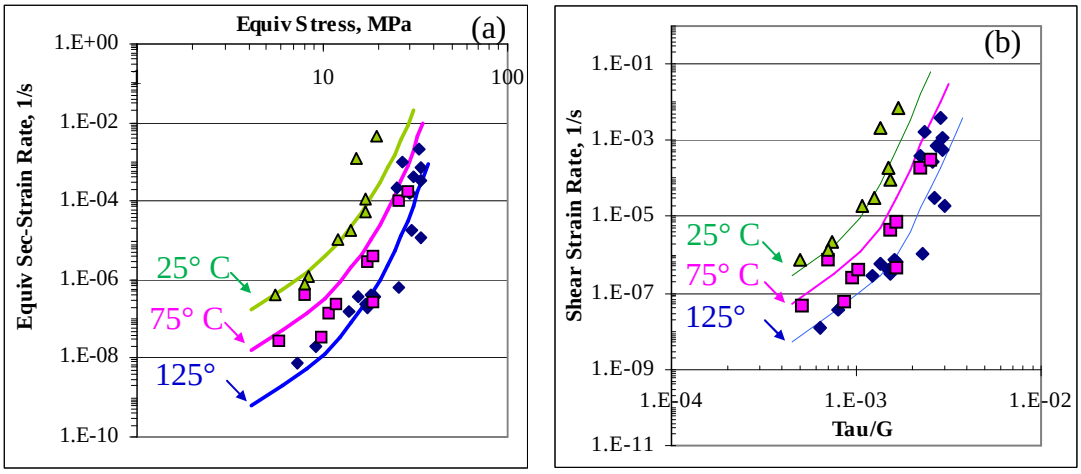

Figure A3.1.2: Secondary creep model fits for (a) Garofalo model and (b) Two-term Weertman model with transition knee at τ/G =1.4E-3

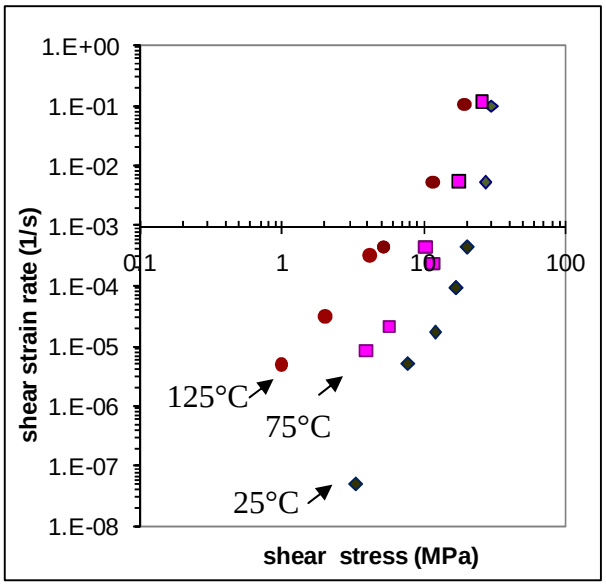

Figure A3.1.3: Secondary creep strain rate versus stress (Shear components) from TMM testing of Sn37Pb solder by Haswell[104]. Creep measurements presented here are from monotonic creep testing and those determined from the strain hardening region of the stress-strain curves generated from monotonic plasticity testing

Appendix 3.2: Evidence of Scatter in Other Constitutive Properties of SAC305

Scatter similar to that observed in the viscoplastic measurements of the as-fabricated microscale SAC305 TMM joints is also evident in the elastic and plastic response measured from these joints. Comprehensive details of the test measurements are provided in Chapter 6**.** The extent of scatter in the elastic measurements as a function of increasing state of damage in solder is depicted in Figure A3.2.1. The elastic modulus varies as much as 60% from one specimen to another. Cyclic damage is induced through isothermal, mechanical cycling tests at high strain rate and room temperature. For comparison purposes, the as-fabricated elastic and plastic response refers to the data at "zero" cycles as depicted by the dotted circle.

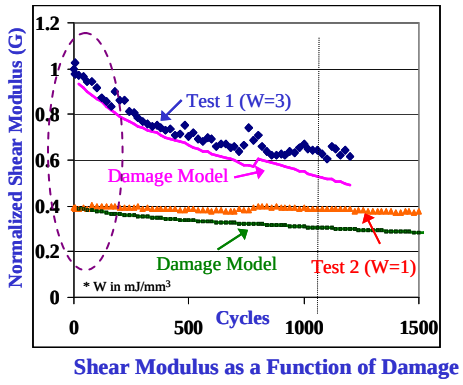

Figure A3.2.1: Extent of Scatter in the Elastic Properties of Microscale SAC305 Solder as a Function of Increasing Damage to the Solder. Dotted circle depict the measurements in the as-fabricated state of solder

Appendix 3.3: Anisotropy of Single Crystal Sn: Elastic, Plastic, Thermal and Creep [30, 37-39]

Tin exists as β - Sn above ~13°C and as α - Sn at lower temperatures. For the range of temperatures used here in the testing, Sn exists as β - Sn, which has a body-centered tetragonal structure (bct), with c/*a* = 0.546. In addition to atoms at the corners of the cell and one at the centroid, four atoms exist at (1/2, 0, 1/4) and (0, 1/2, 3/4) respectively (Figure A3.3.1).

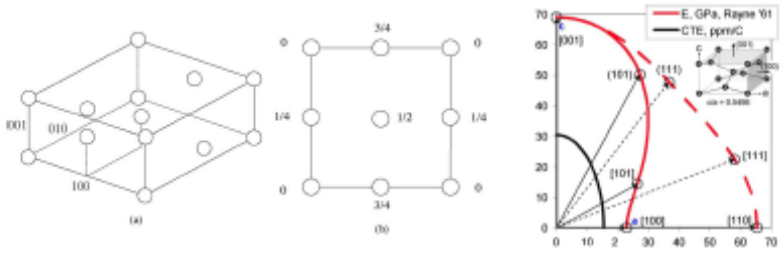

Figure A3.3.1: (a) Sn BCT unit cell. Image adapted from [57] (b) Single crystal elastic and thermal properties provided by [41]. Image adapted from [41]

Sn is known to exhibit significant anisotropy in the elastic and thermal properties as shown in Figure A3.3.1b. The measurements from several investigators has been compiled and presented by Bieler [41].. For example, the elastic modulus of single crystal Sn differs by as much as a factor of 3 based on the orientation. Review of literature on the plastic properties also suggest significant anisotropy in the stress-strain curves based on the orientation (see for example, [32-33, 39].

However based on the review conducted this far, there is significant variation across the reports of various investigators. The discrepancy seems to be due to the purity of Sn samples and test methodologies used. Compared to the elastic properties of single crystal Sn, the reports on the creep properties of single crystal Sn are limited. Furthermore the results vary considerably across different investigators. However the results available do suggest that single crystal Sn does exhibit

anisotropy in the creep behavior as well. Figure A3.3.2 shows the secondary creep rates reported by a single investigator across similar crystal orientations[38].

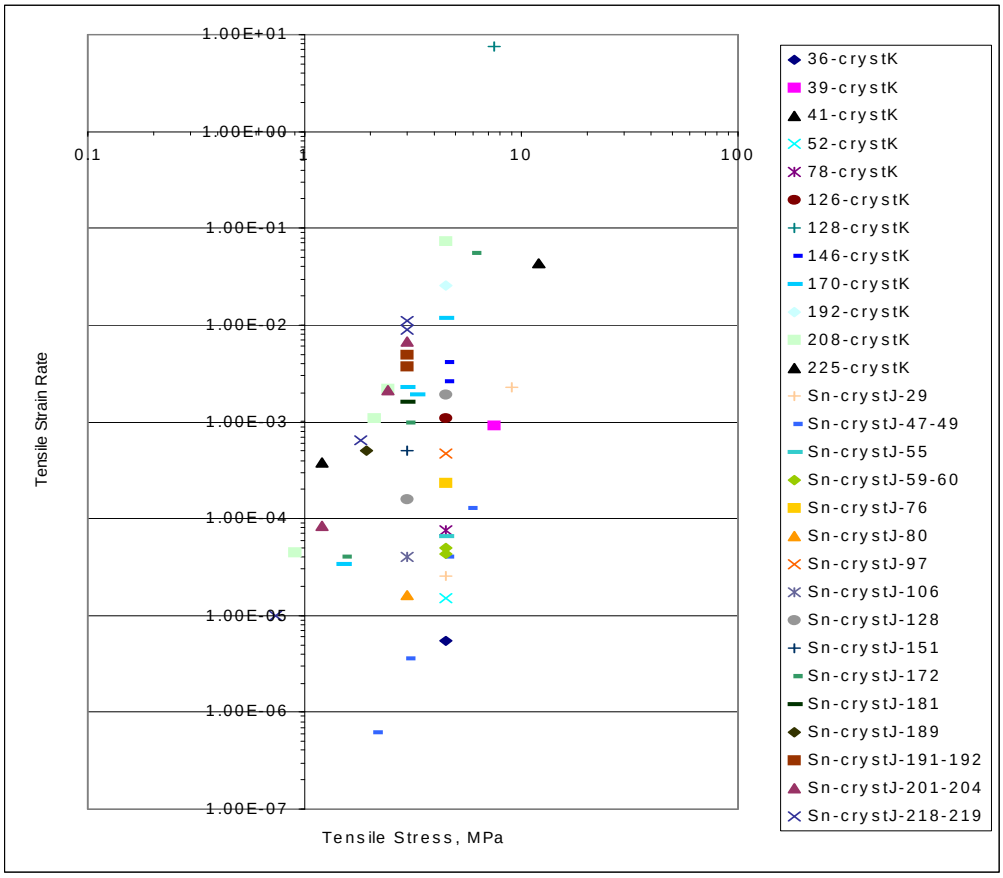

Figure A3.3.2: Variability in the creep properties of single crystal Sn. Data reported by Weertman has been replotted here [38].

Appendix 3.4: Post Processing Details for the OIM Maps

The EBSD maps are post processed using HKL *CHANNEL5* Flamenco software. The grains are distinguished from subgrains using a grain boundary angle definition greater than 5°. In the OIM maps shown in this chapter, low angle grain boundaries are defined as those with angles between 5°- 10° and are distinguished using silver colored lines. High angle grain boundaries are defined as those with angles between

10°-180° and are distinguished using black colored boundaries. All images are first processed to remove “wild spikes” which are incorrectly indexed data points. The zero solutions are then processed and reduced to 0%.

The as-fabricated specimens are analyzed using a step size of 3 μm. In the case of the post-creep specimens (Specimen #5), indexing is first conducted using a step size of 3 μm across the entire joint and locations of recrystallization are identified. These regions are again indexed using a step size of 1 μm to capture finer grains. Figure 3-11 b shows the OIM mapping resulting from a 1 μm step size indexing.

Appendix 4.1: Overview of Length Scales in Multi-scale Modeling Strategies

Various multi-scale modeling schemes exist, which vary from atomistic modeling to capturing the interactions of individual dislocation with obstacles to the meso-scale (cracks) and finally down to structural level models. The merit of each scheme lies in the complexity and accuracy of the material response required. For example, the detachment relaxation factor, 'k', requires to be derived in reality from molecular dynamics simulations that yield the line tensions in the particle and matrix portions of the dislocations after climb. However, in the current study, these values are reverse engineered from the multi-scale mechanistic model and the creep measurements.

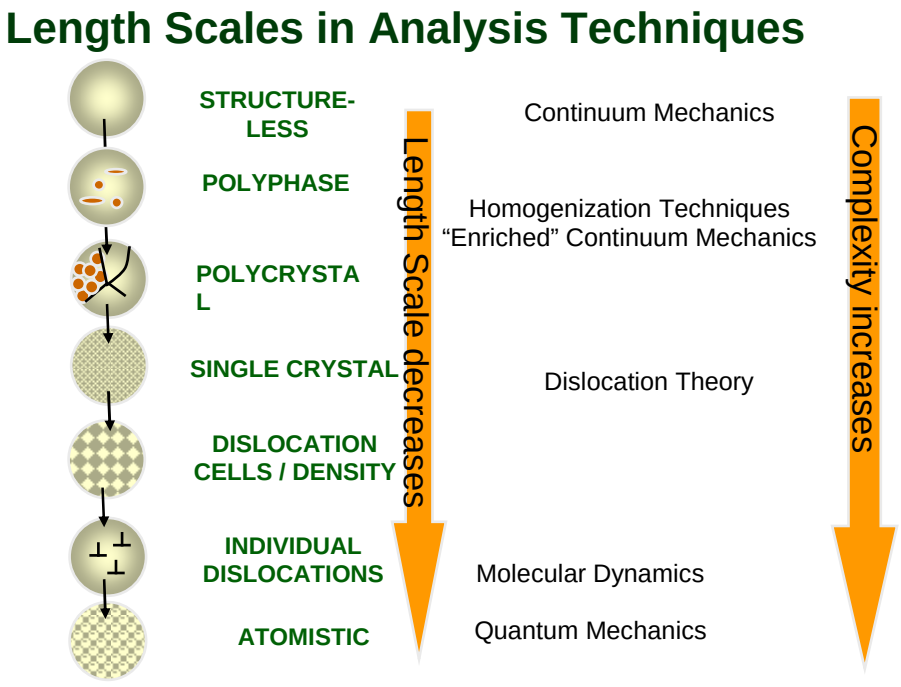

Figure A4.1.1: Multi-scale modeling approaches and corresponding length scales

Appendix 4.2: Scope of Primary Creep Model

The primary creep regions are seen to be sensitive to the grain configurations and orientation. The effect of grains can be included via anisotropic single crystal Sn

constitutive properties (elastic, plastic and creep) along with the influence of the grain boundary. Of all these microstructural features, the effect of the grain boundary is the least understood aspect of this study and in literature. Hence implementing appropriate constitutive models to represent the grain boundary interactions is a non-trivial task. Furthermore prior to understanding the influence of grain configurations and the resulting grain boundaries, the influence of the lower length scales (eutectic Sn-Ag regions, microscale dendrites and Cu_6Sn_5) needs to be sufficiently understood.

An additional challenge posed in implementing this model, is the lack of reliable and comprehensive measurements on creep of all possible single crystal Sn. The properties available in literature do suggest anisotropy in the creep response of single crystal Sn, even though the measurements vary significantly from one investigator to another. Since these properties are the primary feed to the model for the Sn matrix, significant error can be expected in the modeling output if the right constitutive properties are not chosen. However understanding the favorable grain orientations is important enough to warrant future work on implementing a model that accounts for the mechanisms accounting for primary creep (such as evolving dislocation densities to steady state)

Scope: Since the behavior of microscale SAC joints is a function of the Sn grain configuration, a mechanistic microscale model for primary and secondary creep could provide insights into favorable grain orientations that optimize the mechanical behavior of these joints. However, prior to proceeding to the influence of the Sn grains and grain boundaries, the influence of the Sn dendrites and IMCs needs to be understood and quantified using the secondary creep behavior.

Appendix 4.3: Dislocation Density and Burger's Vector

As reported earlier, the extent of piece-to-piece variability in the creep response of SAC305 solder is more significant in the primary creep region compared to the secondary creep. Physically, the reduced influence of Sn grain anisotropy (dominant slip direction for dislocation motion) in the secondary region can be hypothesized to be due to the material achieving a higher dislocation density with increasing primary creep strain. Eventually at the secondary creep region, the dominant slip systems may become so 'clogged' due to high dislocation density that many other secondary slip systems may become active in addition to the primary slip system. Thus, the creep response becomes more isotropic and less sensitive to a preferred slip system or grain orientations.

The dislocation density in the secondary creep phase as used in the current study is based on a hypothetical assumption that all the slip planes in bct Sn are completely clogged with dislocations. Dislocation density is hence assumed to be the ratio of the sum of the perimeters of the intersection of all possible slip planes with unit cell of Sn versus the volume of the Sn unit cell. Possible slip planes in Sn are {110}, {100}, {211} [39, 213] and the dimensions of the unit cell are a = 0.58 nm, b=a, and c = 0.32 nm [39, 242]. Literature shows that the slip has the highest probability in Sn are in the [001] and [101] directions [39]. Burger's vector in the [001] and [101] directions are 0.32nm and 0.66 nm respectively. Since slip has a higher probability of occurrence in the direction with the smallest burger's vector, [001] is chosen as the slip direction and the corresponding burger's vector is chosen for the model.

Appendix 4.4: Dependence of k on Temperature and Stress

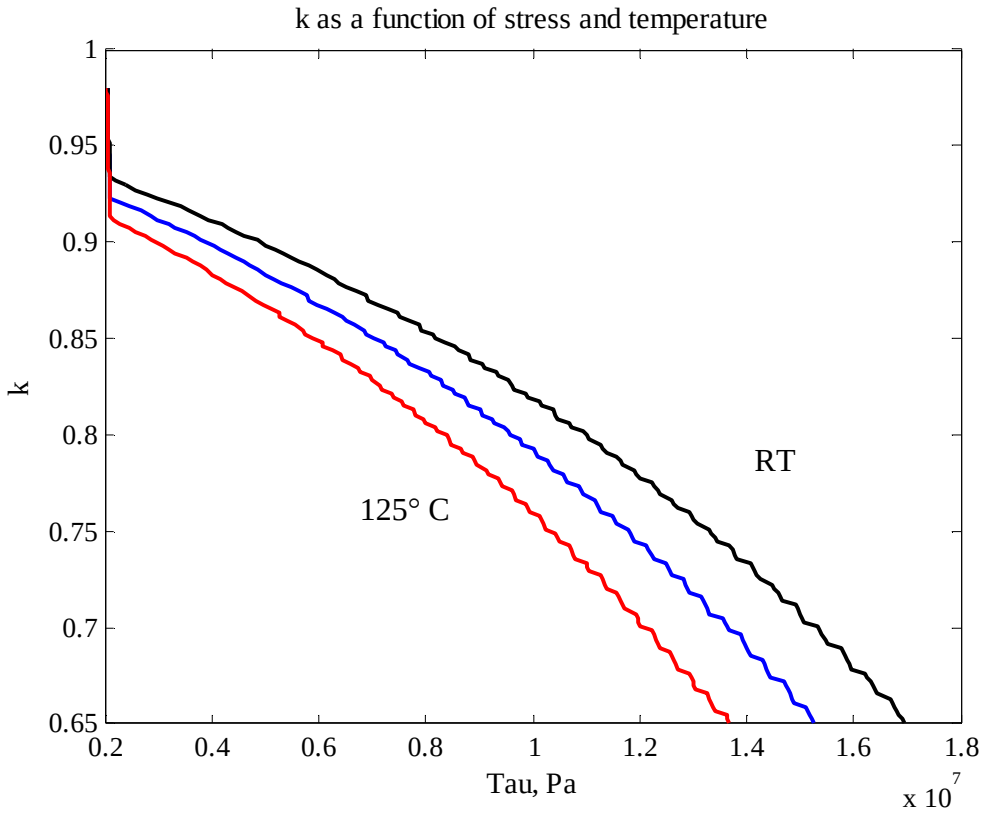

Figure A 4.4.1: Calibrated curves of k as a function of temperature and stress, showing the untruncated data at low stress.

Appendix 4.5: Microstructural Analysis for Parametric Studies on the Effect of % Ag and Isothermal Aging in SAC Alloys

The effect of varying Ag% in SAC solder is modeled by varying the dendritic and eutectic regions in the SAC solder. As the Ag % increases the volume fraction of dendrites increases. Correspondingly the volume fraction of nano-scale Ag_5Sn IMCs in the eutectic Sn-Ag regions increases. In order to demonstrate the change in microstructural features, image analysis is conducted on TMM solder specimens of SAC105 and SAC305. The fabrication methodology is kept consistent across different solder specimens. Figures 4.5.1 a-b show the dendritic and eutectic regions

microstructure at low magnification in TMM SAC105 and SAC305 solder specimens respectively. The volume fraction of the nanoscale Ag_3Sn particles in the eutectic regions is seen to increase in the higher Ag content SAC solder (Figures 4.5.2 a-b).

Similarly, isothermal aging is expected to increase the volume fraction of Sn dendrites per unit volume in addition to microstructural coarsening of the nanoscale IMCs in the eutectic Sn-Ag region, as well as bulk microscale IMCS and interfacial IMCs. Results from literature [5] are presented here to understand these microstructural changes induced by aging in Figure 4.5.3 a-b.

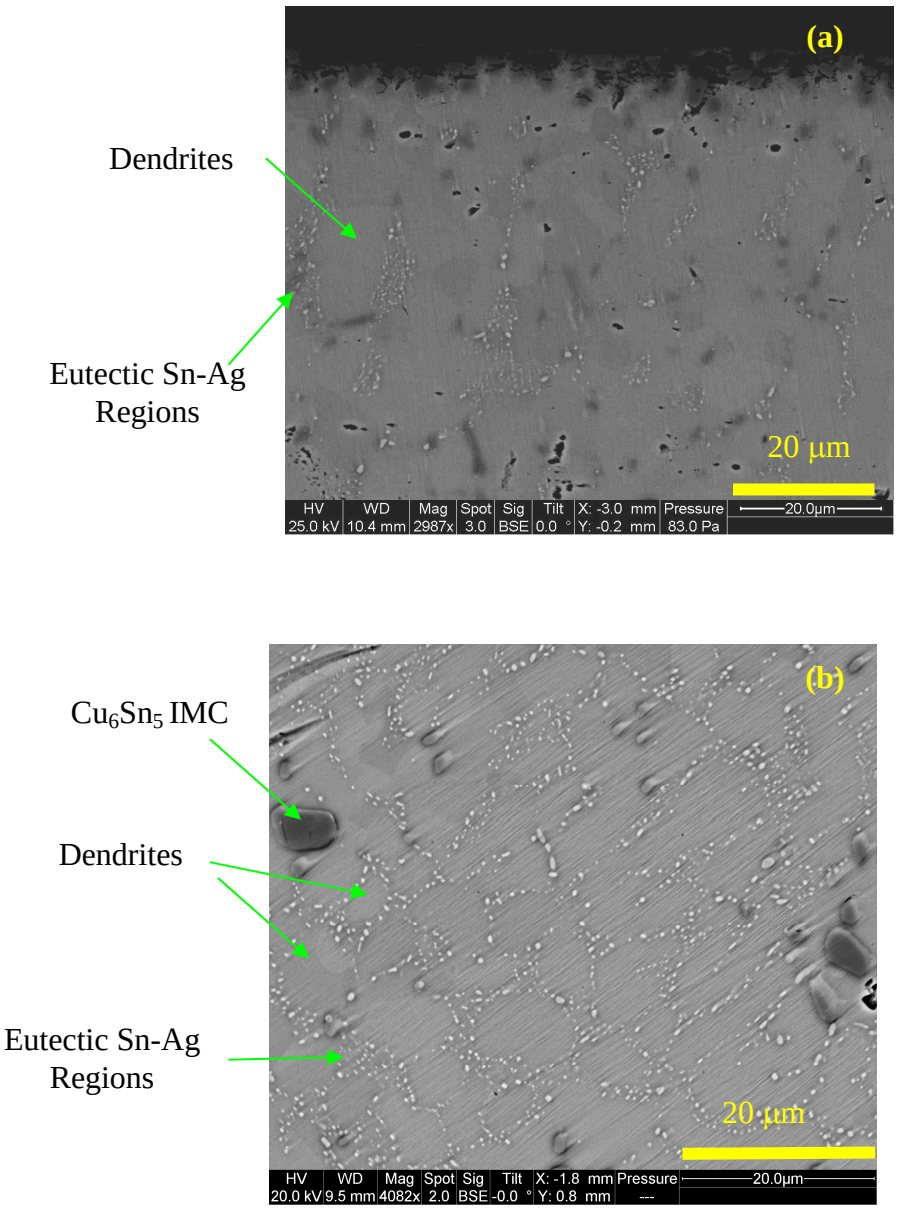

Figure A4.5.1: Dendritic and eutectic Sn-Ag microstructure in TMM specimens of (a) SAC105 and (b) SAC305 solders

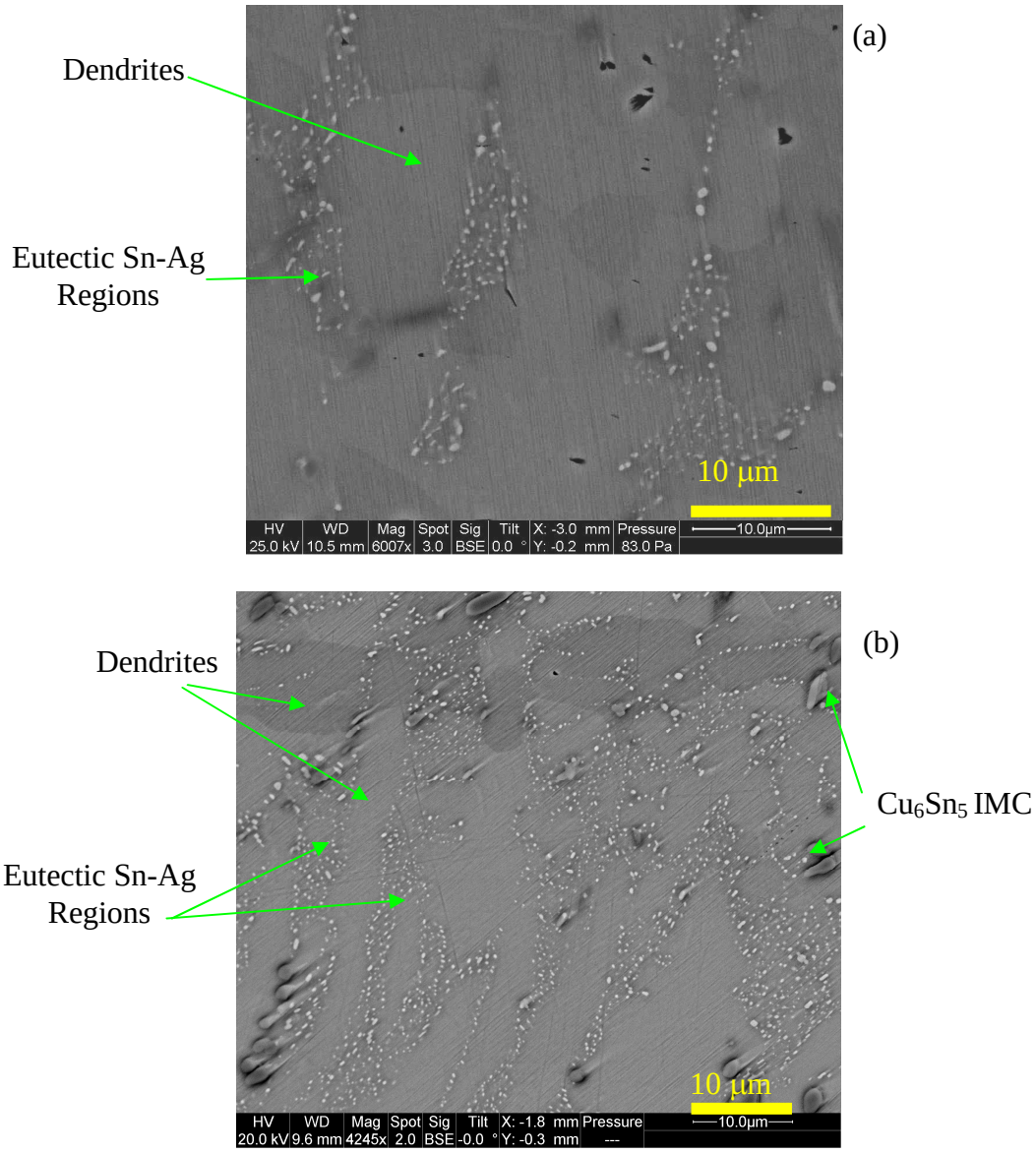

Figure A4.5.2: Lower volume fractions of nanoscale Ag_3Sn IMCs in eutectic Sn-Ag microstructure in TMM specimens of (a) SAC105 compared to (b) SAC305 solders

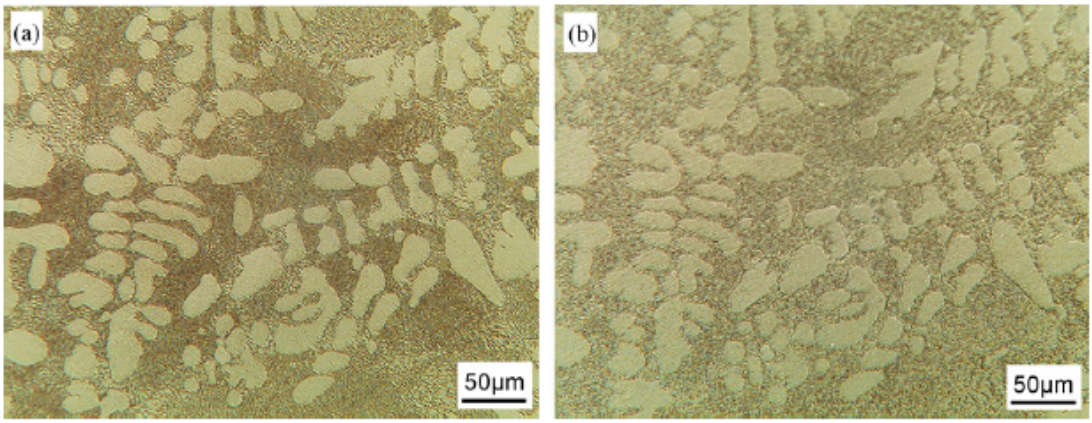

Figure A4.5.3: Smaller sizes of Sn dendritic regions and IMCs in (a) unaged Sn3.5Ag compared to (b) aged version of the same sample. Image has been adapted from literature [5].

Appendix 5.1: Material models used in FEA

1. SAC305 Solder Properties:

$$\varepsilon = \varepsilon_{el} + \varepsilon_{pl} + \varepsilon_{scr} + \varepsilon_{pcr}$$

ε_{el} = elastic strain, ε_{pl} = plastic strain, ε_{scr} = secondary creep strain, ε_{pcr} = primary creep strain

$\varepsilon_{el} = \sigma E(T)$ Hooke's Law

$\varepsilon_{pl} = C_{pl}(T)\sigma^{n(T)}$ Ramberg-Osgood Plastic Law

Poison's ratio: 0.35, CTE = 26E-6 (K^{-1})

E=(-22.1E6*T + 24.7E9) Pa, T is in K,

C_{pl} = 121.6 – 0.4* T (°C) , units $(MPa)^{1/n}$, n(T)= 0.29-4.6E-4 * T (°C) ,

Elastic and plastic constants used here are from TMM measurements made on near-eutectic SAC387 solder from [95].

2. Copper:

E=117E9 Pa, Poison's Ratio =0.31, CTE=17E-6 (K^{-1})

Appendix 5.2: Industrial application - Optimization of Dwell Time for Accelerated Thermal Cycling of Sn3.0Ag0.5Cu Pb-Free Interconnects

ABSTRACT

The optimal hot dwell time in accelerated thermal cycling profiles for Pb-free Sn3.0Ag0.5Cu (SAC305) solder is determined, using viscoplastic testing and physics of failure (PoF) modeling. Thermo-mechanical cyclic fatigue damage saturation in BGA256 SAC305 assemblies is matched with that in traditionally used Sn37Pb assemblies to determine the optimal dwell, using non-linear finite element analysis.

Energy-partitioning methodology is used to predict fatigue life. The damage saturation rate is expressed, in terms of an acceleration factor (AF), relative to the damage in a typical field condition. SAC305 is found to be almost twice as durable as SnPb, for comparable dwell times. As expected, the damage saturation rate in SAC305 is less than that in SnPb. The predicted damage saturation curves are further compared with the measured stress relaxation curves for SAC305 and Sn37Pb at elevated temperature. The optimal dwell times are provided in terms of various damage saturation criteria proposed by sponsor industries. Based on these criteria, the dwell times range from 15 minutes to two hours.

INTRODUCTION

Eutectic Sn3.8Ag0.7Cu solder is among the solders chosen as a substitute for traditionally used Sn37Pb. Owing to cost benefits, the industry is transitioning to low Ag content SnAgCu (SAC) solders. The most popular candidate is the reduced Ag content Sn3.0Ag0.5Cu (SAC305). The solder interconnects are critical to the reliability of the electronics under harsh environments of temperature and mechanical loading, since they form not only the electrical interconnection, but also the load-bearing mechanical interconnection. Consequently, cyclic thermo-mechanical loading throughout the life cycle can cause fatigue failures. Qualification of the electronic components is conducted using accelerated loading conditions.

The material response of Pb-free solder is known to be significantly different from eutectic Sn37Pb owing to the microstructural differences. In particular, the viscoplastic creep resistance of SAC solders is higher than that of Sn37Pb. Hence the stress response and fatigue life of these Pb-free solder interconnects used in typical

electronic packages under typical usage loads is expected to be different from that of SnPb solder. Hence the objective of this study is to determine if the traditionally used accelerated thermal cycling profiles for SnPb would yield the same damage in SAC. In particular the primary focus is to determine if 15 minute dwell time at maximum temperature is valid for SAC solders.

APPROACH

In the current study, the accelerated thermal cycling profile used to qualify the electronic products is designed using a combination of viscoplastic response measurements and modeling. The measured viscoplastic behavior corresponds to constant-stress creep response and constant-strain stress-relaxation response. The optimal dwell time is determined based on matching the relative saturation of thermo-mechanical cyclic fatigue damage in SAC305 assemblies, with that in Sn37Pb assemblies. Since these experiments are very expensive, a physics of failure modeling is conducted. In addition, an alternate economical technique is explored by measuring stress relaxation rates in simple shear specimens [1]. The stress relaxation saturation is correlated with damage saturation rates in thermal cycling.

In the physics of failure modeling, creep measurements conducted in prior work [2] are used for modeling the viscoplastic response of solder. The creep measurements are conducted using modified lap-shear Iosipescu solder specimens. Significant scatter was observed in the creep measurements. Microstructural investigations reveal that at the given length scale, the solder joint has very few grains. Hence due to this lack of statistical homogeneity and isotropy of SAC solder, the properties are dependent on the relative orientation of the grains and loading. It

should be noted that the microstructure in the shear specimen corresponds to the microstructure seen in the solder interconnects of functional electronics. Since the properties derived from the above mentioned microstructure are representative of a wide range of grain orientations, average model constants are used. The applicability of these average creep constants in predicting the measured stress relaxation data [1], in the same average sense that is comparable to the degree of scatter in the measurements has been reported by the authors [3].

Traditionally used primary (generalized exponential) and secondary (Garofalo hyperbolic) creep laws based on a continuum and homogeneous microstructure are used. The saturation rates of thermal cycling damage and durability is determined as a function of different dwell times, using a 3D viscoplastic finite element model of a selected BGA256 assembly (Figure 1). In order to assess the damage in the solder as a function of dwell times, the response to accelerated and field loads are considered. It is important to assess the damage under both conditions so that the accelerated load damage can be related to the damage seen in real field loads.

The accelerated thermal cycling profile used is the standard 125°C to -40°C profile with a heating and cooling ramp of 6°C /min and 10°C /min respectively. The hot dwell time is parametrically varied from traditionally used of 15 minutes for SnPb solder to three hours. Three hours is chosen as the maximum allowable dwell time. The cold dwell is fixed at 15 minutes for all the analyses. The field profile modeled is that seen typically in a laptop. The temperature extremes are room temperature (25°C) and 60°C. The dwell times adopted are three hours at hot and cold ends. The ramps are 2°C/min during heating and cooling.

The SAC305 solder is modeled using a partitioned viscoplastic constitutive model which includes only the measured secondary creep [2]. The primary creep is ignored in this preliminary assessment to be consistent with the methodology used to derive the Energy-Partitioning damage constants [4] used in this study. The elastic and plastic properties used to model SAC305 solder are those measured by Zhang [4] from near-eutectic SAC387 solder. Cyclic plastic and creep work dissipation are extracted to assess fatigue durability. The damage saturation rate is then expressed, in terms of an acceleration factor (AF), relative to the damage caused by a typical field condition.

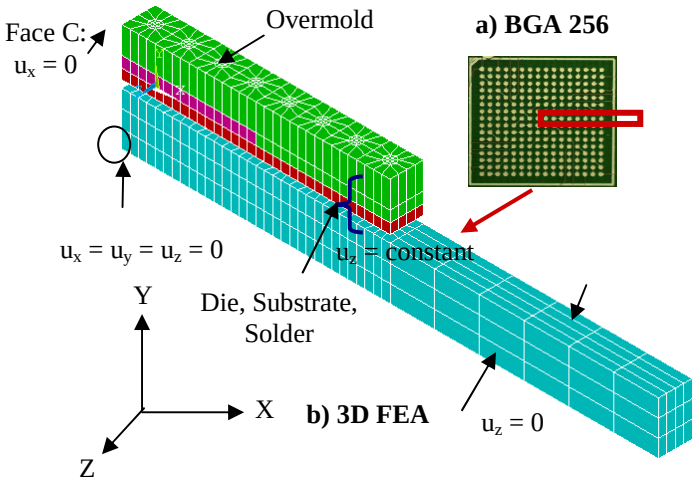

Figure 1: a) BGA 256 IO package b) 3-D finite element slice model of the BGA

RESULTS

The optimal dwell results based on various criteria proposed by the industry sponsors are detailed next. First the predictive capability of the measured creep constants is addressed. Complete details are available elsewhere [3], and only the conclusion is stated here for completeness. As seen in Fig. (2), the measured creep

constants (constant stress loads) can indeed be used to predict the stress relaxation response (variable stress history) [3]. Furthermore the trends of the stress relaxation predictions are consistent with the trends of the creep constants fit. The effect of inclusion and exclusion of primary creep to model the solder's viscoplastic response is also investigated.

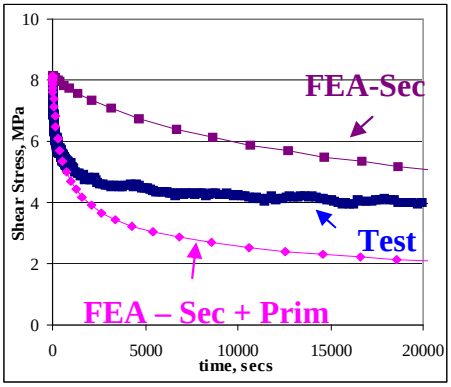

Figure 2: Stress relaxation prediction based on average behavior creep constants relative to measurements - ~8MPa, 25°C

Once the predictive capability of the measured creep constants is verified, the PoF modeling of BGA256 assemblies is conducted to predict the optimal dwell under thermal cycling. The damage metric used for comparing SAC 305 and SnPb assemblies is in terms of AF. Based on the PoF modeling, the AFs for both SnPb and SAC305 assemblies are found to increase asymptotically to a saturated value as the dwell time is increased. SAC305 assemblies are found to be almost double the AFs of the SnPb assembly, for comparable dwell times. The damage saturation rate in SAC305 is less than that in SnPb. These results are consistent with the trends reported in the literature [5]. Consequently, the AFs in SnPb assemblies for the typical 15 min hot dwell can be easily exceeded with a similar dwell in SAC assemblies.

For comparison, the varying magnitudes of damage saturation in SAC305 and SnPb are normalized to a common scale. Thus, if the dwell time is chosen based on

matching the normalized percent damage saturation rate that the SnPb achieves in 15 minutes, the corresponding time for SAC is almost two hours (Figure 3). It is also instructive to examine the damage accumulation rate (i.e. damage per unit time) and the corresponding saturation rate, instead of damage per cycle.

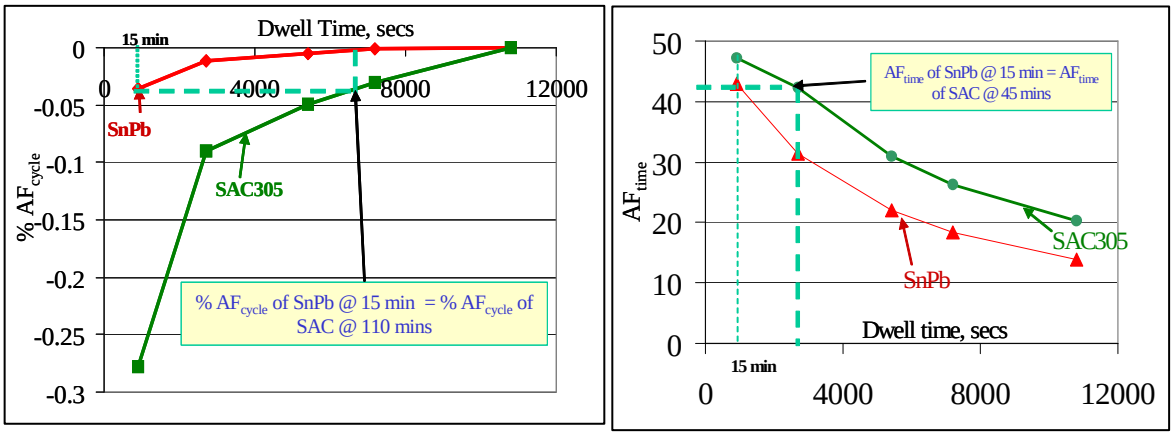

Figure 3: BGA plots of (a) normalized AF_{cycle} versus hot dwell time and (b) normalized AF_{time} versus hot dwell time

When the AFs are re-estimated in terms of time to failure as opposed to cycles to failure, a critical difference is that while the cyclic damage (and related AF curves) monotonically increased with increasing dwell time, the damage rates (and the related AF curves) are found to monotonically decrease. The cycle time grows faster than the cyclic damage with increasing dwell. This is because a significant portion of the total cyclic creep damage occurs during the ramp, and not just during the dwell. Once again, the AF for SAC305 is found to be higher than that of SnPb for comparable dwells (Figure 4).

This implies that SAC305 will require less dwell time than SnPb to achieve comparable durability (in terms of time to failure). Furthermore the time to failure (and AF) will worsen as the dwell time is increased. The conclusions above are

qualitatively generic and quantitatively dependent on the chosen assembly and temperature profiles. Furthermore, these preliminary results are based on modeling of only the secondary creep in the solder and must be re-assessed by including primary creep.

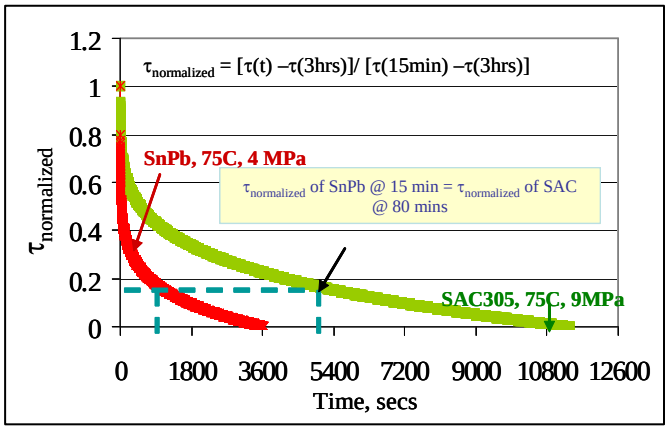

Figure 4: Optimized hot dwell from TMM stress relaxation data

The predicted damage saturation curves are now compared with the measured stress relaxation curves for SAC305 and Sn37Pb at elevated temperature. For consistency, the initial stress for the SAC and SnPb stress relaxation curves are chosen to be the stresses at the start of the hot dwell in the accelerated temperature cycling test (9 and 4 MPa respectively). The normalized data shows that SAC305 will need to dwell almost an hour and a half to achieve the same normalized percent stress relaxation as Sn37Pb at 15 minutes (Figure 4). If the same initial stress is used for comparing stress saturation of both solders, this value corresponds to almost an hour for SAC305.

CONLUSIONS

The optimal hot dwell time in accelerated thermal cycling profiles for Pb-free Sn3.0Ag0.5Cu (SAC305) solder is determined, using viscoplastic testing and physics of failure (PoF) modeling. The fatigue durability of BGA 256 assembly under accelerated thermal cycling and field conditions is predicted using 3D viscoplastic

FEA. The optimal dwell time based on PoF models is predicted by matching the damage saturation of SAC305 with the damage of SnPb at 15 minute hot dwell. PoF predictions show that SAC305 is almost twice as durable as SnPb, for comparable dwell times. As expected, the damage saturation rate in SAC305 is less than that in SnPb. These results are consistent with findings in literature. The predicted damage saturation curves are further compared with the measured stress relaxation curves for SAC305 and Sn37Pb at elevated temperature. The optimal dwell times are provided in terms of various damage saturation criteria proposed by sponsor industries. Based on this study, the optimal hot dwell times to be used for the given 125^0 C to -40^0 C standard accelerated temperature profile range from 15 minutes to two hours, for SAC305.

References

[1] Cuddalorepatta, G., et al., "Stress Relaxation Characterization of Hypoeutectic Sn3.0Ag0.5Cu Pb-free Solder: Experiment and Modeling", *EuroSimE* 2007

[2] Cuddalorepatta, G., et al., "Viscoplastic Behavior of Hypo-Eutectic Sn3.0Ag0.5Cu Pb-Free Alloy under Creep Loading Conditions", *ASME IMECE* 2007

[3] Cuddalorepatta, G., et al., "Effect of Primary Creep Behavior on Fatigue Damage Accumulation Rates in Accelerated Thermal Cycling of Sn3.0Ag0.5Cu Pb-Free Interconnects", *EuroSimE* 2008

[4] Zhang, Q., 2004, "Isothermal Mechanical and Thermo mechanical Durability Characterization of Selected Pb-Free Solders", Ph.D. Dissertation, University of Maryland, College Park, MD, USA.

[5] Chaparala, S., et al., “Effect of Dwell Times and Ramp Rates on the Thermal Cycling Reliability of Pb-free Wafer- Level Chip Scale Packages – Experiments and Modeling”, *ASME IMECE* 2005

Appendix 5.3: Results of sanity check under creep load

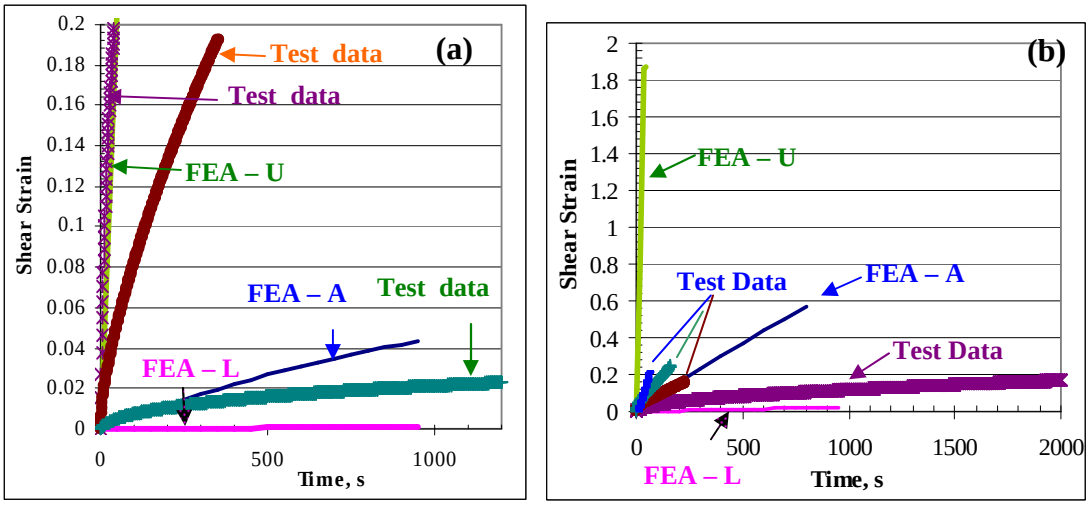

Figure A5.3.1 : Results of creep loading sanity checks at (a) 15 MPa, 25°C, and (b) 20 MPa, 25°C. U, A, and L refer to the predictions from upper bound, average fit and lower bound based creep models. The material model uses both primary and secondary creep.

Appendix 5.4: Stress relaxation predictions at other loads

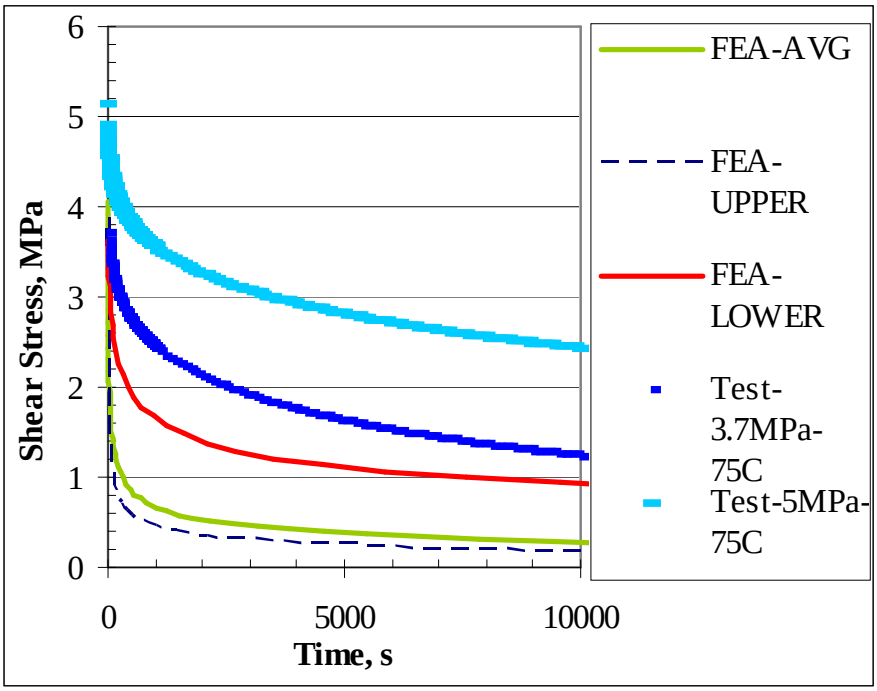

Figure A5.4.1: Stress relaxation predictions at 4 MPa, 75°C, using secondary and primary creep models. The legends upper, avg., and lower refer to the predictions from upper bound, average fit and lower bound based creep models.

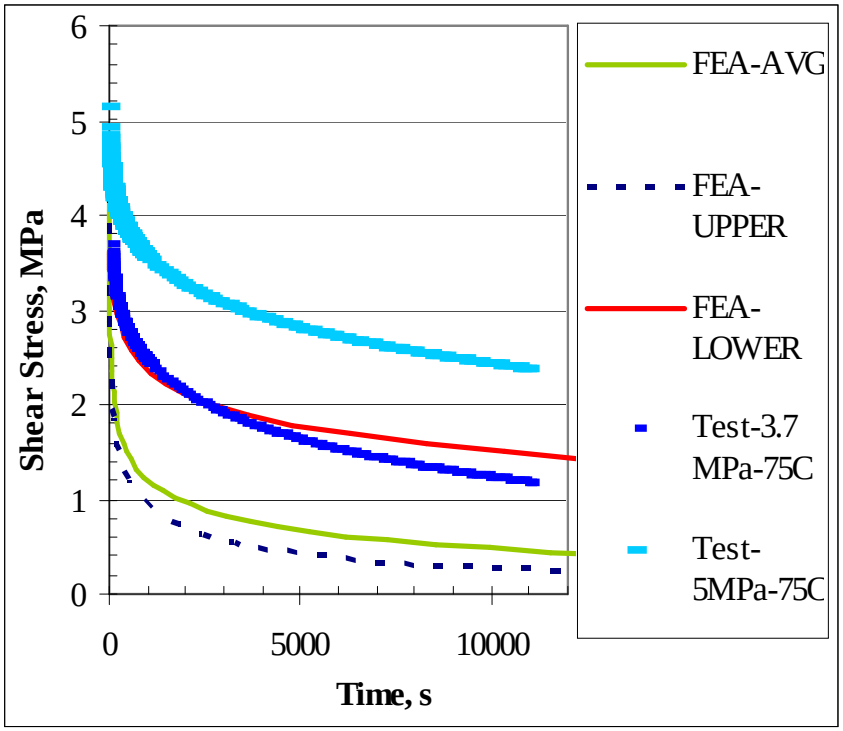

Figure A5.4.2: Stress relaxation predictions at 4 MPa, 75°C, using secondary creep models. The legends upper, avg., and lower refer to the predictions from upper bound, average fit and lower bound based creep models.

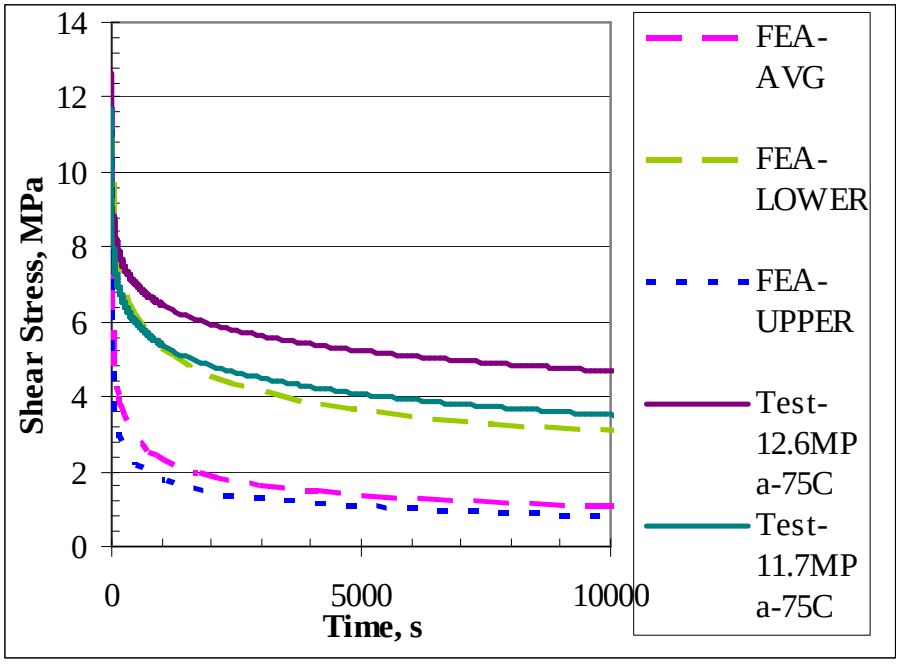

Figure A5.4.3: Stress relaxation predictions at 12 MPa, 75°C, using primary and secondary creep models. The legends upper, avg., and lower refer to the predictions from upper bound, average fit and lower bound based creep models.

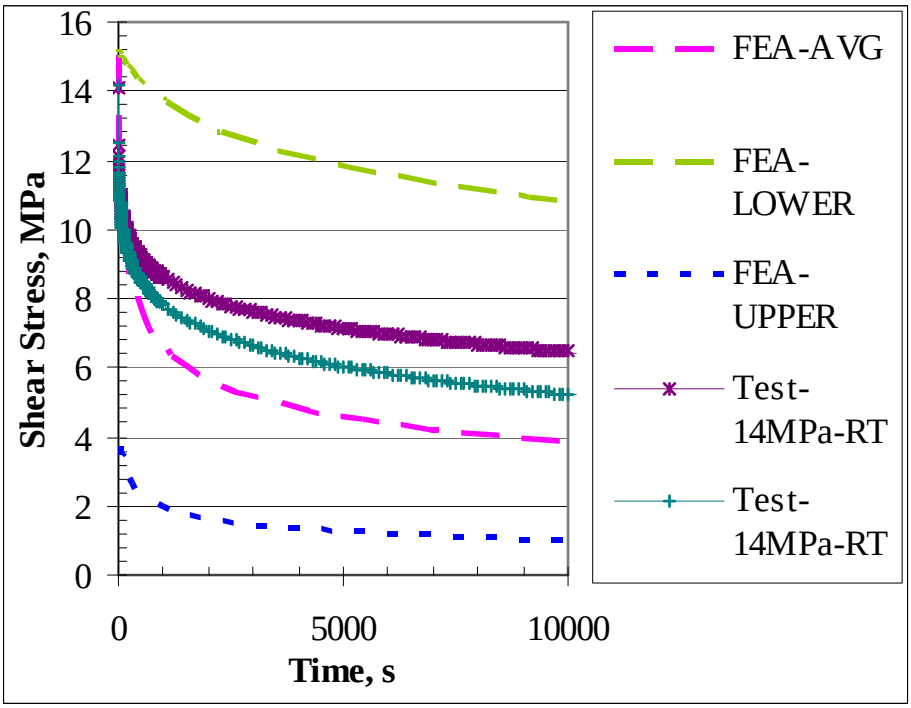

Figure A5.4.4: Stress relaxation predictions at 14 MPa, 25°C, using primary and secondary creep models. The legends upper, avg., and lower refer to the predictions from upper bound, average fit and lower bound based creep models.

Appendix 6.1: Isothermal Mechanical Fatigue Test Load Conditions

Plasticity dominated fatigue results are important for mechanical loading applications such as quasi-static flexure, vibration, drop-impact, where creep damage is minimal. Cyclic mechanical durability at elevated temperatures and low strain rate, where the ratio of creep damage to plastic damage is higher, such as in thermal cycling loads, is labeled as a 'low-plasticity' test, for convenience. Durability data obtained under both the above test conditions can then be consolidated to derive fatigue curves using partitioned cyclic plastic and creep work densities as damage metrics[104].

Appendix 6.2: Cyclic Softening and Evolution of Damage Metrics Used in the Fatigue Curves

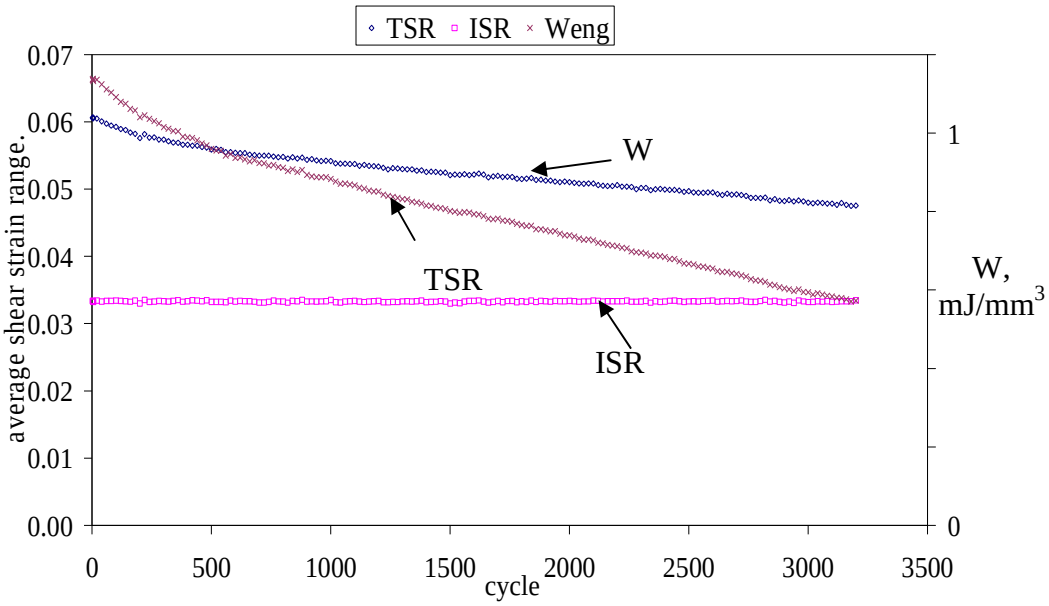

Figure A6.2-1: Variation of W, ISR and TSR in an ISR controlled test (test conditions: creep-minimized 25°C, 5.5E-2 s^{-1} strain rate, 4.4 E-2 strain amplitude)

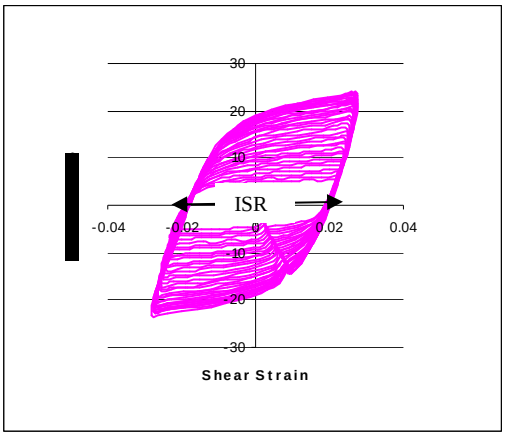

Figure A6.2-2: Cyclic softening evident in the hysteresis loops of SAC305 solder under ISR control low creep loading (25°C, 5.5E-2 s^{-1} strain rate, and 4.4 E-2 strain amplitude)

Appendix 6.3: Creep Contributions to the Stress-Strain Hysteresis Response in the Low Creep Fatigue Loading Regime

The contribution of creep deformation to the hysteresis stress-strain curves measured in the low-creep fatigue load regime is shown in Figure A6.3-1. The plot shows that for the purpose of calculation of the elastic and plastic properties, the contributions of the creep strains to the total strain can be ignored. Hence the stress-total strain curves can be used in place of the elastic-plastic stress-strain curves for evaluating the elastic modulus and the plastic response model constants.

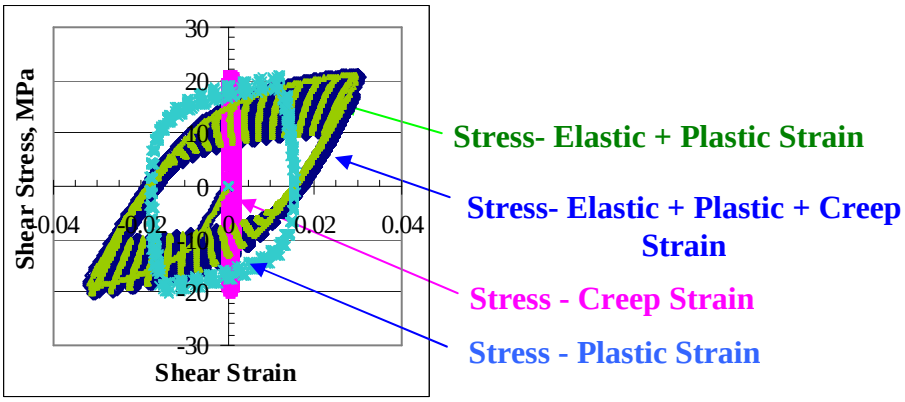

Figure A6.3-1: Contributions of elastic, plastic and creep deformation to the total strain hysteresis loops (25°C, 5.5E-2 s^{-1} strain rate, and 5.5 E-2 strain amplitude)

Appendix 6.4: Elastic-Plastic Measurements

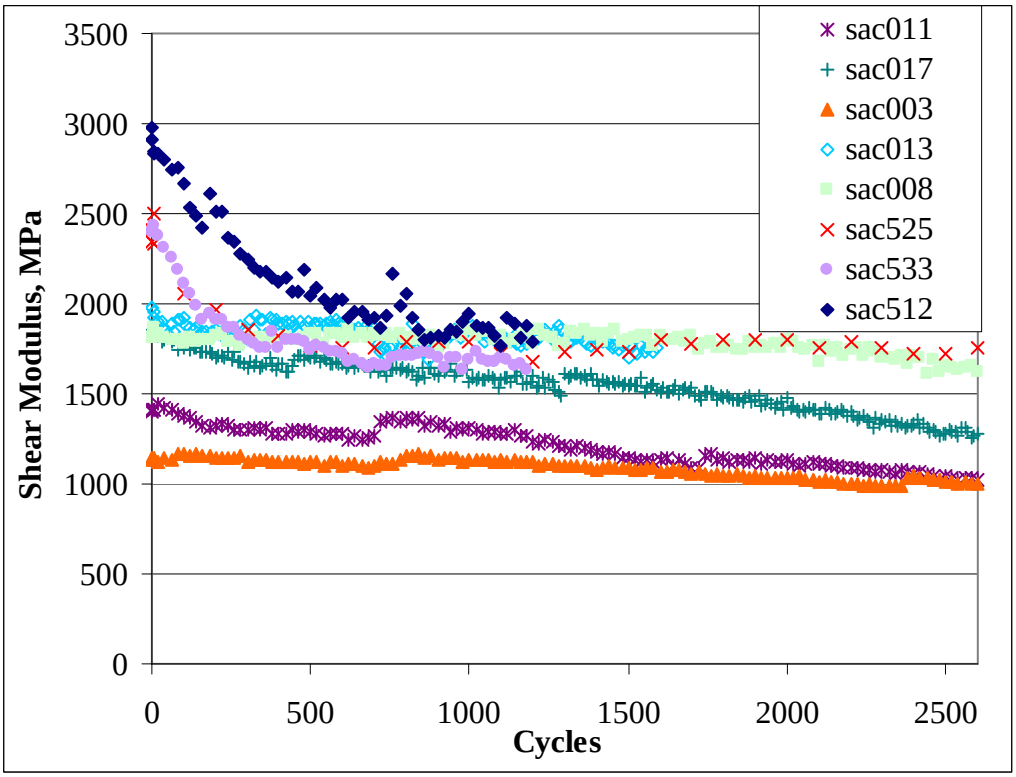

Figure A6.4-1: Shear elastic modulus from isothermal mechanical fatigue data measured at various displacement amplitude loads (25°C, 5.5E-2 s^{-1} strain rate)

Specimen	Cycles to Failure (Φ=0.5)	W (mJ/mm^3)	Load level
SAC512	1200	3.1	Most damaging
SAC 525	8100	0.8	Least Damaging
SAC533	1200	2.3	Intermediate
SAC008	2771	1.2	Repeatability tests at similar (intermediate) damage loads
SAC011	2867	1.4	
SAC003	3208	1.1	
SAC004	3382	1.1	
SAC017	2681	1.3	
SAC013	2732	1.6	

Table A6.4-1: Isothermal mechanical fatigue load amplitude (25°C, 5.5E-2 s^{-1} strain rate)

The shear modulus measurements show that the modulus varies by as much as a factor of 3. In order to understand how this variability changes with increasing damage, measurements conducted at similar load levels should be utilized, namely specimens SAC-0xx series. Specimens SAC-5xx have been included to understand the degradation of properties at different load amplitudes. The measurements on SAC-0xx specimens show that the variability seen in the shear modulus measurements of as-fabricated state does not change significantly with increasing damage. The performance of the damage model in describing the degradation of modulus is provided in Figure A6.4-2.

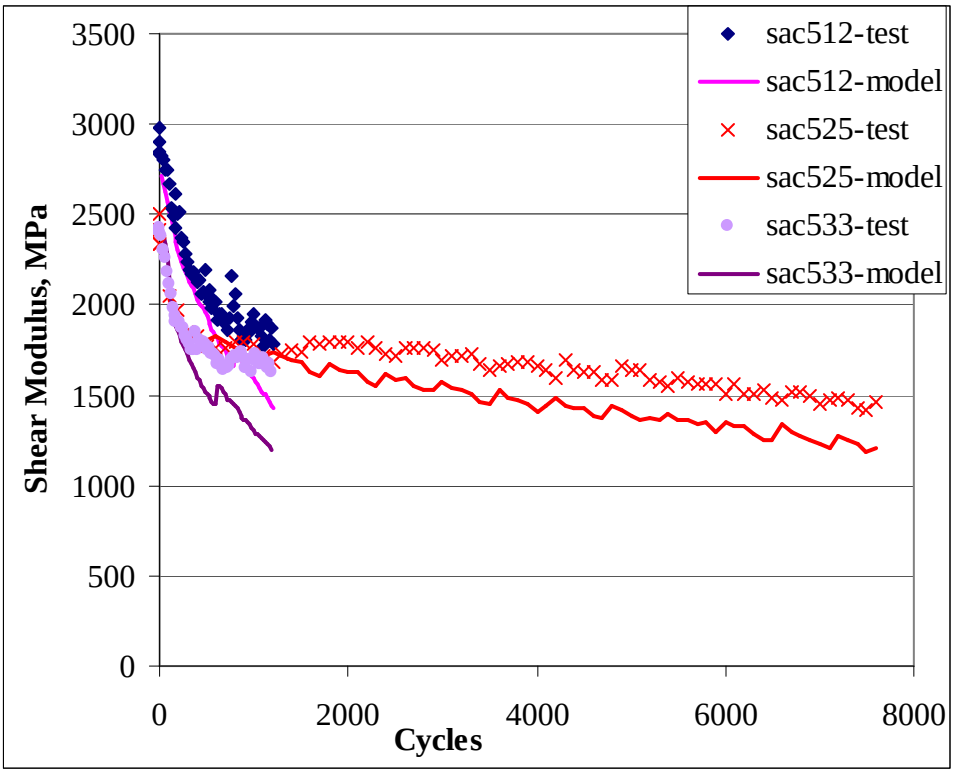

Figure A6.4-2: Comparison of test and damage model performance at various test damage loads – shear modulus

In comparison, the variability in the plastic coefficient, C_p, is as high as a factor of 2.5 in the as-fabricated state and reduces to a factor of 1.5 with increasing damage (Figure A6.4-3). However, only a few specimens exhibit a decrease in variability. The damage model does a better job at capturing the degradation of C_p compared to G, with increasing damage at all load levels. Similarly the variability in the yield stress is as high as a factor of 2 and decreases to 1.5 with increasing damage. The damage model does a reasonably good job of capturing the degradation of yield stress (Figure A6.4-4).

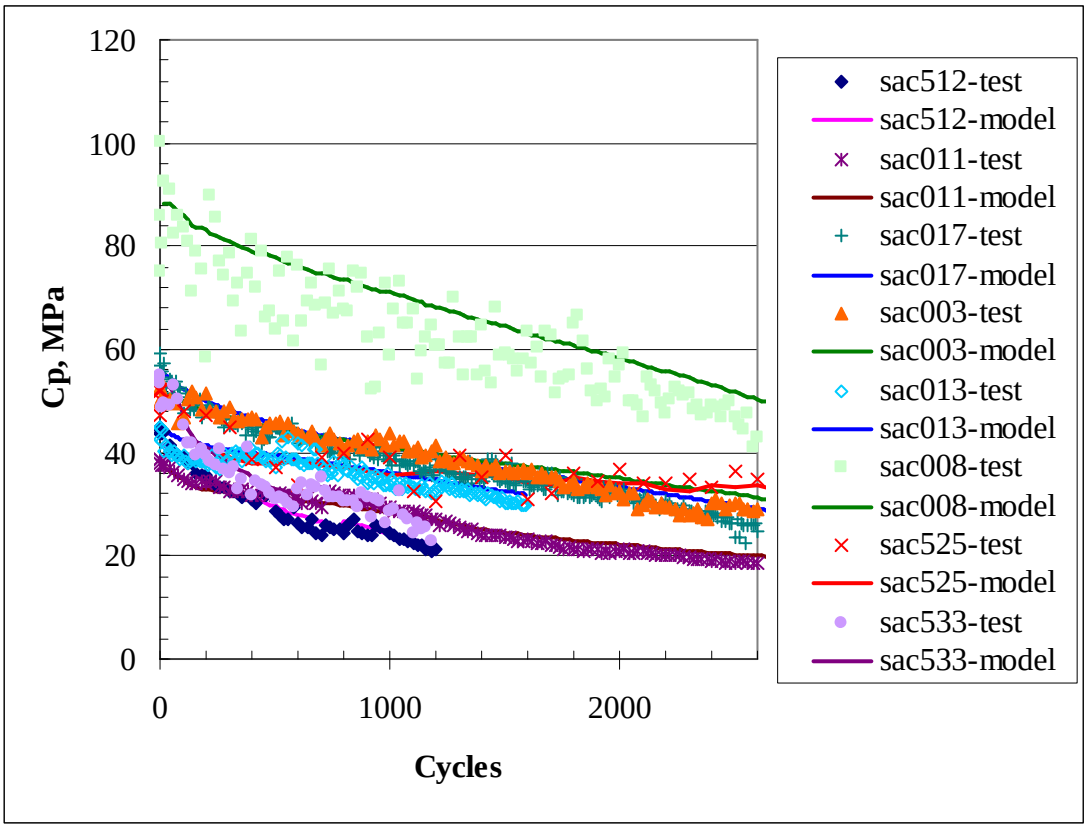

Figure A6.4-3: Comparison of test and damage model performance- C_p

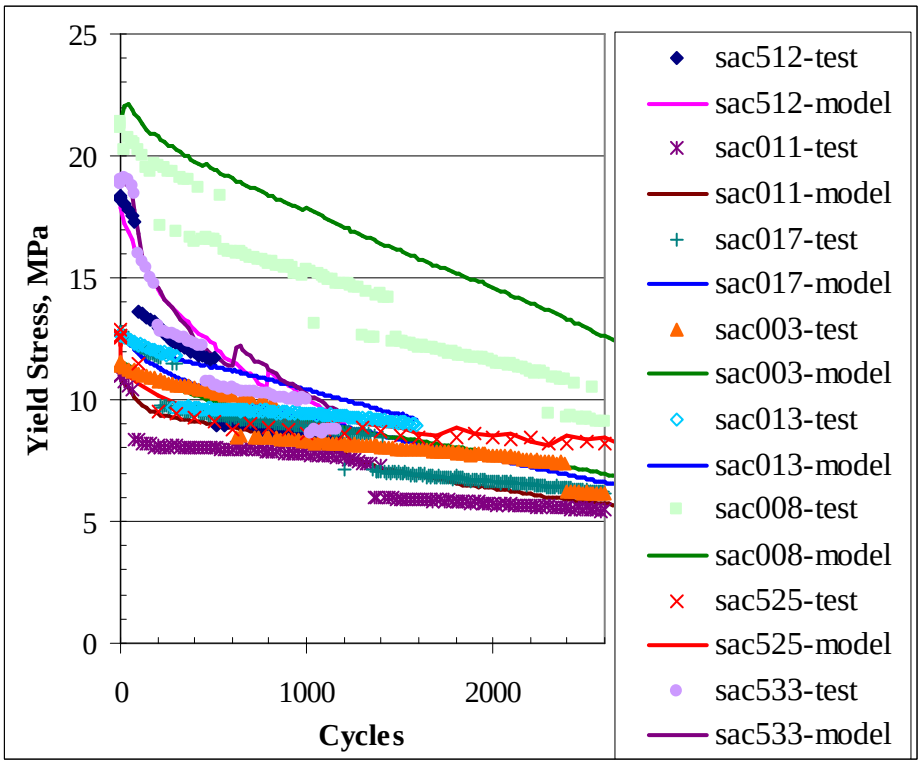

Figure A6.4-4: Comparison of test and damage model performance- yield stress

Appendix 6.5: Possible Reasons for the Deviation of the Damage Model Predictions from the Measured Degradation of Elastic and Plastic Properties.

The fatigue tests are conducted by maintaining the ISR constant (see Figures A6.2-1 and 2 in Appendix 6.2). Hence with an increasing state of fatigue damage to the solder, the displacement amplitude required to maintain the ISR decreases. Since the data acquisition rate is maintained constant, the number of data points available per cycle is decreased. This limits the accuracy of the evaluation the elastic and plastic properties. Another possible reason is due to non-homogeneous damage densities caused by localization phenomena.

Appendix 6.6: Details of FIB analysis and Damage Features in SAC305 TMM specimens in Post-Mechanical Fatigue State

Optical microscopy and ESEM are first used to identify the region of maximum damage (cracks), where recrystallization is possible. In the case of FIB analysis, FIB milling is used to prepare the specimen surface. The region of interest for the milling is set to 100 μm in length, 20 μm in height and 1 μm in depth ($100x20x1\mu m^3$). Figures A6.6.1 a-b show the scale and location FIB cut on the TMM solder specimen. Depending on the crystal orientations relative to the ion beam, the grains are seen as areas of varying contrast in the ion image, due to differences in the reflection and absorption of the ion beams.

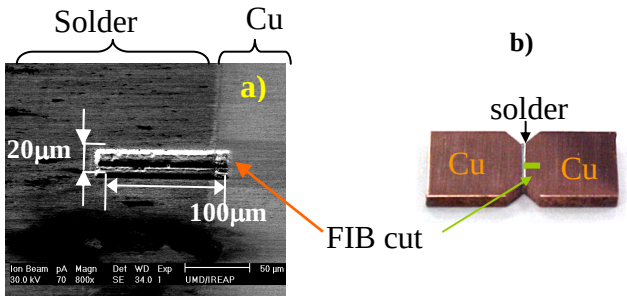

Figure A6.6.1: (a) FIB cut on the (b) TMM specimen

The ion beam and the electron beam are brought into focus at the surface of the specimen. However since the angle between the ion tube and the electron tube is fixed (~53°) , the sample stage needs to be rotated for an appropriate incident beam angle. The quality of the image is hence dependent on the stage tilt angle. Once the region of interest is identified, the material is systematically removed using an accelerated ion beam. The material removal needs to be controlled closely to avoid undercutting of the specimen. In order to view the quality of the cut, the specimen can be viewed simultaneously using the SEM beam. However this requires careful alignment of the stage relative to FIB beam and the SEM beam.

Depending on the crystal orientations relative to the ion beam, the grains appear as areas of varying contrast in the ion image. If the incident ion beam hits the crystal at an angle, such that the ions recoil at the crystal surface or atoms and electrons are sputtered (which can be caught by the detector) then the grains appear very bright in an ion image. If the ion beam hits the surface of the crystal at an angle such that the ions penetrate into the crystal structure of the grain, there will be no recoiling ions, sputtered atoms or electrons (which can be caught by the detector of the FIB device). This results in the grain appearing very dark in the ion-beam image. This method of

imaging can be used to quantitatively detect and distinquish regions of varying crystallographic orientations as well as for making quantitative measurements on the size of these regions.

As an example, the grains as seen in the FIB image from a succesful FIB cut in the polycrystalline copper plates attaching the solder in the TMM specimen are shown in Figure A6.6.2. The grains in the copper region of FIB image show grains with a size range of ~10 to 20µm. The FIB images in the solder region of TMM SAC305 solder specimens is presented in Figure A6.6.3a. The corresponding region when viewed under the XPM is shown in Figure A6.6.3b. Both images reveal two large Sn grains in the solder region.

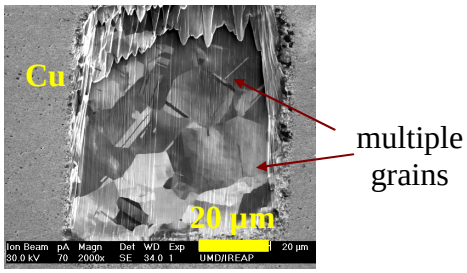

Figure A6.6.2: FIB image of the TMM copper platens showing multiple Cu grains

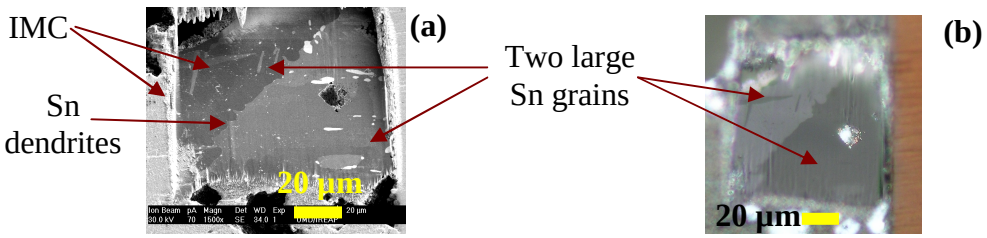

Figure A6.6.3: Images of As-Fabricated TMM joint showing 2 grains from (a) FIB microscopy (b) XPM

Orientation imaging microscopy (OIM) using an electron back-scatter diffraction (EBSD) stage on the SEM is discussed next. The specimens for OIM study are prepared using conventional manual grinding and polishing techniques. Grinding is

carefully conducted using emery paper of 1200 grid and finally polished with diamond paste (10, 4, 1, 0.5 microns) and finally with colloidal silica suspension. As in FIB analysis, regions for local OIM investigation, namely regions near macrocracks, are first identified using SEM. The sample is then scanned in the OIM chamber using a step size of 1 micron and data with confidence index of 0.1 or higher is utilized.

This technique was adopted because the FIB technique cannot distinguish between grains and subgrains. OIM on the other hand, quantitatively identifies and measures not only the boundaries between regions of different crystal orientations but also distinguishes between grains and subgrains. In addition, OIM yields information on the grain boundary angles and characteristics such as subgrain, low angle grain boundary, high angle grain boundary, misorientation angles, twinning regions.

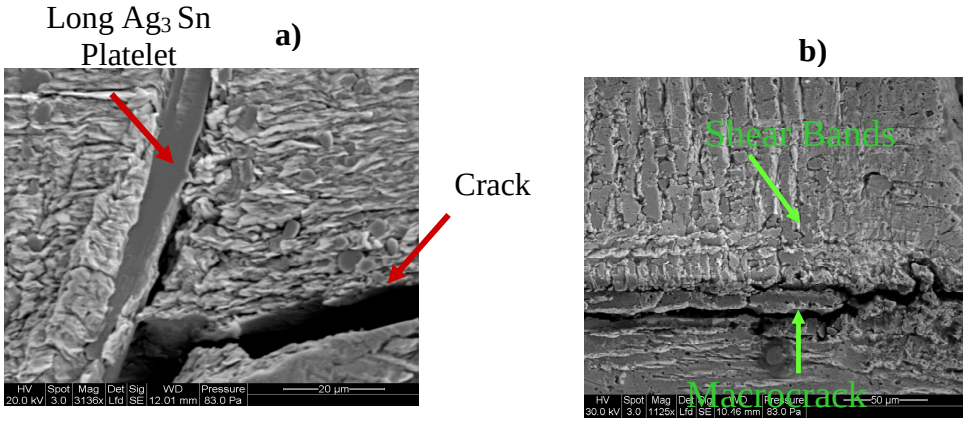

Figure A6.6.4: Post-failure images of SAC305 solder after isothermal mechanical fatigue (no aging) showing (a) the influence of macro-sized IMCs and (b) shear band around macrocrack perpendicular to the loading direction

Bibliography

1. Halford, G.R., Hirschberg, M. H., and Manson, S. S., *Temperature Effects on the Strain-Range Partitioning Approach for Creep Fatigue Analysis.* ASTM STP 520, 1973: p. pp. 658-667.
2. Dasgupta, A., Oyan, C., Barker, D., and Pecht, M., *Solder Creep-Fatigue Analysis by an Energy-Partitioning Approach.* ASME Journal of Electronic Packaging, 1992. 114(2): p. 152-160.
3. Darveaux, R. and K. Banerji, *Constitutive Relations for Tin-Based Solder Joints.* IEEE Transactions on Components Hybrids and Manufacturing Technology 1992. 15(6): p. 1013-1024.
4. *National Electronics Manufacturing Initiative (NEMI) Press Release* http://www.nemi.org/newsroom/PR/2000/PR012400.html. Jan. 24 2000.
5. Ding, Y., et al., *Influence of Aging Treatment on Deformation Behavior of 96.5Sn3.5Ag Lead-Free Solder Alloy During In Situ Tensile Tests.* Journal of Alloys and Compounds, 2007. 428(1-2): p. 274-285.
6. Fouassier, O., et al., *Microstructural Evolution and Mechanical Properties of SnAgCu Alloys.* Journal of Applied Physics, 2006. 100(4).
7. Lauro, P., et al., *Effects of Mechanical Deformation and Annealing on the Microstructure and Hardness of Pb-Free Solders.* 2003: p. 1432-1440.
8. Sidhu, R.S. and N. Chawla, *Microstructure Characterization and Creep Behavior of Pb-Free Sn-Rich Solder Alloys: Part I. Microstructure Characterization of Bulk Solder and Solder/Copper Joints.* Metallurgical and Materials Transactions a-Physical Metallurgy and Materials Science, 2008. 39A(2): p. 340-348.
9. Sigelko, J., et al., *Effect of Cooling Rate on Microstructure and Mechanical Properties of Eutectic Sn-Ag Solder Joints With and Without Intentionally Incorporated Cu_6Sn_5 Reinforcements.* Journal of Electronic Materials, 1999. 28(11): p. 1184-1188.
10. Kerr, M. and N. Chawla, *Creep Deformation Behaviour of Sn-3.5Ag Solder at Small Length Scales.* JOM, 2004. 56(6): p. 50-54.
11. Ochoa, F., X. Deng, and N. Chawla, *Effects of Cooling Rate on Creep Behavior of a Sn-3.5Ag Alloy.* Journal of Electronic Materials 2004. 33 (12): p. 1596-1607.
12. Lee, S.B., I. Kim, and T.S. Park, *Fatigue and Fracture Assessment for Reliability in Electronics Packaging.* International Journal of Fracture, 2008. 150(1-2): p. 91-104.
13. Nurmi, S., Sundelin, J., Ristolainen, E., Lepisto, T., *The Effect of Solder Paste Composition on the Reliability of SnAgCu joints.* Microelectronics Reliability, 2004. 44: p. 485-494.
14. Sidhu, R.S. and N. Chawla, *Thermal Fatigue Behavior of Sn-rich (Pb-Free) Solders.* Metallurgical and Materials Transactions a-Physical Metallurgy and Materials Science, 2008. 39A(4): p. 799-810.

15. Terashima, S., et al., *Effect of Silver Content on Thermal Fatigue Life of Sn-xAg-0.5Cu Flip-chip Interconnects.* Journal of Electronic Materials, 2003. 32(12): p. 1527-1533.
16. Terashima, S., et al., *Improvement of Thermal Fatigue Properties of Sn-Ag-Cu Lead-Free Solder Interconnects on Casio's Wafer-Level Packages Based on Morphology and Grain Boundary Character*. Journal of Electronic Materials, 2009. 38(3): p. 33-38.
17. Terashima, S., M. Tanaka, and K. Tatsumi, *Thermal Fatigue Properties and Grain Boundary Character Distribution in Sn-xAg-0.5Cu (x=1, 1.2 and 3) Lead Free Solder Interconnects.* Science and Technology of Welding and Joining, 2008. 13(1): p. 60-65.
18. Pei, M. and J.M. Qu, *Creep and Fatigue Behavior of SnAg solders with Lanthanum Doping.* IEEE Transactions on Components and Packaging Technologies, 2008. 31(3): p. 712-718.
19. Pei, M. and J.M. Qu, *Effect of Lanthanum Doping on the Microstructure of Tin-Silver Solder Alloys.* Journal of Electronic Materials, 2008. 37(3): p. 331-338.
20. Pei, M., *Effects of Lanthanum Doping on the Microstructure and Mechanical Behavior of a SnAg Alloy*, in *Ph.D. dissertation in Mechanical Engineering*. 2007, Georgia Institute of Technology: Atlanta.
21. K.-W. Moon, W.J.B., U.R. Kattner, F.S. Biancaniello and C.A. Handwerker, , *Experimental and Thermodynamic Assessment of Sn–Ag–Cu Solder Alloys.* Journal of Electronic Materials , 2000. 29 (10): p. pp. 1122-1136.
22. Borgesen, P., et al., *Pb-free Solder: New Materials Considerations for Microelectronics Processing.* MRS Bulletin, 2007. 32(4): p. 360-365.
23. Kang, S.K., et al., *Microstructure and Mechanical Properties of Lead-Free Solders and Solder Joints used in Microelectronic Applications.* IBM Journal of Research and Development, 2005. 49(4-5): p. 607-620.
24. Lehman, L.P., et al., *Growth of Sn and Intermetallic Compounds in Sn-Ag-Cu solder.* Journal of Electronic Materials, 2004. 33(12): p. 1429-1439.
25. H.J. Fecht, M.-X.Z., Y.A. Chang and J.H. Perepezko, Metall. Trans. A, 1989. 20A p. 795-803.
26. National Institute of Standards and Technology (NIST), M.S.E.L. http://www.metallurgy.nist.gov/phase/solder/pbsn.html.
27. Dutta, I., C. Park, and S. Choi, *Impression Creep Characterization of Rapidly Cooled Sn-3.5Ag Solders.* Materials Science and Engineering A-Structural Materials Properties Microstructure and Processing, 2004. 379(1-2): p. 401-410.
28. Bonar, L.G. and G.B. Craig, *Activation Energy for Creep of Tin.* Canadian Journal of Physics, 1958. 36(11): p. 1445-1449.
29. Brar, N.S. and W.R. Tyson, *Elastic and Plastic Anisotropy of White Tin.* Canadian Journal of Physics, 1972. 50(19): p. 2257-&.
30. Chandrasekhar, J.A.R.a.B.S., *Elastic Constants of β Tin from 4.2°K to 300°K.* Phys. Rev. , 1960. 115: p. 1658
31. Chu, S.N.G. and J.C.M. Li, *Impression Creep of Beta-Tin Single-Crystals.* Materials Science and Engineering, 1979. 39(1): p. 1-10.

32. Chu, S.N.G. and J.C.M. Li, *Pencil Slip in Beta-Tin Single-Crystals.* Journal of Materials Science, 1980. 15(11): p. 2733-2742.
33. Ekinci, A.E., et al., *Flow Behaviour of Beta-Sn Single Crystals.* Indian Journal of Engineering and Materials Sciences, 2003. 10(5): p. 416-418.
34. Peirce, D., R.J. Asaro, and A. Needleman, *An Analysis of Nonuniform and Localized Deformation in Ductile Single-Crystals.* Acta Metallurgica, 1982. 30(6): p. 1087-1119.
35. Sahin, O., et al., *Vickers Microindentation Hardness Studies of Beta-Sn Single Crystals.* Materials Characterization, 2007. 58(2): p. 197-204.
36. Sunada, T., et al., *Dynamic Recrystallization of Pure Tin.* Journal of the Japan Institute of Metals, 1999. 63(4): p. 467-473.
37. Weertman, J., *Compressional Creep of Tin Single CrystalS.* Journal of Applied Physics, 1957. 28(2): p. 196-197.
38. Weertman, J. and J.E. Breen, *Creep of Tin Single Crystals.* Journal of Applied Physics, 1956. 27(10): p. 1189-1193.
39. Yang, F.Q. and J.C.M. Li, *Deformation Behavior of Tin and Some Tin Alloys.* Journal of Materials Science-Materials in Electronics, 2007. 18(1-3): p. 191-210.
40. Arafei, B., Cotts, E., et al., *The Effect of Sn Grain Number and Orientation on the Shear Fatigue Life of SnAgCu Solder Joints*, in IEEE ECTC Proceedings. 2008.
41. Bieler, T.R., et al., *Influence of Sn Grain Size and Orientation on the Thermomechanical Response and Reliability of Pb-free Solder Joints.* IEEE Transactions on Components and Packaging Technologies, June 2008. 31(2): p. 12.
42. LaLonde, A., et al., *Quantitative Metallography of Beta-Sn Dendrites In Sn-3.8Ag-0.7Cu Ball Grid Array Solder Balls Via Electron Backscatter Diffraction and Polarized Light Microscopy.* Journal of Electronic Materials, 2004. 33(12): p. 1545-1549.
43. Matin, M.A., W.P. Vellinga, and M.G.D. Geers, *Microstructure Evolution in a Pb-Free Solder Alloy during Mechanical Fatigue.* Materials Science and Engineering a-Structural Materials Properties Microstructure and Processing, 2006. 431(1-2): p. 166-174.
44. Park, S., et al., *Measurement of Deformations in SnAgCu Solder Interconnects under In Situ Thermal Loading.* Acta Materialia, 2007. 55(9): p. 3253-3260.
45. Park, S., et al., *Grain Deformation and Strain in Board Level SnAgCu Solder Interconnects under Deep Thermal Cycling.* IEEE Transactions on Components and Packaging Technologies, 2007. 30(1): p. 178-185.
46. Sylvestre, J. and A. Blander, *Large-scale Correlations in the Orientation of Grains in Lead-Free Solder Joints.* Journal of Electronic Materials, 2008. 37(10): p. 1618-1623.
47. Telang, A.U. and T.R. Bieler, *The Role of Special Boundaries during Solidification and Microstructure Evolution in Lead Free Solder Joints*, in *ICOTOM 14: Textures Of Materials, Parts 1 and 2* P.V. Houtte and L. Kestens, Editors. 2005. p. 1419-1424.

48. Telang, A.U. and T.R. Bieler, *Dislocation Activity and Slip Analysis Contributing to Grain Boundary Sliding and Damage during Thermo Mechanical Fatigue in Dual Shear Lead-Free Solder Joint Specimens*, in *Texture And Anisotropy Of Polycrystals II Book Series: Solid State Phenomena Volume: 105 Pages: 219-225 Published: 2005* C. Esling, et al., Editors. 2005. p. 219-225.
49. Telang, A.U. and T.R. Bieler, *The Orientation Imaging Microscopy of Lead-free Sn-Ag Solder Joints.* JOM, 2005. 57(6): p. 44-49.
50. Telang, A.U., et al., *Orientation Imaging Studies of Sn-Based Electronic Solder Joints.* Journal of Materials Research, 2002. 17(9): p. 2294-2306.
51. Sundelin, J.J., S.T. Nurmi, and T.K. Lepisto, *Recrystallization Behaviour of SnAgCu Solder Joints.* Materials Science and Engineering a-Structural Materials Properties Microstructure and Processing, 2008. 474(1-2): p. 201-207.
52. Mattila, T.T., Vuorinen, V., Kivilahti, J.K., *Impact of Printed Wiring Board Coatings on the Reliability of Lead-Free Chip-Scale Package Interconnections.* Journal of Material Research, 2004. 19(11): p. 3214.
53. Terashima, S., et al., *Recrystallization of Sn Grains due to Thermal Strain in Sn-1.2Ag-0.5Cu-0.05Ni Solder.* Materials Transactions, 2004. 45(4): p. 1383-1390.
54. Fix, A.R., W. Nuchter, and J. Wilde, *Microstructural Changes of Lead-Free Solder Joints during Long-Term Ageing, Thermal Cycling and Vibration Fatigue.* Soldering & Surface Mount Technology, 2008. 20(1): p. 13-21.
55. Laurila, T., et al., *Evolution of Microstructure and Failure Mechanism of Lead-Free Solder Interconnections in Power Cycling and Thermal Shock Tests.* Microelectronics Reliability, 2007. 47(7): p. 1135-1144.
56. Henderson, D.W., Woods, J. J., , *The Microstructure of Sn in Near-eutectic Sn-Ag-Cu Alloy Solder Joints and its Role in Thermomechanical Fatigue.* Journal of Materials Research, 2004. 19(6): p. 1608-1612.
57. Matin, M.A., et al., *Correlation between Thermal Fatigue and Thermal Anisotropy in a Pb-free Solder Alloy.* Scripta Materialia, 2005. 53(8): p. 927-932.
58. Telang, A.U., Bieler, T. R., Mason, D. E., Subramanian, K. N., *Comparisons of Experimental and Computed Crystal Rotations caused by Slip in Crept And Thermomechanically Fatigued Dual-Shear Eutectic Sn-Ag solder joints.* J. Electr. Mater., 2003. 32(12): p. 1455-1462.
59. Telang, A.U., et al., *Incremental Recrystallization/Grain Growth Driven by Elastic Strain Energy Release in a Thermomechanically Fatigued Lead-Free Solder Joint.* Acta Materialia, 2007. 55(7): p. 2265-2277.
60. Zhao, J., Miyashita, Y., Mutoh, Y., *Fatigue Crack Growth Behavior of 95Pb-5Sn Solder under Various Stress Ratios and Frequencies.* International Journal of Fatigue, 2000. 22: p. 665.
61. Reinkainen, T., *Deformation characteristics and microstructure of SAC Solders*, in IEEE ECTC Proceedings. 2007.
62. Mattila, T.T. and J.K. Kivilahti, *Reliability of lead-free interconnections under consecutive thermal and mechanical loadings.* Journal of Electronic Materials, 2006. 35(2): p. 250-256.

63. Vianco, P.T., J.A. Rejent, and A.C. Kilgo, *Time-independent mechanical and physical properties of the ternary 95.5Sn-3.9Ag-0.6Cu solder.* Journal of Electronic Materials, 2003. 32(3): p. 142-151.
64. Korhonen, T.M.K., et al., *Isothermal fatigue behavior of the near-eutectic Sn-Ag-Cu alloy between-25 degrees C and 125 degrees C.* Journal of Electronic Materials, 2007. 36(2): p. 173-178.
65. Jud, P.P., et al., *Local creep in SnAg3.8Cu0.7 lead-free solder*. Journal of Electronic Materials, 2005. 34(9): p. 1206-1214.
66. Sharma, P., *Micro-structural modeling of cyclic creep damage in tin-lead eutectic solder*, in *Ph.D. dissertation in Mechanical Engineering*. 2000, University of Maryland: College Park.
67. Dutta, I., *A constitutive model for creep of lead-free solders undergoing strain-enhanced microstructural coarsening: A first report.* Journal of Electronic Materials, 2003. 32(4): p. 201-207.
68. Andersson, C., et al., *Thermal cycling aging effect on the shear strength, microstructure, intermetallic compounds (IMC) and crack initiation and propagation of reflow soldered Sn-3.8Ag-0.7Cu and wave soldered Sn-3.5Ag ceramic chip components.* IEEE Transactions on Components and Packaging Technologies, 2008. 31(2): p. 331-344.
69. Guo, F., et al., *Processing and aging characteristics of eutectic Sn-3.5Ag solder reinforced with mechanically incorporated Ni particles.* Journal of Electronic Materials, 2001. 30(9): p. 1073-1082.
70. Kang, S.K., et al., *The microstructure, thermal fatigue, and failure analysis of near-ternary eutectic Sn-Ag-Cu solder joints.* Materials Transactions, 2004. 45(3): p. 695-702.
71. Xiao, Q., L. Nguyen, and W.D. Armstrong, *The anomalous microstructural, tensile, and aging response of thin-cast Sn3.9Ag0.6Cu lead-free solder*. Journal of Electronic Materials, 2005. 34(5): p. 617-624.
72. Cugnoni, J., et al., *Experimental and numerical studies on size and constraining effects in lead-free solder joints.* Fatigue & Fracture of Engineering Materials & Structures, 2007. 30(5): p. 387-399.
73. Gong, J.C., et al., *Modelling of Ag3Sn coarsening and its effect on creep of Sn-Ag eutectics.* Materials Science and Engineering a-Structural Materials Properties Microstructure and Processing, 2006. 427(1-2): p. 60-68.
74. Liang, J., N. Dariavach, and D. Shangguan. *Solidification condition effects on microstructures and creep resistance of Sn-3.8Ag-0.7Cu lead-free*. 2007.
75. Ma, H. and J.C. Suhling, *A review of mechanical properties of lead-free solders for electronic packaging*. Journal of Materials Science, 2009. 44(5): p. 1141-1158.
76. Sidhu, R.S., X. Deng, and N. Chawla, *Microstructure characterization and creep behavior of Pb-free Sn-rich solder alloys: Part II. Creep behavior of bulk solder and solder/copper joints.* Metallurgical and Materials Transactions a-Physical Metallurgy and Materials Science, 2008. 39A(2): p. 349-362.
77. Vianco, P.T., J.A. Rejent, and A.C. Kilgo, *Creep behavior of the ternary 95.5Sn-3.9Ag-0.6Cu solder: Part II - Aged condition.* Journal of Electronic Materials, 2004. 33(12): p. 1473-1484.

78. Vianco, P.T., J.A. Rejent, and A.C. Kilgo, *Creep behavior of the ternary 95.5Sn-3.9Ag-0.6Cu solder - Part 1: As-cast condition.* Journal of Electronic Materials, 2004. 33(11): p. 1389-1400.
79. Wielage, B., D. Weber, and T. Lampke, *Evaluation of solders and solder joints processed in lead free solder baths with increasing copper content.* Materialwissenschaft Und Werkstofftechnik, 2008. 39(1): p. 66-74.
80. Wiese, S., et al., *The effect of downscaling the dimensions of solder interconnects on their creep properties.* Microelectronics Reliability, 2008. 48 (6): p. 843-850.
81. Andersson, C., et al., *Comparison of isothermal mechanical fatigue properties of lead-free solder joints and bulk solders.* Materials Science and Engineering a-Structural Materials Properties Microstructure and Processing, 2005. 394(1-2): p. 20-27.
82. Kinyanjui, R., et al., *Effect of sample size on the solidification temperature and microstructure of SnAgCu near eutectic alloys.* Journal of Materials Research, 2005. 20(11): p. 2914-2918.
83. Cugnoni, J., J. Botsis, and J. Janczak-Rusch, *Size and constraining effects in lead-free solder joints.* Advanced Engineering Materials, 2006. 8(3): p. 184-191.
84. Wiese, S., and Wolter, K.-J., *Microstructure and creep behavior of eutectic SnAg and SnAgCu solders.* Microelectronics Reliability, 2004. 44: p. 1923 - 1931.
85. Iosipescu, N., *New Accurate Procedure for Single Shear Testing of Metals.* J. Materials, September 1967. 2(3): p. 537-566.
86. Reinkainen, T., Poech, M., Krumm, M., Kivilahti, J., , *A finite-element and experimental analysis of stress distribution in various shear tests for solder joints.* Journal of Electronic Packaging, Transactions ASME, 1998. 120 (1): p. 106-113.
87. Shen, Y.L., et al., *Deformation analysis of lap-shear testing of solder joints.* Acta Materialia, 2005. 53(9): p. 2633-2642.
88. Unal, O., et al., *Application of an asymmetrical four point bend shear test to solder joints.* Journal of Electronic Materials 2001. 30(9): p. 1206-1213.
89. Unal, O., D.J. Barnard, and I.E. Anderson, *A shear test method to measure shear strength of metallic materials and solder joints using small specimens.* Scripta Materialia, 1999. 40(3): p. 271-276.
90. Shin, S.W. and J. Yu, *Creep deformation of Sn-3.5Ag-xCu and Sn-3.5Ag-xBi solder joints.* Journal of Electronic Materials, 2005. 34(2): p. 188-195.
91. Nieland, S., Bähr, M., Böttger, A., *Advantages of microelectronic packaging for reliable lead free soldering of thin solar cells, 1st International Congress on Microreliability and Nanoreliability in Key Technology Applications*, September 2007, Berlin, Advantages of microelectronic packaging for reliable lead free soldering of thin solar cells, in 1st International Congress on Microreliability and Nanoreliability in Key Technology Applications. September 2007: Berlin, Germany.

92. Cuddalorepatta G., D.A., et. al,, *Durability of Pb-free solder between copper interconnect and silicon in photovoltaic cells.* Progress in Photovoltaics: Research and Applications 2010. 18:168–182, (DOI: 10.1002/pip.944).
93. Kariya, Y., et al., *Assessment of low-cycle fatigue life of Sn-3.5mass%Ag-X (X = Bi or Cu) alloy by strain range partitioning approach.* Journal of Electronic Materials, 2001. 30(9): p. 1184-1189.
94. Schubert A., D., H., Walter, Jung, *Reliability Assessment of Flip-Chip Assemblies with Lead-free Solder Joints*, in IEEE Electronics Components and Technology Conference, 2002. p. 1246.
95. Zhang, Q., Isothermal Mechanical and Thermo-mechanical Durability Characterization of Selected Pb-Free Solders, *Ph.D. Dissertation in Mechanical Engineering,*. Vol. PhD. 2004, College Park, MD USA: University of Maryland.
96. Roettele, S.M., *Probabilistic Physics of Failure Assessment of Thermomechanical Fatigue in High-I/O Area-Array Interconnects*, in MS thesis in Mechanical Engineering. 2009, University of Maryland, College Park.
97. Choi, S., et al., *Microstructural characterization of damage in thermomechanically fatigued Sn-Ag based solder joints.* Journal of Electronic Materials, 2002. 31(4): p. 292-297.
98. Siviour, C.R., et al., *Mechanical properties of SnPb and lead-free solders at high rates of strain.* Journal of Physics D-Applied Physics, 2005. 38(22): p. 4131-4139.
99. Anderson, I.E. and J.L. Harringa, *Elevated temperature aging of solder joints based on Sn-Ag-Cu: Effects on joint microstructure and shear strength.* Journal of Electronic Materials, 2004. 53(12): p. 1485-1496.
100. Jenq, S.T., et al., *High strain rate compression behavior for Sn-37Pb eutectic alloy, lead-free Sn-1Ag-0.5Cu and Sn-3Ag-0.5Cu alloys.* Microelectronics Reliability 2009. 49(3): p. 310-317.
101. Shohji, I., et al., *Effect of specimen size and aging on tensile properties of Sn-Ag-Cu lead-free solders.* Materials Transactions, 2008. 49(5): p. 1175-1179.
102. Vianco, P., J. Rejent, and R. Grant, *Development of Sn-based, low melting temperature Pb-free solder alloys.* Materials Transactions, 2004. 45(3): p. 765-775.
103. Vianco, P.T., J.A. Rejent, and J.J. Martin, *The compression stress-strain behavior of Sn-Ag-Cu solder.* Jom-Journal of the Minerals Metals & Materials Society, 2003. 55(6): p. 50-55.
104. Haswell, P.H., Durability Assessment and Microstructural Observations of Selected Solder Alloys, *Ph.D. Dissertation in Mechanical Engineering,*. Vol. Ph.D. Dissertation. 2001, College Park, MD USA: University of Maryland.
105. Wiese, S. and K.J. Wolter. *Creep of thermally aged SnAgCu-solder joints*. 2007.
106. Choi, S., et al., *Creep properties of Sn-Ag solder joints containing intermetallic particles.* JOM-Journal of the Minerals Metals & Materials Society, 2001. 53(6): p. 22-26.
107. Kerr, M. and N. Chawla, *Creep deformation behavior of Sn-3.5Ag solder/Cu couple at small length scales.* Acta Materialia, 2004. 52(15): p. 4527-4535.
108. Mathew, M.D., S. Movva, and K.L. Murty. *Deformation mechanisms in tin and tin-based electronic solder alloys*. 2000: Transtec Publications Ltd.

109. Mathew, M.D., et al., *High temperature deformation characteristics of tin-based solder alloys: Application to electronic packaging*. 2000, Indian Inst Metals. p. 369-379.
110. Mathew, M.D., et al., *Creep deformation characteristics of tin and tin-based electronic solder alloys.* Metallurgical and Materials Transactions a-Physical Metallurgy and Materials Science, 2005. 36A(1): p. 99-105.
111. McCabe, R.J., Fine, M. E., *High creep resistance tin-based alloys for soldering applications.* Journal of Electronic Materials, 2002. 31(11): p. 1276-1282.
112. McCabe, R.J. and M.E. Fine, *Creep of tin, Sb-solution-strengthened tin, and SbSn-precipitate-strengthened tin.* Metallurgical and Materials Transactions a-Physical Metallurgy and Materials Science, 2002. 33(5): p. 1531-1539.
113. Ogawa, T., R. Kaga, and T. Ohsawa, *Microstructure and mechanical properties predicted by indentation testing of lead-free-solders.* Journal of Electronic Materials, 2005. 34(3): p. 311-317.
114. Park, C., et al., *A comparison of impression and compression creep behavior of polycrystalline Sn.* Journal of Materials Science, 2007. 42(13): p. 5182-5187.
115. Plumbridge, W.J., C.R. Gagg, and S. Peters, *The creep of lead-free solders at elevated temperatures.* Journal of Electronic Materials, 2001. 30(9): p. 1178-1183.
116. Song, H.G., J.W. Morris, and F. Hua, *Anomalous creep in Sn-rich solder joints.* Materials Transactions, 2002. 43(8): p. 1847-1853.
117. Song, H.G., J.W. Morris, and F. Hua, *The creep properties of lead-free solder joints.* Jom-Journal of the Minerals Metals & Materials Society, 2002. 54(6): p. 30-32.
118. Xiao, Q. and W.D. Armstrong, *Tensile creep and microstructural characterization of bulk Sn3.9Ag0.6Cu lead-free solder.* Journal of Electronic Materials, 2005. 34(2): p. 196-211.
119. Xiao, Q., L. Nguyen, and W.D. Armstrong, *Anomalously high tensile creep rates from thin cast Sn3.9Ag0.6Cu lead-free solder.* Journal of Electronic Materials, 2005. 34(7): p. 1065-1075.
120. Chen, T. and I. Dutta, *Effect of Ag and Cu concentrations on the creep behavior of Sn-based solders.* Journal of Electronic Materials, 2008. 37(3): p. 347-354.
121. Dutta, I., et al., *Effect of thermo-mechanically induced microstructural coarsening on the evolution of creep response of SnAg-based microelectronic solders.* Materials Science and Engineering A - Structural Materials Properties Microstructure and Processing, 2005. 410 (Sp. Iss. SI): p. 48-52.
122. Guo, F., et al., *Evaluation of creep behavior of near-eutectic Sn-Ag solders containing small amount of alloy additions.* Materials Science and Engineering a-Structural Materials Properties Microstructure and Processing, 2003. 351(1-2): p. 190-199.
123. Long, X., et al., *Deformation behavior of Sn-3.8Ag-0.7Cu solder at intermediate strain rates: Effect of microstructure and test conditions.* Journal of Electronic Materials, 2008. 37(2): p. 189-200.
124. Ohguchi, K. and K. Sasaki, *Description of temperature dependence and creep deformation of 60 Sn-40Pb solder alloys.* Jsme International Journal Series a-Solid Mechanics and Material Engineering, 2001. 44(1): p. 82-88.

125. Shen, J., et al., *Effects of rapid solidification on the microstructure and microhardness of a lead-free Sn-3.5Ag solder.* Rare Metals, 2006. 25(4): p. 365-370.
126. Fossum, A.F., et al., *A practical viscoplastic damage model for lead-free solder.* Journal of Electronic Packaging, 2006. 128(1): p. 71-81.
127. Pierce, D.M., et al., *Development of the damage state variable for a unified creep plasticity damage constitutive model of the 95.5Sn-3.9Ag-0-6Cu lead-free solder.* Journal of Electronic Packaging, 2008. 130(1): p. 10.
128. Chaparala, S., et al.,, *Effect of Geometry and Temperature Cycle on the Reliability of WLCSP Solder Joints,* IEEE CPMT Transactions, September 2005. 28(3).
129. Lee, J.G. and K.N. Subramanian, *Effect of dwell times on thermomechanical fatigue behavior of Sn-Ag-based solder joints.* Journal of Electronic Materials, 2003. 32(6): p. 523-530.
130. Lee, J.G. and K.N. Subramanian, *Microstructural features contributing to enhanced behaviour of Sn-Ag based solder joints.* Soldering & Surface Mount Technology, 2005. 17(1): p. 33-39.
131. Osterman, M.D., A, *Life expectancies of Pb-free SAC solder interconnects in electronic hardware.* Journal of Material Sciences, 2007. 18: p.:229-236.
132. Rhee, H., K. Subramanian, and A. Lee, *Role of imposed cyclic straining on the stress relaxation behavior of eutectic Sn-3.5Ag solder joints.* Journal of Materials Science-Materials in Electronics, 2005. 16(3): p. 169-176.
133. Rhee, H. and K.N. Subramanian, *Effects of prestrain, rate of prestrain, and temperature on the stress-relaxation behavior of eutectic Sn-3.5Ag solder joints.* Journal of Electronic Materials, 2003. 32(11): p. 1310-1316.
134. Rhee, H. and K.N. Subramanian, *Roles of imposed cyclic strain amplitude and cyclic strain rate on the stress relaxation behaviour of pre-strained eutectic Sn-MAg solder joints.* Soldering & Surface Mount Technology, 2006. 18(1): p. 19-28.
135. Subramanian, K.N., *Assessment of factors influencing thermomechanical fatigue behavior of Sn-based solder joints under severe service environments.* Journal of Materials Science-Materials in Electronics, 2007. 18(1-3): p. 237-246.
136. Bang, W.H., et al., *The correlation between stress relaxation and steady-state creep of eutectic Sn-Pb.* Journal of Electronic Materials, 2005. 34(10): p. 1287-1300.
137. Jadhav, S.G., et al., *Stress relaxation behavior of composite and eutectic Sn-Ag solder joints.* Journal of Electronic Materials, 2001. 30(9): p. 1197-1205.
138. Yang, F.Q., L.L. Peng, and K. Okazaki, *Impression stress relaxation of Sn3.5Ag eutectic alloy.* Journal of Materials Research, 2006. 21(10): p. 2653-2659.
139. Zimprich, P., et al., *Constraining Effects of Lead-Free Solder Joints During Stress Relaxation.* Journal of Electronic Materials, 2009. 38(3): p. 392-399.
140. Arrowwood, R., *Stress Relaxation of a Eutectic Alloy in Superplastic Condition.* Material Science and Engineering, 92 (1987) pp 23-32 and 33-40, 1987. 92: p. 23-40.
141. Kashyap, P., Material Science Engineering, 1981. 50: p. 205.

142. Jud, P.P., et al., *Local fatigue in lead-free SnAg3.8Cu0.7 solder.* Advanced Engineering Materials, 2006. 8(3): p. 179-183.
143. Kanchanomai, C., Y. Miyashita, and Y. Mutoh, *Low-cycle fatigue behavior and mechanisms of a lead-free solder 96.5Sn/3.5Ag.* Journal of Electronic Materials, 2002. 31(2): p. 142-151.
144. Kanchanomai, C., Y. Miyashita, and Y. Mutoh, *Low-cycle fatigue behavior of Sn-Ag, Sn-Ag-Cu, and Sn-Ag-Cu-Bi lead-free solders.* Journal of Electronic Materials, 2002. 31(5): p. 456-465.
145. Kanchanomai, C., et al., *Low cycle fatigue and fatigue crack growth behaviour of Sn-Ag eutectic solder.* Soldering and Surface Mount Technology 2002. 14(3): p. 30-36.
146. Kanchanomai, C. and Y. Mutoh, *Effect of temperature on isothermal low cycle fatigue properties of Sn-Ag eutectic solder.* Materials Science and Engineering a-Structural Materials Properties Microstructure and Processing, 2004. 381(1-2): p. 113-120.
147. Kanchanomai, C. and Y. Mutoh, *Fatigue crack initiation and growth in solder alloys.* Fatigue & Fracture of Engineering Materials & Structures, 2007. 30(5): p. 443-457.
148. Kanda, Y., Y. Kariya, and Y. Mochizuki, *Effect of hold time on low cycle fatigue life of micro solder joint.* Materials Transactions, 2008. 49(7): p. 1524-1530.
149. Kariya, Y., Y. Hirata, and M. Otsuka, *Effect of thermal cycles on the mechanical strength of quad flat pack leads/Sn-3.5Ag-X (X = Bi and Cu) solder joints.* Journal of Electronic Materials 1999. 28(11): p. 1263-1269.
150. Kariya, Y., et al., *Low cycle fatigue properties of Ni added low silver content Sn-Ag-Cu flip chip interconnects.* Materials Transactions, 2004. 45(3): p. 689-694.
151. Kariya, Y., et al., *Effect of silver content on the shear fatigue properties of Sn-Ag-Cu flip-chip interconnects.* Journal of Electronic Materials, 2004. 33(4): p. 321-328.
152. Kariya, Y., et al., *Isothermal fatigue properties of Sn-Ag-Cu alloy evaluated by micro size specimen.* Materials Transactions, 2005. 46(11): p. 2309-2315.
153. Kariya, Y. and M. Otsuka, *Mechanical fatigue characteristics of Sn-3.5Ag-X (X = Bi, Cu, Zn and In) solder alloys.* Journal of Electronic Materials 1998. 27(11): p. 1229-1235.
154. Kariya, Y. and T. Suga, *Low-cycle fatigue properties of eutectic solders at high temperatures.* Fatigue & Fracture of Engineering Materials & Structures, 2007. 30(5): p. 413-419.
155. Kato, H. and H. Kobayashi, *Acoustic Microscopy of Interfacial Crack in Sn-Ag-Cu Alloy Solder Joints under Shear Fatigue Testing.* Materials Transactions, 2008. 49(9): p. 2068-2075.
156. Lee, K.O., Yu, J., Park, T. S., and Lee, S.B., *Low -Cycle Fatigue Characteristics of Sn-Based Solder Joints. Journal of Electronic Materials,* 2004. 33: p. 249-257

157. Lin, C.K. and C.M. Huang, *Effects of strain ratio and tensile hold time on low-cycle fatigue of lead-free Sn-3.5Ag-0.5Cu solder.* Journal of Electronic Materials, 2006. 35(2): p. 292-301.
158. Nozaki, M., et al., *Creep-fatigue life evaluation for Sn-3.5Ag solder.* Journal of Engineering Materials and Technology-Transactions of the Asme, 2006. 128(2): p. 142-150.
159. Pang, J.H.L., B.S. Xiong, and T.H. Low, *Low cycle fatigue models for lead-free solders.* Thin Solid Films 2004. 462: p. 408-412.
160. Pierce, D.M., et al., *Development of the damage state variable for a unified creep plasticity damage constitutive model of the 95.5Sn-3.9Ag-0-6Cu lead-free solder.* Journal of Electronic Packaging, 2008. 130(1).
161. Shang, J.K., et al., *Mechanical fatigue of Sn-rich Pb-free solder alloys.* Journal of Materials Science-Materials in Electronics, 2007. 18(1-3): p. 211-227.
162. Wei, Y., et al., *Isothermal fatigue damage model for lead-free solder.* International Journal of Damage Mechanics 2006. 15(2): p. 109-119.
163. Zeng, Q.L., et al., *Cyclic softening of the Sn-3.8Ag-0.7Cu lead-free solder alloy with equiaxed grain structure.* Journal of Electronic Materials, 2005. 34(1): p. 62-67.
164. Upadhyayula, K., *PhD Thesis*, in *Mechanical Engineering*. 1999, University of Maryland: College Park.
165. Arzt, E. and D.S. Wilkinson, *Threshold Stresses for Dislocation Climb over Hard Particles - The Effect of an Attractive Interaction.* Acta Metallurgica, 1986. 34(10): p. 1893-1898.
166. Besterci, M. and J. Cadek, *Creep in dispersion strengthened materials on Al basis prepared by powder metallurgy.* High Temperature Materials and Processes, 2004. 23(1): p. 51-57.
167. Cadek, J., K. Kucharova, and K. Milicka, *Creep in copper dispersion strengthened with fine alumina particles and reinforced with alumina short fibres - an ODS copper matrix composite.* Journal of Alloys and Compounds, 2004. 378(1-2): p. 123-126.
168. Gibeling, J.C. and W.D. Nix, *The Description of Elevated-Temperature Deformation in Terms of Threshold Stresses and Back Stresses - A Review.* Materials Science and Engineering, 1980. 45(2): p. 123-135.
169. Gittus, J.H., *Theoretical Equation For Steady-State Dislocation Creep In A Material Having A Threshold Stress.* Proceedings of the Royal Society of London Series a-Mathematical Physical and Engineering Sciences, 1975. 342(1629): p. 279-287.
170. Karnesky, R.A., L. Meng, and D.C. Dunand, *Strengthening mechanisms in aluminum containing coherent Al3Sc precipitates and incoherent Al2O3 dispersoids.* Acta Materialia, 2007. 55(4): p. 1299-1308.
171. Kaschner, G.C. and J.C. Gibeling, *Evolution of dislocation glide kinetics during cyclic deformation of copper.* Acta Materialia, 2002. 50(3): p. 653-662.
172. Mackerle, J., *Creep and creep fracture/damage finite element modelling of engineering materials and structures: an addendum.* International Journal of Pressure Vessels and Piping, 2004. 81(5): p. 381-392.

173. Martin, J.L., M. Morris, and M. Carrard, *Structure and Properties Of Creep Subboundaries.* Journal De Physique, 1985. 46(NC-4): p. 417-422.
174. Miracle, D.B., *Metal matrix composites - From science to technological significance.* Composites Science and Technology, 2005. 65(15-16): p. 2526-2540.
175. Orlova, A. and J. Cadek, *Dislocation-Structures and Structural Steady-State in Steady-State Creep.* Materials Science and Engineering, 1986. 81(1-2): p. 371-377.
176. Orlova, A. and J. Cadek, *Dislocation-Structure in the High-Temperature Creep of Metals and Solid-Solution Alloys - A Review.* Materials Science and Engineering, 1986. 77(1-2): p. 1-18.
177. Orlova, A. and J. Cadek, *On Roesler and Arzt's new model of creep in dispersion strengthened alloys.* Acta Metallurgica et Materialia; (United States): 40:8, 1992: p.: 1865-1871.
178. Rosler, J., *Particle strengthened alloys for high temperature applications: strengthening mechanisms and fundamentals of design.* International Journal of Materials & Product Technology, 2003. 18(1-3): p. 70-90.
179. Rosler, J. and M. Baker, *A theoretical concept for the design of high-temperature materials by dual-scale particle strengthening.* Acta Materialia, 2000. 48(13): p. 3553-3567.
180. Tiziani, C., M. Gotting, and J. Rosler, *Processing and mechanical behaviour of a dual scale particle strengthened copper composite.* International Journal of Materials Research, 2006. 97(11): p. 1579-1585.
181. Yawny, A. and G. Eggeler, *Assessment of back stress and load transfer approaches for rationalizing creep of short fiber reinforced aluminum alloys.* Materials Science and Engineering A-Structural Materials Properties Microstructure and Processing 2004. 387: p. 905-909.
182. Rosler, J. and E. Arzt, *A New Model-Based Creep Equation for Dispersion Strengthened Materials.* Acta Metallurgica Et Materialia, 1990. 38(4): p. 671-683.
183. Zhang, Q., Sharma, P. and Dasgupta A. *Prediction of Rate-Dependent Constitutive Behaviorof Pb-Free Solders*. in Proc. Int. Mech. Eng. Congr. Expo. 2003: ASME.
184. Mura, T., *Micromechanics of Defects in Solids* 2nd edition ed, ed. Springer. 1987. 608.
185. Qu, J.M., *Fundamentals of Micromechanics of Solids*. 2006: Wiley
186. Sharma, P., et al., *Prediction of rate-independent constitutive behavior of Pb-free solders based on first principles.* IEEE Transactions on Components and Packaging Technologies, 2003. 26(3): p. 659-666.
187. Erinc, M., P.J.G. Schreurs, and M.G.D. Geers, *Intergranular thermal fatigue damage evolution in SnAgCu lead-free solder.* Mechanics of Materials, 2008. 40(10): p. 780-791.
188. Geers, M.G.D., et al., *Multiscale analysis of microstructural evolution and degradation in solder alloys.* International Journal for Multiscale Computational Engineering 2007. 5(2): p. 93-103.

189. Ubachs, R., P.J.G. Schreurs, and M.G.D. Geers, *Elasto-viscoplastic nonlocal damage modelling of thermal fatigue in anisotropic lead-free solder.* Mechanics of Materials, 2007. 39(7): p. 685-701.
190. Zamiri, A., T.R. Bieler, and F. Pourboghrat, *Anisotropic Crystal Plasticity Finite Element Modeling of the Effect of Crystal Orientation and Solder Joint Geometry on Deformation after Temperature Change.* Journal of Electronic Materials 2009. 38 (2): p. 231-240.
191. http://www.nemi.org/newsroom/PR/2000/PR012400.html, N.E.M.I.N.P.R. Jan. 24 2000.
192. Enke, N.F., Kilinski, T.J., Schroeder, S.A., Lesniak, J.R., *Mechanical Behaviors of 60/40 Tin-lead Solder Lap Joints.* IEEE Trans. CHMT, 1989. 12(4): p. 459-468.
193. Solomon, H.D., *Strain-Life Behavior in 60/40 Solder.* ASME Trans. J. Electronic Packaging, 1989. 111: p. 75-82.
194. Mathew, M.D., S. Movva, and K.L. Murty, *Deformation mechanisms in tin and tin-based electronic solder alloys.* Creep and Fracture of Engineering Materials and Structures, 2000. 171 (1): p. 655-662.
195. Holdermann, K., Cuddalorepatta, G., Dasgupta, A., *Dynamic Recrystallization of Sn3.0Ag0.5Cu Pb-Free Alloy*, in Proceedings of the ASME International Mechanical Engineering Congress and Exposition, Boston, MA, Paper No. 67671. 2008.
196. Telang, A.U. and T.R. Bieler, *Characterization of microstructure and crystal orientation of the tin phase in single shear lap Sn-3.5Ag solder joint specimens.* Scripta Materialia, 2005. 52(10): p. 1027-1031.
197. Henderson, D.W., Woods, J. J., , *The microstructure of Sn in neareutectic Sn-Ag-Cu alloy solder joints and its role in thermomechanical fatigue.* Journal of Materials Research, 2004. 19(6): p. 1608-1612.
198. Ohguchi, K.I., K. Sasaki, and M. Ishibashi, *A quantitative evaluation of time-independent and time-dependent deformations of lead-free and lead-containing solder alloys.* Journal of Electronic Materials, 2006. 35(1): p. 132-139.
199. Herkommer, D., Reid, M., Punch, J., *In Situ Optical Creep Observation of Joint-Scale Tin–Silver–Copper Solder Shear Samples.* Journal of Electronic Materials, 2009. 38(10): p. 2085 - 2095.
200. Garofalo, F., *Fundamentals of Creep and Creep-Rupture in Metals.* . 1965, New York & C. : McMillan.
201. Humphreys, F.J. and M. Hatherly, *Recrystallization and Related Annealing Phenomena*. 2 ed. 2004: Elsevier Ltd.
202. Mueller, M., Wiese, S., *The Twinning Phenomenon in SnAgCu Solder Balls*, in *Proceedings of ECTC* 2009: San Diego.
203. Ding, Y., C.Q. Wang, and M.Y. Li, *Scanning electron microscope in-situ investigation of fracture behavior in 96.5Sn3.5Ag lead-free solder*. Journal of Electronic Materials, 2005. 34(10): p. 1324-1335.
204. Ding, Y., et al., *Evolution of deformation near the triple point of grain junctions in Sn-based solders during in situ tensile test.* Materials Letters, 2005. 59(6): p. 697-700.

205. Frost, H. and M. Ashby, *Deformation-Mechanism Maps: The Plasticity and Creep of Metals and Ceramics* 1982, Oxford: Pergamon.
206. Cuddalorepatta, G., Dasgupta, A., *Cyclic Mechanical Durability of Sn3.0Ag0.5Cu Pb-Free Solder Alloy*, in Proceedings of the ASME International Mechanical Engineering Congress and Exposition, Orlando, FL, Paper No. 81171. 2005.
207. Raj, R., *Nucleation of Cavities at Second Phase Particles in Grain Boundaries.* Acta Metallurgica, 1978. 26.
208. Tvergaard, V., *On the Creep Constrained Diffusive Cavitation of Grain Boundary Facets.* Journal of Mechanics of Physics of Solids, 1984. 32: p. pp. 373-393.
209. Tvergaard, V.H., Y.; and Hutchinson, J.W., *Cavitation instabilities in a power hardening elastic-plastic solid.* European Journal of Mechanics, A/Solids, 1992. 11(2): p. pp. 215-31.
210. Arzt, E. and E. Gohring, *A model for dispersion strengthening of ordered intermetallics at high temperatures.* Acta Materialia, 1998. 46(18): p. 6575-6584.
211. Schroder, J.H.a.E.A., *Weak Beam Studies of Dislocation Dispersoid Interaction in an ODS Superalloy.* Scripta Metallurgica, 1985. 19(9): 1129.
212. Matin, M.A., et al., *Correlation between localized strain and damage in shear-loaded Pb-free solders.* Microelectronics Reliability, 2007. 47(8): p. 1262-1272.
213. Matin, M.A., W.P. Vellinga, and M.G. D Geers, *Thermomechanical fatigue damage evolution in SAC solder joints.* Materials Science and Engineering a-Structural Materials Properties Microstructure and Processing, 2007. 445: p. 73-85.
214. Subramanian, K.N., *Role of anisotropic behaviour of Sn on thermomechanical fatigue and fracture of Sn-based solder joints under thermal excursions.* Fatigue & Fracture of Engineering Materials & Structures, 2007. 30(5): p. 420-431.
215. Rosler, J., and Arzt, E., Acta Metallurgica, 1988. 36.
216. Adeva, P., Caruana, G.,, *Microstructure and high temperature mechanical properties of tin.* Material Science and Engineering A, 1995. 194(17-23).
217. E. Fraizier, M.H.N., R. Oltra, , Jpn. J. Appl. Phys., 2003. 93p. 649
218. Dragone, T.L.a.N., W. D., Acta metall. mater., 1990. 38: p. 1941.
219. Bao, G., Hutchinson, J. W. and McMeeking, R. M., Acta metall., 1991. 39: p. 1871.
220. Chawla, J., MtlSc:MatElect, 2007. 18: p. 175-189.
221. Rangaraj, S., Kokini, K., *Time-dependent behavior of Ceraminc(Zirconia)-Metal (NiCoCrAlY) Particulate Composites.* Mechanics of Time-dependent Materials, 2002. 6: p. 171.
222. Cuddalorepatta, G., M. Williams, and A. Dasgupta, *Viscoplastic Creep Response and Microstructure of As-fabricated Microscale Sn3.0Ag0.5Cu Solder Interconnects.* Journal of Electronic Materials, 2010.
223. W. Koster, Z. Metallkd., 1948. 39, 1.
224. Hull D, B.D., *Introduction to dislocations. 4th ed.*. 2001: Butterworth-Heinemann.

225. Dutta, I., P. Kumar, and G. Subbarayan, *Microstructural coarsening in Sn-Ag-based solders and its effects on mechanical properties.* Jom, 2009. 61(6): p. 29-38.
226. Lee, J.G., et al., *Residual-mechanical behavior of thermomechanically fatigued Sn-Ag based solder joints.* Journal of Electronic Materials, 2002. 31(9): p. 946-952.
227. Bang, W.H.e.a., *The Correlation Between Stress Relaxation And Steady State Creep Of Eutectic Sn-Pb.* Journal of Electronic Materials, 2005. 34(10): p. pp. 1287-1300.
228. Yang, F.Q., *Impression Stress Relaxation of Sn3.5Ag Eutectic Alloy.* J. of Mater. Res, 2006. 21(10): p. 2653-59.
229. Li, J.C.M., *Stress relaxation and creep in an impression test.* Journal of Electronic Materials 1997. 26(7): p. 827-832.
230. Okura, J.H., *Effects of temperature and moisture on durability of low cost flip chip on board (FCoB) Assemblies*, in *Ph.D. dissertation in Mechanical Engineering*. 2001, University of Maryland: College Park, MD.
231. Ladani, L., in *Mechanical Engineering*. 2009, University of Maryland: College Park.
232. Kachanov, L.M., *Continuum Damage Mechanics*. 1986: Martinus Nijhoff Publishers.
233. Ladani, L., Dasgupta, A., International Journal of Fatigue, 2009. 31: p. 703.
234. Skrzypek, J.J., *Plasticity and Creep: Theory, Examples andProblems*. 1993: CRC Press Inc.
235. NIST, M.S.E.L., Database on Solder Properties, http://www.metallurgy.nist.gov/solder/clech/Sn-Ag-Cu_Other.htm#Young.
236. Clech, J.-P., "An Extension of the Omega Method to Primary and Tertiary Creep of Lead-Free Solders", *An Extension of the Omega Method to Primary and Tertiary Creep of Lead-Free Solders*, in IEEE Electronics Components and Technology Conference, 2005. p. 1260.
237. Rafanelli, A.J. *Thermo-Mechanical Creep Characteristics of Electrically Conductive Epoxy Adhesives at Room Temperature*. in IEEE Intersociety Conference on Thermal Phenomena 1996.
238. Li, J.C.M., *Negative Creep and Mechanochemical Spinodal in Amorphous Metals.* Materials Science and Engineering, 1988. 98: p. 465-468.
239. Van Petegem, S., et al., *Internal and effective stresses in nanocrystalline electrodeposited Ni.* Applied Physics Letters, 2006. 89(7).
240. Vianco, P.T. and J.A. Rejent, *Dynamic Recrystallization (DRX) as the Mechanism for Sn Whisker Development. Part II: Experimental Study.* Journal of Electronic Materials, 2009. 38(9): p. 1826-1837.
241. Clech, J.-P., " An Extension of the Omega Method to Primary and Tertiary Creep of Lead-Free Solders", *An Extension of the Omega Method to Primary and Tertiary Creep of Lead-Free Solders*, in IEEE Electronic Components and Technology Conference, 2005 p. 1260.
242. Barry, B.T.K., Thwaites, C. J., *Tin and Its Alloys and Compounds*. 1993: Chichester : Ellis Horwood ; New York : Halsted Press.